Immuno-PET: a navigator in antibody development and applications

Perk, L.R.

2009

document version
Publisher's PDF, also known as Version of record

Immuno-PET: a navigator in antibody development and applications

Lars Rutger Perk

The work described in this thesis was performed at the Section Tumor Biology, Department of Otolaryngology/Head and Neck Surgery, VU University Medical Center, Amsterdam, The Netherlands. The research presented in this thesis was financially supported by the Dutch Technology Foundation (STW, Grant VBC.6120).

Printing of this thesis was financially supported by BV Cyclotron VU.

Cover: Antibodies targeting a tumor. Antibodies and tumors were designed by Heleen Verreijt (www.heleenverreijt.nl).

Printed by PrintPartners Ipskamp, Enschede, The Netherlands

ISBN: 9789086593750

VRIJE UNIVERSITEIT

Immuno-PET: a navigator in antibody development and applications

ACADEMISCH PROEFSCHRIFT

ter verkrijging van de graad Doctor aan
de Vrije Universiteit Amsterdam,
op gezag van de rector magnificus
prof.dr. L.M. Bouter,
in het openbaar te verdedigen
ten overstaan van de promotiecommissie
van de faculteit der Geneeskunde
op woensdag 28 oktober 2009 om 13.45 uur
in de aula van de universiteit,
De Boelelaan 1105

door

Lars Rutger Perk

geboren te Sneek

promotoren:	prof.dr. G.A.M.S. van Dongen
	prof.dr. C.R. Leemans
copromotor:	dr. G.W.M. Visser

Contents

All substances are poisonous, there is none that is not a poison; the right dose differentiates a poison from a remedy.
Paracelsus, alchemist and physician, 1538

CHAPTER 1

General introduction and outline of this thesis

Guus A. M. S. van Dongen
Gerard W.M. Visser
Marjolijn N. Lub-de Hooge
Elisabeth G. de Vries
Lars R. Perk

Adapted from:
The Oncologist 2007;12:1379-1389

General Introduction

Recent advances in molecular and cellular biology have facilitated the discovery of novel molecular targets on tumor cells, including key molecules involved in proliferation, differentiation, cell death and apoptosis, angiogenesis, invasion, and metastasis or associated with cancer cell stemness [1]. This knowledge has boosted the design of targeted pharmaceuticals, with monoclonal antibodies (mAbs) forming the most rapidly expanding category. MAbs can be used as disease-specific contrast agents for diagnostic imaging. To date, the U.S. Food and Drug Administration (FDA) has approved five diagnostic mAbs, including four for the detection of cancer. In addition, mAbs are gaining momentum for the use in disease-selective therapy. Presently, 22 mAbs, of which 19 are intact immunoglobulins, have been approved by the FDA for therapy, most of them for systemic treatment of cancer. The yearly sales of mAbs have been estimated at 8 - 10 billion dollars in 2005, and are expected to rise spectacularly to $20-30 billion in 2010 [2]. Hundreds of new mAbs are under development worldwide.

Introduction of immuno-PET, the combination of positron emission tomography (PET) with mAbs, is an attractive novel option to improve diagnostic tumor characterization, because it combines the high sensitivity and resolution of a PET camera with the specificity of a mAb [3]. Immuno-PET is like performing "comprehensive immunohistochemical staining *in vivo*", for which purpose the mAb has to be labeled with a positron emitter to enable visualization with a PET camera. In fact each mAb, targeting a specific tumor cell surface marker or extracellular matrix component, is a candidate for use in immuno-PET. This allows the development of a new generation of mAb-based imaging probes in addition to existing PET tracers, of which the non-tumor-specific metabolic tracer 18-fluoro-2-deoxy-D-glucose (^{18}FDG) is currently used in more than 90% of all PET imaging procedures.

Apart from its imaging capabilities, PET also has potential for quantification of molecular interactions, which is especially attractive when immuno-PET is used as a prelude to therapy with one of the approved mAbs. In a personalized therapeutic approach, immuno-PET enables the confirmation of tumor targeting and the quantification of mAb accumulation (actually radioactivity uptake). Thus, patients might be selected who have the best chance to benefit from expensive mAb-based therapy, while treatment schedules can be adapted to improve treatment efficacy and/or reduce toxicity. Moreover, immuno-PET might also play a role in the efficient selection, characterization and optimization of novel high-potential mAbs or mAb conjugate candidates for diagnosis and therapy.

The Antibody Revolution

A century ago, Paul Ehrlich postulated that a "magic bullet" could be developed to selectively target disease. He envisioned that antibodies could act as such [4]. The introduction of the hybridoma technology for mAb development by Kohler and Milstein in 1975 turned this "magic bullet" concept into a realistic option [5]. With this technology, an unlimited range of mAbs can be obtained against any particular cellular antigen. However, the first generation of mAbs had limitations for clinical use, because their murine origin made them immunogenic. Developments in recombinant DNA technology circumvented this, resulting in the production of chimeric (cmAb), humanized (hmAb) and complete human mAbs. Besides intact mAb molecules (molecular weight ~150 kDa), mAb fragments and engineered variants are also used; these include $F(ab')_2$, F(ab'), Fab, single chain Fv (scFv) [6], and the covalent dimers $scFv_2$ [7], diabodies [8] and minibodies [9] (molecular weights ranging from 25-100 kDa)[10], as well as several types of protein therapeutics based on nontraditional scaffolds [11] such as domain antibodies [12], affibodies [13], nanobodies [14], and anticalins [15] (Figure 1).

Intact mAbs have a long residence time in humans ranging from a few days to weeks, which results in optimal tumor-to-nontumor ratios at 2-4 days post injection (p.i.). In contrast, mAb fragments have a much faster blood clearance. This will result in higher tumor-to-nontumor ratios at earlier time points p.i., but the absolute tumor uptake is often lower. These characteristics in general make intact mAbs the format of choice for therapy, while the optimal format for diagnosis is still under discussion.

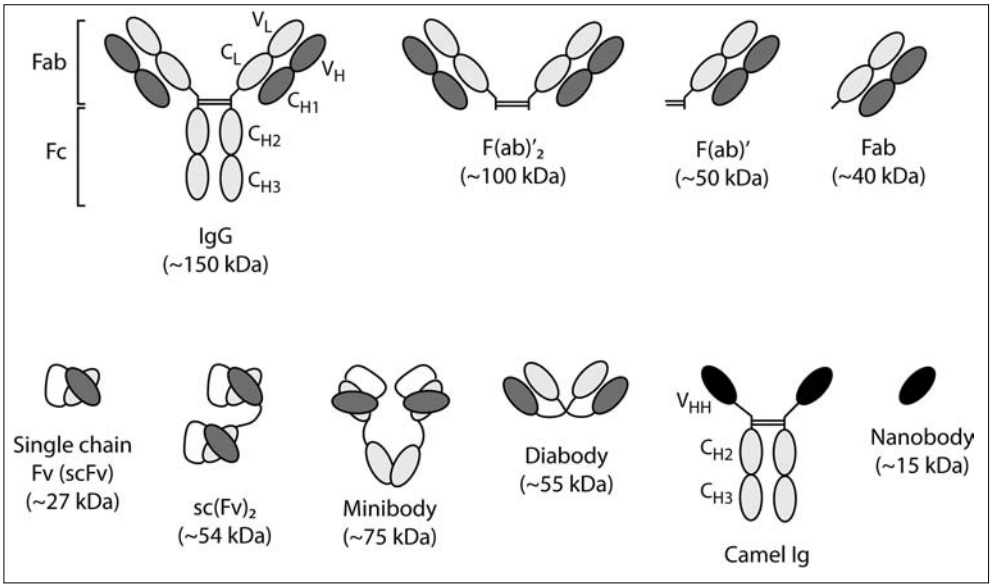

Figure 1. Schematic representation of intact IgG, mAb-fragments, singles chain-based fragments, Camelid heavy-chain only antibody (Camel-Ig) and a Nanobody.

New strategies include the use of pretargeting approaches, which involve separating the targeting antibody from the subsequent delivery of an imaging or therapeutic agent that binds to the tumor-localized antibody [16].

For diagnostic purposes, mAbs have been labeled with γ-emitting radionuclides and imaged with a single photon emission computerized tomography (SPECT) camera. Until now, five technetium-99m-(^{99m}Tc) or indium-111-(^{111}In)-labeled murine mAbs (mmAbs) have been approved by the FDA for diagnostic imaging, of which four are for imaging of cancer [17]. These comprise satumomab pendetide for imaging of ovarian and colorectal cancer (OncoScint™, ^{111}In-IgG binding to the TAG-72 antigen), acritumomab for imaging of colorectal cancer (CEA-Scan™, ^{99m}Tc-F(ab') to CEA), nofetumomab merpentan for imaging small cell lung cancer (Verluma™, ^{99m}Tc-Fab to EPG40) and capromab pendetide for imaging prostate cancer (ProstaScint™, ^{111}In-IgG to PSMA). These early generation diagnostic mAbs are mainly used for staging disease in patients suspected to have recurrent or metastatic disease, but their overall clinical impact has not been impressive thus far. The use of better mAb formats directed against more valuable targets (e.g. also suitable for therapy) in combination with sophisticated cameras for imaging may change this landscape.

Currently, nine mAbs have been approved for cancer therapy, all intact mAbs (Table 1). Five of the mAbs have been approved for treatment of hematological malignancies: rituximab, gemtuzumab ozogamicin, alemtuzumab, ibritumomab tiuxetan, and tositumomab. Four mAbs have been approved for therapy of solid tumors: trastuzumab is used for treatment of metastatic breast cancer; cetuximab, bevacizumab and panitumomab have been approved for treatment of metastatic colorectal cancer; while cetuximab and bevacizumab have also been approved for the treatment of head and neck cancer and non-small cell lung cancer, respectively. These "solid tumor mAbs" are in general most effective when combined with chemo- or radiotherapy. They interfere with signal transduction pathways by targeting growth factors or their receptors, the key drivers of tumor growth and survival. In addition, most of the naked therapeutic mAbs can also act through other effector mechanisms like antibody-dependent cellular cytotoxicity, complement-depending cytotoxicity, or induction of apoptosis.

To enhance its therapeutic potency, gemtuzumab has been armed with the supertoxic drug ozogamicin, while ibritumomab tiuxetan (Zevalin™) and tositumomab (Bexxar™) are radiolabeled mAbs containing the ß⁻-emitters yttrium-90 (^{90}Y) and iodine-131 (^{131}I), respectively. Due to a 'cross-fire' effect radionuclides are especially attractive as warheads to be used in radioimmunotherapy (RIT) since in order to be effective not all tumor cells have to be targeted by radiolabeled mAbs. The therapeutic value of the aforementioned mAbs has been outlined in several excellent reviews [18-20]. Clinical success with the aforementioned therapeutic mAbs has boosted the research and development on new mAbs enormously [21].

Table 1. Therapeutic mAbs approved for cancer treatment [19] (www.fda.gov/cder/biologics/biologics_table.htm).

FDA Approved	Generic name (trade name)	Target	Type	Indication
1997	Rituximab (Rituxan)	CD20	Chimeric IgG1	Lymphoma
1998	Trastuzumab (Herceptin)	HER2/neu	Humanized IgG1	Breast cancer
2000	Gemtuzumab ozogamicin (Myelotarg)[a]	CD33	Humanized IgG4 conjugated to calicheamicin	Acute myeloid leukemia
2001	Alemtuzumab (Campath-1H)	CD52	Humanized IgG1	Chronic lymphatic leukemia
2002	^{90}Y-Ibritumomab tiuxetan (Zevalin)[a]	CD20	^{90}Y-radiolabeled murine IgG1	Non-Hodgkin's lymphoma
2003	^{131}I-Tositumomab (Bexxar)[a]	CD20	^{131}I-radiolabeled murine IgG2a	Non-Hodgkin's lymphoma
2004 2006	Bevacizumab (Avastin)	VEGF	Humanized IgG1	Colorectal cancer Non-small lung cancer
2004 2006	Cetuximab (Erbitux)	EGFR	Chimeric IgG1	Colorectal cancer Head and neck cancer
2006	Panitumumab (Vectibix)	EGFR	Human IgG1	Colorectal cancer

[a]Conjugated antibodies. Abbreviations: CD, cluster of differentiation; HER2/neu, human epidermal growth factor receptor 2; VEGF, vascular endothelial growth factor; EGFR, epidermal growth factor receptor.

Added Value of Antibody Imaging

Despite clinical optimism, it is fair to state that the efficacy of current mAbs is still quite limited, with benefit for just a portion of patients. Moreover, the costs of mAb therapy are excessive, and this issue has become the subject of national discussions regarding the rights of cancer care [22, 23]. The question is how to improve the efficacy of mAb-based therapy and how to identify patients with the highest chance of benefit. In other words: when, how, and for whom should antibody-based therapy be reserved? Stakeholders in these discussions are physicians, pharma and insurance companies, health care authorities and primarily patient groups.

We foresee that quantitative imaging of mAbs could be a valuable tool at several stages of mAb development and application. From first-in-man clinical trials with new mAbs, it is important to learn about the ideal mAb dosing for optimal tumor targeting (e.g. saturation of receptors), the uptake in critical normal organs to anticipate toxicity, and the interpatient variations in pharmacokinetics and tumor targeting. MAb imaging might provide this information in an efficient and safe way, with fewer patients treated at suboptimal doses. This approach is especially attractive when the mAb of interest is directed against a novel tumor target that has not been validated in clinical trials before. Just to exemplify, mAbs directed against new promising tumor cell and tumor stroma targets like c-Met, VEGF receptors, insulin-like growth factor receptors, and death receptors, belong to this category.

Quantitative mAb imaging might also be of value to guide optimal use of FDA approved mAbs. In current practice, tissue analyses are often performed to confirm target expression and to select patients for mAb therapy. For example, patients with metastatic breast cancer are only eligible for therapy with the anti-HER2 mAb trastuzumab, when protein overexpression or gene amplification has been confirmed on a biopsy of the tumor by immunohistochemistry or fluorescence in situ hybridization (in 20-30% of patients [24, 25]). It is questionable, however, whether a representative overview of *in vivo* HER2 expression status can be obtained by analysis of just one single biopsy. It is possible that HER2 expression in primary tumor and metastatic lesions differs, or does not remain stable during the course of the disease for example upon chemo- and/or hormonal therapy [26-29]. Taking multiple or repeated biopsies is not a solution, especially because lesions are often heterogeneous (resulting in non-representative biopsies) and poorly accessible. It is of note that HER2 also has a functional role in normal tissues like the heart. This is probably the explanation for the cardiotoxicity induced by trastuzumab, especially when combined with anthracyclines. Interestingly, shortly after completion of anthracycline treatment, myocardial HER2 over-expression has been demonstarted in 50% of the patients [30]. Therefore, it seems worthwhile to evaluate the value of trastuzumab imaging for prediction of cardiotoxicity [30, 31].

Pretherapy imaging might have added value for patient selection, because it can be used to assess target expression and mAb accumulation in all tumor lesions and normal tissues, non-invasively, quantitatively, and even over time (4D). This information might be particularly relevant when mAb therapy is combined with other treatment modalities like chemo- and radiotherapy in order to find routes for maximum synergism. Ideally, topographic information on tumor extension is obtained to enable assessment of homogeneity of mAb tumor accumulation.

Antibody Imaging: from SPECT to PET

Before PET technology became broadly available, extensive experience has been gained with SPECT camera imaging of mAbs (radioimmunoscintigraphy, RIS). For this purpose, a gamma emitting radionuclide has to be coupled to the mAb, e.g. ^{99m}Tc, ^{111}In, ^{131}I, or rhenium-186 (^{186}Re). The type of information obtained with this technology is illustrated by images from our own archives (Figures 2 and 3) using mAbs that were promising at those days on the basis of preclinical data. Figure 2 shows a planar image obtained with ^{186}Re-cmAb U36 in a patient with a tumor of the oropharynx. cMAb U36 is an antibody directed against CD44v6, a target associated with tumor metastasis and cancer cell stemness**.** cMAb U36 showed selective tumor targeting, and even 14 days p.i. there were still high tumor levels of cmAb U36 [32]. These images justified further development of cmAb U36 and other anti-CD44v6 mAbs for therapeutic purposes [32-35]. This was not the case for a second cmAb called SF-25. cMAb SF-25 had shown a very promising reactivity profile on a large panel of normal and tumor tissues, had demonstrated anti-metastatic potential in tumor-bearing nude mice, but had never been evaluated in patients before [36]. Figure 3 shows an image with ^{99m}Tc-cmAb SF-25 of the first head and neck cancer patient in study [37]. Instead of selective tumor targeting, extensive uptake was observed in the liver, spleen, skeleton, and brain. The latter appeared to be due to mAb cross-reactivity with endothelium of blood vessels in the brain, which had not been noticed in previous immunohistochemical analyses. The massive accumulation in the liver, spleen, and bone marrow can be explained by the reactivity of SF-25 with Kupffer cells in the liver, the red pulpa and follicle centra in the spleen, and cellular components in the sediment of bone marrow aspirates, as was observed in immunohistochemical evaluation of SF-25. This single image led the sponsor of this study decide to discontinue clinical development of this particular mAb.

Although these SPECT camera images were very informative, there was still room for improvements as illustrated by Figure 2. For example, the images did not provide much detail about non-target organs. The fact that the tumor looked much larger than in reality also had to do with limited resolution. No anatomical details are visible. Most importantly, a need for more accurate quantification was a reason to explore the potential of PET for mAb imaging.

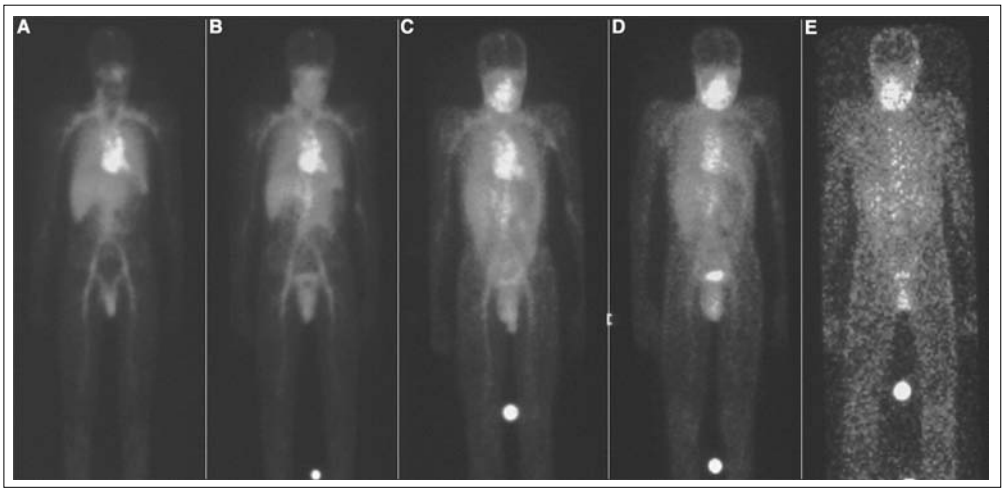

Figure 2. Planar whole body scans acquired 1 (A), 24 (B), 72 (C), 144 (D), and 312 hours (E) after administration of ^{186}Re-cmAb U36 to a patient with a tumor in the right oropharynx. Immediately after injection the mAb resides in the blood pool. Relative uptake of the radioimmunoconjugate in the tumor increases over time, while the tumor becomes better delineated as background activity decreases.

Immuno-PET: Principles and Technical Developments

Immuno-PET is based on coincidence detection of a mAb labeled with a positron-emitting radionuclide. The emitted positron will travel a distance of a few millimeters, depending on the initial positron energy and the density of the surroundings (Table 2). After having lost its kinetic energy, combining with an electron leads to the so-called annihilation process, yielding two photons each with an energy of 511 keV emitted simultaneously in opposite directions. The distribution of a PET conjugate in a patient can be monitored by detection of the annihilated photon pairs with a PET camera. A PET camera consists of a ring of detectors placed around the body of a patient. If two photons are registered by detectors on opposite sides of the body within a very short time interval (typically 5-15 nanoseconds), it is assumed that somewhere along the line between the two detectors an annihilation event has taken place. By calculating the crossing of all lines, the location of the radiation source (radiolabeled mAb) can be determined. For quantification, PET can provide reliable information when appropriate corrections are performed [3].

In 1975, the first real PET scanner containing thallium-doped sodium iodide detectors was developed [38]. Since then, the PET scanner has undergone several improvements with respect to scintillation crystals and system design. Scintillation materials have been developed with much better efficiency for detecting 511 keV photons. One of the most recent achievements is the revival of time-of-flight scanners

[39], after their introduction in the beginning of the 1980s [40]. It is clear that these technical advances will further improve PET sensitivity (less radioactivity needed) and resolution.

To facilitate accurate interpretation of PET images and quantification, PET can be combined with CT or MRI to allow simultaneous registration of both biologic function and anatomy. Currently, approximately 90% of all PET sales comprise PET/CT scanners. Although combining PET with MRI is technologically more challenging because of the strong magnetic fields restricting the use of certain electronic components, the first MRI compatible PET scanners have been developed [41, 42].

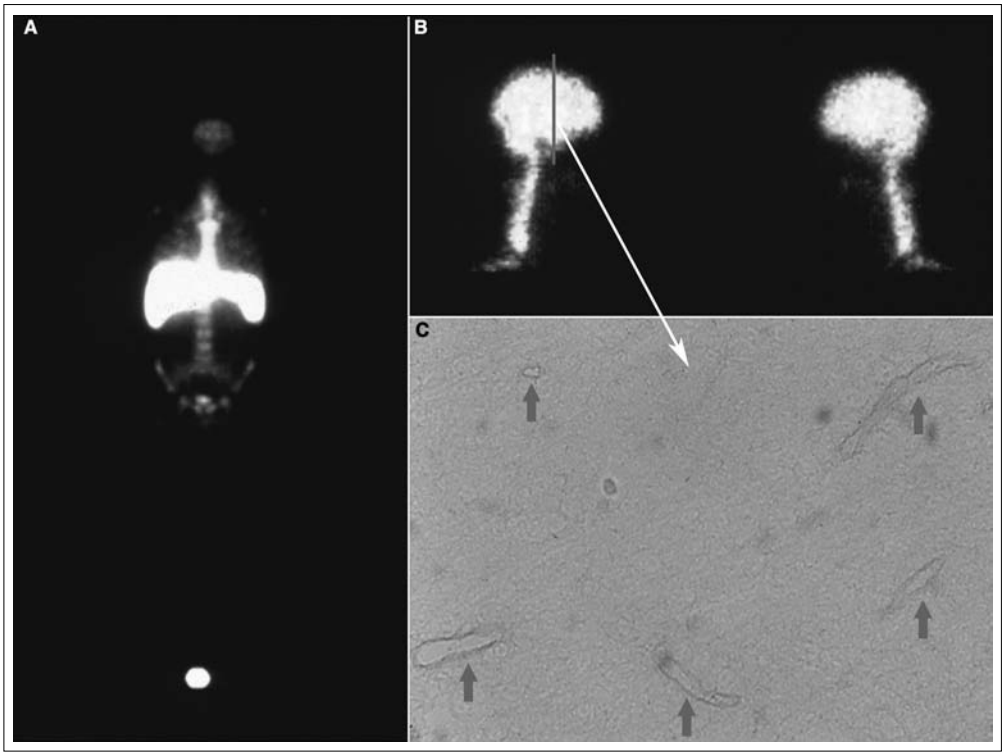

Figure 3. (A) Planar whole body scan acquired immediately after administration of ^{99m}Tc-cmAb SF25 to a patient with a primary tumor in the right tonsil. Note the extensive uptake in liver, spleen and bone marrow. No radioimmunoconjugate is left in the blood pool. (B) Planar right lateral image of the head and neck of the same patient 21 hours p.i., showing activity in the whole brain area. The primary tumor is not visualized. (C) Immunoperoxidase staining of brain tissue with cmAb SF25. There is distinct staining of endothelium of blood vessels.

Table 2. Main characteristics of positron emitters used in preclinical and clinical RIS studies

Positron emitter	Common production routes	Half-life (h)	Main ß$^+$-Energies (keV)	(%)	Intrinsic spatial Resolution loss (mm)
^{68}Ga	^{68}Ge/^{68}Ga-generator	1.13	1899	87.9	2.4
^{18}F	^{18}O(p,n)*	1.83	634	100.0	0.7
^{64}Cu	^{64}Ni(d,2n)*	12.7	653	17.4	0.7
	^{64}Ni(p,n)*				
^{86}Y	^{86}Sr(p,n)*	14.7	1221	11.9	1.8
			1545	5.6	
^{76}Br	^{76}Se(p,n)*	16.2	871	6.3	5.3
			990	5.2	
			3382	25.8	
			3941	6.0	
^{89}Zr	^{89}Y(p,n)‡	78.4	897	22.7	1.0
^{124}I	^{124}Te(p,n)*	100.3	1535	11.8	2.3
	^{124}Te(d,2n)*		2138	10.9	
	^{125}Te(p,2n)*				

‡No enrichment of the target isotope is required

*Using enriched isotopes as target material

Positron Emitters for Immuno-PET

For a positron emitter to be appropriate for immuno-PET, it has to fulfill several requirements. The positron emitter should have appropriate decay characteristics for optimal resolution and quantitative accuracy, its production should be easy and inexpensive, and it should allow facile, efficient, and stable coupling to mAbs. Maintenance of the antibody's *in vivo* binding and biodistribution characteristics is imperative, while the physical half-life ($t_{1/2}$) of the positron emitter should be compatible with the time needed for a mAb or mAb fragment to achieve optimal tumor-to-nontumor ratios (typically 2-4 days and 2-6 hours, respectively).

Given these considerations, the following positron emitters for immuno-PET are under investigation at this moment: gallium-68 (^{68}Ga; $t_{1/2}$: 1.13 hours), fluorine-18 (^{18}F; $t_{1/2}$: 1.83 hours), copper-64 (^{64}Cu; $t_{1/2}$: 12.7 hours), yttrium-86 (^{86}Y; $t_{1/2}$: 14.7 hours), bromine-76 (^{76}Br; $t_{1/2}$: 16.2 hours), zirconium-89 (^{89}Zr; $t_{1/2}$: 78.4 hours), and iodine-124 (^{124}I; $t_{1/2}$: 100.3 hours) (Table 2). While the very short-lived positron

emitters ^{68}Ga and ^{18}F can only be used in combination with mAb fragments, nontraditional scaffolds or in pretargeting approaches, ^{89}Zr and ^{124}I are particularly suitable in combination with intact mAbs, because their long half-life allows imaging at late time points for obtaining maximum information. The long half-life also offers an advantage for logistics related to transportation. A possible disadvantage is an increased radiation burden to patients, estimated at 20-40 mSv when using a 75 MBq radioactivity dose, but this aspect will become less critical when scanners become more sensitive. While the positron emitters ^{76}Br and ^{124}I can be coupled directly to mAbs, the others require indirect labeling methods using bifunctional chelates or other prosthetic groups.

Another important consideration in the choice of a positron emitter is whether the mAb becomes internalized after binding to the target antigen. Degradation of ^{76}Br- and ^{124}I-labeled mAbs upon internalization will result in rapid clearance of these radionuclides from the target cells, and therefore the PET image will show less tumor contrast and will not reflect the actual mAb distribution. In contrast, when ^{68}Ga-, ^{64}Cu-, ^{86}Y-, and ^{89}Zr-labeled mAbs are processed, the positron emitters will be trapped intracellularly in lysosomes. This phenomenon of residualization should be taken into account when selecting a positron emitter for immuno-PET applications. For example, imaging of trastuzumab, cetuximab and bevacizumab can best be performed using a residualizing positron emitter.

Another option is the use of immuno-PET as a scouting procedure for selection of RIT candidate patients on the basis of dosimetry. For this purpose, the radioimmunoconjugates used for immuno-PET and RIT should demonstrate a similar biodistribution, and therefore radionuclides (and if required chelates) with comparable chemical properties have to be chosen. The most commonly used beta emitters in RIT studies are copper-67 (^{67}Cu; $t_{1/2}$: 62 hours), lutetium-177 (^{177}Lu; $t_{1/2}$: 161 hours), ^{90}Y ($t_{1/2}$: 64 hours), and ^{131}I ($t_{1/2}$: 192 hours). Examples of PET/RIT radionuclide pairs are ^{64}Cu/^{67}Cu, ^{124}I/^{131}I, ^{86}Y/^{90}Y, ^{89}Zr/^{177}Lu and ^{89}Zr/^{90}Y.

To allow routine clinical application of immuno-PET, a larger spectrum of positron emitters that are readily available and of clinical grade, e.g. produced according to good manufacturing practice (GMP) guidelines, will be needed. A recent questionnaire, sent to 134 nuclear medicine centers in Europe to evaluate the expectations of European researchers in terms of innovative radionuclides, revealed that positron emitters with a longer half-life that would foster precise quantification of mAb biodistribution within the body were considered to be the most interesting positron-emitting radionuclides for the near future [43, 44].

Production of Positron Emitters

Most of the nowadays clinically applied positron emitters are produced with the aid of a cyclotron. The most widely distributed cyclotrons across research institutes and commercial PET isotope distribution sites are small low-energy biomedical cyclotrons (e.g. CTI RDS 11 MeV cyclotrons; 16 MeV GE PETtrace; 18/9 MeV IBA Cyclone). This latter development has been made possible by focusing on low-energy nuclear reactions. Low-energy nuclear reactions like (p,n) are the best guarantee for efficient production of radioisotopes with control over competing nuclear reactions like (p,2n) that can affect the radionuclidic purity. However, notwithstanding this controlled (p,n) reaction, in order to arrive at a high radionuclidic purity often also isotopically enriched target material is required, which is usually rather expensive (Table 2).

For example, the most widely applied production route for ^{124}I is the ^{124}Te(p,n)^{124}I reaction on highly enriched tellurium-124 [45-48]. The high cost of the enriched target material makes recovery of the target material essential. In contrast, the target material (^{89}Y) for the production of ^{89}Zr is relatively inexpensive, does not

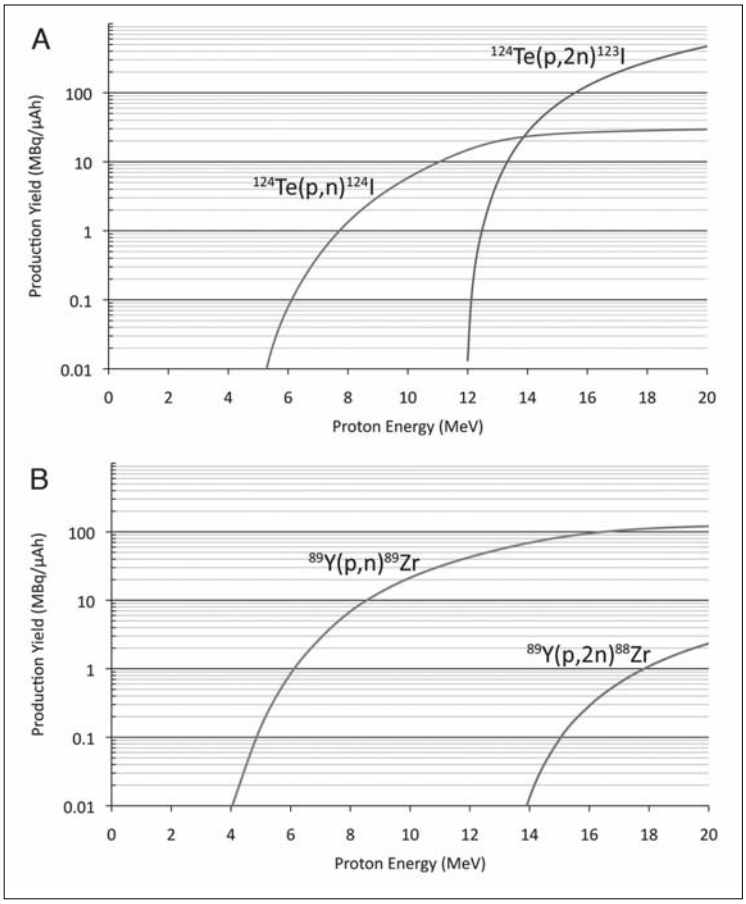

Figure 4. (A) Thick target integral yields of ^{124}I and ^{123}I plotted as a function of proton energy on ^{124}Te. (B) Yields of ^{89}Zr and ^{88}Zr plotted as a function of proton energy on ^{89}Y. The data were calculated using cross-section data for the ^{124}Te(p,n)^{124}I, ^{124}Te(p,2n)^{123}I, ^{89}Y(p,n)^{89}Zr, and ^{89}Y(p,2n)^{88}Zr nuclear reactions, respectively. Assumption: irradiation time << half-life. Courtesy of Frans van Langevelde [105-108].

require enrichment due to its 100% natural abundance, and therefore recycling is not needed [49]. Depending on the incident energy as well as the quality of the enriched target material, competing nuclear reactions will arise resulting in radionuclidic impurities. For instance, above energies of ~12 MeV the ^{124}Te(p,2n)^{123}I will start to compete with the ^{124}Te(p,n)^{124}I reaction resulting in ^{123}I ($t_{1/2}$: 13.2 hours) as a radionuclidic impurity (Figure 4; cross-section data). In this case, a slightly lower enrichment level leads to the formation of ^{125}I ($t_{1/2}$: 59.4 days) from the (p,n) reaction on the ^{125}Te atoms. In the case of ^{89}Zr, a small amount of ^{88}Zr (<0.01%; $t_{1/2}$: 83.4 days) is formed as the result of a (p,2n) reaction on ^{89}Y [49]. But also in this case, formation of ^{88}Zr will increase when a higher incident energy is applied (Figure 4).

In order to be able to produce sufficiently large amounts of the desired radionuclide, the used target materials and target holders should be designed in such a way that they can withstand high beam fluxes of charged particles, i.e., efficient heat distribution and cooling should be applied. Finally, the desired positron emitter has to be separated from the irradiated target material and formed byproducts, while in most cases the target material should be recovered for reuse. This processing step should be efficient in order to obtain the product in high yield and with the highest possible purity (e.g. radionuclidic, radiochemical, and chemical purity). In the case of ^{124}I production, the preferred method involves the irradiation of highly enriched tellurium dioxide (TeO_2) targets [46, 47]. This compound has a relatively low melting point (733°C). However, upon mixing with 5-6% Al_2O_3 (w/w), an improved rigidity upon heating is obtained that helps stabilizing the material during irradiation (48). Separation of ^{124}I from these $^{124}TeO_2$-targets is based on a dry distillation process. A simplified sketch of a quartz distillation apparatus for separation of radioiodine from irradiated $^{124}TeO_2$ targets can be found in Figure 5. An important aspect in this distillation process is the effect of temperature and time on the removal of radioiodine and the unwanted loss of tellurium from the target. Temperatures above ~780°C and a long distillation time leads to enhanced loss of TeO_2 [46].

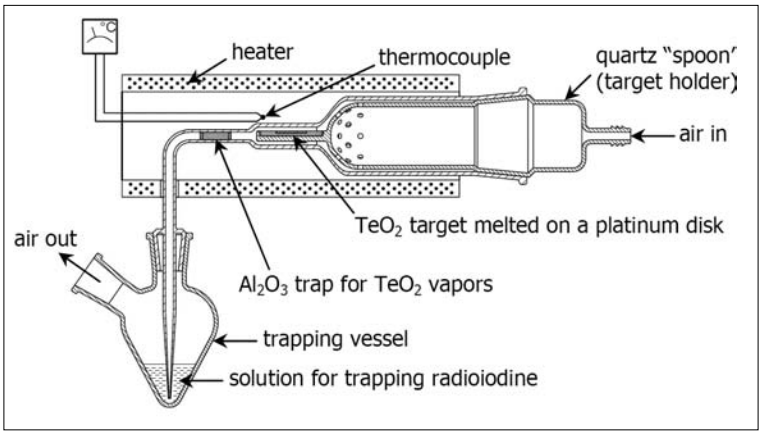

Figure 5. Simplified sketch of quartz distillation apparatus (TERIMO) for thermo-chromatographic separation of ^{124}I from the irradiated $^{124}TeO_2$ targets.

^{89}Zr is separated from the ^{89}Y-target material by first slowly dissolving the target material in 4 M HCl to form $ZrCl_6^{2-}$, followed by purification using a hydroxamate column. After isolation, no-carrier added ^{89}Zr oxalate with a high radionuclidic purity and high yield is obtained [49]. Particle-induced x-ray emission (PIXE) and inductively coupled plasma mass spectroscopy (ICP-MS) analysis of the isolated ^{89}Zr oxalate revealed the absence of unwanted high levels of nonradioactive metals. Metal contaminants such as Fe^{2+} and Al^{3+} can compete with the chelate in the radiolabeling reaction, resulting in low labeling yields.

The clinically interesting short living positron emitter ^{68}Ga forms a special case. ^{68}Ga can be obtained from a commercially available long life-span ^{68}Ge/^{68}Ga-generator (half-life 271 days), making it continuously available even for centers without a cyclotron, and at reasonable costs. Aspects subject of continuing research for wide use of ^{68}Ga in clinical PET are: its chemical form ($GaCl_{6-n}O_n$) and elution volume after being eluted from the generator, the level of ^{68}Ge-breakthrough, and the contamination of the eluate with generator column material [50].

Radiolabeling of mAbs with Positron Emitters

Various methods have been developed that enable efficient labeling of mAbs with the positron emitters ^{68}Ga, ^{18}F, ^{64}Cu, ^{86}Y, ^{76}Br, ^{89}Zr, and ^{124}I. While the positron emitters ^{76}Br and ^{124}I can be coupled directly to mAbs, the others require indirect labeling methods using bifunctional chelates or other prosthetic groups. Bifunctional chelates are compounds that are able to form a stable complex with the radionuclide while containing a reactive group that can be used for coupling to the mAb. During the labeling procedure either the chelate-radionuclide complex can be prepared first, followed by coupling to the mAb (prelabeling method), or the chelate can be coupled to the mAb first, after which the premodified mAb is radiolabeled (postlabeling method). Advantages of the latter method are the often higher overall radiolabeling yields and the possibility to formulate labeling kits, enabling easy use in multicenter trials with low radiation exposure of laboratory personnel.

The most common method for the radioiodination of mAbs involves the covalent attachment of iodine to tyrosine residues in the presence of an oxidizing agent such as *N*-chloro-*p*-toluene-sulfonamide (chloramine-T) or 1,3,4,6-tetrachloro-3α,6α-diphenylglycoluril (IODO-GEN) (Figure 6). A limitation of this iodination method is that upon internalization and lysosomal degradation of the radioiodinated mAb, iodotyrosine residues are formed, which are rapidly excreted out of the cell with distribution (or sequestration) of radioactivity throughout the blood and normal organs [51]. In order to increase tumor retention of radioiodine, novel labeling methods have been developed, wherein a labeled prosthetic group is conjugated to mAbs through modification of lysine ε-amino groups [52]. Labeling yields, however,

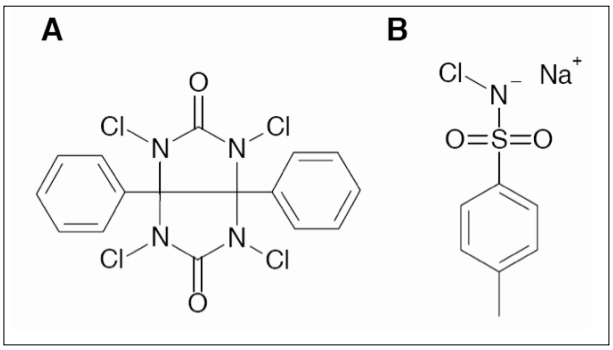

Figure 6. Chemical structures of the oxidants Iodogen (A) and chloramine-T (B). These oxidants are commonly used for radiohalogenation of tyrosine residues of mAbs.

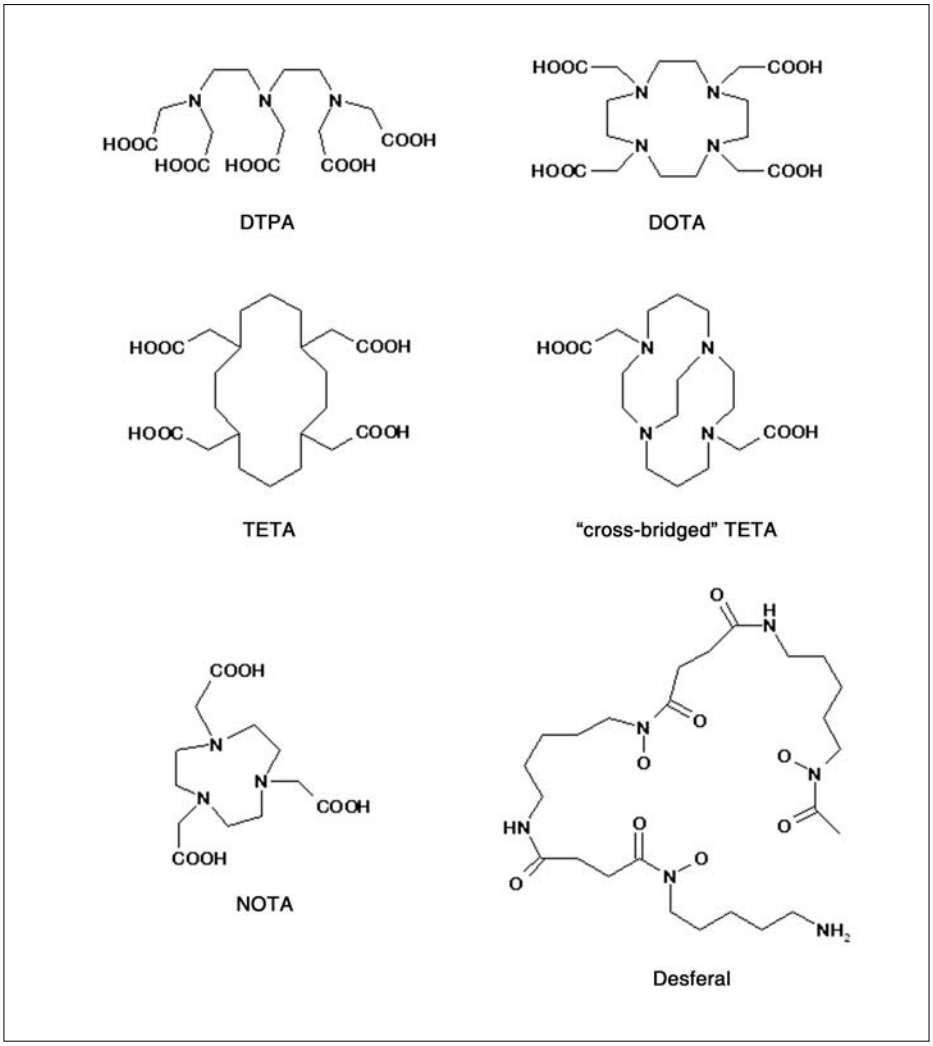

Figure 7. Chemical structures of the chelates DTPA, DOTA, TETA, "cross-bridged" TETA, NOTA and Desferal.

are rather low for these indirect labeling methods. Direct labeling of proteins with bromine also leads to poor cellular retention; moreover, bromide (the major radiocatabolite of directly radiobrominated mAbs) clears slowly from the body [52].

Several strategies for the radiofluorination of proteins have been developed [53]. However, until now, most strategies are characterized by low labeling yield, long radiosynthesis time and loss of immunoreactivity. Recently, Cheng *et al.* [54] developed a method for site-specific radiofluorination of an aminooxy-functionalized protein with an aldehyde-funtionalized ^{18}F-synthon, 4-[^{18}F]fluorobenzaldehyde (4-[^{18}F]FBA). This method had a relatively short radiosynthesis time and a moderate yield (100 min; 13-18% yield).

For the coupling of the positron emitters ^{68}Ga, ^{64}Cu, ^{86}Y, and ^{89}Zr to mAbs, indirect labeling with a bifunctional chelate is the only option. Several acyclic and cyclic bifunctional chelates have been developed for this purpose (Figure 7). The most widely used bifunctional chelates are active ester derivatives of diethylenetriaminepentaacetic acid (DTPA) and 1,4,7,10-tetraazacyclododecane-1,4,7,10-tetraacetic acid (DOTA). Both DTPA and DOTA derivatives have been used for coupling of ^{68}Ga, ^{64}Cu, and ^{86}Y to mAbs. The metallic complexes of the macrocyclic DOTA chelate have generally higher thermodynamic stability and kinetic inertness than those of DTPA, but suffer from the disadvantages that initial formation of the complexes is slower and more difficult. A heating step is therefore often required to achieve high labeling efficiencies, and this can cause problems with thermolabile proteins [55].

Other macrocyclic ligands such as 1,4,7-triazacyclononane-N,N',N''-triacetic acid (NOTA) and 1,4,8,11-tetraazacyclotetradecane-N,N',N'',N'''-tetraacetic acid (TETA) have been reported for binding of radiometals. NOTA is well established to form a very stable complex with Ga(III) [56, 57]. Surprisingly, DOTA seems to remain the preferred chelate for Ga labeling despite the lack of real substantiation as to the stability of the DOTA-Ga(III) complex [58]. The tetraazamacrocyclic ligand TETA has been extensively used as a radioligand for ^{64}Cu [59-61]. Although ^{64}Cu-TETA complexes are more stable than ^{64}Cu-DOTA and ^{64}Cu-labeled complexes of acyclic ligands, their instability *in vivo,* resulting in increased liver uptake, has been well documented [62, 63]. In an attempt to overcome this problem, several new ligand systems, including those based upon the *cis,cis*-1,3,5-triamino-cyclohexane scaffold, the sarcophagine ligands and especially the cross-bridged tetraazamacrocycles, have been developed to complex ^{64}Cu more stably [63].

For stable coupling of ^{89}Zr to mAbs, Verel *et al.* developed a somewhat complicated, yet robust and elegant protocol using the clinically validated chelate desferrioxamine B (Desferal, Df; Novartis) [49]. To this end, Df was initially succinylated, temporarily filled with Fe(III), converted into an active ester (TFP-*N*-

sucDf-Fe), and coupled to a mAb (see Figure 8 for a reaction scheme). After conjugation, the Fe(III) was removed and the premodified mAb was labeled with ^{89}Zr. The resulting ^{89}Zr-mAb conjugates appeared to be optimal with respect to radiochemical purity, integrity, immunoreactivity, and *in vivo* stability [49]. Several (pre)clinical studies have been started with ^{89}Zr-Df-mAb conjugates to evaluate the future perspectives of ^{89}Zr-immuno-PET. It is important to note that Df can also be utilized to stably label proteins with ^{68}Ga.

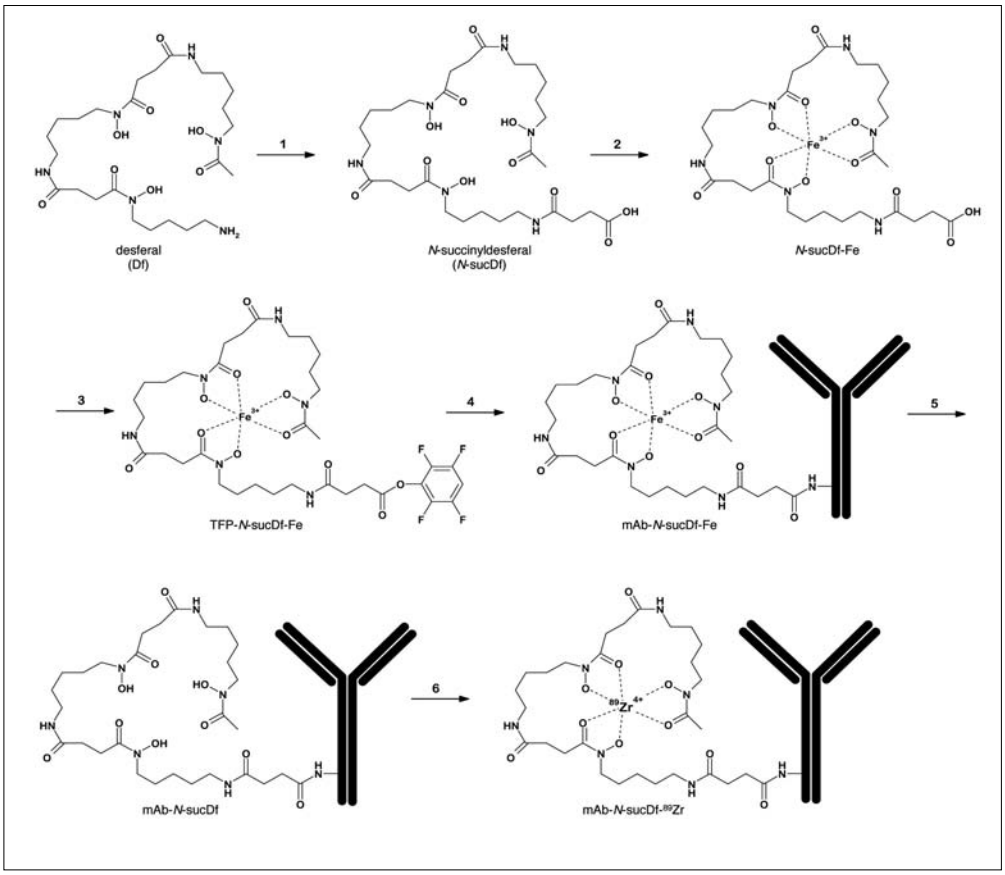

Figure 8. Schematic representation of premodification and postlabeling of mAbs with ^{89}Zr. Step 1 synthesis of *N*-sucDf; Step 2 complexation of *N*-sucDf with Fe(III); Step 3 esterification of *N*-sucDf-Fe; Step 4 conjugation of TFP-*N*-sucDf-Fe to mAb; Step 5 removal of Fe(III) from mAb-*N*-sucDf-Fe; Step 6 labeling of mAb-*N*sucDf with ^{89}Zr. *Desferal* (Df) (Novartis) is term used instead of desferrioxamine B, and *Df-Fe* is term used to represent corresponding iron(III) complex (ferrioxamine).

Good Manufacturing Practices

To translate immuno-PET from preclinical investigation to a phase I clinical trial, it is necessary to create a pharmaceutical quality formulation, manufactured under current good manufacturing practice (cGMP). The European Commission adopted two directives laying down principles and guidelines of GMP for medicinal products. Directive 2003/94/EC applies to medicinal products for human use and Directive 91/412/EEC for veterinary use. Detailed guidelines in accordance with those principles are published in the Guide to Good Manufacturing Practice (http://ec.europa.eu/enterprise/pharma-ceuticals/eudralex/homev4.htm). They are also relevant for all other large-scale pharmaceutical manufacturing processes, such as those undertaken in hospitals, and for the preparation of products for use in clinical trials. Central components discussed in the guide to GMP are:

- Quality management;
- Personnel;
- Facilities and equipment;
- Documentation;
- Production;
- Quality control;
- Storage and distribution.

Meeting GMP requirements is one of the major challenges facing radiopharmaceutical scientists who conduct translational research and work at a university or hospital setting with limited resources [64, 65], especially because of the sometimes-incompatible guidelines between radiation safety aspects and GMP. For example, in order to avoid the spread of radioactive particles, it may be necessary for the air pressure to be lower where products are exposed, compared with the surrounding areas. However, it is still necessary to protect the product from environmental contamination. This may be achieved by using barrier technology or airlocks that act as pressure sinks (Annex 3, Manufacture of radiopharmaceuticals; http://ec.europa.eu/enterprise/pharma-ceuticals/eudralex/homev4.htm). An example of a GMP-facility for production of radiopharmaceuticals can be seen in Figure 9A.

In most cases the radionuclides used for radiolabeling are to be considered as an active pharmaceutical ingredient (API), especially when the final preparation is released for use without further purification (Table 3) [66]. Also the compounds intended to carry or bind the radionuclide (e.g. desferal) are to be considered as an API. API's must comply with the requirements described in GMP part II (http://ec.europa.eu/enterprise/ pharmaceuticals/eudralex/homev4.htm). Quality aspects that must be documented for radionuclides used for labeling are: 1) identification (e.g. half-life, gamma emission spectrum); 2) (radio)chemical purity; 3)

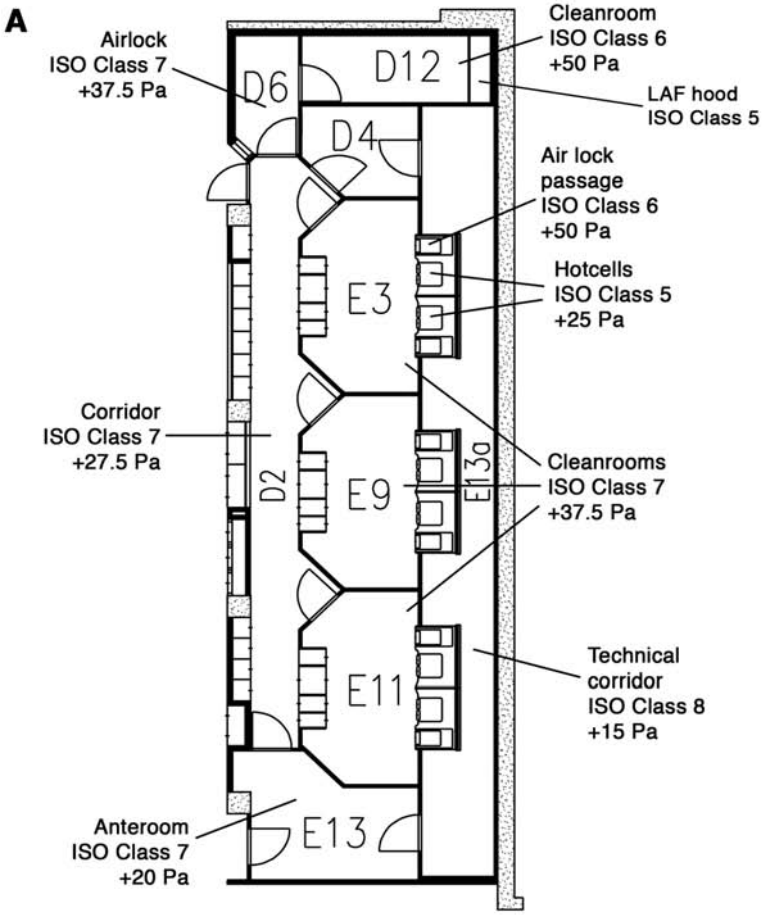

B

FDA vs GMP Air Classifications (in operation)						
FDA	FDA	FDA	GMP	FDA	GMP	GMP
Clean Area Classifications 0.5 µm particles/ft^3	ISO designation	≥0.5 µm particles/m^3	GMP grade	Microbiological Active Air Action Levels (cfu/m^3)		Type of process
100	ISO 5	3520	A	1	<1	Aseptic preparation and filling
1000	ISO 6	35200	not defined	7	not defined	-
10000	ISO 7	352000	B	10	10	Background to grade A
100000	ISO 8	3520000	C	100	100	Preparation of solutions to be filtered
not defined	not defined	not defined	D	not defined	200	Preparation of products to be terminally sterilized

Figure 9. (A) Floor plan and air balance of the cleanroom facility for the production of PET-tracers situated in the Radionuclide Center of the department of Nuclear Medicine & PET research, VU university medical center. (B) FDA guidance (2004), European GMP (Annex 1, 2009) and ISO 14644-1 cleanroom air classifications.

Table 3. GMP requirements for manufacturing of radiopharmaceuticals (Annex 3, http://ec.europa.eu/enterprise/pharmaceuticals/eudralex/homev4.htm).

Type of manufacture	Non-GMP*	GMP part II & I (Increasing) including relevant annexes‡			
Radiopharmaceuticals PET tracers Radioactive Precursors	Reactor/Cyclotron production	Chemical synthesis	Purification steps	Processing, formulation and dispensing	Aseptic or final sterilization
Radionuclide Generators	Reactor/Cyclotron production	Processing			

*Target and transfer system from cyclotron to synthesis rig may be considered as the first step of active substance manufacture.

‡GMP part I: Basic Requirements for Medicinal Products. GMP part II: Basic Requirements for Active Substances used as Starting Materials (API's).

stability data; 4) storage conditions; 5) expiry; 6) batch identity; and 7) impurity profile. Preferably, quality analysis must be performed as described in the pharmacopoeia [67] or otherwise using validated methods.

An example of quality control tests that are performed on a final radioimmunoconjugate at our institute before it is released for use can be found in Table 4. This radioimmunoconjugate has been successfully tested clinically, neither adverse reactions in the patient nor significant changes in blood and urine values were observed [68].

Production of radionuclides and preparation of radiolabeled mAbs should preferably be performed in a dedicated work area, e.g., clean room, isolator and/or LAF-hood. Especially air quality in the processing area should be adequately controlled and monitored to limit the presence of microorganisms and particulate matter. An overview of the current cleanroom air classifications for work areas can be found in Figure 9B

Immuno-PET: State of the Art

Essential tools for immuno-PET have only become available very recently. Most immuno-PET studies have been performed in animal models, while the number of clinical evaluations is rising.

The most widely available positron emitter is ^{18}F, because of its use in ^{18}FDG-PET. With a half-life of 110 minutes, ^{18}F-immuno-PET is restricted to mAb fragments. Efforts have been made on development of ^{18}F-mAb conjugates since 1992 [69], but the inefficient labeling has hampered the routine clinical application until now. Very recently, anti-CEA diabodies were labeled with ^{18}F, and yielded promising high-contrast small animal PET images within a few hours p.i. [70, 71]. Neumaier and colleagues recently developed a ^{18}F-labeled anti-CD66 mAb and presented an

Table 4. Quality control testing of ^{89}Zr-*N*-sucDf-cmAb U36 final product before release.

Test	Specification
Desferal substitution	0.5-2.0 Df/mAb
Labeling efficiency	>80%
Radioactivity	72-78 MBq
Radiochemical purity	>95%
Volume	20-22 ml
Appearance	Clear and colorless
pH	5-6
Size-exclusion HPLC	1 major peak t_R 24 min, both UV and gamma
Receptor binding (Lindmo)	>70%
Apyrogenicity	<5 EU/ml
Pressure hold test on 0.22 µm end-filter	>3.0 bar

intraindividual comparison between PET and conventional scintigraphy using ^{18}F- and ^{99m}Tc-labeled anti-CD66 mAb, respectively [72]. Both labeled antibodies displayed a similar distribution pattern with a high preferential uptake in bone marrow.

Another interesting short-lived positron emitter is ^{68}Ga, because it is easily eluted from a germanium-68 generator, and therefore always readily available. This positron emitter is especially applied in pretargeting strategies [73, 74] and for labeling of small mAb fragments. Pretargeted PET with ^{68}Ga has been evaluated in patients with primary breast cancer. Patients received an anti-MUC1/anti-Ga-chelate bispecific mAb, followed 18 hours later by the ^{68}Ga-chelate [73]. Fourteen of 17 biopsy proven lesions, averaging 25 ± 16 mm in size, were clearly visualized. No false-positive readings were obtained. Albeit the small number of patients, it was concluded that PET offered better sensitivity than conventional RIS for tumor detection. PET imaging with ^{68}Ga-trastuzumab F(ab')$_2$ was used to monitor HER2 expression in animal tumors during treatment with 7-allylaminogeldanamycin, a Hsp90 inhibitor causing HER2 degradation [75]. This study confirmed the potential of quantitative immuno-PET imaging: a linear correlation (R^2 = 0.972) was found between tracer uptake quantified by radioactivity measurement of excised tumors and tracer uptake estimated non-invasively by PET.

In 1995, the anti-colorectal carcinoma mmAb 1A3 was labeled with the longer-lived positron emitter ^{64}Cu using a TETA-chelate and evaluated in 36 patients with suspected advanced primary or metastatic colorectal cancer [76]. Immuno-PET was performed 4 to 36 hours p.i., and all patients underwent CT or MRI. In 29 patients, all 17 primary and recurrent sites were clearly visualized, and 23 of 39 metastases were detected. Absence of tumor was confirmed in five patients, while tumor status was not confirmed in two patients. Interestingly, 11 new occult tumor sites were

detected by immuno-PET. The sensitivity of immuno-PET was best in the abdomen and pelvis. Detection of metastases in the liver and lung, the most important sites of this disease, was difficult because of high blood-pool activity at the early imaging time points, which were chosen because of the short half-life of ^{64}Cu (12.7 hours). Detection of liver metastases was also hampered by accumulation of ^{64}Cu-chelate complexes in the liver. These results prompted the search for other ^{64}Cu-chelates and suggest a preference for even longer-living positron emitters when using intact mAbs to enable imaging at late time points.

The genetically engineered anti-CEA minibody T84.66/GS18 was labeled with ^{64}Cu via DOTA, and PET studies were performed in human colon carcinoma bearing mice [77]. Two to 24 hours p.i., tumors ranging from 27 to 395 mg could readily be detected. Also with this chelate, however, significant non-specific uptake was seen in the kidneys and liver, hampering detection of hepatic lesions. High liver uptake is due to extensive Cu(II) dissociation from the chelator, followed by binding of the Cu(II) to natural ligands. Recently, new chelates for coupling of ^{64}Cu have been reported that lead to less liver uptake, but these chelates are awaiting clinical evaluation [63].

Several studies have demonstrated the value of ^{64}Cu-immuno-PET imaging for non-invasive quantification of receptor expression [78-81]. Most notably, the Chen group pioneered quantitative PET-imaging using ^{64}Cu-labeled DOTA-mAb conjugates. In a study performed by this group, ^{64}Cu-DOTA-cetuximab was used for targeting of seven xenograft models with different levels of EGFR expression [78]. A good correlation (R^2 = 0.80) was found between tracer uptake measured by PET and EGFR expression as measured by Western blotting. The same group reported selective tumor targeting with ^{64}Cu-DOTA-Abegrin™, a humanized mAb directed against the human integrin $\alpha_v\beta_3$ [80].

Immuno-PET with ^{86}Y-labeled mAbs has especially been studied in the context of RIT for the prediction of biodistribution and dosimetry of therapeutic ^{90}Y-mAb conjugates [82, 83]. A problem of ^{86}Y, however, is its half-life of 14.7 hours, which is relatively short for optimal ^{90}Y ($t_{1/2}$: 64 hours) dosimetry prediction.

The first studies with ^{76}Br-mAbs were performed more than 10 years ago [84]. More recently, the ^{76}Br-labeled human recombinant antibody fragment L19-SIP, directed against extra domain B (ED-B) of fibronectin, was shown to be an attractive probe for immuno-PET imaging of tumor angiogenesis [85]. Since L19-SIP is also explored in several therapeutic approaches for destruction of tumor vasculature [86-88], such an imaging probe might be of value for patient-tailored therapy.

The long-lived positron emitters ^{124}I and ^{89}Zr are particularly suitable for immuno-PET when used in combination with intact mAbs [89]. ^{124}I-labeled mAbs have already been used for clinical immuno-PET about 15 years ago, but the number of patients included in these studies was small [90, 91]. Diagnostic results were far from

optimal, among others because of the poor quality of the mmAbs used, which were lacking the specificity of nowadays mAbs. Currently, interest in ^{124}I-labeled mAbs has been renewed, especially because of the broad introduction of experimental and clinical PET and PET/CT scanners. Excellent visualization and quantification results were obtained with several ^{124}I-mAb constructs in a variety of xenograft models [92-95]. PET imaging of ^{124}I-mAbs may also form an attractive option as scouting procedure prior to ^{131}I-RIT. For this purpose, ^{124}I- and ^{131}I-labeled mAbs should show congruent biodistribution, which can be achieved with well standardized iodination methods [96].

Two clinical applications have attracted attention. Jayson *et al*. [97] used various doses of ^{124}I-HuMV833, a mAb binding to $VEGF_{121}$ and $VEGF_{165}$, to perform PET imaging studies in 12 patients with various progressive solid tumors. Antibody distribution and clearance were markedly heterogeneous between and within patients and between and within individual tumors. These differences may represent the variation in available targets for the mAb, which could have implications for anti-VEGF therapy. Whether or not mAb dose and type of radionuclide (residualizing or not) play a role in imaging results will be a topic of future studies.

In the other clinical application, ^{124}I-Immuno-PET was used for in vivo profiling of renal cancer. Divgi *et al*. [98] used ^{124}I-cmAb G250 to predict the presence of clear cell renal carcinomas in 25 patients scheduled for surgical tumor resection. G250 is directed against carbonic anhydrase-IX and over-expressed in clear-cell renal carcinoma. It might be informative to know which renal cancer patients have this aggressive tumor type because of treatment decisions, although opinions on this point deviate [99]. 15 of 16 clear-cell carcinomas were identified accurately by immuno-PET, and all nine non-clear-cell renal masses were negative for the tracer. This study illustrates how molecular imaging with specific probes can contribute to personalized medicine. Still a limitation in ^{124}I-immuno-PET, however, is the availability of clinical grade ^{124}I.

Since the introduction of the long-lived positron emitter ^{89}Zr as a residualizing radionuclide for immuno-PET, procedures were developed for large-scale production of ^{89}Zr and its stable coupling to mAbs [49, 100, 101]. At the start of the current doctoral thesis project, some preclinical immuno-PET studies had been performed with ^{89}Zr-labeled mAbs as a prelude to clinical trials, e.g. with cmAb U36 [49] and G250 [102]. Also for ^{89}Zr-labeled mAbs sensitive tumor detection and accurate quantification with PET was demonstrated [103].

Given the promising results obtained with cmAb-U36 in previous clinical RIS studies (Figure 2), and to allow comparison of imaging modalities, a clinical immuno-PET feasibility trial has been conducted with ^{89}Zr-cmAb U36 [68, 104]. The aim was to determine the diagnostic value of immuno-PET with ^{89}Zr-cmAb U36 in patients with

head and neck squamous cell carcinoma (HNSCC) who were at high risk of having neck lymph node metastases. Twenty patients were scheduled to undergo resection of the primary tumor and uni- or bilateral neck dissection, and underwent CT and/or MRI and ^{89}Zr-cmAb U36 immuno-PET prior to surgery. Immuno-PET detected all primary tumors (n = 17) as well as lymph node metastases in 18 of 25 positive neck levels. Missed lymph nodes were relatively small and contained only a small proportion of tumor tissue. Representative images are shown in Figure 10 and 11. Note the level of detail (e.g. compare heart region Figure 2 and 10). It was concluded that immuno-PET with ^{89}Zr-cmAb U36 performs at least as good for detection of HNSCC lymph node metastases (and probably distant metastases) as CT/MRI, and that the use of PET-CT might further support image interpretation.

These encouraging findings justified further exploitation and dissemination of ^{89}Zr-immuno-PET by setting up procedures for large scale GMP production and worldwide distribution of ^{89}Zr, development of procedures for facile labeling of proteins with ^{89}Zr, and further demonstration of the preclinical and clinical potential of ^{89}Zr-immuno-PET.

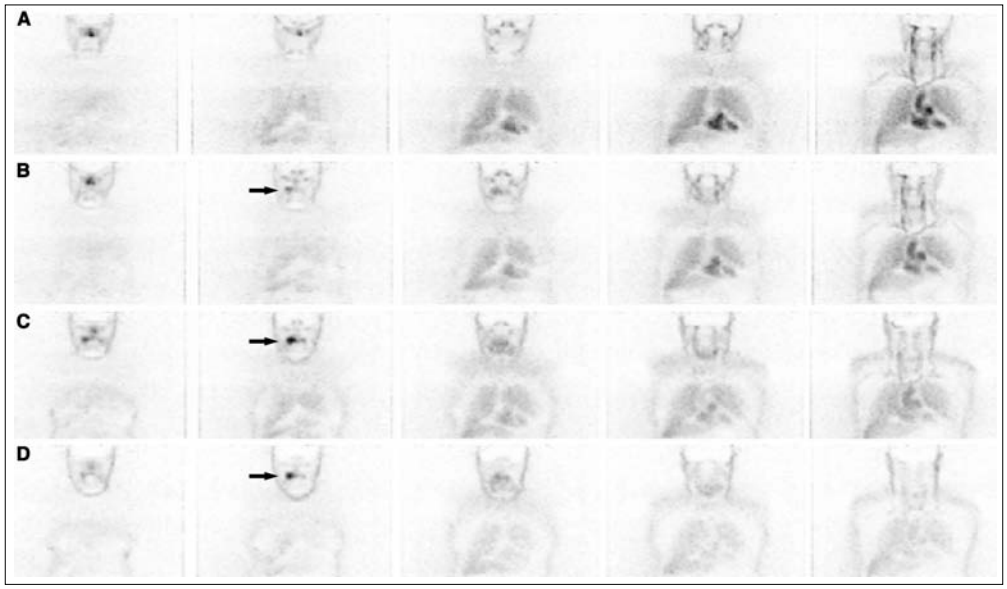

Figure 10. Immuno-PET image with ^{89}Zr-cmAb U36 in a patient with a tumor of the right tonsil. Images were obtained within 1 hour (A), at 24 hours (B), at 72 hours (C), and at 120 hours p.i. (D). Slices from anterior (left) to posterior (right). Early images show mainly blood-pool activity with visualization of nose, heart, lungs and liver. At later images the primary tumor is clearly visualized (arrow).

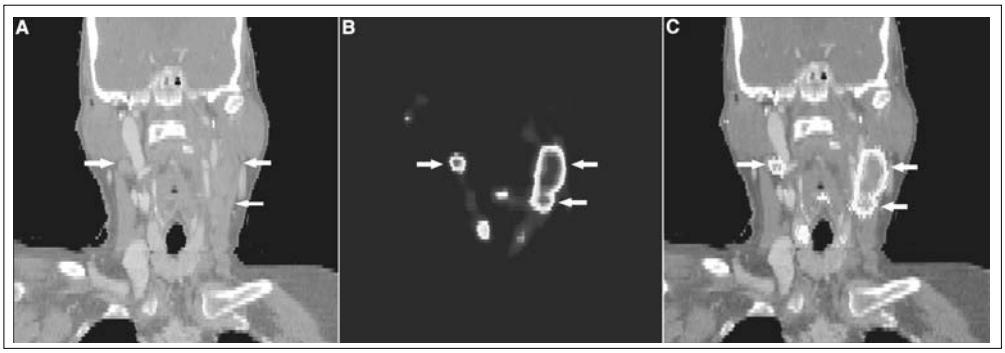

Figure 11. Fusion (C) of CT (A) and coronal immuno-PET (B) images with ^{89}Zr-cmAb U36 of a head and neck cancer patient with a tumor in the left tonsil and lymph node metastases (small arrows) at the left (level II and III) and right (level II) side of the neck. Images were obtained 72 hours p.i.. In these slices, only the lymph node metastases are visible.

Aim and outline of this thesis

Monoclonal antibodies have been approved for use as diagnostics and therapeutics in a broad range of medical indications, especially in oncology. In addition, hundreds of new mAbs, engineered mAb fragments and nontraditional antibody-like scaffolds, directed against either validated or novel tumor targets, are under development. Immuno-PET, the tracking and quantification of mAbs with PET *in vivo*, is an exciting novel option to improve diagnostic imaging and to guide mAb-based therapy. The availability of proper positron emitters, sophisticated radiochemistry, and advanced PET and PET-CT scanners is crucial in these developments. Immuno-PET might play an important future role in cancer staging, in the improvement and tailoring of therapy with existing mAbs, as well as in the efficient development of novel therapeutic mAbs.

The project leading to this thesis aimed the further implementation of immuno-PET in preclinical and clinical antibody applications by: providing procedures for the efficient production, purification, and processing of the short-lived positron emitter ^{68}Ga and of the long-lived positron emitters ^{89}Zr and ^{124}I; providing methods for the stable coupling of ^{68}Ga, ^{89}Zr, and ^{124}I to mAbs and mAb-fragments; performing preclinical as well as clinical proof of principle studies.

Procedures for the efficient production, purification, and processing of ^{68}Ga, ^{89}Zr, and ^{124}I have partly been described in a scattered way throughout the different chapters. Due to commercial reasons, not all details have been described. Procedures for production of ^{89}Zr and ^{124}I have been implemented by industry to enable worldwide distribution/availability of ^{89}Zr- and ^{124}I-immuno-PET technology.

Immuno-PET as a scouting procedure prior to RIT aims at the confirmation of tumor-targeting as well as the accurate estimation of radiation dose delivery to both tumor and normal tissues, and might therefore be of value for selection of RIT candidate patients. A prerequisite for this approach is that PET- and RIT-radioimmunoconjugates show a similar biodistribution. In **Chapter 2** we evaluated the potential of the long-lived positron emitter ^{89}Zr to predict the biodistribution of the residualizing therapeutic radiometals ^{90}Y (^{88}Y was used as a substitute for ^{90}Y) and ^{177}Lu, when labeled to a monoclonal antibody via different types of chelates. Cetuximab was selected as a model mAb, because it abundantly internalizes after binding to the epidermal growth factor receptor.

In the next study, the use of ^{89}Zr-immuno-PET as a scouting procedure prior to RIT was clinically implemented. The ^{90}Y-labeled anti-CD20 mAb ibritumomab tiuxetan (^{90}Y-Zevalin™) has been approved by the FDA for treatment of patients with relapsed or refractory low grade, follicular, or transformed B-cell non-Hodgkin's lymphoma (NHL). Recently, promising results have also been obtained in the treatment of aggressive NHL. In these trials, ^{90}Y-Zevalin RIT was added to high-dose chemotherapy followed by autologous stem cell transplantation. Because high doses of ^{90}Y are used, guidance of these studies with accurate dosimetry is highly desirable for prevention of unacceptable dose exposition to normal organs, and for evaluation of dose-response relationships. Therefore, the introduction of ^{89}Zr-Zevalin-PET in high-dose myeloablative ^{90}Y-Zevalin RIT might be an attractive option for prediction of ^{90}Y-Zevalin biodistribution and dosimetry, and of toxicity and tumor response. In **Chapter 3**, we evaluated the newly developed ^{89}Zr-Zevalin conjugate. The ^{89}Zr-Zevalin conjugate was measured for stability in serum and for preservation of immunoreactivity, also during storage. For the analysis of the pharmacokinetic behavior, the biodistribution of ^{89}Zr-Zevalin was compared with ^{88}Y-Zevalin upon coinjection in NHL xenograft-bearing nude mice. The preliminary clinical performance of ^{89}Zr-Zevalin-PET was evaluated in a patient with CD20+ B-cell NHL.

As indicated in the introduction chapter of this thesis, immuno-PET might have value for guidance of the optimal use of FDA approved mAbs like cetuximab and ibritumomab tiuxetan in Chapters 2 and 3, but also for in vivo characterization of new targeting ligands directed against novel critical tumor targets. Angiogenesis is one of the hallmarks of cancer [1], and therefore considerable efforts have been made recently to image as well as to eradicate tumor vasculature, preferably in a combined fashion. One of the appealing targets for both approaches is the splice variant of fibronectin containing extra domain B (ED-B). Recently, a human bivalent "small immunoprotein" directed against ED-B, designated L19-SIP, has been developed. L19-SIP is explored in several therapeutic approaches, including RIT with ^{131}I-L19-SIP. In **Chapter 4**, we developed ^{124}I-labeled L19-SIP for immuno-PET imaging of tumor

neovasculature, and for prediction of biodistribution and dosimetry of ^{131}I-L19-SIP in RIT. In addition, GMP complied ^{124}I-production procedures were developed. ^{124}I-L19-SIP was evaluated by comparing its biodistribution with ^{131}I-L19-SIP upon coinjection in xenograft-bearing nude mice and by imaging with a high-resolution research tomograph (HRRT) PET scanner.

Another appealing target in oncology is the c-Met-receptor (Met-receptor). This receptor is frequently overexpressed in tumors of many histotypes. Besides, the prevalence of abnormal Met expression is typically higher in metastases than in primary tumors, and is associated with poor clinical prognosis. Intriguingly, very recent findings indicate that tumors can become resistant to anti-EGFR therapy as a result of amplification of the *MET* oncogene. This makes the Met-receptor, on the analogy of e.g. EGFR, an interesting target for tumor detection, cancer prognostication, and anti-cancer therapy. For optimal application of anti-Met mAbs in therapeutic approaches, it must be demonstrated that the receptor is expressed, and that the mAb accumulates selectively and in sufficient amounts in the tumor. In **Chapter 5**, we investigated the potential of PET imaging with either ^{89}Zr- or ^{124}I-labeled anti-Met mAb DN30 for assessment of the biodistribution of mAb DN30 and the in vivo Met expression status. For this study, two human xenograft lines were selected, the gastric cancer line GTL-16 with high Met expression, and the head and neck cancer line FaDu with low Met expression. Biodistribution of coinjected ^{89}Zr- and ^{131}I-labeled DN30 (^{131}I as a substitute for ^{124}I to facilitate dual isotope counting) was assessed in xenograft bearing nude mice. The potential of ^{89}Zr-DN30 for tumor detection was evaluated using a HRRT PET scanner. Moreover, the potential of PET for *in vivo* ^{89}Zr-DN30 quantification was evaluated by relating image-derived tumor uptake data (non-invasive method) to ^{89}Zr data from excised tumors (invasive method).

An important step in the further implementation of immuno-PET is the availability of facile yet robust radiolabeling procedures for the stable coupling of positron emitters to mAbs and mAb-fragments. In **Chapter 6**, a new candidate bifunctional chelate, *p*-isothiocyanatobenzyl-desferrioxamine (Df-Bz-NCS), is introduced and standardized /universal protocols are provided to enable efficient and rapid preparation of ^{89}Zr- and ^{68}Ga-labeled mAbs. In vitro stability was assessed under challenging conditions and its in vivo behavior was evaluated by biodistribution and PET-imaging studies in xenograft-bearing nude mice.

In **chapter 7**, a general discussion of the results presented in this thesis is provided.

References

1. Hanahan D, Weinberg RA. The Hallmarks of Cancer. Cell 2000;100:57-70.
2. Lawrence S. Billion dollar babies--biotech drugs as blockbusters. Nat Biotechnol 2007;25:380-2.
3. Verel I, Visser GWM, Van Dongen GAMS. The promise of immuno-PET in radioimmunotherapy. J Nucl Med 2005;46:164S-71S.
4. Himmelweit F, editor. The collected papers of Paul Ehrlich. London: Pergamon Press; 1956, 1960.
5. Kohler G, Milstein C. Continuous cultures of fused cells secreting antibody of predefined specificity. Nature 1975;256:495-7.
6. Bird RE, Hardman KD, Jacobson JW, Johnson S, Kaufman BM, Lee SM, et al. Single-chain antigen-binding proteins. Science 1988;242:423-6.
7. Adams GP, McCartney JE, Tai MS, Oppermann H, Huston JS, Stafford WF, et al. Highly specific in-vivo tumor targeting by monovalent and divalent forms of 741F8 anti-C-Erbb-2 single-chain Fv. Cancer Res 1993;53:4026-34.
8. Holliger P, Prospero T, Winter G. Diabodies - Small bivalent and bispecific antibody fragments. Proc Natl Acad Sci USA 1993;90:6444-8.
9. Hu SZ, Shivery L, Raubitschek A, Sherman M, Williams LE, Wong JYC, et al. Minibody: A novel engineered anti-carcinoembryonic antigen antibody fragment (single-chain Fv-C(H)3) which exhibits rapid, high-level targeting of xenografts. Cancer Res 1996;56:3055-61.
10. Holliger P, Hudson PJ. Engineered antibody fragments and the rise of single domains. Nat Biotechnol 2005;23:1126-36.
11. Sheridan C. Pharma consolidates its grip on post-antibody landscape. Nat Biotechnol 2007;25:365-6.
12. Ward ES, Gussow D, Griffiths AD, Jones PT, Winter G. Binding activities of a repertoire of single immunoglobulin variable domains secreted from Escherichia-Coli. Nature 1989;341:544-6.
13. Nord K, Gunneriusson E, Ringdahl J, Stahl S, Uhlen M, Nygren PA. Binding proteins selected from combinatorial libraries of an alpha-helical bacterial receptor domain. Nat Biotechnol 1997;15:772-7.
14. Roovers RC, Van Dongen GAMS, Henegouwen PM. Nanobodies in therapeutic applications. Curr Opin Mol Ther 2007;9:327-35.
15. Beste G, Schmidt FS, Stibora T, Skerra A. Small antibody-like proteins with prescribed ligand specificities derived from the lipocalin fold. Proc Natl Acad Sci USA 1999;96:1898-903.
16. Goldenberg DM, Sharkey RM, Paganelli G, Barbet J, Chatal JF. Antibody pretargeting advances cancer radioimmunodetection and radioimmunotherapy. J Clin Oncol 2006;24:823-34.
17. Zuckier LS, DeNardo GL. Trials and tribulations: Oncological antibody imaging comes to the fore. Semin Nucl Med 1997;27:10-29.
18. Stern M, Herrmann R. Overview of monoclonal antibodies in cancer therapy: present and promise. Crit Rev Oncol Hematol 2005;54:11-29.
19. Adams GP, Weiner LM. Monoclonal antibody therapy of cancer. Nat Biotechnol 2005;23:1147-57.

20. Carter PJ. Potent antibody therapeutics by design. Nat Rev Immunol 2006;6:343-57.
21. Zafir-Lavie I, Michaeli Y, Reiter Y. Novel antibodies as anticancer agents. Oncogene 2007;26:3714-33.
22. Mano M. The burden of scientific progress: growing inequalities in the delivery of cancer care. Acta Oncol 2006;45:84-6.
23. Neyt M, Albrecht J, Cocquyt V. An economic evaluation of Herceptin® in adjuvant setting: The Breast Cancer International Research Group 006 trial. Ann Oncol 2006;17:381-90.
24. Slamon DJ, Clark GM, Wong SG, Levin WJ, Ullrich A, Mcguire WL. Human-breast cncer - correlation of relapse and survival with amplification of the HER2/neu oncogene. Science 1987;235:177-82.
25. Hynes NE, Stern DF. The biology of erbB-2/neu/HER-2 and its role in cancer. Biochim Biophys Acta 1994;1198:165-84.
26. Rasbridge SA, Gillett CE, Seymour AM, Patel K, Richards MA, Rubens RD, et al. The effects of chemotherapy on morphology, cellular proliferation, apoptosis and oncoprotein expression in primary breast-carcinoma. Br J Cancer 1994;70:335-41.
27. Gancberg D, Di Leo A, Cardoso F, Rouas G, Pedrocchi M, Paesmans M, et al. Comparison of HER-2 status between primary breast cancer and corresponding distant metastatic sites. Ann Oncol 2002;13:1036-43.
28. Zidan J, Dashkovsky I, Stayerman C, Basher W, Cozacov C, Hadary A. Comparison of HER-2 overexpression in primary breast cancer and metastatic sites and its effect on biological targeting therapy of metastatic disease. Br J Cancer 2005;93:552-6.
29. Gong Y, Booser DJ, Sneige N. Comparison of HER-2 status determined by fluorescence in situ hybridization in primary and metastatic breast carcinoma. Cancer 2005;103:1763-9.
30. De Korte MA, de Vries EGE, Lub-de Hooge MN, Jager PL, Gietema JA, van der Graaf WTA, et al. (111)Indium-trastuzumab visualises myocardial human epidermal growth factor receptor 2 expression shortly after anthracycline treatment but not during heart failure: A clue to uncover the mechanisms of trastuzumab-related cardiotoxicity. Eur J Cancer 2007;43:2046-51.
31. Behr TM, Behe M, Wormann B. Trastuzumab and breast cancer. N Engl J Med 2001;345:995-6.
32. Colnot DR, Quak JJ, Roos JC, van Lingen A, Wilhelm AJ, van Kamp GJ, et al. Phase I therapy study of Re-186-labeled chimeric monoclonal antibody U36 in patients with squamous cell carcinoma of the head and neck. J Nuc Med 2000;41(12):1999-2010.
33. Borjesson PKE, Postema EJ, Roos JC, Colnot DR, Marres HAM, van Schie MH, et al. Phase I therapy study with Re-186-labeled humanized monoclonal antibody BIWA 4 (bivatuzumab) in patients with head and neck squamous cell carcinoma. Clin Cancer Res 2003;9:3961S-72S.
34. Colnot DR, Ossenkoppele GJ, Roos JC, Quak JJ, de Bree R, Borjesson PK, et al. Reinfusion of unprocessed, granulocyte colony-stimulating factor-stimulated whole blood allows dose escalation of ^{186}Re labeled chimeric monoclonal antibody U36 radioimmunotherapy in a phase I dose escalation study. Clin Cancer Res 2002;8(11):3401-6.
35. Tijink BM, Buter J, de Bree R, Giaccone G, Lang MS, Staab A, et al. A phase I dose escalation study with anti-CD44v6 bivatuzumab mertansine in patients with incurable squamous cell carcinoma of the head and neck or esophagus. Clin Cancer Res 2006;12:6064-72.
36. Takahashi H, Nakada T, Nakaki M, Wands JR. Inhibition of hepatic metastases of human

colon-cancer in nude-mice by a chimeric SF-25 monoclonal-antibody. Gastroenterology 1995;108:172-82.
37. De Bree R, Roos JC, Quak JJ, Den Hollander W, Snow GB, Van Dongen GAMS. Clinical screening of monoclonal-antibodies 323/A3, cSF-25 and K928 for suitability of targeting tumors in the upper aerodigestive and respiratory-tract. Nucl Med Commun 1994;15:613-27.
38. Phelps ME, Hoffman EJ, Mullani NA, Ter-Pogossian MM. Application of annihilation coincidence detection to transaxial reconstruction tomography. J Nucl Med 1975;16:210-24.
39. Surti S, Kuhn A, Werner ME, Perkins AE, Kolthammer J, Karp JS. Performance of Philips gemini TF PET/CT scanner with special consideration for its time-of-flight imaging capabilities. J Nucl Med 2007;48:471-80.
40. Budinger TF. Time-of-flight positron emission tomography: status relative to conventional PET. J Nucl Med 1983;24:73-8.
41. Lucignani G. Time-of-flight PET and PET/MRI: recurrent dreams or actual realities? Eur J Nucl Med Mol Imaging 2006;33:969-71.
42. Judenhofer MS, Wehrl HF, Newport DF, Catana C, Siegel SB, Becker M, et al. Simultaneous PET-MRI: a new approach for functional and morphological imaging. Nat Med 2008;14:459-65.
43. Haddad F, Ferrer L, Guertin A, Carlier T, Michel N, Barbet J, et al. ARRONAX, a high-energy and high-intensity cyclotron for nuclear medicine. Eur J Nucl Med Mol Imaging 2008;35:1377-87.
44. Barbet J, Chatal JF, Gauche F, Martino J. Which radionuclides will nuclear oncology need tomorrow? Eur J Nucl Med Mol Imaging 2006;33:627-30.
45. Kondo K, Lambrecht RM, Norton EF, Wolf AP. Cyclotron isotopes and radiopharmaceuticals--XXII. Improved targetry and radiochemistry for production of ^{123}I and ^{124}I. Int J Appl Radiat Isot 1977;28:765-71.
46. Qaim SM, Hohn A, Bastian T, El-Azoney KM, Blessing G, Spellerberg S, et al. Some optimisation studies relevant to the production of high-purity ^{124}I and ^{120g}I at a small-sized cyclotron. Appl Radiat Isot 2003;58:69-78.
47. Sajjad M, Bars E, Nabi HA. Optimization of ^{124}I production via ^{124}Te(p,n)^{124}I reaction. Appl Radiat Isot 2006;64:965-70.
48. Nye JA, Avila-Rodriguez MA, Nickles RJ. A new binary compound for the production of ^{124}I via the ^{124}Te(p,n)^{124}I reaction. Appl Radiat Isot 2007;65:407-12.
49. Verel I, Visser GWM, Boellaard R, Stigter-Van Walsum M, Snow GB, Van Dongen GAMS. Zr-89 immuno-PET: comprehensive procedures for the production of Zr-89-labeled monoclonal antibodies. J Nucl Med 2003;44:1271-81.
50. Maecke HR, Hofmann M, Haberkorn U. ^{68}Ga-labeled peptides in tumor imaging. J Nucl Med 2005;46:172S-8S.
51. Shih LB, Thorpe SR, Griffiths GL, Diril H, Ong GL, Hansen HJ, et al. The processing and fate of antibodies and their radiolabels bound to the surface of tumor-cells in-vitro - a comparison of 9 radiolabels. J Nucl Med 1994;35:899-908.
52. Tolmachev V, Orlova A, Lundqvist H. Approaches to improve cellular retention of radiohalogen labels delivered by internalising tumour-targeting proteins and peptides. Curr Med Chem 2003;10:2447-60.
53. Shively JE. ^{18}F labeling for immuno-PET: where speed and contrast meet. J Nucl Med

2007;48:170-2.
54. Cheng Z, De Jesus OP, Namavari M, De A, Levi J, Webster JM, et al. Small-animal PET imaging of human epidermal growth factor receptor type 2 expression with site-specific ^{18}F-labeled protein scaffold molecules. J Nucl Med 2008;49:804-13.
55. Cooper MS, Sabbah E, Mather SJ. Conjugation of chelating agents to proteins and radiolabeling with trivalent metallic isotopes. Nat Protoc 2006;1:314-7.
56. Clarke ET, Martell AE. Stabilities of the Fe(III), Ga(III) and In(III) chelates of N,N',N''-triazacyclononanetriacetic acid. Inorganica Chimica Acta 1991;181:273-80.
57. Lee J, Garmestani K, Wu C, Brechbiel MW, Chang HK, Choi CW, et al. In vitro and in vivo evaluation of structure-stability relationship of ^{111}In- and ^{67}Ga-labeled antibody via 1B4M or C-NOTA chelates. Nucl Med Biol 1997;24:225-30.
58. Brechbiel MW. Bifunctional chelates for metal nuclides. Q J Nucl Med Mol Imaging 2008;52:166-73.
59. Wadas TJ, Anderson CJ. Radiolabeling of TETA- and CB-TE2A-conjugated peptides with copper-64. Nat Protoc 2006;1:3062-8.
60. Anderson CJ, Schwarz SW, Connett JM, Cutler PD, Guo LW, Germain CJ, et al. Preparation, biodistribution and dosimetry of copper-64-labeled anti-colorectal carcinoma monoclonal antibody fragments 1A3-F(ab')$_2$. J Nucl Med 1995;36:850-8.
61. Lewis MR, Boswell CA, Laforest R, Buettner TL, Ye D, Connett JM, et al. Conjugation of monoclonal antibodies with TETA using activated esters: biological comparison of ^{64}Cu-TETA-1A3 with ^{64}Cu-BAT-2IT-1A3. Cancer Biother Radiopharm 2001;16:483-94.
62. Boswell CA, Sun X, Niu W, Weisman GR, Wong EH, Rheingold AL, et al. Comparative in vivo stability of copper-64-labeled cross-bridged and conventional tetraazamacrocyclic complexes. J Med Chem 2004;47:1465-74.
63. Wadas TJ, Wong EH, Weisman GR, Anderson CJ. Copper chelation chemistry and its role in copper radiopharmaceuticals. Curr Pharm Des 2007;13:3-16.
64. Reilly RM, Scollard DA, Wang J, Mondal H, Chen P, Henderson LA, et al. A kit formulated under good manufacturing practices for labeling human epidermal growth factor with ^{111}In for radiotherapeutic applications. J Nucl Med 2004;45:701-8.
65. Hung JC, Anderson MM. Mayo Clinic approaches to meet United States Pharmacopeia <797> requirements for facility design and environmental controls of nuclear pharmacy. J Nucl Med 2009;50:156-64
66. Verbruggen A, Coenen HH, Deverre JR, Guilloteau D, Langstrom B, Salvadori PA, et al. Guideline to regulations for radiopharmaceuticals in early phase clinical trials in the EU. Eur J Nucl Med Mol Imaging 2008;35:2144-51.
67. European Pharmacopoeia. 6 ed. Strasbourg: European Directive for the Quality of Medicine (EDQM); 2008.
68. Borjesson PK, Jauw YW, Boellaard R, de Bree R, Comans EF, Roos JC, et al. Performance of immuno-positron emission tomography with zirconium-89-labeled chimeric monoclonal antibody U36 in the detection of lymph node metastases in head and neck cancer patients. Clin Cancer Res 2006;12:2133-40.
69. Vaidyanathan G, Bigner DD, Zalutsky MR. Fluorine-18-labeled monoclonal-antibody fragments - a potential approach for combining radioimmunoscintigraphy and positron emission tomography. J Nucl Med 1992;33:1535-41.

70. Cai W, Olafsen T, Zhang X, Cao Q, Gambhir SS, Williams LE, et al. PET imaging of colorectal cancer in xenograft-bearing mice by use of an ^{18}F-labeled T84.66 anti-carcinoembryonic antigen diabody. J Nucl Med 2007;48:304-10.
71. Shively JE. F-18 labeling for immuno-PET: Where speed and contrast meet. J Nucl Med 2007;48:170-2.
72. Neumaier B, Mottaghy FM, Buck AK, Glatting G, Blumstein NM, Mahren B, et al. ^{18}F-immuno-PET: Determination of anti-CD66 biodistribution in a patient with high-risk leukemia. Cancer Biother Radiopharm 2008;23:819-24.
73. Schuhmacher J, Kaul S, Klivenyi G, Junkermann H, Magener A, Henze M, et al. Immunoscintigraphy with positron emission tomography: gallium-68 chelate imaging of breast cancer pretargeted with bispecific anti-MUC1/anti-Ga chelate antibodies. Cancer Res 2001;61:3712-7.
74. Griffiths GL, Chang C-H, McBride WJ, Rossi EA, Sheerin A, Tejada GR, et al. Reagents and methods for PET using bispecific antibody pretargeting and ^{68}Ga-radiolabeled bivalent hapten-peptide-chelate conjugates. J Nucl Med 2004;45:30-9.
75. Smith-Jones PM, Solit DB, Akhurst T, Afroze F, Rosen N, Larson SM. Imaging the pharmacodynamics of HER2 degradation in response to Hsp90 inhibitors. Nat Biotechnol 2004;22:701-6.
76. Philpott GW, Schwarz SW, Anderson CJ, Dehdashti F, Connett JM, Zinn KR, et al. Radioimmuno-PET: detection of colorectal carcinoma with positron-emitting copper-64-labeled monoclonal antibody. J Nucl Med 1995;36:1818-24.
77. Wu AM, Yazaki PJ, Tsai S, Nguyen K, Anderson AL, McCarthy DW, et al. High-resolution microPET imaging of carcinoembryonic antigen-positive xenografts by using a copper-64-labeled engineered antibody fragment. Proc Natl Acad Sci USA 2000;97:8495-500.
78. Cai W, Chen K, He L, Cao Q, Koong A, Chen X. Quantitative PET of EGFR expression in xenograft-bearing mice using ^{64}Cu-labeled cetuximab, a chimeric anti-EGFR monoclonal antibody. Eur J Nucl Med Mol Imaging 2007;34:850-8.
79. Cai W, Ebrahimnejad A, Chen K, Cao Q, Li ZB, Tice DA, et al. Quantitative radioimmuno-PET imaging of EphA2 in tumor-bearing mice. Eur J Nucl Med Mol Imaging 2007;34:2024-36.
80. Cai WB, Wu Y, Chen K, Cao QZ, Tice DA, Chen XY. In vitro and in vivo characterization of Cu-64-labeled Abegrin (TM) a humanized monoclonal antibody against integrin alpha(v)beta(3). Cancer Research 2006;66:9673-81.
81. Eiblmaier M, Meyer LA, Watson MA, Fracasso PM, Pike LJ, Anderson CJ. Correlating EGFR expression with receptor-binding properties and internalization of ^{64}Cu-DOTA-cetuximab in 5 cervical cancer cell lines. J Nucl Med 2008;49:1472-9.
82. Lovqvist A, Humm JL, Sheikh A, Finn RD, Koziorowski J, Ruan S, et al. PET imaging of ^{86}Y-labeled anti-Lewis Y monoclonal antibodies in a nude mouse model: comparison between ^{86}Y and ^{111}In radiolabels. J Nucl Med 2001;42:1281-7.
83. Garmestani K, Milenic DE, Plascjak PS, Brechbiel MW. A new and convenient method for purification of ^{86}Y using a Sr(II) selective resin and comparison of biodistribution of ^{86}Y and ^{111}In labeled Herceptin. Nucl Med Biol 2002;29:599-606.
84. Lovqvist A, Sundin A, Ahlstrom H, Carlsson J, Lundqvist H. Pharmacokinetics and experimental PET imaging of a bromine-76-labeled monoclonal anti-CEA antibody. J Nucl Med 1997;38:395-401.

85. Rossin R, Berndorff D, Friebe M, Dinkelborg LM, Welch MJ. Small-animal PET of tumor angiogenesis using a ^{76}Br-labeled human recombinant antibody fragment to the ED-B domain of fibronectin. J Nucl Med 2007;48:1172-9.
86. Nilsson F, Kosmehl H, Zardi L, Neri D. Targeted delivery of tissue factor to the ED-B domain of fibronectin, a marker of angiogenesis, mediates the infarction of solid tumors in mice. Cancer Res 2001;61:711-6.
87. Neri D, Bicknell R. Tumour vascular targeting. Nat Rev Cancer 2005;5:436-46.
88. Tijink BM, Neri D, Leemans CR, Budde M, Dinkelborg LM, Stigter-Van Walsum M, et al. Radioimmunotherapy of head and neck cancer xenografts using ^{131}I-Labeled antibody L19-SIP for selective targeting of tumor vasculature. J Nucl Med 2006;47:1127-35.
89. Verel I, Visser GWM, Boerman OC, Van Eerd JEM, Finn R, Boellaard R, et al. Long-lived positron emitters zirconium-89 and iodine-124 for scouting of therapeutic radioimmunoconjugates with PET. Cancer Biother Radiopharm 2003;18:655-61.
90. Wilson CB, Snook DE, Dhokia B, Taylor CV, Watson IA, Lammertsma AA, et al. Quantitative measurement of monoclonal antibody distribution and blood flow using positron emission tomography and ^{124}I in patients with breast cancer. Int J Cancer 1991;47:344-7.
91. Larson SM, Pentlow KS, Volkow ND, Wolf AP, Finn RD, Lambrecht RM, et al. PET scanning of iodine-124-3F9 as an approach to tumor dosimetry during treatment planning for radioimmunotherapy in a child with neuroblastoma. J Nucl Med 1992;33:2020-3.
92. Lee FT, Hall C, Rigopoulos A, Zweit J, Pathmaraj K, O'keefe GJ, et al. Immuno-PET of human colon xenograft- bearing BALB/c nude mice using ^{124}I-CDR-grafted humanized A33 monoclonal antibody. J Nucl Med 2001;42:764-9.
93. Sundaresan G, Yazaki PJ, Shively JE, Finn RD, Larson SM, Raubitschek AA, et al. I-124-labeled engineered anti-CEA minibodies and diabodies allow high-contrast, antigen-specific small-animal PET imaging of xenografts in athymic mice. J Nucl Med 2003;44:1962-9.
94. Jain M, Batra SK. Genetically engineered antibody fragments and PET imaging: A new era of radioimmunodiagnosis. J Nucl Med 2003;44:1970-2.
95. Robinson MK, Doss M, Shaller C, Narayanan D, Marks JD, Adler LP, et al. Quantitative immuno-positron emission tomography imaging of HER2-positive tumor xenografts with an iodine-124 labeled anti-HER2 diabody. Cancer Res 2005;65:1471-8.
96. Verel I, Visser GW, Vosjan MJ, Finn R, Boellaard R, Van Dongen GA. High-quality ^{124}I-labelled monoclonal antibodies for use as PET scouting agents prior to ^{131}I-radioimmunotherapy. Eur J Nucl Med Mol Imaging 2004;31:1645-52.
97. Jayson GC, Zweit J, Jackson A, Mulatero C, Julyan P, Ranson M, et al. Molecular imaging and biological evaluation of HuMV833 anti-VEGF antibody: implications for trial design of antiangiogenic antibodies. J Natl Cancer Inst 2002;94:1484-93.
98. Divgi CR, Pandit-Taskar N, Jungbluth AA, Reuter VE, Gonen M, Ruan S, et al. Preoperative characterisation of clear-cell renal carcinoma using iodine-124-labelled antibody chimeric G250 (^{124}I-cG250) and PET in patients with renal masses: a phase I trial. Lancet Oncol 2007;8:304-10.
99. Powles T, Ell PJ. Does PET imaging have a role in renal cancers after all? Lancet Oncol 2007;8:279-81.
100. Meijs WE, Herscheid JDM, Haisma HJ, Wijbrandts R, Van Langevelde F, Van Leuffen PJ, et al. Production of highly pure no-carrier added Zr-89 for the labeling of antibodies with a

positron emitter. Appl Radiat Isot 1994;45:1143-7.
101. Lee FT, Scott AM. Immuno-PET for tumor targeting. J Nucl Med 2003;44:1282-3.
102. Brouwers A, Verel I, Van Eerd J, Visser G, Steffens M, Oosterwijk E, et al. PET radioimmunoscintigraphy of renal cell cancer using ^{89}Zr-labeled cG250 monoclonal antibody in nude rats. Cancer Biother Radiopharm 2004;19:155-63.
103. Verel I, Visser GWM, Boellaard R, Boerman OC, Van Eerd J, Snow GB, et al. Quantitative Zr-89 immuno-PET for in vivo scouting of Y-90-labeled monoclonal antibodies in xenograft-bearing nude mice. J Nucl Med 2003;44:1663-70.
104. Zalutsky MR. Potential of immuno-positron emission tomography for tumor imaging and immunotherapy planning. Clin Cancer Res 2006;12:1958-60.
105. Charged particle cross-section database for medical radioisotope production: diagnostic radioisotopes and monitor reactions. International Atomic Energy Agency; 2001. Report No.: IAEA-TECDOC-1211.
106. Mustafa MG, West HI, Jr., O'Brien H, Lanier RG, Benhamou M, Tamura T. Measurements and a direct-reaction-plus-Hauser-Feshbach analysis of ^{89}Y(p,n)^{89}Zr, ^{89}Y(p,2n)^{88}, and ^{89}Y(p,pn)^{88}Y reactions up to 40 MeV. Phys Rev C Nucl Phys 1988;38:1624-37.
107. Uddin MS, Hagiwara M, Baba M, Tarkanyi F, Ditroi F. Experimental studies on excitation functions of the proton-induced activation reactions on yttrium. Appl Radiat Isot 2005;63:367-74.
108. Krasnov NN. Thick target yield. Int J Appl Radiat and Isot 1974;25:223-7.

CHAPTER 2

^{89}Zr as a PET surrogate radioisotope for scouting biodistribution of the therapeutic radiometals ^{90}Y and ^{177}Lu in tumor-bearing nude mice after coupling to the internalizing antibody cetuximab

Lars R. Perk
Gerard W. M. Visser
Maria J. W. D. Vosjan
Marijke Stigter-van Walsum
Bernard M. Tijink
C. René Leemans
Guus A. M. S. van Dongen

The Journal of Nuclear Medicine 2005;46:1898-1906

Abstract

Immuno-PET as a scouting procedure before radioimmunotherapy (RIT) aims at confirming tumor targeting and accurately estimating radiation dose delivery to both tumor and normal tissues and might therefore be of value for selection of patient candidates for RIT. A prerequisite for this approach is that PET radioimmunoconjugates and RIT radioimmunoconjugates must show a similar biodistribution. In the present study, we evaluated the potential of the long-lived positron emitter ^{89}Zr to predict biodistribution of the residualizing therapeutic radiometals ^{90}Y (^{88}Y used as a substitute for ^{90}Y) and ^{177}Lu when labeled to the monoclonal antibody (mAb) cetuximab via different types of chelates. Cetuximab was selected as a model mAb because it abundantly internalizes after binding to the epidermal growth factor receptor.

Methods: Cetuximab was labeled with ^{89}Zr using succinylated desferrioxamine B (N-sucDf). The chelates p-benzyl isothiocyanate-1,4,7,10-tetraazacyclododecane-1,4,7, 10-tetraacetic acid (p-SCN-Bz-DOTA) and p-isothiocyanatobenzyl diethylenetriamine-pentaacetic acid (p-SCN-Bz-DTPA) were both used for radiolabeling with ^{88}Y and ^{177}Lu. For measurement of the in vitro stability of each of the 5 radioimmunoconjugates, samples were incubated in freshly prepared human serum at 37°C up to 16 d. Biodistribution was assessed at 24, 48, 72, and 144 h after intraperitoneal coinjection of the PET and RIT conjugates in nude mice bearing the squamous cell carcinoma xenograft line A431.

Results: Cetuximab premodification with N-sucDf, p-SCN-Bz-DOTA, or p-SCN-Bz-DTPA resulted in chelate-to-mAb molar ratios of about 1. After radiolabeling and purification, the radiochemical purity and immunoreactive fraction of the conjugates always exceeded 97% and 93%, respectively. All conjugates were stable in serum, showing a radioactivity release of less than 5% until day 7. From day 7 until day 16, an enhanced release was observed for the ^{89}Zr-N-sucDf, ^{88}Y-p-SCN-Bz-DTPA, and ^{177}Lu-p-SCN-Bz-DTPA conjugates. The coinjected PET and RIT conjugates showed similar biodistributions, except for the thighbone and sternum. For example, the ^{89}Zr-N-sucDf conjugate showed a 2.0–2.5 times higher radioactivity accretion in the thighbone than did the RIT conjugates at 72 h after injection.

Conclusion: In view of the advantages of PET over SPECT, ^{89}Zr-immuno-PET is a promising modality for in vivo scouting of ^{90}Y- and ^{177}Lu-labeled mAbs, although care should be taken when estimating bone marrow doses.

Introduction

Tumor targeting using radiolabeled monoclonal antibodies (mAbs) in radioimmunotherapy (RIT) is developing into an attractive approach to cancer treatment. In the past few years, the U.S. Food and Drug Administration has approved 2 RIT pharmaceuticals for the treatment of non-Hodgkin's lymphoma: the anti-CD20 mAbs ibritumomab tiuxetan (Zevalin; IDEC and Schering) and tositumomab (Bexxar; Corixa and GlaxoSmithKline) labeled with the β^--emitter yttrium-90 (^{90}Y) or iodine-131 (^{131}I), respectively. Several new radioimmunoconjugates are currently being evaluated in clinical trials [1]. Besides ^{90}Y and ^{131}I, also lutetium-177 (^{177}Lu) is a commonly used ß-emitter in these RIT trials. ^{90}Y and ^{177}Lu are residualizing radiometals that show higher retention in tumors than do the nonresidualizing labels ^{131}I and rhenium-186 (^{186}Re) and therefore are especially attractive in combination with internalizing mAbs [2–4]. The ß$^-$ energy of ^{177}Lu and the related maximal particle range of 1.5 mm make this radionuclide particularly well suited for eradication of minimal residual disease, whereas ^{90}Y is the radionuclide of choice for treatment of bulky tumors because of its higher ß– energy and related maximal particle range of 12.0 mm [5]. The most effective approach when tumors of various sizes have to be treated might even be combination of both radionuclides in a single therapy [6].

Both the ^{90}Y-ibritumomab tiuxetan and the ^{131}I-tositumomab treatment regimens are preceded by a gamma-camera imaging procedure for selection of patient candidates for RIT [7, 8]. Performing radioimmunoscintigraphy with trace-labeled mAbs as a scouting procedure before RIT aims at confirming tumor targeting and quantifying biodistribution to allow estimation of dose delivery to tumors and normal tissues [9]. Alternatively, this approach can also be used for in vivo characterization of new mAb candidates for use in RIT. For pretherapy imaging in such a setting, gamma-emitters are coupled to mAbs, whereas optimal prediction is obtained only when imaging and therapeutic radioimmunoconjugates show similar biodistributions. ^{177}Lu emits a small proportion of gamma-radiation (208 keV, 11%) but until now has not been used at a trace dose for clinical scouting. ^{90}Y is a pure ß-emitter, and therefore indium-111 (^{111}In) is often used as a gamma-emitting surrogate for tracing the biodistribution of the ^{90}Y-labeled mAbs. For coupling of ^{177}Lu, ^{90}Y, and ^{111}In to mAbs, DOTA and DTPA chelates are mostly used. Although DOTA gives the most stable complexes, DTPA is the chelate of choice for obtaining reliable high labeling yields and conjugates with high specific activities [2, 10]. Unfortunately, the current use of gamma-camera imaging for quantification of ^{111}In/^{177}Lu-labeled mAbs has intrinsic limitations, primarily on account of scatter and partial absorption of gamma-photons in the patient. Besides this, differences in biodistribution between ^{111}In-mAb and ^{90}Y-mAb conjugates have been observed in vivo in tumor-bearing mice and in cancer patients [11–13].

Recently, we introduced the long-lived positron emitter zirconium-89 (^{89}Zr; half-life, 78.4 h) as a promising residualizing radionuclide for PET of mAbs (^{89}Zr-immuno-PET). PET is better qualified for tracer quantification because of more accurate scatter and attenuation correction and superior spatial and temporal resolution for imaging. ^{89}Zr was coupled to mAbs—the chimeric mAb U36 among them—via the chelate *N*-succinyldesferrioxamine B (*N*-sucDf). We demonstrated that quantitative PET with ^{89}Zr was feasible [14]. Moreover, in preliminary studies the chimeric mAb U36-*N*-sucDf-^{89}Zr showed a biodistribution similar to that of the chimeric mAb U36-*p*-SCN-Bz-DOTA-^{88}Y (with ^{88}Y as a gamma-emitting substitute for ^{90}Y) in nude mice bearing the head and neck cancer xenograft line HNX-OE [14]. This model, however, was not representative of more extensively internalizing antibodies.

In the present study, we extended the scope of ^{89}Zr-immuno-PET by using cetuximab (Erbitux; ImClone Systems) as an abundantly internalizing model mAb and nude mice bearing the squamous cell carcinoma xenograft line A431 as the tumor model [15]. Cetuximab is a chimeric IgG_1 mAb that binds with high affinity to the epidermal growth factor receptor (EGFR) [16]. The cell line A431 shows abundant expression of EGFR [17]. The potential of ^{89}Zr to predict the biodistribution of the residualizing labels ^{177}Lu and ^{90}Y was evaluated in a comprehensive way by coinjection of conjugates. To this end, cetuximab-*N*-sucDf-^{89}Zr was administered with cetuximab-*p*-SCN-Bz-DOTA-^{88}Y, cetuximab-*p*-SCN-Bz-DOTA-^{177}Lu, cetuximab-*p*-SCN-Bz-DTPA-^{88}Y, or cetuximab-*p*-SCN-Bz-DTPA-^{177}Lu, and biodistribution in mice was assessed up to 6 d after injection. Before these biodistribution studies, the in vitro stability of the conjugates in human plasma was analyzed.

Materials and Methods

MAb, Cell Line, and Radioactivity

The mAb cetuximab was purchased from ImClone Systems. Cetuximab is a chimeric IgG_1 mAb that binds with high affinity to the EGFR, blocks ligand-induced activation of the receptor tyrosine kinase, and induces dimerization and downregulation of the EGFR, which prevents further binding and activation by the ligands [16]. The human squamous cell carcinoma cell line A431, carrying an amplification of the EGFR gene, was obtained from the American Type Culture Collection (ATCC number CRL-1555).

^{89}Zr (2.7 GBq/mL in 1 mol/L oxalic acid) was produced by Cyclotron BV by a (p,n) reaction on natural ^{89}Y and purified with a hydroxamate column [18]. ^{88}Y (37 MBq/mL in 0.1 mol/L HCl) was obtained from Isotope Products Europe, ^{177}Lu (9.25 GBq/mL in 0.05 mol/L HCl) from Perkin-Elmer, ^{111}In (370 MBq/mL in 0.05 mol/L HCl) from Tyco Healthcare, and ^{125}I (3.7 GBq/mL in 0.01 mol/L NaOH) from Amersham.

Radiolabeling

For ^{89}Zr, ^{88}Y, and ^{177}Lu labeling of mAbs, modification procedures were established to arrive at a chelate-to-mAb molar ratio of 1:1.

Preparation of ^{89}Zr-labeled cetuximab: mAb labeling with ^{89}Zr was achieved starting with the chelate desferrioxamine B (Df) (Desferal; Novartis) as described previously [18]. In short, Df was succinylated (*N*-sucDf), temporarily filled with iron (Fe(III)), and coupled to cetuximab by means of a tetrafluorophenol-*N*-sucDf ester. After removal of Fe(III) by transchelation to ethylenediaminetetraacetic acid (EDTA), the premodified mAb was purified on a PD10 column (eluent: 0.9% NaCl/gentisic acid, 5 mg/mL; pH 5.0). Subsequently, *N*-sucDf-cetuximab was labeled with ^{89}Zr in *N*-2-hydroxyethylpiperazine-*N*-2-ethanesulfonic acid (HEPES) buffer at pH 7.0. Finally, ^{89}Zr-*N*-sucDf-cetuximab was purified on a PD10 column (eluent: 0.9% NaCl/gentisic acid, 5 mg/mL; pH 5.0) to remove any unbound ^{89}Zr.

Preparation of ^{88}Y- or ^{177}Lu-labeled cetuximab: cetuximab was conjugated with *p*-benzyl isothiocyanate-1,4,7,10-tetraazacyclododecane-1,4,7,10-tetraacetic acid (*p*-SCN-Bz-DOTA) or *p*-isothiocyanatobenzyl diethylenetriaminepentaacetic acid (*p*-SCN-Bz-DTPA) (Macrocyclics). All steps were performed under strict metal-free conditions. Before use, cetuximab was extensively dialyzed (Slide-A-Lyzer dialysis cassettes; Pierce Biotechnology) against metal-free $NaHCO_3$ (0.1 mol/L, pH 9.0) containing 2 g of Chelex 100 (Bio-Rad) per liter. For conjugation, 125 µL of *p*-SCN-Bz-DOTA or *p*-SCN-Bz-DTPA (1.6 mg/mL in $NaHCO_3$, 0.1 mol/L; pH 9.0), 175 µL of $NaHCO_3$ (0.1 mol/L, pH 9.0), and 700 µL of dialyzed cetuximab (1.4 mg) were incubated for 30 min at 37°C. The modified cetuximab was purified using a prewashed

PD-10 column and eluted with CH_3COONH_4 (0.25 mol/L, pH 5.5). The cetuximab-*p*-SCN-Bz-DOTA and cetuximab-*p*-SCN-Bz-DTPA conjugates (~0.5 mg) were labeled with either ^{88}Y (1.5 MBq) or ^{177}Lu (28 MBq) in CH_3COONH_4 (0.25 mol/L, pH 5.5) for 60 min at 45°C (*p*-SCN-Bz-DOTA conjugates) or at room temperature (*p*-SCN-Bz-DTPA conjugates), in a total reaction volume of 1 mL. After labeling, 50 µL of EDTA, 0.05 mol/L, were added to the reaction vial, and the mixture was incubated for another 5 min. Nonconjugated ^{88}Y or ^{177}Lu was removed using a PD-10 column with 0.9% NaCl as eluent. The first 2.5 mL (1.0-mL sample volume and the first 1.5 mL) were discarded, and the radiolabeled cetuximab was collected in the next 1.5 mL.

Preparation of ^{125}I-labeled cetuximab: iodination of cetuximab with ^{125}I was performed essentially as described previously [19]. In short, 20-mL ß-scintillation glass vials were coated with 75 µg of IODO-GEN (Pierce Biotechnology) in CH_2Cl_2 and dried under a stream of N_2 gas, resulting in a thin coating of IODO-GEN on the bottom surface of the vial. The vials were stored under N_2 atmosphere. To an IODO-GEN–coated glass vial, 50 µL of Na_2HPO_4 (0.5 mol/L, pH 7.4), 194 µL of Na_2HPO_4 (0.1 mol/L, pH 6.8), 250 µL of cetuximab (2 mg/mL), and 55 MBq of ^{125}I in 6.4 µL of NaOH (1 mmol/L) were successively added. After gentle shaking for 4 min at room temperature, 0.1 mL of ascorbic acid (25 mg/mL, pH 5) was added. After an additional 5 min, the reaction mixture was transferred to a syringe connected to a filter (0.2-µm Acrodisc; Gelman Sciences) followed by 0.4 mL of Na_2HPO_4 (0.1 mol/L, pH 6.8), used for an additional rinsing of the reaction vial. This combined solution was filtered and then purified on a PD-10 column with 0.9% NaCl/ascorbic acid (5 mg/mL, pH 5) as eluent. The first 2.5 mL (1.0-mL sample volume and the first 1.5 mL) were discarded, and the radioiodinated cetuximab was collected in the next 1.5 mL.

Analyses

All conjugates were analyzed by instant thin-layer chromatography (ITLC) for radiochemical purity, by high-performance liquid chromatography and sodium dodecylsulfate-polyacrylamide gel electrophoresis followed by phosphor imager analyses for integrity, and by a cell-binding assay for immunoreactivity. ITLC analysis of radiolabeled cetuximab was performed on silica gel–impregnated glass fiber sheets (Gelman Sciences). As the mobile phase, citrate buffer (20 mmol/L, pH 5.0) was used for ^{125}I- and ^{89}Zr-labeled mAbs. ITLC samples of ^{88}Y- and ^{177}Lu-labeled mAbs were first incubated for 5 min in an EDTA solution (20 mmol/L) and subsequently spotted on ITLC. As the mobile phase, 0.9% NaCl was used. The radioimmunoconjugates were monitored by high-performance liquid chromatography as described previously [18]. Gel electrophoresis was performed on a Pharmacia Phastgel System (Amersham Biosciences) using 7.5% sodium dodecylsulfate–polyacrylamide gel electrophoresis gels (Amersham Biosciences) under nonreducing conditions and analyzed on a

phosphor imager. In vitro binding characteristics of radiolabeled cetuximab were determined in an immunoreactivity assay essentially as described by Lindmo et al. [20], using A431 cells fixed with 2.0% paraformaldehyde.

Determination of Chelate-to-mAb Ratio

The Desferal-to-cetuximab molar ratio was determined by high-performance liquid chromatography analysis using ^{59}Fe as described by Verel et al. [18]. *p*-SCN-Bz-DOTA-to-mAb and *p*-SCN-Bz-DTPA-to-mAb molar ratios were determined following a method described by Meares et al. [21]. In short, conjugates were labeled according to the aforementioned procedures, with a known excess of indium acetate spiked with ^{111}In. After labeling, the solution was challenged with EDTA and subsequently spotted on ITLC. Antibody-bound ^{111}In remained at the origin, whereas unreacted ^{111}In (as ^{111}In-EDTA) moved with R_f 0.8–1.0. ITLC data were used to calculate the chelate-to-mAb molar ratio. For double-checking of *p*-SCN-Bz-DOTA-to-mAb and *p*-SCN-Bz-DTPA-to-mAb molar ratios, the same procedure was performed using an excess of lutetium acetate spiked with ^{177}Lu.

Serum Stability

For measurement of the in vitro stability of each of the individual radioimmunoconjugates, samples containing 100 μg of mAb were incubated in freshly prepared human serum (1:1 v/v dilution; total volume, 1 mL) at 37°C in a humidified incubator maintained at 5% CO_2 and 95% air. At various intervals (1, 3, 5, 7, 9, 13, and 16 d), aliquots were taken and analyzed by ITLC and high-performance liquid chromatography.

Biodistribution Study

Nude mice bearing subcutaneously implanted xenografts of the human tumor line A431 were used. The female mice we used for this experiment (athymic nu/nu, 21–31 g; Harlan CPB) were 8–10 wk old at the time of the experiment. All animal experiments were performed according to National Institutes of Health principles of laboratory animal care and Dutch national law ("Wet op de dierproeven", Stb 1985, 336).

In 4 experiments (Table 1), 64 mice were simultaneously injected intraperitoneally with ^{89}Zr-labeled cetuximab combined with either ^{88}Y- or ^{177}Lu-labeled cetuximab. In all animals, unlabeled cetuximab was added to the injection up to a total of 500 μg. At 24, 48, 72, and 144 h after injection, 4 mice per group and time point were anesthetized, bled, killed, and dissected. Blood, tumor, skin, sternum, heart, lung, liver, spleen, kidney, muscle, thighbone, colon, ileum, and stomach were weighed, and the amount of radioactivity in each tissue was assessed in a gamma-well counter

(Wallac LKB-CompuGamma 1282; Pharmacia). The 511-keV gamma-energy of ^{89}Zr and the 1,837-keV gamma-energy of ^{88}Y were used for dual-isotope counting of the coinjected ^{88}Y/^{89}Zr-labeled mAbs, and the 909-keV gamma-energy of ^{89}Zr and the 208-keV gamma-energy of ^{177}Lu were used for dual-isotope counting of the coinjected ^{177}Lu/^{89}Zr-labeled mAbs. Crossover corrections from one radionuclide into the alternate window were performed using a standard of each radionuclide. To correct for radioactive decay, injection standards were counted simultaneously.

In a fifth experiment (Table 1), 14 mice were injected intraperitoneally with cetuximab-^{125}I combined with cetuximab-*p*-SCN-Bz-DOTA-^{177}Lu, and unlabeled cetuximab was added to the injection up to a total of 1 mg. At 24 h (n = 3), 48 h (n = 4), 72 h (n = 3), and 120 h (n = 4) after injection, the mice were anesthetized, bled, killed, and dissected, with further processing according to the above procedure.

Radioactivity uptake was calculated as the percentage of the injected dose per gram of tissue (%ID/g). Differences in tissue uptake between coinjected conjugates were statistically analyzed for each time point with SPSS 11.0 (SPSS Inc.) using the Student t-test for paired data. Two-sided significance levels were calculated, and $P < 0.05$ was considered statistically significant. Statistical analysis of differences in thighbone uptake between groups was performed using 1-way ANOVA.

Table 1. Radioimmunoconjugates used for the biodistribution study.

	Radioimmunoconjugate	Activity per mouse (kBq)	Radiochemical Purity (%)	Immunoreactivity (%)
Exp. 1	Cetuximab-*p*-SCN-Bz-DOTA-^{88}Y	60	99.2	94
	Cetuximab-*N*-sucDf-^{89}Zr	500	98.0	93
Exp. 2	Cetuximab-*p*-SCN-Bz-DOTA-^{177}Lu	370	98.8	97
	Cetuximab-*N*-sucDf-^{89}Zr	500	98.0	93
Exp. 3	Cetuximab-*p*-SCN-Bz-DTPA-^{88}Y	47	98.0	97
	Cetuximab-*N*-sucDf-^{89}Zr	320	97.8	97
Exp. 4	Cetuximab-*p*-SCN-Bz-DTPA-^{177}Lu	170	99.4	96
	Cetuximab-*N*-sucDf-^{89}Zr	320	97.8	97
Exp. 5	Cetuximab-*p*-SCN-Bz-DOTA-^{177}Lu	370	99.0	96
	Cetuximab-^{125}I	370	99.8	98

Results

Conjugation and Radiolabeling

Within the applied stoichiometry, premodification of cetuximab resulted in 0.8–1.2 *N*-sucDf, *p*-SCN-Bz-DOTA, or *p*-SCN-Bz-DTPA moieties per mAb. Subsequent labeling of cetuximab-*N*-sucDf with ^{89}Zr and cetuximab-*p*-SCN-Bz-DOTA or cetuximab-*p*-SCN-Bz-DTPA with ^{88}Y or ^{177}Lu resulted in overall labeling yields of >70%. The radiochemical purity was at least 97% for all 5 products (Table 1). Labeling of cetuximab with ^{125}I resulted in an overall labeling yield of 89%, and the radiochemical purity was 99.8% for the purified product. Immunoreactivity for all cetuximab conjugates was more than 93% at the highest cell concentration. The specific activities for the biodistribution studies were 78 MBq/mg for cetuximab-*N*-sucDf-^{89}Zr, 0.49 MBq/mg for cetuximab-*p*-SCN-Bz-DOTA-^{88}Y, 37 MBq/mg for cetuximab-*p*-SCN-Bz-DOTA-^{177}Lu, 0.41 MBq/mg for cetuximab-*p*-SCN-Bz-DTPA-^{88}Y, 26 MBq/mg for cetuximab-*p*-SCN-Bz-DTPA-^{177}Lu, and 109 MBq/mg for cetuximab-^{125}I.

In Vitro Stability

All conjugates were individually tested for stability in human serum. These results are shown in Table 2. Cetuximab-*N*-sucDf-^{89}Zr, cetuximab-*p*-SCN-Bz-DOTA-^{88}Y, and cetuximab-*p*-SCN-Bz-DOTA-^{177}Lu were stable until day 7; <3% of the radiolabel was released during this incubation period. Cetuximab-*p*-SCN-Bz-DTPA-^{88}Y and cetuximab-*p*-SCN-Bz-DTPA-^{177}Lu showed a slightly faster radiometal release during this period (4.6% and 4.3%, respectively). After day 7, the latter conjugates and also cetuximab-*N*-sucDf-^{89}Zr showed an accelerated release of radiolabel when compared with cetuximab-*p*-SCN-Bz-DOTA-^{88}Y and cetuximab-*p*-SCN-Bz-DOTA-^{177}Lu. At day 16, there was a total release of 22.4%, 23.5%, and 17.4% for cetuximab-*p*-SCN-Bz-DTPA-^{88}Y, cetuximab-*p*-SCN-Bz-DTPA-^{177}Lu, and cetuximab-*N*-sucDf-^{89}Zr, respectively, versus 4.0% and 2.9% for cetuximab-*p*-SCN-Bz-DOTA-^{88}Y and cetuximab-*p*-SCN-Bz-DOTA-^{177}Lu, respectively.

Biodistribution Study

For comparison of the biodistribution of ^{89}Zr-labeled mAb with ^{88}Y- or ^{177}Lu-labeled mAb, cetuximab-*N*-sucDf-^{89}Zr was coinjected in tumor-bearing mice with cetuximab-*p*-SCN-Bz-DOTA-^{88}Y (experiment 1), cetuximab-*p*-SCN-Bz-DOTA-^{177}Lu (experiment 2), cetuximab-*p*-SCN-Bz-DTPA-^{88}Y (experiment 3), or cetuximab-*p*-SCN-Bz-DTPA-^{177}Lu (experiment 4). The essential characteristics of the radiolabeled immunoconjugates used in the biodistribution study are shown in Table 1, and the corresponding biodistributions are summarized in Figures 1- 4. At the time of dissection, the tumor

Table 2. In vitro stability of radioimmunoconjugates upon incubation at 37°C in human serum.

	Radiochemical purity							
Conjugate	**0 d**	**1 d**	**3 d**	**5 d**	**7 d**	**9 d**	**13 d**	**16 d**
^{89}Zr-Df-MAb	97.5	98.0	97.0	96.7	95.3	94.4	88.9	80.1
^{88}Y-*p*-SCN-Bz-DOTA-MAb	99.6	97.1	96.7	96.8	96.7	96.8	96.8	95.6
^{177}Lu-*p*-SCN-Bz-DOTA-MAb	99.7	98.5	97.6	98.7	98.6	97.9	97.5	96.8
^{88}Y-*p*-SCN-Bz-DTPA-MAb	97.5	98.4	95.2	93.8	92.9	89.7	81.9	75.1
^{177}Lu-*p*-SCN-Bz-DTPA-MAb	97.2	94.7	93.9	94.5	92.9	90.6	86.3	73.7

weights (mean ± SD) were 61 ± 72, 78 ± 65, 189 ± 176, and 148 ± 110 mg for experiments 1, 2, 3, and 4, respectively. The radioactivity uptake in tumor and most other tissues was comparable between ^{89}Zr-labeled cetuximab on the one hand and ^{88}Y- or ^{177}Lu-labeled cetuximab on the other hand (Figs. 1–4). The only consistent difference observed was a significantly higher uptake for ^{89}Zr than for ^{88}Y and ^{177}Lu in thighbone and sternum at all time points except 24 h after injection in thighbone for experiment 1 (Fig. 1, P = 0.176) and experiment 3 (Fig. 3, P = 0.096). At 72 h after injection, the mean thighbone uptake was between 3.2 and 4.7 %ID/g for ^{89}Zr, compared with 1.6 and 1.3 %ID/g for ^{88}Y- and ^{177}Lu-*p*-SCN-Bz-DOTA, respectively, and 2.3 and 2.0 %ID/g for ^{88}Y- and ^{177}Lu-*p*-SCN-Bz-DTPA, respectively. These data revealed that radioactivity accretion in thighbone was 2.0, 2.5, 2.0, and 2.4 times higher for the N-sucDf-^{89}Zr conjugates than for the *p*-SCN-Bz-DOTA-^{88}Y, *p*-SCN-Bz-DOTA-^{177}Lu, *p*-SCN-Bz-DTPA-^{88}Y, and *p*-SCN-Bz-DTPA-^{177}Lu conjugates, respectively. At 144 h, differences in thighbone were larger, with a mean uptake of between 4.8 and 6.9 %ID/g for ^{89}Zr, compared with 1.5 and 1.0 %ID/g for ^{88}Y- and ^{177}Lu-*p*-SCN-Bz-DOTA, respectively, and 2.4 and 2.0 %ID/g for ^{88}Y- and ^{177}Lu-*p*-SCN-Bz-DTPA, respectively.

An ANOVA showed that the thighbone uptake for both ^{177}Lu and ^{88}Y was significantly higher (P < 0.05) for the *p*-SCN-Bz-DTPA conjugates than for the *p*-SCN-Bz-DOTA conjugates at 72 h and 144 h. An exceptional observation was seen in mice coinjected with cetuximab-*N*-sucDf-^{89}Zr and cetuximab-*p*-SCN-Bz-DTPA-^{88}Y at 144 h after injection (Fig. 3). For both conjugates, we observed a much higher accumulation of activity in the liver and a concomitant enhanced drop in blood and tumor uptake when compared with the other experiments.

To illustrate the effect of abundant conjugate internalization and radionuclide residualization on radioactivity distribution, the biodistribution of coinjected ^{177}Lu-*p*-SCN-Bz-DOTA-cetuximab and ^{125}I-cetuximab was compared in the same animal model

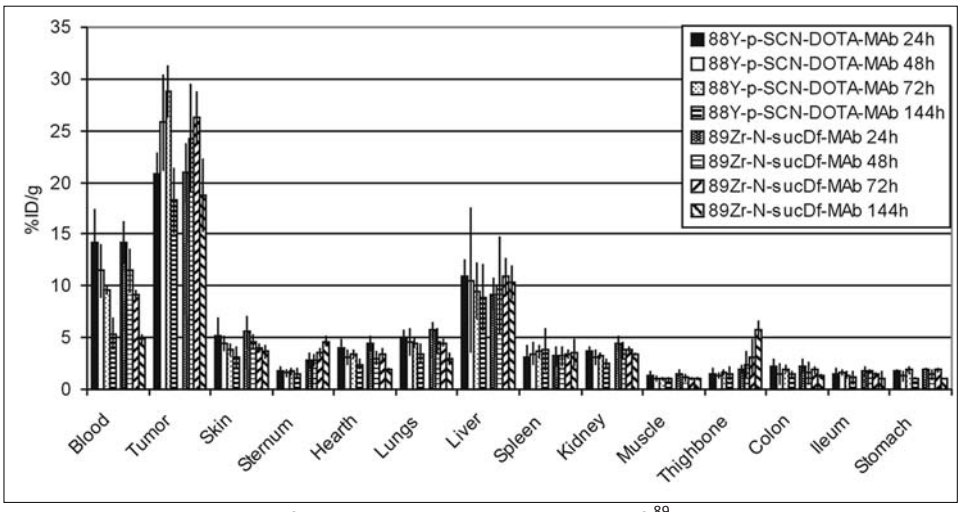

Figure 1. Biodistributions of i.p. coinjected cetuximab-*N*-sucDf-^{89}Zr and cetuximab-*p*-SCN-Bz-DOTA-^{88}Y (Exp. 1, total of 500 μg MAb) in A431 xenograft-bearing nude mice at 24, 48, 72, and 144 h after injection.

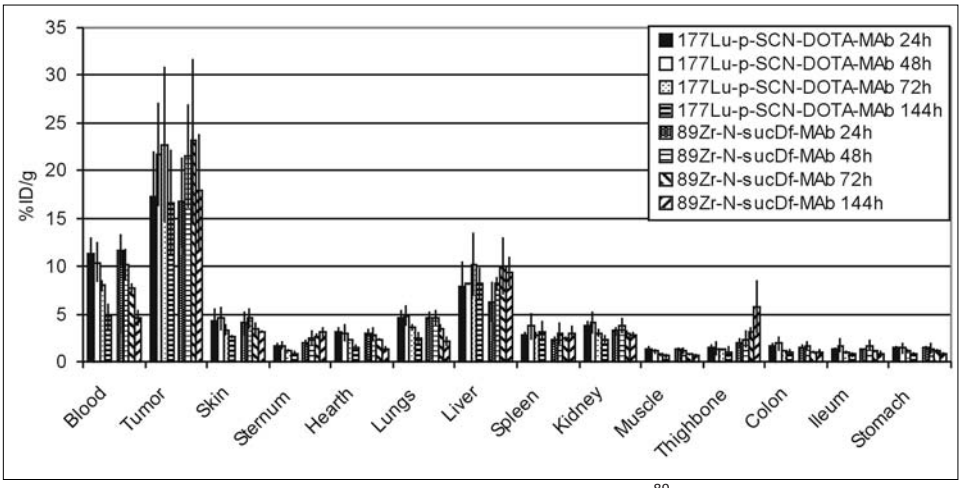

Figure 2. Biodistributions of i.p. coinjected cetuximab-*N*-sucDf-^{89}Zr and cetuximab-*p*-SCN-Bz-DOTA-^{177}Lu (Exp. 2, total of 500 μg MAb) in A431 xenograft-bearing nude mice at 24, 48, 72, and 144 h after injection.

(experiment 5; Fig. 5). At the time of dissection, the tumor weight was 132 ± 72 mg (mean ± SD). The radioactivity uptake in tumor differed markedly; for example, at 72 h after injection, the mean tumor uptake was 21.9 %ID/g for the residualizing radionuclide ^{177}Lu, compared with 4.5 %ID/g for the nonresidualizing radionuclide ^{125}I. Also, radioactivity uptake levels in liver and, to a lesser degree, spleen, kidney, and skin differed substantially, with a higher uptake for ^{177}Lu than for ^{125}I. Blood values

and values in all other organs were similar. For ^{125}I-cetuximab, the tumor-to-blood ratio never exceeded 1, notwithstanding the fact that ^{125}I-cetuximab was of the highest quality with respect to integrity and immunoreactivity.

Discussion

Biodistribution may be accurately predicted—and delivery of radiation dose to tumors and critical organs estimated—by performing an immuno-PET scouting procedure before RIT. A prerequisite for this approach is that the PET and RIT conjugates of the mAb of interest must provide similar radioactivity biodistributions. Differences in radionuclide distribution might occur in several instances: when the mAb conjugates show altered and deviating pharmacokinetics (e.g., as a result of radiolabeling), when the radionuclide–chelate complexes exhibit different in vivo stabilities, when the radionuclides show deviating redistributions after release from the conjugate or catabolism (e.g., after internalization of the radioimmunoconjugate by the tumor cell), or when combinations of these and possibly other factors occur.

Recently, Verel et al. reported that the chimeric mAb U36-*N*-sucDf labeled with the positron emitter ^{89}Zr was able to monitor the biodistribution of the chimeric mAb U36-*p*-SCN-DOTA-^{88}Y in nude mice bearing HNSCC xenografts and that quantitative PET with ^{89}Zr is feasible [14]. The conclusion from these studies was that ^{89}Zr and ^{90}Y form a perfect PET/RIT isotope pair. However, because only a minor proportion of

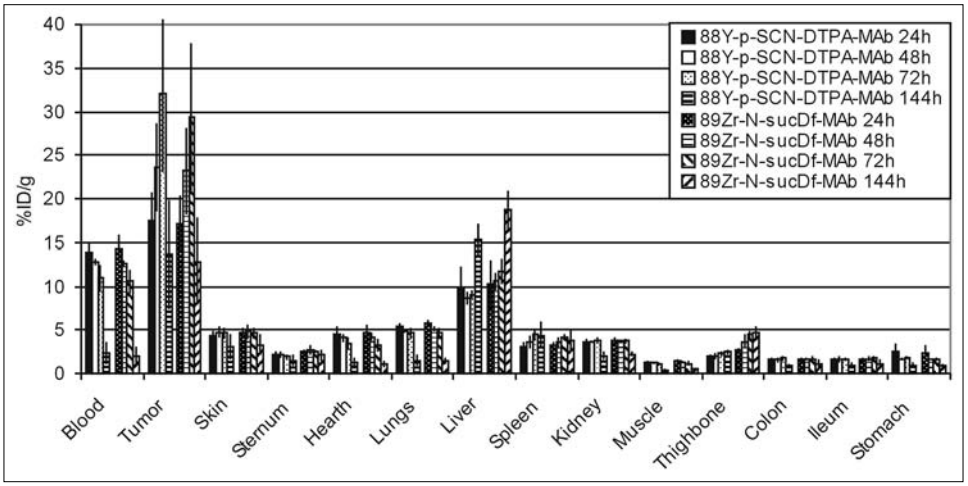

Figure 3. Biodistributions of i.p. coinjected cetuximab-*N*-sucDf-^{89}Zr and cetuximab-*p*-SCN-Bz-DTPA-^{88}Y (Exp. 3, total of 500 μg MAb) in A431 xenograft-bearing nude mice at 24, 48, 72, and 144 h after injection.

chimeric mAb U36 internalizes after binding to its target antigen CD44v6, it might be that this does not hold true for abundantly internalizing mAbs.

Studies were therefore extended to assess the full potential of ^{89}Zr for predicting the biodistribution of residualizing therapeutic radiometals. First, the anti-EGFR mAb cetuximab was used for in vivo targeting of the xenograft line A431, because of the high rate of internalization (as illustrated by using a residualizing and a nonresidualizing radiolabel; Figure 5). Second, the residualizing RIT radionuclide ^{88}Y (as a substitute for ^{90}Y) was tested along with ^{177}Lu. Finally, the chelate *p*-SCN-Bz-DOTA used for coupling of ^{90}Y and ^{177}Lu was tested along with *p*-SCN-Bz-DTPA. Although the pathlength and energy of its ß– particles make ^{90}Y the most suitable for RIT of large tumors, ^{177}Lu is the more favorable radionuclide for treatment of small tumors. Although complexes of these RIT radionuclides with DOTA are considered to be more stable than complexes with DTPA-like molecules [22], DTPA-like molecules are sometimes preferred because of the better labeling efficiency [2, 10].

We adopted procedures for stable coupling of all 3 radiolabels to cetuximab without loss of immunoreactivity. The modification of the mAb and subsequent labeling of the mAb–chelate conjugate with ^{89}Zr has already been described in detail by Verel et al. [18]. These procedures resulted in high labeling yields and specific activities. Coupling of DOTA and DTPA to mAbs and labeling with ^{88}Y or ^{177}Lu has been documented extensively. We standardized conjugation procedures to obtain a chelate-to-mAb molar ratio of 1:1, because higher ratios can dramatically alter the pharmacokinetics of the mAb [23].

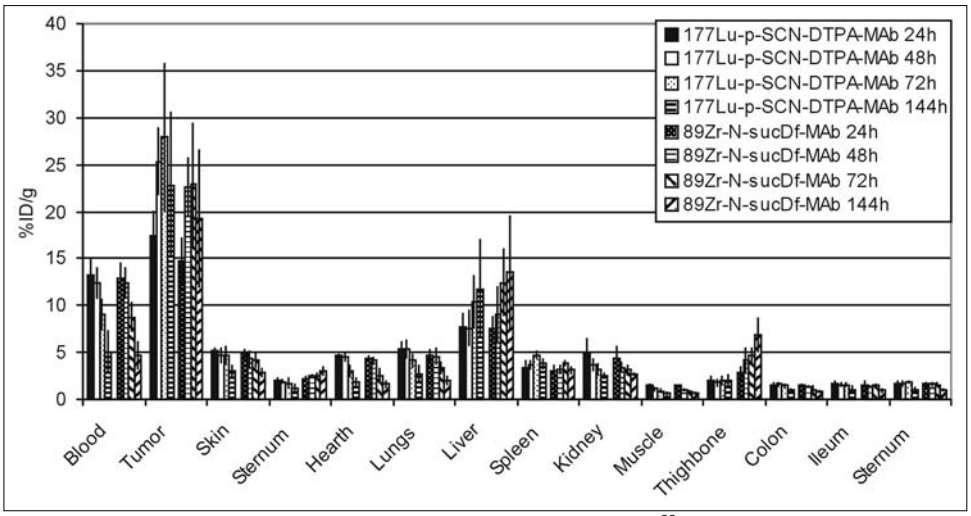

Figure 4. Biodistributions of i.p. coinjected cetuximab-*N*-sucDf-^{89}Zr and cetuximab-*p*-SCN-Bz-DTPA-^{177}Lu (Exp. 4, total of 500 μg MAb) in A431 xenograft-bearing nude mice at 24, 48, 72, and 144 h after injection.

Preceding the biodistribution studies, the in vitro stability of the 5 radiometal conjugates in human serum was analyzed. The stability of all conjugates under these conditions was comparable and high until day 7. The ^{89}Zr-*N*-sucDf conjugate and the ^{88}Y/^{177}Lu-*p*-SCN-Bz-DOTA conjugates were especially stable during this period, showing less than 3% release. At later times, the ^{88}Y/^{177}Lu-*p*-SCN-Bz-DTPA conjugates and the ^{89}Zr-*N*-sucDf conjugate were less stable than the ^{88}Y/^{177}Lu-*p*-SCN-Bz-DOTA conjugates (at day 16, 22.4%/23.5% release for the ^{88}Y/^{177}Lu-*p*-SCN-Bz-DTPA conjugates and 17.4% for the ^{89}Zr-N-sucDf conjugate, vs. 4.0%/2.9% for the ^{88}Y/^{177}Lu-*p*-SCN-Bz-DOTA conjugates). Comparable differences in in vitro stability between ^{90}Y-DOTA-hLL2 and ^{90}Y-DTPA-hLL2 (0% vs. 3.6% dissociation after a 5-d incubation and 0.4% vs. 10.7% dissociation after an 11-d incubation) were previously reported by Govindan et al. [22]. For ^{89}Zr-*N*-sucDf-mAb conjugates, stability data on later time points have been scarce thus far. Brouwers et al. [24] mentioned a less than 10% release of ^{89}Zr from cG250-*N*-sucDf during a 4-d incubation.

For easy comparison of the biodistributions, cetuximab-*N*-sucDf-^{89}Zr was administered to A431-bearing nude mice simultaneously with cetuximab-*p*-SCN-Bz-DOTA-^{88}Y, cetuximab-*p*-SCN-Bz-DOTA-^{177}Lu, cetuximab-*p*-SCN-Bz-DTPA-^{88}Y, or cetuximab-*p*-SCN-Bz-DTPA-^{177}Lu. Blood clearance was similar for all 5 conjugates. These results indicate that the pharmacokinetics of the mAb remained preserved on radiolabeling, irrespective of the type of chelate or radionuclide that had been used. Furthermore, the congruency of radioactivity levels in blood and several other organs in each individual mouse also indicated that the in vivo stability of the different chelate–radionuclide complexes was similar, results that agree with the in vitro serum

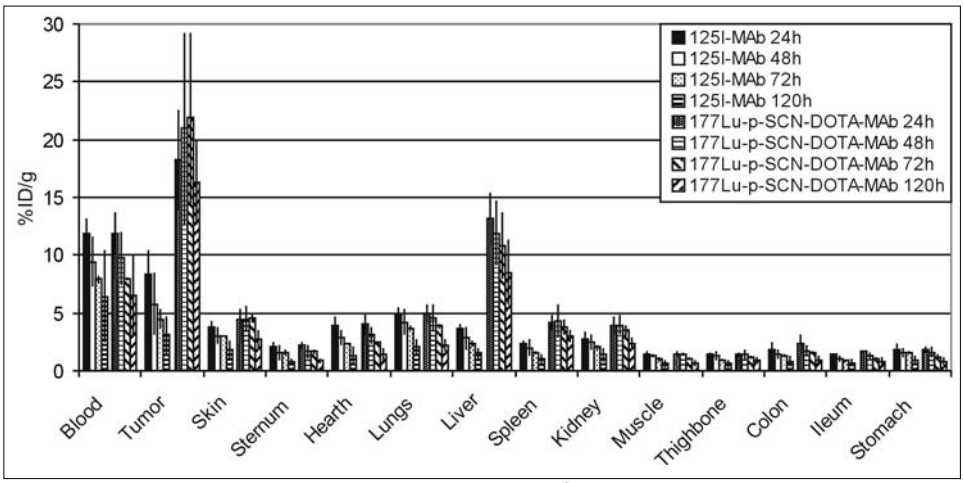

Figure 5. Biodistributions of i.p. coinjected cetuximab-^{125}I and cetuximab-*p*-SCN-Bz-DOTA-^{177}Lu (Exp.5, total of 1 mg MAb) in A431 xenograft-bearing nude mice at 24, 48, 72, and 120 h after injection.

stability measurements. Finally, tumor uptake levels indicate that the internalization rate of the radiolabeled conjugates and residualization of the 3 radiometals were similar within the period studied. Still, some differences in uptake between cetuximab-*N*-sucDf-^{89}Zr on the one hand and ^{88}Y- and ^{177}Lu-labeled cetuximab-*p*-SCN-Bz-DOTA/DTPA on the other hand were found in thighbone and, to a lesser degree, in sternum at all time points except 24 h after injection in thighbone for experiments 1 and 3. These data suggest that released ^{89}Zr or ^{89}Zr-containing metabolites might have a higher preference for thighbone and sternum than do the ^{88}Y and ^{177}Lu counterparts. Difference in bone accumulation has already been reported by Verel et al. [14]. Between coinjected ^{89}Zr-labeled chimeric mAb U36 and ^{88}Y-labeled chimeric mAb U36, they found a difference of 2.5% ± 0.1 %ID/g versus 1.3% ± 0.1 %ID/g in thighbone at 72 h after injection and of 3.5% ± 0.4 %ID/g versus 1.1% ± 0.1 %ID/g at 144 h. The higher thighbone uptake of ^{89}Zr in our study might be related to the faster internalization rate of cetuximab than of chimeric mAb U36, which probably results in more extensive redistribution of bone-seeking ^{89}Zr-metabolites.

The bone marrow is generally the dose-limiting organ in nonmyeloablative RIT and is therefore important for dosimetric evaluations. For prediction of dose delivery to bone marrow in a combined immuno-PET/RIT setting, estimation of the bone marrow self-dose does not seem a problem, because blood levels were the same for the 3 radiometals. Dose delivery originating from radioactivity in the bone, however, will require an adjustment. Alternatively, differences in bone accumulation might be avoided by the development of a single chelate that binds ^{89}Zr, ^{88}Y, and ^{177}Lu with exactly the same high in vivo stability. The search for such an ideal chelate is part of our ongoing research. However, the use of the same chelate is not a guarantee for a congruent bone uptake. For example, differences in bone uptake have been observed between ^{111}In-mAb and ^{90}Y-mAb conjugates in vivo in tumor-bearing mice and in cancer patients, despite the fact that a single DTPA- or DOTA-like chelate was used for coupling of ^{111}In and ^{90}Y to the mAbs [11, 12].

Intergroup differences make it difficult to draw firm conclusions about mutual differences in biodistribution between ^{88}Y and ^{177}Lu or between *p*-SCN-Bz-DOTA and *p*-SCN-Bz-DTPA conjugates. However, comparisons with the biodistribution of the ^{89}Zr-labeled-mAb that was coinjected as a reference conjugate in each case allow one to conclude that the in vivo behaviors of ^{88}Y and ^{177}Lu are similar. This conclusion is in accordance with previous findings of Stein et al. [25]. With respect to the *p*-SCN-Bz-DOTA versus the *p*-SCN-Bz-DTPA chelate, there is an indication of higher thighbone accumulation in the case of ^{88}Y/^{177}Lu-*p*-SCN-Bz-DTPA conjugates, an observation also described by others [2, 22, 26].

An alternative positron-emitting surrogate for estimation of the pharmacokinetics and biodistribution of ^{177}Lu/^{90}Y-labeled pharmaceuticals could be

^{86}Y (33% ß+; half-life, 14.7 h) [12, 27, 28]. An advantage of ^{86}Y over ^{89}Zr is that the same chelate can be used for complexation of both ^{86}Y and ^{177}Lu/^{90}Y. Moreover, when ^{86}Y is used as a surrogate for ^{90}Y, decomplexation of the same element should result in identical tissue distribution, provided radioimmunoconjugate quality is identical. Unfortunately, ^{86}Y has 2 drawbacks: First, the half-life of ^{86}Y (14.7 h) might be ideal for imaging mAb fragments and peptides but is rather short for optimal imaging of intact mAbs. It takes typically 48–96 h for intact mAbs to achieve optimal tumor-to-nontumor ratios. This shorter half-life of ^{86}Y, compared with the half-life of ^{89}Zr (78.4 h), will also have disadvantages for logistics related to transportation and labeling of mAbs. Second, in contrast to ^{89}Zr, ^{86}Y emits prompt gamma-photons, which together with 511-keV annihilation photons can result in so-called spurious true coincidences and therefore can introduce quantification artifacts [29]. Solutions to these artifacts are under investigation [30, 31].

Conclusion

In the present study, we showed that ^{89}Zr can perfectly predict the biodistribution of the residualizing labels ^{177}Lu and ^{88}Y in combination with the internalizing mAb cetuximab. The average uptake levels in tumor and other organs, except for thighbone and sternum, were similar for cetuximab-*N*-sucDf-^{89}Zr when compared with cetuximab-*p*-SCN-Bz-DOTA-^{88}Y, cetuximab-*p*-SCN-Bz-DOTA-^{177}Lu, cetuximab-*p*-SCN-Bz-DTPA-^{88}Y, and cetuximab-*p*-SCN-Bz-DTPA-^{177}Lu. In view of the advantages of PET over SPECT, ^{89}Zr-immuno-PET is a promising modality for in vivo scouting of ^{90}Y- and ^{177}Lu-labeled mAbs, although care should be taken when estimating bone marrow doses.

Acknowledgements

This project was financially supported by STW (grant VBC.6120) and by the European Union FP6, LSHC-CT-2003–5032, STROMA. The content reflects only the authors' view. The European Commission is not liable for any use that may be made of the information. The authors thank BV Cyclotron for performing irradiations, Jan H. Rector (Solid State Physics, VU University) for sputtering ^{89}Y-copper supports, and Marianne Budde (VU University Medical Center) for contributing to the experiments.

References

1. Sharkey RM, Goldenberg DM. Perspectives on cancer therapy with radiolabeled monoclonal antibodies. J Nucl Med 2005;46(suppl):115S–27S.
2. Brouwers AH, Van Eerd JEM, Frielink C, et al. Optimization of radioimmunotherapy of renal cell carcinoma: labeling of monoclonal antibody cG250 with ^{131}I, ^{90}Y, ^{177}Lu, or ^{186}Re. J Nucl Med 2004;45:327–37.
3. Press OW, Shan D, Howell-Clark J, et al. Comparative metabolism and retention of iodine-125, yttrium-90, and indium-111 radioimmunoconjugates by cancer cells. Cancer Res 1996;56:2123–9.
4. Sharkey RM, Behr TM, Mattes MJ, et al. Advantage of residualizing radiolabels for an internalizing antibody against the B-cell lymphoma antigen, CD22. Cancer Immunol Immunother 1997;44:179–88.
5. Börjesson PKE, Postema EJ, de Bree R, et al. Radioimmunodetection and radioimmunotherapy of head and neck cancer. Oral Oncol 2004;40:761–72.
6. de Jong M, Breeman WA, Valkema R, Bernard BF, Krenning EP. Combination radionuclide therapy using ^{177}Lu- and ^{90}Y-labeled somatostatin analogs. J Nucl Med 2005;46(suppl):13S–7S.
7. Fink-Bennett DM, Thomas K. ^{90}Y-Ibritumomab tiuxetan in the treatment of relapsed or refractory B-cell non-Hodgkin's lymphoma. J Nucl Med Technol 2003;31:61–8.
8. Seldin DW. Techniques for using Bexxar for the treatment of non-Hodgkin's lymphoma. J Nucl Med Technol 2002;30:109–14.
9. Verel I, Visser GWM, van Dongen GAMS. The promise of immuno-PET in radioimmunotherapy. J Nucl Med 2005;46(suppl):164S–71S.
10. Milenic DE, Garmestani K, Chappell LL, et al. In vivo comparison of macrocyclic and acyclic ligands for radiolabeling of monoclonal antibodies with ^{177}Lu for radioimmunotherapeutic applications. Nucl Med Biol 2002;29:431–42.
11. Carrasquillo JA, White JD, Paik CH, et al. Similarities and differences in ^{111}In- and ^{90}Y-labeled 1B4M-DTPA antiTac monoclonal antibody distribution. J Nucl Med 1999;40:268–276.
12. Camera L, Kinuya S, Garmestani K, et al. Comparative biodistribution of indium- and yttrium-labeled B3 monoclonal antibody conjugated to either 2-(p-SCN-Bz)-6-methyl-DTPA (1B4M-DTPA) or 2-(p-SCN-Bz)-1,4,7,10-tetraazacyclododecane tetraacetic acid (2B-DOTA). Eur J Nucl Med 1994;21:640–46.
13. Garmestani K, Milenic DE, Plascjak PS, Brechbiel MW. A new and convenient method for purification of ^{86}Y using a Sr(II) selective resin and comparison of biodistribution of ^{86}Y and ^{111}In labeled Herceptin. Nucl Med Biol 2002;29:599–606.
14. Verel I, Visser GWM, Boellaard R, et al. Quantitative ^{89}Zr immuno-PET for in vivo scouting of ^{90}Y-labeled monoclonal antibodies in xenograft-bearing nude mice. J Nucl Med 2003;44:1663–70.
15. Fan Z, Lu Y, Wu X, Mendelsohn J. Antibody-induced epidermal growth factor receptor dimerization mediates inhibition of autocrine proliferation of A431 squamous carcinoma cells. J Biol Chem 1994;269:27595–602.
16. Mendelsohn J, Baselga J. Status of epidermal growth factor receptor antagonists in the biology and treatment of cancer. J Clin Oncol 2003;21:2787–99.

17. Sunada H, Peacock J, Mendelsohn J. Ligand induced internalization of epidermal growth factor receptors by A431 cells decreases at high cell densities in culture. Growth Factors 1991;5:45–55.
18. Verel I, Visser GWM, Boellaard R, Stigter-Van Walsum M, Snow GB, Van Dongen GAMS. ^{89}Zr Immuno-PET: comprehensive procedures for the production of ^{89}Zr-labeled monoclonal antibodies. J Nucl Med 2003;44:1271–81.
19. Visser GWM, Klok RP, Gebbinck JWK, Ter Linden T, Van Dongen GAMS, Molthoff CF. Optimal quality ^{131}I-monoclonal antibodies for high-dose labeling in a large reaction volume and temporarily coating the antibody with IODO-GEN. J Nucl Med 2001;42:509–19.
20. Lindmo T, Boven E, Cuttitta F, Fedorko J, Bunn PA. Determination of the immunoreactive fraction of radiolabeled monoclonal-antibodies by linear extrapolation to binding at infinite antigen excess. J Immunol Methods 1984;72:77–89.
21. Meares CF, McCall MJ, Reardan DT, Goodwin DA, Diamanti CI, McTigue M. Conjugation of antibodies with bifunctional chelating agents: isothiocyanate and bromoacetamide reagents, methods of analysis, and subsequent addition of metal ions. Anal Biochem 1984;142:68–78.
22. Govindan SV, Shih LB, Goldenberg DM, et al. ^{90}Yttrium-labeled complementarity-determining-region-grafted monoclonal antibodies for radioimmunotherapy: radiolabeling and animal biodistribution studies. Bioconjug Chem. 1998;9:773–782.
23. van Gog FB, Visser GW, Stroomer JW, Roos JC, Snow GB, Van Dongen GAMS. High dose rhenium-186-labeling of monoclonal antibodies for clinical application: pitfalls and solutions. Cancer 1997;80(suppl):2360S–70S.
24. Brouwers A, Verel I, van Eerd J, et al. PET radioimmunoscintigraphy of renal cell cancer using ^{89}Zr-labeled cG250 monoclonal antibody in nude rats. Cancer Biother Radiopharm 2004;19:155–63.
25. Stein R, Govindan SV, Chen S, et al. Radioimmunotherapy of a human lung cancer xenograft with monoclonal antibody RS7: evaluation of ^{177}Lu and comparison of its efficacy with that of ^{90}Y and residualizing ^{131}I. J Nucl Med 2001;42:967–74.
26. Griffiths GL, Govindan SV, Sharkey RM, Fisher DR, Goldenberg DM. ^{90}Y-DOTA-hLL2: an agent for radioimmunotherapy of non-Hodgkin's lymphoma. J Nucl Med 2003;44:77–84.
27. Pauwels S, Barone R, Walrand S, et al. Practical dosimetry of peptide receptor radionuclide therapy with ^{90}Y-labeled somatostatin analogs. J Nucl Med 2005;46(suppl):92S–98S.
28. Lovqvist A, Humm JL, Sheikh A, et al. PET imaging of ^{86}Y-labeled anti-Lewis Y monoclonal antibodies in a nude mouse model: comparison between ^{86}Y and ^{111}In radiolabels. J Nucl Med 2001;42:1281–7.
29. Pentlow KS, Finn RD, Larson SM, Erdi YE, Beattie BJ, Humm JL. Quantitative imaging of yttrium-86 with PET: the occurrence and correction of anomalous apparent activity in high density regions. Clin Positron Imaging 2000;3:85–90.
30. Buchholz HG, Herzog H, Forster GJ, et al. PET imaging with yttrium-86: comparison of phantom measurements acquired with different PET scanners before and after applying background subtraction. Eur J Nucl Med Mol Imaging 2003;30:716–20.
31. Walrand S, Jamar F, Mathieu I, et al. Quantitation in PET using isotopes emitting prompt single gammas: application to yttrium-86. Eur J Nucl Med Mol Imaging 2003;30:354–61.

CHAPTER 3

Preparation and evaluation of ^{89}Zr-Zevalin for monitoring of ^{90}Y-Zevalin biodistribution with positron emission tomography

Lars R. Perk
Otto J. Visser
Marijke Stigter-van Walsum
Maria J. W. D. Vosjan
Gerard W. M. Visser
Josée Zijlstra
Peter C. Huygens
Guus A. M. S. van Dongen

European Journal of Nuclear Medicine and Molecular Imaging 2006;33:1337-1345

Abstract

Purpose: To evaluate whether ^{89}Zr can be used as a PET surrogate label for quantification of ^{90}Y-ibritumomab tiuxetan (^{90}Y-Zevalin) biodistribution and dosimetry before myeloablative radioimmunotherapy.

Methods: Zevalin was labeled with ^{89}Zr by introducing *N*-succinyldesferal (*N*-sucDf) as a second chelate. For comparison of the in vitro stability of ^{89}Zr-Zevalin and ^{88}Y-Zevalin (as a substitute for ^{90}Y), samples were incubated in human serum at 37°C up to 6 days. Biodistribution of ^{89}Zr-Zevalin and ^{88}Y-Zevalin was assessed at 24, 48, 72 and 144 h p.i. by co-injection in nude mice bearing the non-Hodgkin's lymphoma (NHL) xenograft line Ramos. The clinical performance of ^{89}Zr-Zevalin-PET was evaluated via a pilot imaging study in a patient with NHL, who had undergone [^{18}F]FDG-PET 2 weeks previously.

Results: Modification of Zevalin with *N*-sucDf resulted in an *N*-sucDf-to-antibody molar ratio of 0.83±0.04. After radiolabeling and purification, the radiochemical purity and immunoreactivity of ^{89}Zr-Zevalin always exceeded 95% and 80%, respectively. ^{89}Zr-Zevalin showed the same stability in serum as ^{88}Y-Zevalin, with a radiochemical purity >95% during a period of 6 days. The co-injected ^{89}Zr-Zevalin and ^{88}Y-Zevalin conjugates showed a very similar biodistribution, except for liver and bone accumulation at 72 and 144 h p.i., which was significantly higher for ^{89}Zr than for ^{88}Y. PET images obtained after injection of ^{89}Zr-Zevalin showed clear targeting of all known tumor lesions.

Conclusion: ^{89}Zr-Zevalin and ^{88}Y-Zevalin showed a very similar biodistribution in mice, implying that ^{89}Zr-Zevalin-PET might be well suited for prediction of ^{90}Y-Zevalin biodistribution in a myeloablative setting.

Introduction

The yttrium-90 (^{90}Y) labeled anti-CD20 murine monoclonal antibody (mAb) ibritumomab tiuxetan (^{90}Y-Zevalin, Biogen IDEC and Schering AG) was approved by the U.S. Food and Drug Administration in 2002 for the treatment of patients with relapsed or refractory low-grade, follicular or transformed B-cell non-Hodgkin's lymphoma (NHL), including rituximab-refractory follicular NHL [1, 2]. In 2004, the European Medicines Agency (EMEA) approved ^{90}Y-Zevalin for the treatment of adult patients with rituximab-relapsed or refractory CD20+ follicular B-cell NHL [3]. The Zevalin radioimmunotherapy (RIT) procedure is preceded by administration of 250 mg/m^2 rituximab (Rituxan, Biogen IDEC and Genentech) to clear peripheral B cells and to improve biodistribution of the radiolabeled Zevalin. Recently, promising results have also been obtained in the treatment of aggressive NHL. In these studies, high-dose ^{90}Y-Zevalin RIT was added to high-dose chemotherapy followed by autologous stem cell transplantation (AuSCT) [4, 5]. The optimal use of ^{90}Y-Zevalin in this kind of myeloablative RIT, however, remains to be determined.

^{90}Y has a physical half-life of 64.1 h and emits high-energy β^- particles. The absence of γ-ray emission minimizes dose radiation burden for medical personnel and relatives and enables outpatient treatment. Whereas these characteristics make ^{90}Y attractive for therapy, the lack of associated photon emission does not allow external imaging of the in vivo distribution of the ^{90}Y-labeled mAb. Therefore, to confirm tumor targeting and to estimate the absorbed dose (dosimetry) by tumors as well as normal tissues, in the studies on myeloablative RIT a pretherapy single-photon emission computed tomography (SPECT) imaging study with indium-111 (^{111}In, $t_{1/2}$=67.3 h) labeled Zevalin was performed [4, 5]. For coupling of ^{111}In and ^{90}Y to Zevalin, the chelator 1-isothiocyanatobenzyl-3-methyldiethylene triamine penta-acetic acid designated MX-DTPA (tiuxetan) was used, because it binds these three-valent radionuclides with high stability.

In myeloablative RIT, high doses of ^{90}Y are used and therefore dosimetry as accurate as possible will be highly desirable for prevention of exposure of normal organs to unacceptable doses and for evaluation of dose-response relationships. Positron emission tomography (PET) is better suited than SPECT for tracer quantification [6], while targeting information can be combined with anatomical information when PET-CT is used.

Visualization and quantification of mAb biodistribution with a PET camera (immuno-PET) requires a suitable positron-emitting radionuclide. As a potential PET surrogate for ^{90}Y, the positron emitter ^{86}Y is receiving attention [7, 8]. An advantage in the use of the same element would be that one type of chelator can be used for coupling of both isotopes. ^{86}Y, however, emits prompt gammas, which can hamper

accurate quantification; furthermore, its half-life of 14.7 h is relatively short for optimal imaging and dosimetry with an intact mAb like Zevalin, as typically 2–4 days are required to achieve optimal tumor to non-tumor ratios. The positron emitter zirconium-89 (^{89}Zr) might be a better candidate for prediction and monitoring of the biodistribution of ^{90}Y in RIT studies, especially because of its long half-life of 78.4 h. Procedures for the production and purification of large batches of ^{89}Zr have recently been established at our institute. A versatile method for stable coupling of ^{89}Zr to mAbs, including mAb U36, which is at an early stage of development for detection of head and neck cancer, was developed using the desferal-chelate precursor tetrafluorophenol-N-succinyldesferal-Fe (TPF-*N*-sucDf-Fe) [9]. Preliminary clinical evaluation of ^{89}Zr-mAb U36 revealed that tumor deposits can be clearly visualized after administration of 74 MBq ^{89}Zr [6]. Moreover, in nude mice bearing head and neck cancer xenografts, ^{89}Zr-*N*-sucDf-U36 and ^{88}Y-DOTA-U36 (^{88}Y as a substitute for ^{90}Y) conjugates showed a highly similar biodistribution, while accurate ^{89}Zr quantification appeared feasible, these being prerequisites to justify the use of ^{89}Zr-immuno-PET for scouting ^{90}Y-RIT [10].

Therefore, introduction of ^{89}Zr-Zevalin-PET in high-dose ^{90}Y-Zevalin RIT might be an attractive option for prediction of ^{90}Y-Zevalin biodistribution and dosimetry, and of toxicity and tumor response upon high-dose ^{90}Y-Zevalin RIT in a myeloablative setting. To enable the use of ^{89}Zr-Zevalin in such a setting, the present study was conducted to develop a route to an ^{89}Zr-Zevalin conjugate capable of monitoring the biodistribution of the therapeutic ^{90}Y-Zevalin conjugate in the clinic. Since only MX-DTPA premodified ibritumomab is available for clinical use, and MX-DTPA does not bind the four-valent ^{89}Zr, N-sucDf was coupled as a second chelate to Zevalin. The resulting newly developed double-chelator modified ^{89}Zr-Zevalin conjugate was measured for stability in serum and for preservation of immunoreactivity, including during storage. For the analysis of the pharmacokinetic behaviour, the biodistribution of ^{89}Zr-Zevalin was compared with that of ^{88}Y-Zevalin upon co-injection in NHL xenograft-bearing nude mice. The preliminary clinical performance of ^{89}Zr-Zevalin-PET was evaluated in a patient with CD20+ B-cell NHL.

Materials and Methods

Monoclonal antibody, Radioactivity, and Cell Lines

The monoclonal antibody ibritumomab tiuxetan (Zevalin™) was obtained from Schering Nederland BV, The Netherlands. ^{89}Zr (2.7 GBq/mL in 1 M oxalic acid) was produced by the BV Cyclotron by a (p,n) reaction on natural ^{89}Y and isolated with the use of a hydroxamate column [9]. ^{88}Y (37 MBq/mL in 0.1 M HCl) was obtained from Isotope Products Europe, and ^{90}Y (18.5 GBq/mL in 0.05 M HCl) was obtained from PerkinElmer. The CD20+ B-cell lymphoma cell line Ramos was obtained from the American Type Culture Collection (ATCC number CRL-1596).

Radiolabeling

Labeling of Zevalin with ^{89}Zr was achieved starting from the chelate TFP-*N*-sucDf-Fe, as described previously [9]. In short, the TFP-*N*-sucDf-Fe ester was coupled to the lysine residues of Zevalin (1.6 mg). After removal of Fe(III) by transchelation to ethylene diamine tetra-acetic acid (EDTA) and purification on a PD10 column (Amersham Biosciences; eluent: 0.9% NaCl/gentisic acid 5 mg/mL, pH 5.0), the premodified Zevalin was labeled with ^{89}Zr in 0.5 M N-2-hydroxyethylpiperazine-N-2-ethanesulphonic acid (HEPES) buffer at pH 7.0 to arrive at a specific activity of approximately 74 MBq/mg. Finally, ^{89}Zr-Zevalin was purified on a PD10 column (eluent: 0.9% NaCl/gentisic acid 5 mg/mL, pH 5.0) to remove unbound ^{89}Zr. A schematic representation of ^{89}Zr-Zevalin (i.e. ^{89}Zr-*N*-sucDf-ibritumomab tiuxetan) in comparison with the routinely used ^{90}Y-Zevalin conjugate is shown in Figure 1.

^{90}Y-Zevalin was prepared according to the instructions of the supplier entitled: "Preparation and dispensing information on ^{90}Y and ^{111}In-ibritumomab tiuxetan". With this procedure, ^{90}Y was coupled to Zevalin at a specific activity of approximately 740 MBq/mg mAb, and formulated in a phosphate-buffered saline (PBS) containing 7.5% human serum albumin (HSA) and 1 mM diethylene triamine penta-acetic acid (DTPA), pH 7.2 (formulation buffer). Zevalin was labeled with ^{88}Y according to the same procedure, but with reaction volume modifications.

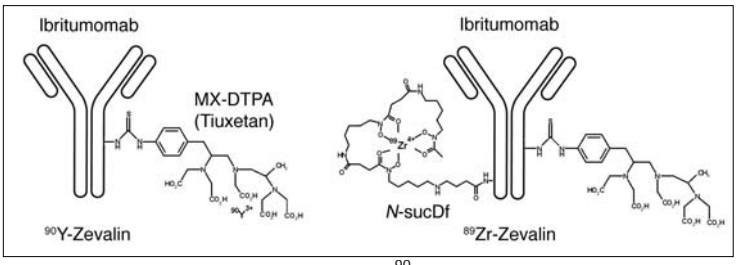

Figure 1. Schematic representation of ^{90}Y-labeled Zevalin, consisting of the mAb ibritumomab and the chelate MX-DTPA (left), and of ^{89}Zr-labeled Zevalin, consisting of the mAb ibritumomab and the chelates MX-DTPA (empty) as well as the chelate *N*-sucDf used for complexation of $^{89}Zr^{4+}$ (right)

Analyses

Conjugates were analyzed by instant thin-layer chromatography (ITLC) and high-performance liquid chromatography (HPLC) for radiochemical purity, by sodium dodecylsulphate-polyacrylamide gel electrophoresis (SDS-PAGE) followed by phosphor imager analyses for integrity, and by a cell-binding assay for immunoreactivity. ITLC analysis of radiolabeled Zevalin was performed on silica gel impregnated glass fiber sheets (Gelman Sciences). As the mobile phase, 20 mM citrate buffer pH 5.0 was used for ^{89}Zr-Zevalin and 0.9% NaCl for ^{88}Y- and ^{90}Y-Zevalin. Antibody-bound ^{89}Zr, ^{88}Y and ^{90}Y remained at the origin (Rf 0.0), whereas unreacted ^{89}Zr, ^{88}Y and ^{90}Y (as ^{89}Zr-citrate or ^{88}Y/^{90}Y-DTPA) moved with Rf 0.8–1.0. HPLC monitoring of the synthesis of ^{89}Zr-Zevalin and of the labeling to arrive at ^{88}Y/^{90}Y-Zevalin was performed on a Jasco HPLC system using a Superdex 200 10/300 GL size exclusion column (Amersham Biosciences). As eluent, a mixture of 0.05 M sodium phosphate/0.15 M NaCl (pH 6.8) was used at a flow rate of 0.5 mL/min.

The *N*-sucDf-to-mAb molar ratio was quantified using HPLC analysis with TFP-*N*-sucDf-Fe ester spiked with ^{59}Fe in the modification step, and measuring the amount of mAb bound *N*-sucDf-^{59}Fe and unreacted *N*-sucDf-^{59}Fe.

Single isotope counting was performed with a γ-well counter (Compugamma, LKB Wallac) for ^{89}Zr, ^{88}Y and ^{59}Fe, and with a β-counter (Rackbeta, LKB Wallac) for ^{90}Y using Čerenkov radiation. The 511-keV γ-energy of ^{89}Zr and the 1,837-keV γ-energy of ^{88}Y were used for dual-isotope counting in the biodistribution study. Crossover corrections from one radionuclide into the alternate window were performed using a standard of each radionuclide. When ^{89}Zr was measured with the γ-well counter in the presence of ^{90}Y, a similar procedure was applied to correct for background caused by ^{90}Y bremsstrahlung. When ^{90}Y was measured with the β-counter in the presence of ^{89}Zr, corrections were applied to adjust for background caused by ^{89}Zr.

Gel electrophoresis was performed on a Pharmacia Phastgel System (Amersham Biosciences) using preformed 7.5% SDS-PAGE gels (Amersham Biosciences) under non-reducing conditions. In vitro binding characteristics of radiolabeled Zevalin were determined in an immunoreactivity assay essentially as described by Lindmo et al. [11], using Ramos cells fixed with 2.0% paraformaldehyde. Data were graphically analyzed in a modified Lineweaver-Burk (double-reciprocal) plot and the immunoreactivity was determined by extrapolating to conditions representing infinite antigen excess.

In Vitro Stability of Radiolabeled Zevalin

Three sets of stability tests were performed, each with a particular design, of relevance for the clinical studies planned: For validation of ^{89}Zr labeling in compliance with Good

Manufacturing Practice (GMP), three clinical batches of ^{89}Zr-Zevalin were produced and quality tests were performed. To this end, ^{89}Zr-Zevalin (1.8 mg, 74 MBq) was diluted in 20 mL 0.9% NaCl/gentisic acid 5 mg/mL, pH 5.0 (clinical formulation) and incubated at 4°C or room temperature for 48 h. At 0, 24 and 48 h, aliquots were taken and analyzed by ITLC as well as HPLC. In addition, the immunoreactivity was assessed at these time points.

In forthcoming clinical myeloablative RIT studies, we anticipate the possibility of administration of ^{89}Zr-Zevalin alone for pretherapy imaging as well as administration in combination with high-dose ^{90}Y-Zevalin (for RIT). In the latter case, the PET and RIT conjugate might be administered together as a mixture. For testing the stability of both conjugates in such a mixture at challenging radioactivity concentrations, 37 MBq ^{89}Zr-Zevalin (0.5 mg) and 720 MBq ^{90}Y-Zevalin (1 mg) in formulation buffer (PBS buffer containing 7.5% HSA and 1 mM DTPA, pH 7.2) were combined in a final volume of 6.5 mL and stored at 4°C. At various time intervals (2, 4, 7 and 24 h), samples were taken for quality testing of both conjugates, including ITLC, HPLC and binding assay.

For testing the in vitro stability in human serum of ^{89}Zr-Zevalin and ^{88}Y-Zevalin, samples of 0.1 mL containing the radiolabeled mAbs were added to 0.9 mL of freshly prepared human serum and incubated at 37°C in a humidified incubator maintained at 5% CO^2 and 95% air. In this case, ^{88}Y was used instead of ^{90}Y to facilitate quantification in serum. At various time intervals (1, 2, 4, 6 days), aliquots were taken and analyzed by ITLC and HPLC.

Biodistribution

Nude mice bearing the subcutaneously implanted B-cell lymphoma cell line Ramos were used. Female mice (athymic nu/nu, 21–31 g, Harlan CPB) were 10–14 weeks old at the time of the experiment. All animal experiments were performed according to National Institutes of Health principles of laboratory animal care and Dutch national law ("Wet op de dierproeven", Stb 1985, 336).

The mice (n=16) were injected intravenously with a mixture of 0.37 MBq ^{89}Zr-Zevalin and 0.13 MBq ^{88}Y-Zevalin. Unlabeled Zevalin was added to this mixture so that all animals received 100 µg mAb in total. At 24, 48, 72 and 144 h post injection, groups of four mice were anaesthetized, bled, killed and dissected. After blood, tumor, normal tissues and gastrointestinal contents had been weighed, the amount of radioactivity in each was measured in a γ-well counter. Radioactivity uptake was calculated as the percentage of the injected dose per gram of tissue (%ID/g). Differences in tissue uptake between co-injected conjugates were statistically analyzed for each time point with SPSS 11.0 software using Student's t test for paired data. Two-sided significance levels were calculated and $p<0.05$ was considered statistically significant.

PET Imaging

The preliminary clinical performance of ^{89}Zr-Zevalin PET was evaluated in a male patient (aged 49 years) who had an indolent CD20+ NHL, with transformation to diffuse large B-cell NHL, with relapsed disease after AuSCT. This feasibility study, ahead of the planned study "^{90}Y-Zevalin myeloablative RIT and ^{89}Zr-Zevalin-PET in conditioning for stem cell transplantation in patients with aggressive B-cell NHL", was reviewed and approved by the Medical Ethics Committee of the VU University Medical Centre. The patient gave written informed consent after receiving a thorough explanation of the study.

PET scanning was performed using a dedicated full ring PET scanner (ECAT EXACT HR+, CTI/Siemens). A PET session with ^{89}Zr-Zevalin was performed to assess biodistribution and to confirm targeting of tumor lesions that had been delineated 2 weeks previously by [^{18}F]fluorodeoxyglucose (FDG) PET scanning.

In the case of ^{89}Zr-Zevalin immuno-PET, whole-body scans were performed, consisting of seven bed positions covering the patient from the base of the skull to the upper femur. At each bed position a 3-min transmission scan, acquired using three germanium-68 rod sources, and a 7-min emission scan in 3D mode were acquired. The patient first received rituximab, 250 mg/m^2 over 3.5 h, followed within 4 h by 74 MBq ^{89}Zr-Zevalin. The patient received a total of 1.8 mg Zevalin by adding unlabeled Zevalin. Whole-body scans were performed at 2 and 96 h after intravenous injection of ^{89}Zr-Zevalin. All scans were normalized and corrected for randoms, scatter, attenuation and decay. Reconstructions were performed using an attenuation- and normalization-weighted ordered subset expectation maximization (OSEM) algorithm (ECAT software, version 7.2, CTI/Siemens) with two iterations and 16 subsets followed by post-smoothing of the reconstructed image using a 5-mm FWHM Gaussian filter. OSEM reconstructions without attenuation correction were performed as well. Interpretation of the scans was performed using these non-attenuation-corrected images and was based on asymmetry and retention of activity on the late image.

[^{18}F]FDG-PET was performed essentially as described previously [12]. In short, the patient was required to fast for at least 6 h before the scan. A whole-body scan was performed consisting of eight bed positions from the crown to the midfemur. At each bed position a 7-min emission scan in 2D mode was performed. Scanning started about 60 min after intravenous injection of 400 MBq [^{18}F]FDG (BV Cyclotron, The Netherlands). The scan was corrected in the same way as described above for the ^{89}Zr-Zevalin scans; however, no attenuation correction was performed. The PET image was read visually using standard ECAT software: foci with increased uptake versus background were considered abnormal, taking physiological biodistribution of [^{18}F]FDG into account.

Results

Modification and Radiolabeling

Labeling of Zevalin-MX-DTPA with ^{89}Zr resulted in a labeling yield below 0.1%, confirming the lack of affinity of ^{89}Zr for DTPA chelates. Modification of Zevalin with the chelate TFP-*N*-sucDf-Fe resulted in a reproducible *N*-sucDf-to-mAb molar ratio of 0.83±0.04 (mean±SD, n=8). Subsequent labeling of *N*-sucDf-Zevalin with ^{89}Zr resulted in overall labeling yields of >60% and radiochemical purity always exceeded 95% after purification on PD10. Labeling of Zevalin with ^{88}Y or ^{90}Y resulted in overall labeling yields of >96% and the radiochemical purity was more than 96% for both products. Immunoreactivity of ^{89}Zr-Zevalin was more than 80% at infinite antigen excess and similar to the immunoreactivity of ^{88}Y/^{90}Y-labeled Zevalin conjugates. No physical evidence of antibody degradation was observed for any of the three products, as determined by SDS-PAGE followed by phosphor imager analyses.

In vitro Stability Testing

The in vitro stability was evaluated by three sets of experiments: The results of the first set, the validation productions according to GMP procedures, are shown in Table 1. ^{89}Zr-Zevalin formulated in 20 mL 0.9% NaCl/gentisic acid 5 mg/mL (pH 5.0) can be stored for 48 h at 4°C and also at room temperature without decrease in radiochemical purity to a level below 95%. Immunoreactivity of the conjugate remained above 80% when stored at 4°C for 48 h and at room temperature for 24 h. This procedure resulted in a sterile final product with endotoxin levels <1.28 EU/mL (acceptance level <5 EU/mL).

In the second set, ^{89}Zr-Zevalin and ^{90}Y-Zevalin were joined in a formulation mixture to observe the damaging effect of radiolysis upon storage at high radioactivity concentration (111 MBq ^{90}Y/mL). The radiochemical purity and immunoreactivity of both products were determined at various time points. Upon storage at 4°C for 4 h, the radiochemical purity of ^{89}Zr-Zevalin remained >95%. At 24 h it decreased to 94.3%. The radiochemical purity of ^{90}Y-Zevalin remained >96% during 24 h. For both products, immunoreactivity remained above 80% during this period. These data indicate that both conjugates will meet the clinical release specification as set for ^{90}Y-

Table 1. *In vitro* stability of clinically-formulated ^{89}Zr-Zevalin.

Incubation Time (h)	Radiochemical purity (%)[a] ITLC	HPLC
0	97.3 ± 0.9	96.1 ± 0.6
4 (4°C)	97.2 ± 0.4	96.1 ± 1.0
4 (RT)	96.6 ± 0.5	96.7 ± 1.3
24 (4°C)	97.2 ± 0.3	96.5 ± 1.6
24 (RT)	97.0 ± 0.1	97.4 ± 1.0
48 (4°C)	97.3 ± 0.3	96.8 ± 0.3
48 (RT)	96.1 ± 0.5	95.6 ± 1.0

[a]At each time point 3 samples were analysed for radiochemical purity by ITLC and HPLC.

Zevalin (radiochemical purity >95%), when the mixture of ^{89}Zr-Zevalin with high-dose ^{90}Y-Zevalin is administered to the patient within 4 h after production and formulation.

In the third set, ^{89}Zr-Zevalin and ^{88}Y-Zevalin were individually tested for stability in human serum. Both conjugates were stable in serum (radiochemical purity >95%) for a period of at least 6 days.

Biodistribution

For comparison of the biodistribution of ^{89}Zr-Zevalin and ^{88}Y-Zevalin, the two conjugates were co-injected in nude mice bearing Ramos B-cell tumors. At 24, 48, 72 and 144 h post injection, the average uptake (%ID/g, mean±SD) in tumor, blood, normal tissues and gastrointestinal contents was determined. These results are shown in Figure 2. In general, ^{89}Zr-Zevalin and ^{88}Y-Zevalin showed similar uptake in tumor and most other organs at all time points. Significant differences ($p<0.05$) between the two conjugates were found at 72 and 144 h after injection in liver, thigh bone and sternum. Tumor uptake levels of ^{89}Zr-Zevalin were 17.0±7.6 %ID/g at 24 h, 20.9±4.4 %ID/g at 48 h, 19.6±4.1 %ID/g at 72 h and 9.8±2.5 %ID/g at 144 h; for ^{88}Y-Zevalin these levels were 16.7±8.3 %ID/g at 24 h, 20.6±5.7 %ID/g at 48 h, 20.7±4.6 %ID/g at 72 h and 10.0±2.5 %ID/g at 144 h. Blood levels slowly decreased from 14.6±2.0 %ID/g at 24 h to 5.0±0.5 %ID/g at 144 h for ^{89}Zr-Zevalin and from 15.2±2.2 %ID/g at 24 h to 5.4±0.6 %ID/g at 144 h for ^{88}Y-Zevalin.

PET imaging

For evaluation of the clinical performance of ^{89}Zr-Zevalin, a pilot PET imaging study (without RIT) was conducted in a patient with CD20+ B-cell NHL. The patient had undergone [^{18}F]FDG-PET scanning previously, the scan indicating cervical, mediastinal, left caput humeri, splenic, para-aortic and inguinal tumor involvement (Figure 3A, tumor lesions are indicated by arrows). Whole-body images obtained 96 h after administration of ^{89}Zr-Zevalin revealed clear uptake of the conjugate in all tumor lesions (Figure 3B). No increased uptake in normal organs was observed except for the liver. None of the tumor sites were clearly delineated on the early ^{89}Zr-Zevalin-PET image (2 h p.i.), which showed mainly blood pool activity (diminishing over time) with visualization of nose, heart, lungs, liver and spleen (Figure 4).

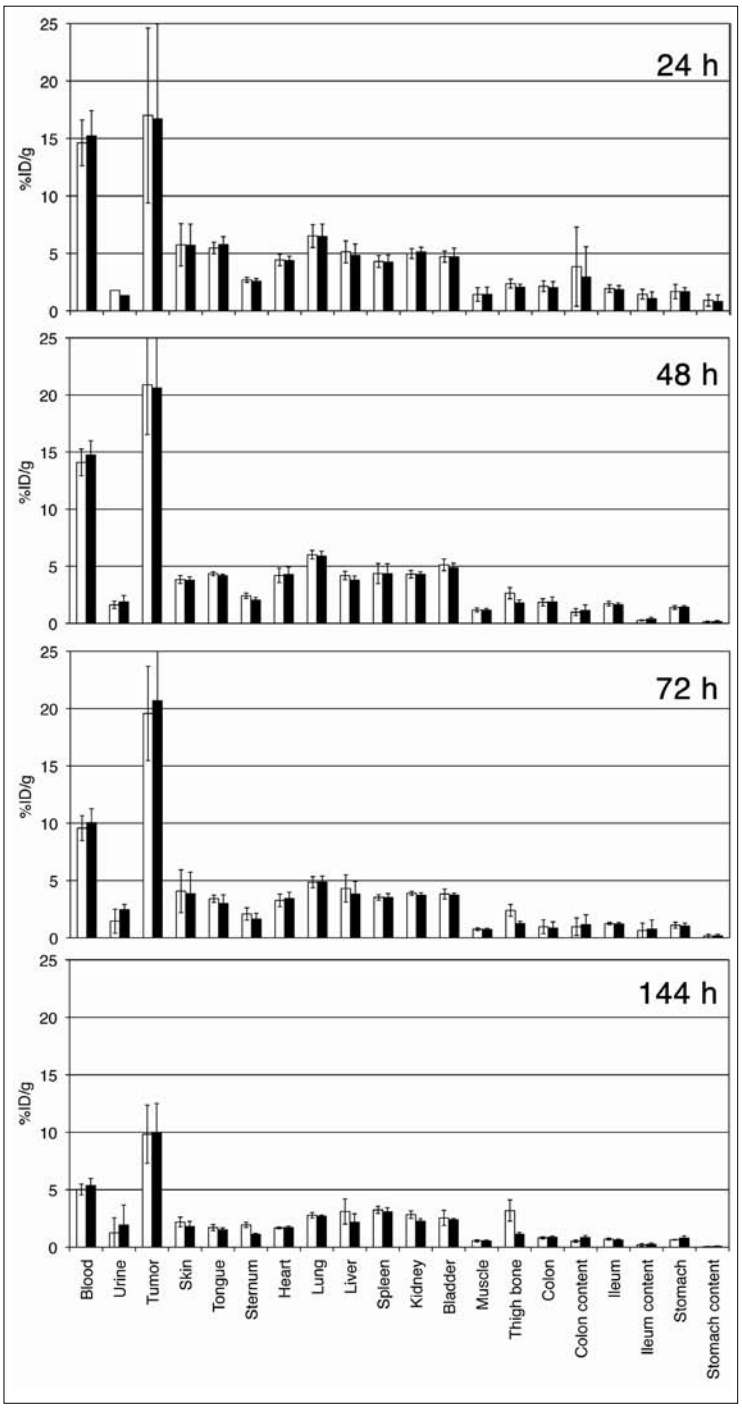

Figure 2. Biodistribution of co-injected ^{89}Zr-Zevalin (white bars) and ^{88}Y-Zevalin (black bars) in nude mice bearing the B-cell lymphoma cell line Ramos at 24, 48, 72 and 144 h after injection.

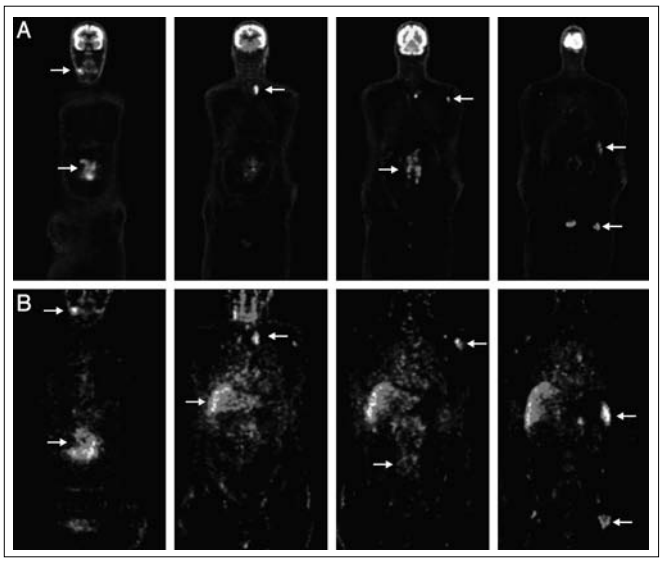

Figure 3. (A) [^{18}F]FDG-PET scan of the NHL patient. Coronal images from anterior (left) to posterior (right), with visualization of cervical, mediastinal, left caput humeri, splenic, para-aortic and inguinal lymphomas. Localizations are indicated by white arrows. (B) ^{89}Zr-Zevalin immuno-PET scan 96 h p.i. of the same NHL patient. Coronal images from anterior (left) to posterior (right); slices correspond to those of the [^{18}F]FDG-PET scan. Tumor localizations are indicated by white arrows. Note targeting of tumor localizations also visualized by [^{18}F]FDG-PET. Liver uptake (yellow arrow) is probably due to retention of ^{89}Zr after catabolism of the conjugate.

Discussion

An important issue in RIT is confirmation of tumor targeting and assessment of dose delivery, especially in high-dose RIT studies. This might be accomplished by performing an immuno-PET imaging procedure prior to RIT. At least three requirements need to be met for optimal use of an imaging radioimmunoconjugate as a predictor of the biodistribution of a therapeutic radioimmunoconjugate. First, imaging and RIT conjugate should have a similar biodistribution. Second, radionuclides used for imaging and RIT should have similar physical half-lives, preferably matching with the biological half-life of the mAb (typically 2–4 days for intact mAbs). Third, procedures for quantification of uptake and subsequent dose calculations should be reasonably accurate.

The choice of the positron emitter is an important factor for a successful pretherapy scouting procedure with PET. Only two long-lived positron emitters seem well suited for imaging intact mAbs, namely ^{89}Zr ($t_{1/2}$=78.4 h) and iodine-124 (^{124}I, $t_{1/2}$=100.3 h). Of these isotopes, ^{89}Zr can be obtained in high yield and with high

radionuclidic purity by a (p,n) reaction on ^{89}Y, which is an attractive target material because of its 100% natural abundance [9]. As a result, production costs are relatively low. Moreover, ^{89}Zr has no prompt gammas that can hamper image quality and accurate quantification [10]. Recent studies at our institute revealed that ^{89}Zr residualizes after catabolism, a phenomenon also observed with ^{90}Y, ^{111}In and lutetium-177 (^{177}Lu) [13]. Such residualization is not observed with, for example, rhenium-186 (^{186}Re), ^{131}I or ^{124}I [14], and therefore ^{124}I-Zevalin cannot be used for monitoring ^{90}Y-Zevalin biodistribution.

^{89}Zr cannot be stably bound by the chelate MX-DTPA. Therefore, we coupled a second chelate, *N*-sucDf, to Zevalin. The *N*-sucDf-to-mAb molar ratio was chosen to be kept below 1, since one cannot unlimitedly modify lysine groups without alteration of the biodistribution [15, 16]. Subsequent labeling of this double-chelator modified

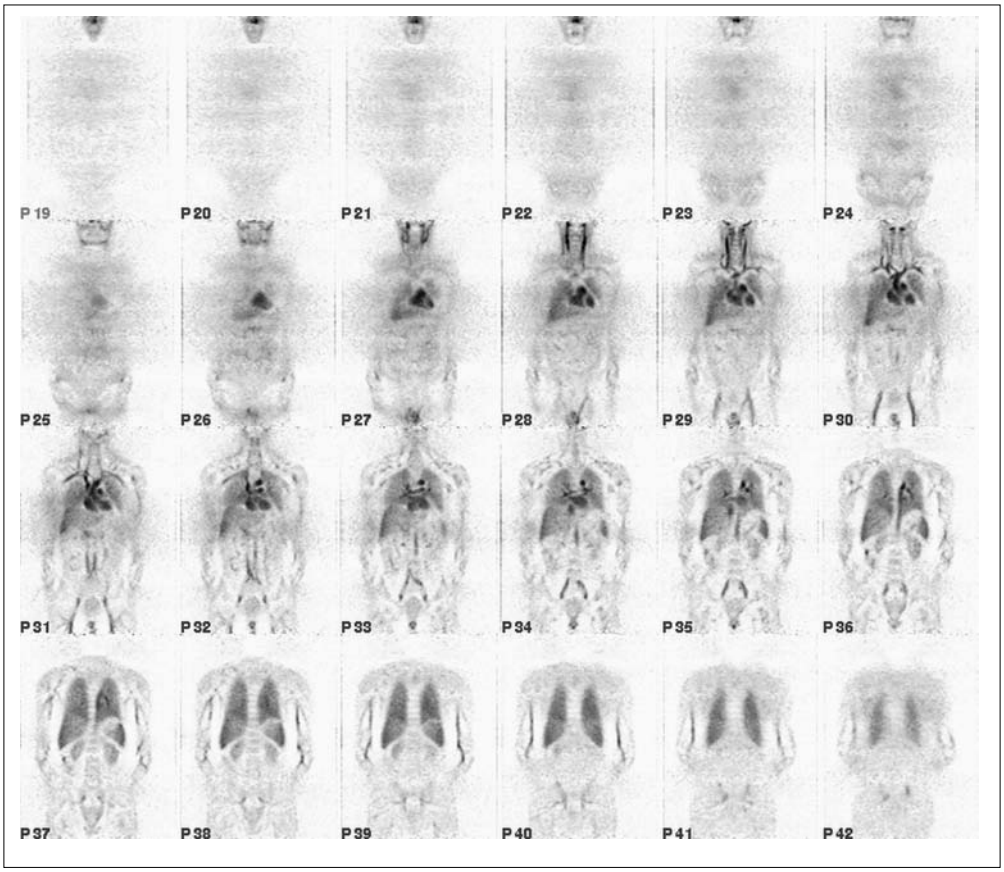

Figure 4. ^{89}Zr-Zevalin immuno-PET scan 2 h p.i. Coronal images from anterior (upper left) to posterior (lower right), showing mainly blood pool activity with visualization of nose, heart, lungs, liver and spleen.

conjugate with ^{89}Zr resulted in reproducible labeling yields and specific activities of at least 74 MBq/mg Zevalin, while preserving immunoreactivity and integrity of the mAb. Validation productions of ^{89}Zr-Zevalin according to GMP showed reproducibility of labeling procedures, and the possibility of storing ^{89}Zr-Zevalin in a clinical formulation for 48 h at 4°C and for 24 h at room temperature without unacceptable loss of radiochemical purity and immunoreactivity. In addition, we joined ^{89}Zr-Zevalin and ^{90}Y-Zevalin in a formulation mix at clinical dose concentration. The high β-energy of ^{90}Y can result in radiolytic damage to the radiolabeled mAbs. ^{89}Zr-Zevalin remained stable in this formulation solution, without impairment of immunoreactivity. This offers the flexibility to administer both conjugates either together in one single mixture, or separately directly after each other. Preceding the biodistribution study, the in vitro stability of ^{89}Zr-Zevalin and ^{88}Y-Zevalin in human serum was analyzed. Stability of both conjugates under these conditions was comparable and high, and radiochemical purity was always above 95% for both radioimmunoconjugates over a period of 6 days. These results indicate that ^{89}Zr had been coupled in a stable way to Zevalin, without affecting the quality of the mAb.

To demonstrate that the newly developed double-chelator modified Zevalin labeled with ^{89}Zr can be used for localization of the therapeutic Zevalin labeled with ^{90}Y, a biodistribution study was conducted in nude mice bearing Ramos B-cell tumors. This study revealed that ^{89}Zr-Zevalin and ^{88}Y-Zevalin have a very comparable distribution (Fig. 2). It is of note that the apparent loss (in %ID/g) of the residualizing ^{89}Zr and ^{88}Y in tumors at 144 h post injection relative to earlier time points is most probably the result of fast tumor growth, since the mean tumor masses at the time of dissection were 192±68 mg at 72 h compared with 406±162 mg at 144 h. Nevertheless, there were some differences ($p<0.05$) between ^{89}Zr-Zevalin and ^{88}Y-Zevalin in liver and bone at later time points. This difference in uptake in these organs was in the same range as previously observed in biodistribution studies with ^{89}Zr- and ^{88}Y-labeled mAbs [10, 13]. Differences in biodistribution were also reported between ^{111}In- and ^{90}Y-labeled Zevalin [17], with, for example, a difference of 1.7±0.3 versus 3.2±0.3%ID/g in bone at 72 h post injection for ^{111}In-Zevalin versus ^{90}Y-Zevalin, respectively. Deviating bone uptake is probably due to subtle differences in the in vivo stability of the ^{111}In- and ^{90}Y-DTPA complexes [18].

In the case of myeloablative RIT, where bone marrow toxicity is not dose limiting, ^{89}Zr-Zevalin seems well suited to predict ^{90}Y-Zevalin dosimetry. For prediction of dose delivery to bone marrow in non-myeloablative RIT, ^{89}Zr-immuno-PET seems unsuitable owing to differing bone uptake of ^{89}Zr and ^{90}Y. Marrow dosimetry in this setting is challenging anyhow, particularly in the case of tumor involvement of the bone marrow.

For evaluation of the clinical performance of ^{89}Zr-Zevalin PET, a pilot imaging study was conducted in one patient with CD20+ B-cell NHL. Serial PET camera images showed selective uptake in all tumor lesions that had previously been identified by [^{18}F]FDG-PET. Evaluation of these ^{89}Zr-PET images suggests that the favorable biodistribution of ^{89}Zr-Zevalin would make such an NHL patient a suitable candidate for high-dose ^{90}Y-Zevalin RIT.

The general aim of our forthcoming RIT study is to assess whether addition of high-dose ^{90}Y-Zevalin RIT to standard conditioning regimens for AuSCT in the treatment of aggressive NHL is safe, tolerable and effective. Dose escalation will be performed at fixed dose steps (not individualized). The implementation of ^{89}Zr-immuno-PET in these studies will reveal whether it is recommendable to exclude patients with an unfavorable biodistribution (e.g. no tumor targeting or >1,500 cGy to organs) from treatment with standardized high-dose RIT.

Conclusion

To enable clinical PET imaging of Zevalin, procedures were developed for stable and reproducible coupling of the long-lived positron emitter ^{89}Zr. Similar in vitro stability and biodistribution in NHL-bearing nude mice suggest that ^{89}Zr-Zevalin can be safely used for monitoring ^{90}Y-Zevalin biodistribution in a clinical setting. A pilot PET imaging study with ^{89}Zr-Zevalin in a patient with CD20+ B-cell NHL showed clear uptake of ^{89}Zr-Zevalin in all previously known tumor deposits. PET with ^{89}Zr-Zevalin seems attractive for the quantitative prediction of pharmacokinetics, biodistribution and dosimetry of ^{90}Y-Zevalin in high-dose RIT.

Acknowledgements

This project was financially supported by the Dutch Technology Foundation (STW, grant VBC.6120). The authors thank Schering Nederland BV (The Netherlands) for supply of Zevalin and for reviewing the manuscript, the technical staff of BV Cyclotron and the Radionuclide Centre for supply and processing of ^{89}Zr, Jan H. Rector (Solid State Physics, VU university) for sputtering ^{89}Y on copper supports, Adriaan A. Lammertsma for providing PET imaging facilities, and Yvonne W.S. Jauw and Ronald Boellaard for performing PET reconstructions.

References

1. Witzig TE, Gordon LI, Cabanillas F, Czuczman MS, Emmanouilides C, Joyce R, et al. Randomized controlled trial of yttrium-90-labeled ibritumomab tiuxetan radioimmunotherapy versus rituximab immunotherapy for patients with relapsed or refractory low-grade, follicular, or transformed B-cell non-Hodgkin's lymphoma. J Clin Oncol 2002;20:2453–63.
2. Witzig TE, Flinn IW, Gordon LI, Emmanouilides C, Czuczman MS, Saleh MN, et al. Treatment with ibritumomab tiuxetan radioimmunotherapy in patients with rituximab-refractory follicular non-Hodgkin's lymphoma. J Clin Oncol 2002;20:3262–9.
3. Hagenbeek A, Lewington V. Report of a European consensus workshop to develop recommendations for the optimal use of ^{90}Y-ibritumomab tiuxetan (Zevalin) in lymphoma. Ann Oncol 2005;16:786–92.
4. Winter JN. Combining yttrium 90-labeled ibritumomab tiuxetan with high-dose chemotherapy and stem cell support in patients with relapsed non-Hodgkin's lymphoma. Clin Lymphoma 2004;5 Suppl 1:22–6.
5. Nademanee A, Forman S, Molina A, Fung H, Smith D, Dagis A, et al. A phase 1/2 trial of high-dose yttrium-90-ibritumomab tiuxetan in combination with high-dose etoposide and cyclophosphamide followed by autologous stem cell transplantation in patients with poor-risk or relapsed non-Hodgkin lymphoma. Blood 2005;106:2896–902.
6. Verel I, Visser GWM, van Dongen GAMS. The promise of immuno-PET in radioimmunotherapy. J Nucl Med 2005;46 Suppl 1:164–71.
7. Pauwels S, Barone R, Walrand S, Borson-Chazot F, Valkema R, Kvols LK, et al. Practical dosimetry of peptide receptor radionuclide therapy with ^{90}Y-labeled somatostatin analogs. J Nucl Med 2005;46 Suppl 1:92–8.
8. Lövqvist A, Humm JL, Sheikh A, Finn RD, Koziorowski J, Ruan S, et al. PET imaging of ^{86}Y-labeled anti-Lewis Y monoclonal antibodies in a nude mouse model: comparison between ^{86}Y and ^{111}In radiolabels. J Nucl Med 2001;42:1281–7.
9. Verel I, Visser GWM, Boellaard R, Stigter-Van Walsum M, Snow GB, Van Dongen GAMS. Zr-89 immuno-PET: comprehensive procedures for the production of Zr-89-labeled monoclonal antibodies. J Nucl Med 2003;44:1271–81.
10. Verel I, Visser GWM, Boellaard R, Boerman OC, Van Eerd J, Snow GB, et al. Quantitative Zr-89 immuno-PET for in vivo scouting of Y-90-labeled monoclonal antibodies in xenograft-bearing nude mice. J Nucl Med 2003;44:1663–70.
11. Lindmo T, Boven E, Cuttitta F, Fedorko J, Bunn PA. Determination of the immunoreactive fraction of radiolabeled monoclonal-antibodies by linear extrapolation to binding at infinite antigen excess. J Immunol Methods 1984;72:77–89.
12. Zijlstra JM, Hoekstra OS, Raijmakers PGHM, Comans EFI, van der Hoeven JJM, Teule GJJ, et al. ^{18}FDG positron emission tomography versus ^{67}Ga scintigraphy as prognostic test during chemotherapy for non-Hodgkin's lymphoma. Br J Haematol 2003;123:454–62.
13. Perk LR, Visser GWM, Vosjan MJWD, Stigter-van Walsum M, Tijink BM, Leemans CR, et al. ^{89}Zr as a PET surrogate radioisotope for scouting biodistribution of the therapeutic radiometals ^{90}Y and ^{177}Lu in tumor-bearing nude mice after coupling to the internalizing antibody cetuximab. J Nucl Med 2005;46:1898–906.

14. Verel I, Visser GWM, Boerman OC, Van Eerd JEM, Finn R, Boellaard R, et al. Long-lived positron emitters zirconium-89 and iodine-124 for scouting of therapeutic radioimmunoconjugates with PET. Cancer Biother Radiopharm 2003;18:655–61.
15. van Gog FB, Visser GWM, Klok R, van der Schors R, Snow GB, van Dongen GAMS. Monoclonal antibodies labeled with rhenium-186 using the MAG3 chelate: relationship between the number of chelated groups and biodistribution characteristics. J Nucl Med 1996;37:352–62.
16. van Gog FB, Visser GWM, Stroomer JWG, Roos JC, Snow GB, van Dongen GAMS. High dose rhenium-186-labeling of monoclonal antibodies for clinical application: pitfalls and solutions. Cancer 1997;80:2360–370.
17. Chinn PC, Leonard JE, Rosenberg J, Hanna N, Anderson DR. Preclinical evaluation of ^{90}Y-labeled anti-CD20 monoclonal antibody for treatment of non-Hodgkin's lymphoma. Int J Oncol 1999;15:1017–25.
18. Camera L, Kinuya S, Garmestani K, Brechbiel MW, Wu C, Pai LH, et al. Comparative biodistribution of indium- and yttrium-labeled B3 monoclonal antibody conjugated to either 2-(p-SCN-Bz)-6-methyl-DTPA (1B4M-DTPA) or 2-(p-SCN-Bz)-1,4,7,10-tetraazacyclododecane tetraacetic acid (2B-DOTA). Eur J Nucl Med 1994;21:640–6.

CHAPTER 4

^{124}I-L19-SIP for immuno-PET imaging of tumor vasculature and guidance of ^{131}I-L19-SIP radioimmunotherapy

Bernard M. Tijink
Lars R. Perk
Marianne Budde
Marijke Stigter-van Walsum
Gerard W.M. Visser
Reina W. Kloet
Ludger M. Dinkelborg
C. René Leemans
Dario Neri
Guus A.M.S. van Dongen

European Journal of Nuclear Medicine and Molecular Imaging 2009;36:1235-1244

Abstract

Purpose: The human monoclonal antibody (MAb) fragment L19-SIP is directed against extra domain B (ED-B) of fibronectin, a marker of tumor angiogenesis. A clinical radioimmunotherapy (RIT) trial with ^{131}I-L19-SIP was recently started. In the present study, after GMP production of ^{124}I and efficient production of ^{124}I-L19-SIP, we aimed to demonstrate the suitability of ^{124}I-L19-SIP immuno-PET for imaging of angiogenesis at early stage tumor development and as a scouting procedure prior to clinical ^{131}I-L19-SIP RIT.

Methods: ^{124}I was produced in a GMP compliant way via ^{124}Te(p,n)^{124}I reaction and using a TERIMO™ module for radioiodine separation. L19-SIP was radioiodinated by using a modified version of the IODO-GEN method. The biodistribution of coinjected ^{124}I- and ^{131}I-L19-SIP was compared in FaDu xenograft bearing nude mice, while ^{124}I-PET images were obtained from mice with tumors of <50 to ~700 mm^3.

Results: ^{124}I was produced highly pure with an average yield of 15.4 ± 0.5 MBq/μAh, while separation yield was ~90% efficient with <0.5% loss of TeO_2. Overall labeling efficiency, radiochemical purity and immunoreactive fraction were for ^{124}I-L19-SIP: ~80%, 99.9% and >90%, respectively. Tumor uptake was 7.3 ± 2.1, 10.8 ± 1.5, 7.8 ± 1.4, 5.3 ± 0.6 and 3.1 ± 0.4 %ID/g at 3, 6, 24, 48 and 72 h p.i., resulting in increased tumor-to-blood ratios ranging from 6.0 at 24 h to 45.9 at 72 h p.i.. Fully concordant labeling and biodistributions results were obtained with ^{124}I- and ^{131}I-L19-SIP. Immuno-PET with ^{124}I-L19-SIP using a high-resolution research tomograph PET scanner revealed clear delineation of the tumors as small as 50 mm^3, and no adverse uptake in other organs.

Conclusions: ^{124}I-MAb conjugates for clinical immuno-PET can be efficiently produced. Immuno-PET with ^{124}I-L19-SIP appeared qualified for sensitive imaging of tumor neovasculature and for predicting ^{131}I-L19-SIP biodistribution.

Introduction

Angiogenesis is one of the hallmarks of cancer, and therefore, considerable efforts have been made recently to image as well as to eradicate tumor vasculature, preferably in a combined fashion [1, 2]. One of the appealing targets for both approaches is the splice variant of fibronectin containing extra domain B (ED-B). ED-B is abundantly expressed around the vasculature of a variety of human cancers, primary tumors as well as metastases [3-6]. Interestingly, ED-B is undetectable in normal tissues, with the exception of tissues undergoing physiological modeling (e.g. endometrium and ovary) and during wound healing [3]. This target is highly conserved in different species, having 100% homology in many mammalian species (e.g. human, rat, mouse), and therefore making proof of principle studies in tumor bearing mice of special relevance [7].

Recently, a human recombinant scFv fragment directed against ED-B, designated L19, has been developed [8]. Using its variable regions, several other L19 formats were constructed, including dimeric scFv ($(scFv)_2$), a human bivalent "small immunoprotein" (SIP, ~80 kDa) and a complete human IgG1 [9]. Radiolabeled L19 constructs have been evaluated in tumor bearing nude mice to identify the most appropriate conjugate for radioimmunotherapy (RIT) of solid tumors [9-12]. To this end, the L19 derivatives were labeled with iodine-125 (^{125}I) or indium-111 (^{111}In) [10]. The resulting biodistribution data were used to perform dosimetry for the corresponding therapeutic counterparts labeled with ^{131}I and yttrium-90 (^{90}Y), respectively, and to select a conjugate for clinical RIT. The most favorable therapeutic index was found for ^{131}I-L19-SIP, while this index was a poor one for ^{90}Y-labeled derivatives [10]. RIT with ^{131}I-L19-SIP at maximum tolerated dose caused significant tumor growth delay and improved survival in several animal models [10-12].

On the basis of aforementioned bright perspectives, a clinical RIT trial with ^{131}I-L19-SIP was designed [13]. This trial comprises the selection of RIT candidate patients on the basis of pretherapy SPECT imaging and dosimetry. Rationales for this approach are the variable ED-B expression in tumors, with higher expression in the more aggressive ones, and the potential occurrence of ED-B expression in normal tissues.

We and others recently proposed immuno-PET as a high-resolution quantitative imaging procedure before or concomitant with RIT to improve confirmation of tumor targeting and to assess radiation dose delivery to both tumors and normal tissues [14-16]. Important in such approach is the choice of the positron emitting radionuclide to be used for radiolabeling. Among others, its physical half-life ($t_{1/2}$) should be compatible with the time needed for a MAb to achieve optimal tumor-to-nontumor ratios, being >24 h for L19-SIP. In addition, when immuno-PET is used

for selection of RIT candidates, the radioimmunoconjugates used for immuno-PET and RIT should demonstrate a similar biodistribution, and therefore, by preference, radionuclides with comparable in vivo behavior must be used. The starting positron emitter solution should meet appropriate radiopharmaceutical quality standards when used for clinical purposes.

The halogens ^{76}Br ($t_{1/2}$ = 16.2 h) and ^{124}I ($t_{1/2}$ = 4.18 d) are promising candidate positron emitters for L19-SIP immuno-PET in combination with ^{131}I-L19-SIP RIT, however, availability of GMP compliant material is a problem for both. Rossin et al. [17] recently described ^{76}Br-L19-SIP for imaging of tumor neovasculature in xenograft bearing nude mice. While tumor uptake of ^{76}Br-L19-SIP was high, a disadvantage was the long retention of radioactivity in blood and the very slow renal excretion. As a consequence, the background activity in nontarget organs was higher than that reported for ^{125}I-labeled-L19-SIP, and this resulted in lower target-to-nontarget ratios.

Taking aforementioned aspects into account, we hypothesized that ^{124}I-L19-SIP might be the most optimal candidate for immuno-PET imaging of tumor neovasculature, and for prediction of biodistribution and dosimetry of ^{131}I-L19-SIP in RIT. Although the choice for ^{124}I-L19-SIP immuno-PET seems logical, no such studies have been reported as yet, and several technical hurdles had to be taken to enable future clinical evaluation. For this purpose, and to facilitate the translation to clinical application, we developed the production and purification of ^{124}I in a GMP compliant setting, and its coupling to L19-SIP with the aid of IODO-GEN. With respect to the latter, procedures were established for efficient coupling of no-carrier-added ^{124}I. ^{124}I-L19-SIP was evaluated by comparison of biodistribution with ^{131}I-L19-SIP upon coinjection in xenograft-bearing nude mice and by imaging of mice with tumors of < 50 to ~700 mm^3 with a high-resolution research tomograph (HRRT) PET scanner.

Materials and Methods

Monoclonal Antibody, Xenograft Line, and Radioactivity

Antibody L19-SIP (conc. 1.23 mg/mL), directed against the ED-B domain of fibronectin, was obtained from Bayer Schering Pharma, Berlin, Germany. Selection, construction and production of L19-SIP (Mw = ~80 kD) have been described previously [8, 9]. The MAb cetuximab (Erbitux® conc. 2.0 mg/mL) was used as reference for optimization of ^{124}I labeling and was purchased from Merck, Darmstadt, Germany. The human HNSCC cell line FaDu has been described before [18], was obtained from KH Heider (Boehringer Ingelheim Austria), and has been characterized for ED-B expression [11]. Iodine-131 (^{131}I; 66.4 GBq/mL; specific activity 611 GBq/mg) was purchased from Perkin Elmer.

Iodine-124 Production and Quality Tests

^{124}I was produced at BV Cyclotron VU (Amsterdam, The Netherlands) via a ^{124}Te(p,n)^{124}I reaction and isolated by use of dry distillation essentially as described by Qaim et al. [19]. In short, the target consisted of a glassy layer of $^{124}TeO_2$ (enrichment of 99.8%; Isoflex, USA) mixed with 5% (w/w) Al_2O_3. The physical thickness of the target was 250 mg/cm^2. A platinum (Pt) disc (Ø = 25 mm; thickness = 2 mm) containing a cavity (Ø = 14 mm; depth = 1 mm) was used as backing. The target was loaded on an in house made solid target station installed on a IBA Cyclone 18/9 cyclotron and irradiated with 12.5 MeV protons using a beam current of up to 20 μA for 2-10 h. During irradiation, the target was cooled in front using helium-cooling and at the back using water-cooling. A TERIMO module (Elex Commerce, Belgrade, Serbia) was used for radioiodine separation by dry distillation. Trapping of ^{124}I was performed in 1 mL 50 mM NaOH.

Assessment of the radiochemical purity of the ^{124}I preparations was performed by HPLC analysis, using a LiChrospher 100 RP-18 column (125 x 4 mm, 5 μm; Merck). As eluent 0.1 mol/L NaCl/0.004 mol/L octylamine (pH 7) + 5% (v/v) MeCN was used at a flow rate of 1.5 mL/min. The HPLC retention times were 1.5 min for IO_3^- and 5.0 min for I^- [20]. For identification and quantification of radionuclidic contaminants a germanium(lithium) (Ge(Li)) detector was used coupled to a multichannel analyzer [21]. The tellurium content was assessed by a spectrophotometric method as described by Qui-e et al. [22]. The endotoxine levels were assessed by use of an FDA-licensed LAL test system according to the instructions provided by the supplier (Endosafe®-PTS, Charles River, USA). Autoclaving was not performed but can be used as an option to assure sterility.

Radiolabeling

Preparation of ^{124}I-L19-SIP: Three sets of labeling experiments with L19-SIP were performed within the following general frame [23]: 20 mL ß-scintillation glass vials were coated with 25 µg IODO-GEN (Pierce) in dichloromethane, dried under a stream of N_2 gas, resulting in a thin coating of IODO-GEN on the bottom surface of the vial. The vials were stored under N_2 atmosphere. To a IODO-GEN-coated glass vial, successively 50 µl 0.5 M Na_2HPO_4 (pH 7.4), 450-X-Y µl 0.1 M Na_2HPO_4 (pH 6.8), X µl L19-SIP and Y µl radioiodine solution were added. After gentle shaking for 4 min at room temperature, 0.1 mL ascorbic acid (25 mg/mL, pH 5) was added to reduce the IODO-GEN and to protect the L19-SIP against radiation damage. After an additional 5 min, the reaction mixture was transferred to a syringe connected to a filter (0.22 µm Acrodisc, Gelman Sciences) followed by 0.4 mL 0.1 M Na_2HPO_4 (pH 6.8), used for an additional rinsing of the reaction vial. This combined solution was filtered and purified on a PD-10 column (GE Healthcare Life Sciences) with 0.9% NaCl/ascorbic acid (5 mg/mL, pH 5) as eluent. The first 2.5 mL (1.0 mL sample volume and the first 1.5 mL) were discarded and the radiolabeled antibody was collected in the next 1.5 mL.

In the first set, the ^{124}I-labeling efficiency was optimized by varying the amount of NaI present during the reaction. In these experiments X was 82 µl (100 µg, 1.33 nmol) L19-SIP, while Y was 50 µl of a series of pre-equilibrated (5 min) ^{124}I/NaI mixtures, each containing 2.4 MBq ^{124}I and respectively, 6700, 1675, 838, 419, 209, 105, 52, 26 and 0 pmol NaI. A similar series of labeling reactions was performed with the control MAb cetuximab, for which X was 50 µl (100 µg, 0.66 nmol). It is of note that the 2.4 MBq ^{124}I-activity used in each reaction in the case of carrier-free ^{124}I corresponds with 2.1 pmol iodine.

In the second set, ^{124}I-L19-SIP and ^{131}I-L19-SIP were synthesized for a biodistribution study. The labeling was carried out with X = 163 µl (200 µg, 2.66 nmol) L19-SIP; Y was 83 µl ^{124}I-solution (14.8 MBq, 266 pmol NaI). For ^{131}I, X was also 163 µl L19-SIP solution, Y was 2 µl of a diluted ^{131}I-batch (14.8 MBq). No NaI carrier was added to this solution, because 14.8 MBq ^{131}I already corresponds with 190.7 pmol ^{127}I and 61.4 pmol ^{131}I.

In the third set, ^{124}I-L19-SIP was synthesized for PET studies. The labeling was carried out with X is 142 µl (175 µg, 2.33 nmol) L19-SIP; Y was 90 µl ^{124}I-solution (38.5 MBq, 232 pmol NaI).

Analyses

All conjugates were analyzed by instant thin layer chromatography (ITLC) and high performance liquid chromatography (HPLC), by SDS-PAGE followed by phosphor imager analysis for integrity, and by a cell-binding assay for immunoreactivity.

HPLC monitoring of the final product was performed on a Jasco HPLC system

using a Superdex™ 200 10/300 GL size exclusion column (GE Healthcare Life Sciences). As eluent a mixture of 0.05 M sodium phosphate and 0.15 M sodium chloride (pH 6.8) was used at a flow rate of 0.5 mL/min.

Instant thin layer chromatography (ITLC) analysis of radiolabeled antibodies was carried out on silica gel impregnated glass fiber sheets (Gelman Sciences Inc., USA). As mobile phase, 20 mM citrate buffer, pH 5.0 was used. The integrity of the radioimmunoconjugates was monitored by electrophoresis on a Phastgel System (Pharmacia Biotech), using preformed high density SDS-PAGE gels under nonreducing conditions. Analysis and quantification of the radioactivity in the bands was performed with the use of Phosphor Imager screens and subsequent scanning by a Phosphor Imager (B&L-Isogen Service Laboratory).

In vitro binding characteristics of radiolabeled L19-SIP were determined in an immunoreactivity assay essentially as described before [11], using ED-B-coated Sepharose resin in PBS containing 1% bovine serum albumin (BSA). Five serial dilutions, ranging from 100 to 6.2 µL resin per tube, were prepared in triplicate in PBS/1% BSA. L19-SIP (125 ng), labeled with ^{124}I or ^{131}I, was added to the tubes and the samples were incubated overnight at 4°C for binding. Excess unlabeled L19-SIP antibody (10 µg per tube) was added to a second set of tubes with the lowest concentration of resin to determine non-specific binding. After incubation, resin was spun down and radioactivity in the pellet and supernatant was determined in a gamma counter and the percentage bound and free radioactivity was calculated. Binding data were graphically analyzed in a modified Lineweaver-Burk plot and the immunoreactive fraction was determined by linear extrapolation to conditions representing infinite antigen excess.

Biodistribution Studies

For the biodistribution experiments with L19-SIP, nude mice bearing the subcutaneously implanted human head and neck squamous cell carcinoma (HNSCC) xenograft line FaDu were used. No control SIP constructs were included in the current evaluations, because previous studies had shown the specificity of L19-SIP for targeting of ED-B expressing tumors in a direct comparison with the control D1.3-SIP directed against hen egg white lysosyme [9]. Female mice (Hsd athymic *nu/nu,* 25-32 g; Harlan CPB) were 8-10 weeks old at the time of the experiments. Animal experiments were performed according to National Institutes of Health principles of laboratory animal care and Dutch National Law ("Wet op de dierproeven", Stb 1985, 336).

At t = 0, FaDu-bearing nude mice (n = 20) received 25 µg of L19-SIP including 0.37 MBq of ^{124}I-labeled format and 0.37 MBq of ^{131}I-labeled format, by i.v. injection in the retro-orbital plexus. Two days before the experiments, 0.1% of potassium iodide

was added to the drinking water to block thyroid uptake of $^{124}I/^{131}I$. For assessment of biodistribution, 4 mice containing 2 tumors each were sacrificed at 3, 6, 24, 48, and 72 hours after injection. All animals were anaesthetized, bled, killed and dissected. Besides the tumors, the following organs were removed: tongue, sternum, heart, lung, liver, spleen, kidney, bladder, muscle, colon, ileum and stomach. Also content of stomach was retained. After blood, tumor, normal tissues, and stomach content were weighed, the amount of radioactivity in each was counted in a γ-counter (Wallac LKB-CompuGamma 1282, Kabi Pharmacia), using the corresponding window settings for ^{124}I and ^{131}I (for the 603 keV and 364 keV gamma energy, respectively). In this dual-isotope biodistribution study, cross-over corrections from one radionuclide into the alternate window were automatically performed using a standard of each radionuclide. Radioactivity uptake was calculated as the percentage of the injected dose per gram of tissue (%ID/g), corrected for radioactive decay.

The mean tumor size of 8 tumors at dissection was 234 ± 204, 384 ± 192, 273 ± 144, 371 ± 213, 315 ± 201 mm^3 for the groups that were dissected at 3, 6, 24, 48 and 72 hours after injection, respectively.

PET Imaging Procedures

Two animal PET studies for imaging of tumor targeting with ^{124}I-L19-SIP were performed essentially as described by Verel et al. [21]. During scanning mice were placed on a temperature controlled animal bed. In the first experiment, but not in the second experiment, 0.1% of potassium iodide was added to the drinking water to block thyroid uptake of ^{124}I. PET studies were performed using a double-crystal-layer HRRT PET scanner (Siemens/CTI Knoxville), a dedicated small animal and human brain scanner [24] with a spatial resolution transaxial between 2.3 and 3.2 full width half a maximum (FWHM) and in axial direction between 2.5 and 3.4 FWHM. A detailed description of the performance of the scanner and the software is given by De Jong et al. [24]. Transmission scans for attenuation and scatter correction were routinely obtained with each scan in two-dimensional mode using a single point ^{137}Cs source. Three-dimensional emission scans were acquired in 64-bit list mode during 60 min using a 400-650 keV window. The 64-bit list mode file was first converted into a single-frame sinogram using a span of 9, and subsequently reconstructed using a 3D ANW-OSEM reconstruction with 2 iterations and 16 subsets and matrix size 256x256 including corrections for normalization, decay and dead time. 3D ANW-OSEM is a 3D attenuation and normalization weighted ordered subset expectation maximalization reconstruction [25].

In a first PET imaging study, three FaDu xenograft-bearing nude mice were injected i.v. with 3.7 MBq ^{124}I-L19-SIP (25 μg). The mean tumor size at the start of the experiment was 266 ± 158 mm^3. During scanning at 1 and 2 days p.i., the animals were

sedated using isoflurane.

Because of clear tumor visualization in the first experiment, a second PET imaging experiment was performed to determine at which stage of tumor development tumors can be readily imaged by ^{124}I-L19-SIP immuno-PET. To this end, at 1, 2 and 3 weeks after subcutaneous tumor implantation, 6 mice were injected i.v. with 3.7 MBq ^{124}I-L19-SIP (25 µg) and imaged 48 h after each injection. Before each PET imaging procedure, the size of the tumors was measured with calipers. Because of inaccurate measurement of tumors smaller than 50 mm^3, size of these tumors was indicated to be < 50 mm^3.

Statistics

Differences in tissue uptake between coinjected conjugates were statistically analyzed for each time point with Excel 2003 software (Microsoft) using the Student *t*-test for paired data. Differences in average tumor volume between the various groups were statistically analysed for each time point with the Student's *t*-test for unpaired data. Two-sided significance levels were calculated, and $P < 0.01$ was considered statistically significant

Results

GMP-Compliant Production of ^{124}I

Production of ^{124}I via ^{124}Te(p,n)^{124}I reaction at incident energy of 12.5 MeV resulted in an average target yield (n=15) of 15.4 ± 0.5 MBq/µAh at the end of bombardment (EOB). During typical commercial runs, bombardment durations of 8 hours at 18 µA resulted in a yield of 2.2 GBq ^{124}I in-target. Subsequent dry distillation resulted in >90% recovery of radioiodine from the TeO_2 target into the 50 mM NaOH solution, while less than 0.5% TeO_2 was lost from the target. To allow for GMP compliant harvesting of ^{124}I, the TERIMO module was localized in a hot-cell integrated in a clean room meeting GMP conditions (GMP grade C, Figure 1). Visual inspection of the final product always revealed a clear, colorless solution. The radiochemical purity as assessed by HPLC analysis was >99.6% (specification for release >95% as iodide). After storage for 11 days, the radiochemical purity was still greater than 99.5%. Three days after production (considered the time of application) the radionuclidic purity was 99.6 ± 0.06 %, fulfilling the specification for release (>99.0 %). The main radionuclidic contaminants were ^{123}I (<0.5%) and ^{125}I (<0.03%), other radionuclidic impurities, if any, were below detection limit. The tellurium content of the ^{124}I-NaOH solution was 6 ± 1.6 ng/mL (specification for release <1 µg/mL). The endotoxine levels were <1.5 EU/mL (specification for release <5 EU/mL).

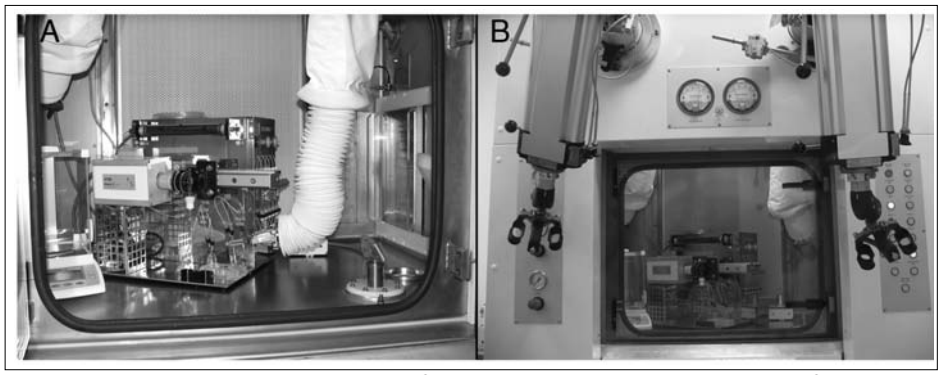

Figure 1. GMP compliant harvesting of ^{124}I. A TERIMO module for harvesting ^{124}I from the target disc by dry distillation (A) is localized in a hot-cell (B) integrated in a clean room meeting GMP conditions (GMP grade C).

Radiolabeling

Despite being >99% in the iodide form, the overall labeling yield of L19-SIP with in house produced ^{124}I was only at around 50%. This low labeling yield is inherent to the fact that ^{124}I is carrier-free, and not because the oxidative power of 25 µg vial-coated IODO-GEN is insufficient (25 µg IODO-GEN = 57 nmol and corresponds to 228 nmol N-Cl groups). In the presence of the excessive amount of 6.7 nmol NaI the ^{124}I- labeling yield was 96% upon using the same amount of L19-SIP (100 µg, 1.33 nmol) and the same amount (25 µg vial-coated) IODO-GEN. For a study on the fine-tuning of I/MAb molar ratios, the labeling of L19-SIP was evaluated in relation to the amount of NaI present during labeling. Figure 2 shows that in the presence of 200 pmol NaI or more, the labeling efficiency was 85-95%. It is of note that the same data as shown in Figure 2 were also obtained when cetuximab was used as a model substrate (data not shown).

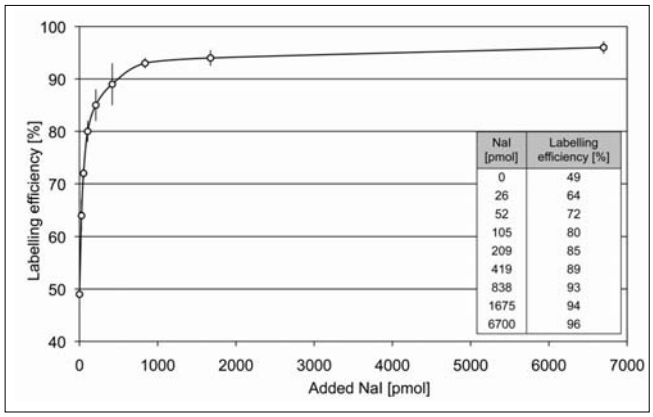

Figure 2. Labeling of L19-SIP with ^{124}I: labeling efficiency in relation to the amount of NaI carrier added. Labeling efficiency was assessed by ITLC.

For the biodistribution study, the amount of NaI was selected in such a way that the I/MAb of the ^{124}I-product was the same as that of the ^{131}I-product. As a result, the I/MAb molar ratio of both resulting conjugates was about 1 to 10. For the subsequent ^{124}I-animal PET studies the same I/MAb molar ratio was created. The radiochemical purity of the injected products was 99.9% for ^{124}I-L19-SIP as well as for ^{131}I-L19-SIP. Phosphor imager analysis of SDS-PAGE gels as well as HPLC analysis revealed optimal integrity of the antibody (Figure 3). The immunoreactivity of ^{124}I-L19-SIP was 93.1 ± 4.2% at the highest resin concentration and 100% at infinite antigen excess (for ^{131}I-L19-SIP these figures were 89.6 and 100%, respectively).

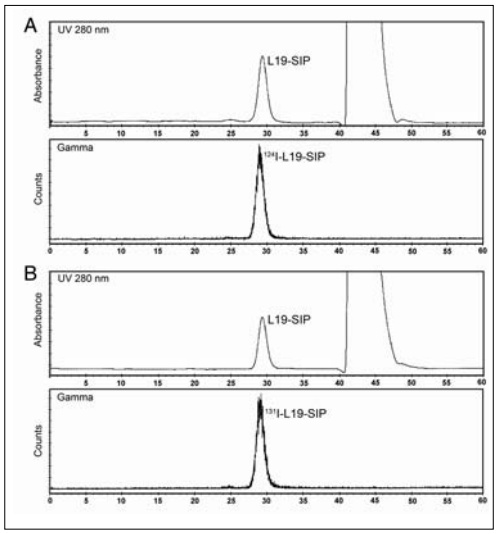

Figure 3. Representative HPLC chromatogram of ^{124}I-L19-SIP (A) and ^{131}I-L19-SIP (B). Upper panels show UV signal at λ280 nm, with retention time 29.4 min for L19-SIP and ~45 min for ascorbic acid. Lower panels show the radioactivity signal for iodinated L19-SIP.

Biodistribution Studies

For comparison of the biodistribution of ^{124}I- and ^{131}I-L19-SIP in tumor bearing nude mice, both conjugates were coinjected. At 3, 6, 24, 48 and 72 h after injection, the average uptake (%ID/g, mean ± SEM) in tumor, blood, normal tissues, and gastrointestinal contents was determined, and shown by Figure 4 for a selected panel of tissues. Blood values were similar for both conjugates at all time points, indicating that (1) radiolabeling had not differentially altered the pharmacokinetics of the antibody, and (2) serum stability was comparable for both conjugates. There was no significant difference in uptake of ^{124}I and ^{131}I in majority of normal organs (differences indicated by asterisk in Figure 4).

Tumor uptake of ^{124}I was 7.3 ± 2.1, 10.8 ± 1.5, 7.8 ± 1.4, 5.3 ± 0.6 and 3.1 ± 0.4 %ID/g tissue at 3, 6, 24, 48 and 72 h p.i.. In comparison, ^{131}I levels at these time points were 7.3 ± 2.0, 10.4 ± 1.4, 7.4 ± 1.2, 5.0 ± 0.5 and 2.7 ± 0.4 %ID/g, respectively. From 6 h p.i. onwards, ^{124}I-L19-SIP uptake in tumors was higher than in any normal organ or tissue. During the same period, blood levels decreased from 14.0 ± 2.7 %ID/g at 3 h after injection, to 0.08 ± 0.03 %ID/g at 72 h after injection. This resulted in very favorable tumor-to-blood ratios at later time points ranging from 6.0 at 24 h p.i. to 45.9 at 72 h p.i. (Table 1). Also tumor-to-normal tissue ratios were relatively high from 24 h after injection onwards, for most organs exceeding the value 4 (Table 1).

Table 1. Tumor-to-normal tissue ratios of coinjected ^{124}I-L19-SIP and ^{131}I-L19-SIP in FaDu xenograft bearing nude mice.

Biodistribution time	**3h**	**6h**	**24h**	**48h**	**72h**
Tumor-to-tissue ratios of ^{124}I-L19-SIP					
Blood	0.49	1.07	6.04	15.00	45.90
Tongue	1.11	1.69	4.14	5.84	14.76
Sternum	2.20	3.74	9.65	13.19	20.37
Heart	1.23	2.43	12.39	28.69	75.36
Lung	1.18	1.65	6.72	12.09	25.61
Liver	2.07	4.44	18.50	46.73	96.01
Spleen	1.80	3.37	11.48	27.95	53.25
Kidney	0.69	1.42	6.15	14.26	31.30
Bladder	1.80	1.96	1.83	3.72	9.99
Muscle	5.49	8.24	22.57	49.97	118.89
Colon	2.72	2.99	4.44	3.25	3.92
Ileum	1.58	2.71	4.90	5.85	4.80
Stomach	1.49	1.84	7.22	7.13	11.62
Stomach content	1.23	1.98	15.83	9.86	24.92
Tumor-to-tissue ratios of ^{131}I-L19-SIP					
Blood	0.48	1.00	5.45	13.54	43.44
Tongue	1.09	1.61	4.34	6.13	15.40
Sternum	2.12	3.39	9.24	12.54	20.49
Heart	1.20	2.23	11.39	27.44	59.17
Lung	1.17	1.55	6.31	11.52	22.06
Liver	2.08	4.16	16.92	41.59	81.63
Spleen	1.84	3.28	11.32	26.23	50.53
Kidney	0.68	1.30	5.50	12.06	27.88
Bladder	1.73	1.81	1.73	4.23	8.57
Muscle	5.26	7.60	21.65	45.77	103.17
Colon	2.66	2.78	4.25	3.31	5.27
Ileum	1.62	2.73	5.42	6.56	5.47
Stomach	1.41	1.73	7.01	7.32	12.67
Stomach content	1.17	1.83	14.50	9.53	22.88

Biodistribution assessed at 3, 6, 24, 48 and 72 h after intravenous injection. Data is presented as average of four animals. Data derived from Figure 4.

Rapid blood clearance during the first 24 h was accompanied by high radioactivity uptake in kidney, stomach, and stomach contents. This is indicative for rapid renal excretion and catabolism of the conjugate with partial reabsorption of ^{124}I-metabolites, which can accumulate in the stomach and are released from the body via intestines and colon.

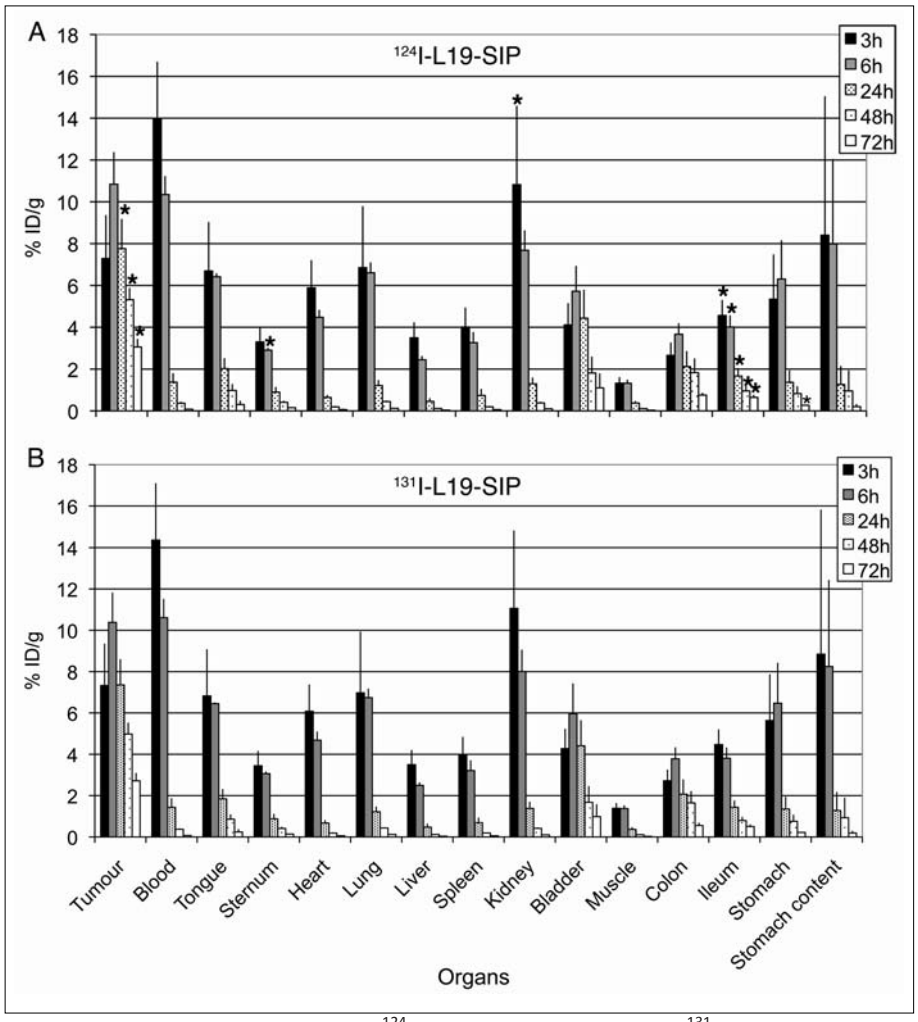

Figure 4. Biodistribution of coinjected ^{124}I-L19-SIP (0.37 MBq) (A) and ^{131}I-L19-SIP (0.37 MBq) (B) in FaDu xenograft bearing nude mice at 3, 6, 24, 48 and 72 h after intravenous injection. Significant differences in uptake of the conjugates are marked with an asterisk. Data is presented as average of four animals and standard deviation

PET Imaging

Immuno-PET with ^{124}I-L19-SIP revealed clear delineation of the tumors at 24 h p.i. (Figure 5A). In addition, slight uptake was visible in the stomach region, as was previously observed in the biodistribution experiments (Fig. 4). Prominent uptake of radioactivity was also observed in the bladder region, and from this single scan it was not clear whether uptake was due to targeting of ED-B expressing normal tissues by ^{124}I-L19-SIP (e.g. endometrium and ovary), or due to excretion of ^{124}I containing catabolites via the urine. Later scans of the same tumor bearing nude mice at 48 h p.i., however, showed only clear retention of ^{124}I-L19-SIP in the tumors (Figure 5B). This observation confirms that temporarily high levels of ^{124}I in the stomach regions were related to the presence of catabolites of ^{124}I-L19-SIP and/or free iodine.

Since tumor size in previous imaging experiment was relatively large, 266 ± 158 mm^3 at the time of conjugate injection, we examined how early after transplantation FaDu tumors can be visualized. To this end, at 1, 2 and 3 weeks after transplantation of the FaDu tumors a freshly produced ^{124}I-L19-SIP sample was injected, and 48 h later an imaging procedure was performed. As illustrated by Fig. 6, tumor delineation was possible from 1 week after implantation onwards, when tumor size was still <50 mm^3.

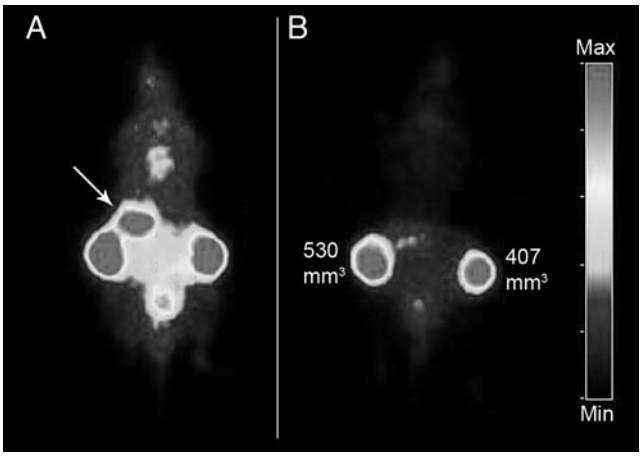

Figure 5. PET images of FaDu xenograft bearing nude mouse injected with ^{124}I-L19-SIP (3.7 MBq, 25 µg). Coronal images were acquired at 24 (A) and 48 h (B) after injection. Image planes have been chosen where both tumors were visible. Uptake of ^{124}I in the stomach (arrow) and to some extend in bladder (urine) is visible at 24 h p.i., but has disappeared at 48 h p.i.

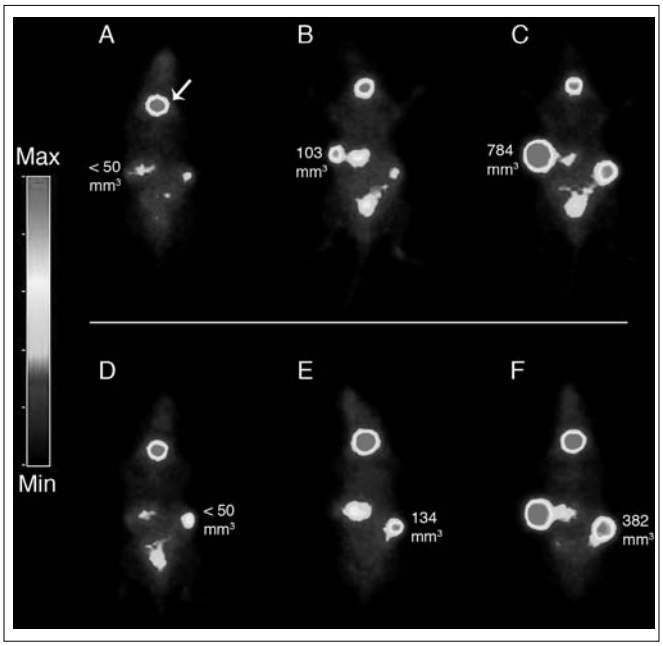

Figure 6. Serial PET images of FaDu xenograft bearing nude mouse injected with ^{124}I-L19-SIP (3.7 MBq, 25 µg). At 1 (A, D), 2 (B, E) and 3 (C, F) weeks after tumor implantation ^{124}I-L19-SIP was administered, and 48 h later coronal images were acquired. Image planes have been chosen where the left tumor (upper panel, A, B, C) or right tumor (lower panel, D, E, F is optimally visible. In contrast to Fig. 5, the thyroid (arrow) is visible because this organ was not blocked by potassium iodide in this experiment.

Discussion

Molecular imaging of tumor angiogenesis, one of the hallmarks of cancer, has clinical perspectives for lesion detection, patient stratification, new drug development and validation, treatment monitoring, and dose optimization [26]. To date, the application of PET for imaging of tumor vasculature has mostly exploited the use of radiolabeled RGD peptides for imaging of integrin $\alpha_v\beta_3$ expression, and radiolabeled peptides and MAbs for imaging VEGF/VEGFR expression [26]. Most recently the antibody fragment L19-SIP, directed against the ED-B domain of fibronectin, was identified as another attractive candidate for imaging of tumor vasculature, particularly because of its high and prolonged uptake in angiogenic tumor vessels and limited uptake in non-target organs. These targeting characteristics make L19-SIP, when armed with toxic payloads, also a promising ligand for therapy. Radioimmunotherapy is among the most advanced therapeutic approaches in the clinical development of L19-SIP, and for this purpose the antibody fragment is radiolabeled with ^{131}I [13].

After introduction of ^{131}I- and ^{99m}Tc-labeled derivatives of L19 for SPECT imaging of tumor angiogenesis [27, 28], in 2007 the first PET imaging derivative of L19-SIP has been described: ^{76}Br-L19-SIP [17]. Besides clear tumor targeting, ^{76}Br-L19-SIP also showed persistent activity in blood, stomach and several other normal organs, most probably due to in vivo debromination. The ^{76}Br-L19-SIP conjugates used in these studies were slightly less stable and immunoreactive than corresponding ^{125}I-L19-SIP conjugates, and appeared vulnerable for aggregate formation. The formation

of free $^{76}Br^-$ due to catabolism, and its prolonged retention in blood, was also observed by Lövqvist et al., who compared the biodistribution of the ^{76}Br-38S1 and ^{125}I-38S1 antibody conjugates in tumor bearing nude mice [29]. Aforementioned studies revealed that ^{76}Br can not be used as a PET radionuclide substitute for iodine radioisotopes. Another limitation of ^{76}Br is its limited availability, and the lack of supply of clinical grade ^{76}Br. Limited availability of long-lived positron emitters for immuno-PET made us a few years ago decide to put effort on the large scale GMP production of zirconium-89 (to be used for internalizing MAbs) and ^{124}I (to be used for non-internalizing MAbs), and on the development of standardized and easy-to-use radiolabeling procedures to facilitate the broad scale use of immuno-PET in clinical trials [15].

In the present study, we aimed the development of ^{124}I-L19-SIP immuno-PET, not only for imaging of tumor angiogenesis, but also as a scouting procedure prior to clinical ^{131}I-L19-SIP RIT, to confirm selective tumor targeting and to enable dosimetry. We considered ^{124}I to be the most suitable positron emitter for these applications (see introduction section), but realized that availability of clinical grade ^{124}I would be a problem. The urgent need for this positron emitter also became clear from a survey performed in 2005, in which the expectations of European researchers in terms of innovative radionuclides was evaluated [30]. A questionnaire was sent to 134 nuclear medicine centers in Europe, and the fifty-four responding centers expressed the strongest interest in the availability of ^{124}I. This made us decide to make the production of large batches of clinical grade ^{124}I starting point of the present studies. As demonstrated herein, infrastructure and procedures were developed for efficient GMP-compliant production of large batches of ^{124}I (>2 GBq) at high radionuclidic (>99.0%) and radiochemical (>95% as iodide) purity and low tellurium (<1 μg/mL) and endotoxin (<1.5 EU/mL) content.

Although labeling with radioiodine isotopes has been a widespread practice for decades, in several studies ^{124}I-labeled compounds were damaged and obtained in low yields [31-34]. Herein, L19-SIP was labeled with ^{124}I according to a direct labeling method with the use of a low amount of the mild oxidant IODO-GEN, and taking the I/MAb molar ratio and interference of radiolytic processes into account to arrive at optimal quality ^{124}I-L19-SIP conjugates. As convincingly shown by Fig. 2, addition of NaI as carrier to the reaction mixture during ^{124}I labeling, provides a means to increase the labeling yield with this precious isotope. This carrier approach was found to be generally applicable. Of course, caution should be taken when applying these procedures for MAbs containing an overabundance of tyrosines in the complementarity determining regions (CDR), so when the I/MAb molar ratio may be the prime parameter for immunoreactivity [35]. In that case, even single iodine incorporation on a tyrosine moiety in CDR might destroy the immunoreactivity of the

MAb molecule owing to the bulkiness of the ion atom and/or change in pK_a value of the tyrosine moiety (from 10.00 to 8.51). Therefore, in this study we decided to take the I/MAb ratio not higher than strictly necessary for obtaining high labeling yields and optimal immunoreactivity. However, when aiming the use of a ^{124}I-MAb for scouting of a ^{131}I-MAb conjugate in RIT, the I/MAb molar ratios of the conjugates can be easily synchronized, since this provides the best guarantee that the biodistribution of the therapeutic agent will be accurately predicted by the scouting agent. As another precaution to obtain optimal quality conjugates, immediately after radiolabeling ascorbic acid was added to the reaction mixture to reduce the IODO-GEN and to protect the L19-SIP against radiation damage.

L19-SIP labeled with ^{124}I according to aforementioned procedures demonstrated optimal integrity and immunoreactivity, and exhibited the same pharmacokinetic behavior as the corresponding ^{131}I conjugate. Moreover, biodistribution studies revealed high and selective tumor targeting, resulting in tumor-to-blood ratios ranging from 6.0 at 24 h to 45.9 at 72 h p.i.. Normal tissue accumulation of ^{124}I-L19-SIP was significantly lower than previously reported for ^{76}Br-L19-SIP. For example, while ^{76}Br-L19-SIP showed blood levels of 7.6 ± 1.8 and 8.1 ± 1.7 %ID/g at 24 and 48 h p.i., respectively, for ^{124}I-L19-SIP these values were 1.37 ± 0.43 and 0.37 ± 0.07, respectively. As a result, high tumor-to-normal tissue ratios were obtained with ^{124}I-L19-SIP, resulting in clear visualization of tumors by PET imaging, even when tumors were small (~50 mm^3). These achievements will open new possibilities for ^{124}I-immuno-PET in general, and for PET imaging of tumor angiogenesis with ^{124}I-L19-SIP in particular.

Acknowledgements

This project is financially supported by the European Union FP6, LSHC-CT-2003-5032, STROMA. The publication reflects only the authors view. The European Commission is not liable for any use that may be made of the information contained. The authors thank Maria J.W.D. Vosjan for her contribution to the experiments, and BV Cyclotron VU for assistance in ^{124}I production and installment of GMP production facilities.

References

1. Neri D, Bicknell R. Tumor vascular targeting. Nat Rev Cancer 2005;5:436-46.
2. Rybak JN, Trachsel E, Scheuermann J, Neri D. Ligand-based vascular targeting of disease. Chem Med Chem 2007;2:22-40.
3. Carnemolla B, Balza E, Siri A, Zardi L, Nicotra MR, Bigotti A, et al. A tumor-associated fibronectin isoform generated by alternative splicing of messenger RNA precursors. J Cell Biol 1989;108:1139-48.
4. Castellani P, Viale G, Dorcaratto A, Nicolo G, Kaczmarek J, Querze G, et al. The fibronectin isoform containing the ED-B oncofetal domain: a marker of angiogenesis. Int J Cancer 1994;59:612-8.
5. Birchler MT, Milisavlijevic D, Pfaltz M, Neri D, Odermatt B, Schmid S, et al. Expression of the extra domain B of fibronectin, a marker of angiogenesis, in head and neck tumors. Laryngoscope 2003;113:1231-7.
6. Ebbinghaus C, Scheuermann J, Neri D, Elia G. Diagnostic and therapeutic applications of recombinant antibodies: targeting the extra-domain B of fibronectin, a marker of tumor angiogenesis. Curr Pharm Des 2004;10:1537-49.
7. Zardi L, Carnemolla B, Siri A, Petersen TE, Paolella G, Sebastio G, et al. Transformed human cells produce a new fibronectin isoform by preferential alternative splicing of a previously unobserved exon. EMBO J 1987;6:2337-42.
8. Pini A, Viti F, Santucci A, Carnemolla B, Zardi L, Neri P, et al. Design and use of a phage display library. Human antibodies with subnanomolar affinity against a marker of angiogenesis eluted from two-dimensional gel. J Biol Chem 1998;273:21769-76.
9. Borsi L, Balza E, Bestagno M, Castellani P, Carnemolla B, Biro A, et al. Selective targeting of tumor vasculature: comparison of different formats of an antibody (L19) to the ED-B domain of fibronectin. Int J Cancer 2002;102:75-85.
10. Berndorff D, Borkowski S, Sieger S, Rother A, Friebe M, Viti F, et al. Radioimmunotherapy of solid tumors by targeting extra domain B fibronectin: Identification of the best-suited radioimmunoconjugate. Clin Cancer Res 2005;11:7053s-63s.
11. Tijink BM, Neri D, Leemans CR, Budde M, Dinkelborg LM, Stigter-van Walsum M, et al. Radioimmunotherapy of head and neck cancer xenografts using ^{131}I-labeled antibody L19-SIP for selective targeting of tumor vasculature. J Nucl Med 2006;47:1127-35.
12. El-Emir E, Dearling JLJ, Huhalov A, Robson MP, Boxer G, Neri D, et al. Characterization and radioimmunotherapy of L19-SIP, an anti-angiogenic antibody against the extra domain B of fibronectin, in colorectal tumor models. Br J Cancer 2007;96:1862-70.
13. Schliemann C, Neri D. Antibody-based targeting of the tumor vasculature. Biochim Biophys Acta 2007;1776:175-92.
14. Verel I, Visser GWM, van Dongen GAMS. The promise of immuno-PET in radioimmunotherapy. J Nucl Med 2005;46:Suppl 1:164S-71S.
15. Van Dongen GAMS, Visser GMW, Lub-de Hooge MN, De Vries EG, Perk LR. Immuno-PET: a navigator in monoclonal antibody development and applications. Oncologist 2007;12:1379-89.
16. Boswell CA, Brechbiel MW. Development of radioimmunotherapeutic and diagnostic antibodies: an inside-out view. Nucl Med Biol 2007;34:757-87.

17. Rossin R, Berndorff D, Friebe M, Dinkelborg LM, Welch MJ. Small-animal PET of tumor angiogenesis using a ^{76}Br-labeled human recombinant antibody fragment to the ED-B domain of fibronectin. J Nucl Med 2007;48:1172-9.
18. Rangan SR. A new human cell line (FaDu) from a hypopharyngeal carcinoma. Cancer. 1972;29:117-21.
19. Qaim SM, Hohn A, Bastian T, El-Azoney KM, Blessing G, Spellerberg S, et al. Some optimisation studies relevant to the production of high-purity ^{124}I and ^{120g}I at a small-sized cyclotron. Appl Radiat Isot 2003;58:69-78.
20. Monograph 01/2008:2314 Sodium Iodide (123I) Solution for Radiolabeling. European Pharmacopoeia. Strasbourg: European Directorate for the Quality of Medicines & HealthCare (EDQM); 2007:1010.
21. Verel I, Visser GWM, Vosjan MJWD, Finn R, Boellaard R, Van Dongen GAMS. High quality ^{124}I-labeled monoclonal antibodies for use as PET-scouting agent prior to ^{131}I-radioimmunotherapy. Eur J Nucl Med Mol Imaging 2004;31:1645-52.
22. Qiu-e C, Zhide H, Zubi L, Jialin W, Qiheng X. Highly sensitive spectrophotometric determination of trace amounts of tellurium(IV) with the tungstate-basic dyes-poly(vinyl alcohol) system. Analyst 1998;123:695-7.
23. Visser GWM, Klok RP, Klein-Gebbink JW, Ter Linde T, Van Dongen GAMS, Molthoff CF. Optimal quality Iodine-131-monoclonal antibodies upon high dose labeling in a large reaction volume and temporarily coating the antibody with iodogen. J Nucl Med 2001;42:509-19.
24. De Jong HWAM, Van Velden FHP, Kloet RW, Buijs FL, Boellaard R, Lammertsma AA. Performance evaluation of the ECAT HRRT: an LSO-LYSO double layer high resolution, high sensitivity scanner. Phys Med Biol 2007;52:1505-26.
25. Comtat C, Bataille F, Michel C, Jones JP, Sibomana M, Janeiro L, et al. OSEM-3D reconstruction strategies for the ECAT HRRT. IEEE NSS Conf. Rec 2004;6:3492-6.
26. Cai W, Chen X. Multimodality molecular imaging of tumor angiogenesis. J Nucl Med 2008;48:113S-28S.
27. Santimaria M, Moscatelli G, Viale GL, Giovannoni L, Neri G, Viti F, et al. Immunoscintigraphic detection of the ED-B domain of fibronectin, a marker of angiogenesis, in patients with cancer. Clin Cancer Res 2003;9:571-9.
28. Berndorff D, Borkowski S, Moosmayer D, Viti F, Müller-Tiemann B, Sieger S, et al. Imaging of tumor angiogenesis using ^{99m}Tc-labeled human recombinant anti-ED-B fibronectin antibody fragments. J Nucl Med 2006;47:1707-16.
29. Lövqvist A, Sundin A, Alström H, Carlsson J, Lundqvist H. Pharmacokinetics and experimental PET imaging of a bromine-67-labeled monoclonal anti-CEA antibody . J Nucl Med 1997;38:395-401.
30. Barbet J, Chatal J-F, Gauche F, Martino J. Which radionuclides will nuclear medicine need tomorrow? Eur J Nucl Med Mol Imaging 2006;33:627-30.
31. Finn R, Cheung NKV, Divgi C, St Germain J, Graham M, Pentlow K, et al. Technical challenges associated with the radiolabeling of monoclonal antibodies utilizing short-lived, positron emitting radionuclides. Nucl Med Biol 1991;18:9-13.
32. Lee FT, Hall C, Rigopoulos A, Zweit J, Pathmaraj K, O'Keefe GJ, et al. Immuno-PET of human colon xenograft-bearing BALB/c nude mice using ^{124}I-CDR-grafted humanized A33

monoclonal antibody. J Nucl Med 2001;42:764-9.
33. Collingridge DR, Carroll VA, Glaser M, Aboagye EO, Osman S, Hutchinson OC, et al. The development of [^{124}I]iodinated-VG76e: a novel tracer for imaging vascular endothelial growth factor in vivo using positron emission tomography. Cancer Res 2002;62:5912-9.
34. Glaser M, Collingridge DR, Aboagye EO, Bouchier-Hayes L, Hutchinson OC, Martin SJ, et al. Iodine-124 labelled annexin-V as a potential radiotracer to study apoptosis using positron emission tomography. Appl Radiat Isot 2003;58:55-62.
35. Nikula TK, Bocchia M, Curcio MJ, Sgouros G, Ma Y, Finn RD, et al. Impact of the high tyrosine fraction in complementarity determining regions: measured and predicted effects of radiodination on IgG immunoreactivity. Mol Immunol 1995;32:865-72.

CHAPTER 5

Quantitative PET imaging of Met-expressing human cancer xenografts with ^{89}Zr-labeled monoclonal antibody DN30

Lars R. Perk
Marijke Stigter-van Walsum
Gerard W. M. Visser
Reina W. Kloet
Maria J. W. D. Vosjan
C. René Leemans
Giuseppe Giaccone
Raffaella Albano
Paolo M. Comoglio
Guus A. M. S. van Dongen

European Journal of Nuclear Medicine and Molecular Imaging 2008;35:1857-1867

Abstract

Purpose: Targeting the c-Met receptor with monoclonal antibodies (mAbs) is an appealing approach for cancer diagnosis and treatment because this receptor plays a prominent role in tumor invasion and metastasis. Positron emission tomography (PET) might be a powerful tool for guidance of therapy with anti-Met mAbs like the recently described mAb DN30 because it allows accurate quantitative imaging of tumor targeting (immuno-PET). We considered the potential of PET with either ^{89}Zr-labeled (residualising radionuclide) or ^{124}I-labeled (non-residualising radionuclide) DN30 for imaging of Met-expressing tumors.

Materials and Methods: The biodistribution of co-injected ^{89}Zr-DN30 and iodine-labeled DN30 was compared in nude mice bearing either the human gastric cancer line GLT-16 (high Met expression) or the head-and-neck cancer line FaDu (low Met expression). PET images were acquired in both xenograft models up to 4 days post-injection (p.i.) and used for quantification of tumor uptake.

Results: Biodistribution studies in GTL-16-tumor-bearing mice revealed that ^{89}Zr-DN30 achieved much higher tumor uptake levels than iodine-labeled DN30 (e.g. 19.6%ID/g vs 5.3%ID/g, 5 days p.i.), while blood levels were similar, indicating internalization of DN30. Therefore, ^{89}Zr-DN30 was selected for PET imaging of GLT-16-bearing mice. Tumors as small as 11 mg were readily visualized with immuno-PET. A distinctive lower ^{89}Zr uptake was observed in FaDu compared to GTL-16 xenografts (e.g. 7.8%ID/g vs 18.1%ID/g, 3 days p.i.). Nevertheless, FaDu xenografts were also clearly visualized with ^{89}Zr-DN30 immuno-PET. An excellent correlation was found between PET-image-derived ^{89}Zr tumor uptake and ex-vivo-assessed ^{89}Zr tumor uptake ($R^2 = 0.98$).

Conclusion: The long-lived positron emitter ^{89}Zr seems attractive for PET-guided development of therapeutic anti-c-Met mAbs.

Introduction

The MET oncogene, encoding the tyrosine kinase receptor for hepatocyte growth factor (HGF), controls genetic programs leading to cell growth, invasion, metastasis, and protection from apoptosis [1]. Deregulated activation of Met is critical not only for the acquisition of tumorigenic properties but also for the achievement of the invasive phenotype. The role of Met in human tumors emerged from several experimental approaches and was unequivocally proven by the discovery of Met-activating mutations in inherited forms of carcinomas [2]. Moreover, Met constitutive activation is frequent also in sporadic cancers and it has been shown that Met is over-expressed in tumors of many histotypes or is activated through autocrine mechanisms [3–5] (see http://www.vai.org/met). Besides, the prevalence of abnormal Met expression is typically higher in metastases than in primary tumors and is associated with poor clinical prognosis [6]. As an example, the MET gene is amplified in haematogenous metastases of colorectal carcinomas [7]. What is more, Engelman et al. [8] recently showed that lung tumors can develop resistance to epidermal growth factor receptor (EGFR) inhibitors as a result of amplification of the MET oncogene, while inhibition of Met signaling restored their sensitivity to EGFR inhibitors. This makes Met, on the analogy of, e.g. EGFR, an interesting target for tumor detection, cancer prognostication and anti-cancer therapy, even in the absence of genetic alterations [9]. Amongst others, monoclonal antibodies (mAbs) are particularly attractive for this purpose. Especially intact mAbs (150 kDa) have shown value because their long residence time allows neutralization–blockage of growth factors or growth factor receptors for a prolonged period of time. Neutralizing anti-HGF mAbs have been used, but their application is limited to tumors with HGF-dependent Met activation [10]. Recently, it emerged that probably the best way to block the HGF–Met-induced invasive program is the competition with the Met receptor itself. MAb DN30, directed against the extracellular portion of Met, has been shown to inhibit growth of established xenografts and metastatic spread of cancer cells to the lungs in nude mouse models [11].

Aforementioned data indicate that Met is an exciting novel target for antibody-based diagnosis and therapy. With respect to the latter process, upcoming challenges include the optimization of mAb-based anti-Met therapy, its clinical evaluation and the selection of patient populations that will benefit mostly from treatment. Because HGF–Met signaling has been implicated in chemo- and radio-resistant tumors [8, 12], the combination of anti-Met mAbs with current cancer drugs might very well result in a more effective but less toxic therapy.

For optimal application of anti-Met mAbs in therapeutic approaches, it must be demonstrated that the receptor is expressed and that the mAb accumulates selectively and in sufficient amounts in the tumor. For this, nuclear molecular imaging

procedures can be used. Traditionally for imaging of radioactivity, planar imaging with a gamma-camera or single-photon emission computerised tomography has been used. More recently, positron emission tomography (PET) emerged as an attractive option for in vivo imaging of mAbs (immuno-PET). PET offers a high resolution and sensitivity combined with the unique ability to measure tissue concentrations of radioactivity in three dimensions, and therefore immuno-PET might be a valuable navigator in mAb development and applications [13, 14].

The positron emitters ^{89}Zr (half-life 78.4 h) and ^{124}I (half-life 100.3 h) are particularly attractive for imaging intact mAbs; their half-lives allow the assessment of long-term biodistribution of these antibody formats. In previous studies, we described procedures for production and purification of large amounts of these positron emitters and for their stable coupling to mAbs, with maintenance of the in vivo biodistribution characteristics of the latter [15, 16]. While ^{89}Zr is coupled via a chelate to the lysine residues of a mAb, ^{124}I can be coupled directly via tyrosine residues. Moreover, we demonstrated that ^{89}Zr is particularly suitable for PET imaging of internalizing mAbs and ^{124}I for non-internalizing mAbs. In contrast to directly labeled ^{124}I, ^{89}Zr is trapped in the cell after internalization of the mAb (residualization) [17, 18]. Residualization also occurs to some extent in organs of mAb catabolism like liver, kidney and spleen. The clinical potential of ^{89}Zr-immuno-PET and PET–CT for tumor detection was recently demonstrated in head-and-neck cancer patients [19].

In this study, we investigated the potential of PET imaging with either ^{89}Zr- or ^{124}I-labeled anti-Met mAb DN30 for assessment of in vivo Met expression status. For in vivo evaluation of tumor targeting with radiolabeled DN30, two human xenograft lines were selected, the gastric cancer line GLT-16 with high Met expression and the head-and-neck cancer line FaDu with low Met expression. Biodistribution of co-injected ^{89}Zr- and ^{131}I-labeled DN30 (^{131}I as substitute for ^{124}I to facilitate dual isotope counting) was assessed in xenograft-bearing nude mice. The potential of ^{89}Zr-DN30 for tumor detection was evaluated using a high-resolution research tomograph (HRRT) PET scanner. The potential of PET for in vivo ^{89}Zr-DN30 quantification was evaluated by relating image-derived tumor uptake data (non-invasive method) to ^{89}Zr data from excised tumors (invasive method).

Materials and Methods

Monoclonal Antibodies, Cell Lines, and Radioactivity

The murine immunoglobulin G2a (IgG2a) mAb DN30 (7.0 mg/mL), directed against the extracellular domain of Met (K_d of 2.64×10^{-9} M), was obtained from the Institute for Cancer Research and Treatment (IRCC), University of Turin Medical School, Italy. Selection, construction and production of DN30 have been described previously [20]. In the mean time, a humanized version of DN30 is under development for clinical evaluation.

The human gastric carcinoma cell line GTL-16, in which the MET proto-oncogene is amplified and over-expressed [21], was obtained from IRCC. The head-and-neck squamous cell carcinoma (HNSCC) cell line FaDu was obtained from Karl-Heinz Heider (Boehringer Ingelheim, Vienna, Austria) [22].

^{89}Zr (2.7 GBq/mL in 1 M oxalic acid) was produced by BV Cyclotron (Amsterdam, The Netherlands) by a (p,n) reaction on natural ^{89}Y and isolated with a hydroxamate column [16]. ^{131}I (7.4 GBq/mL in 0.01 M sodium hydroxide) was purchased from GE Healthcare Life Sciences (Uppsala, Sweden).

Immunohistochemical Staining of Cell Lines and Xenografts

The cell lines GTL-16 and FaDu were characterized for Met expression by performing immunocytochemistry with biotinylated DN30. In short, cells were trypsinized and spun onto glass slides at a density of 5×10^4 cells per spin, and the glass slides were air dried overnight. After fixing the cells with freshly prepared 2% paraformaldehyde for 10 min, the slides were incubated in Tris buffer (50 mM, pH 7.2) containing 2% bovine serum albumin for 30 min, followed by incubation with biotinylated DN30 for 1 h at room temperature. After extensive washing with the Tris buffer, the cells were incubated with streptavidin–alkaline phosphatase (ChemMate Detection Kit; Dako, Glostrup, Denmark) for 1 h at room temperature. Color developing was performed using freshly prepared substrate from the kit, followed by washing with demineralized water.

In addition, immunohistochemistry was performed on frozen sections of GTL-16 and FaDu xenografts. Cryostat sections (5 μm) were air dried and fixed in 2% paraformaldehyde for 10 min. Met staining was performed as described above.

Radiolabeling

For radiolabeling of DN30 with ^{89}Zr, a bi-functional metal-chelating moiety had to be conjugated to the mAb as described previously by Verel et al. [16]. Briefly, the chelate desferal (Df; Novartis, Basel, Switserland) was succinylated (*N*-sucDf), temporarily filled with stable iron [Fe(III)] and coupled to the lysine residues of DN30 by means of a tetrafluorophenol-*N*-sucDf ester. After removal of Fe(III) by trans-chelation to ethylenediaminetetraacetic acid, the pre-modified mAb was purified on a PD10 column (GE Healthcare Life Sciences). Approximately one *N*-sucDf moiety was coupled per DN30 molecule as assessed by using ^{59}Fe [23]. Subsequently, *N*-sucDf-DN30 (0.5 mg) was labeled with ^{89}Zr (max. 37 MBq) in 0.5 M 4-(2-hydroxyethyl)-1-piperazineethanesulfonic acid buffer at pH 7.0. Finally, ^{89}Zr-*N*-sucDf-DN30 was purified on a PD10 column (eluent: 0.9% sodium chloride/gentisic acid 5 mg/mL, pH 5.0). ^{89}Zr-*N*-sucDf-DN30 will be abbreviated to ^{89}Zr-DN30 in the rest of this article.

Radio-iodination of DN30 with ^{131}I was performed essentially as described previously [24]. ^{131}I was used as substitute of ^{124}I to facilitate dual isotope counting together with ^{89}Zr in the biodistribution studies (see later). The justification to do so was provided previously [15]. In short, to a 20-mL ß-scintillation glass vial coated with 75 µg IODO-GEN (Pierce Biotechnology, Rockford, IL, USA), 0.05 mL of 0.5 M sodium phosphate (pH 7.4), 50–200 µg DN30 in 0.45 mL of 0.1 M sodium phosphate (pH 6.8), and 9–18.5 MBq of ^{131}I were added, successively. After gentle shaking for 4 min at room temperature, the reaction was quenched by the addition of 0.1 mL of 25 mg/mL ascorbic acid (pH 5.0). Finally, ^{131}I-DN30 was separated from non-reacted ^{131}I by purification on a PD10 column (eluent: 0.9% sodium chloride/ascorbic acid 5 mg/mL, pH 5.0).

Analyses

After each preparation of ^{89}Zr-DN30 or ^{131}I-DN30, the conjugates were analyzed by instant thin-layer chromatography (ITLC) for radiolabeling efficiency and radiochemical purity, by high-performance liquid chromatography (HPLC) and sodium dodecyl sulfate–polyacrylamide gel electrophoresis (SDS-PAGE) followed by phosphor imager analysis for integrity and by a cell-binding assay for immunoreactivity. ITLC analyses of radiolabeled DN30 were performed on silica-gel-impregnated glass fiber sheets (Pall Corp., East Hills, NY, USA). As the mobile phase, 0.02 M citrate buffer (pH 5.0) was used.

HPLC monitoring of the final products was performed on a Jasco HPLC system using a Superdex™ 200 10/300 GL size exclusion column (GE Healthcare Life Sciences). As eluent, a mixture of 0.05 M sodium phosphate and 0.15 M sodium chloride (pH 6.8) was used at a flow rate of 0.5 mL/min. Electrophoresis was performed on a Phastgel

System (GE Healthcare Life Sciences) using preformed 7.5% SDS-PAGE gels under non-reducing conditions.

The immunoreactivity was determined by measuring binding of ^{89}Zr-DN30 and ^{131}I-DN30 (10,000 cpm/mL) to a serial dilution of 2% paraformaldehyde-fixed GTL-16 cells essentially as described by Lindmo et al. [25]. Data were graphically analyzed in a modified Lineweaver–Burk (double-reciprocal) plot and the immunoreactivity was determined by extrapolating to conditions representing infinite antigen excess.

Biodistribution

Nude mice bearing subcutaneously implanted xenografts of the human gastric carcinoma cell line GTL-16 or the HNSCC cell line FaDu were used. Female mice (HSD:Athymic Nude-Foxn1 nu, 21–31 g, Harlan CPB) were 10–14 weeks old at the time of the experiment. All animal experiments were performed according to National Institutes of Health principles of laboratory animal care and Dutch national law ("Wet op de dierproeven", Stb 1985, 336).

Three sets of biodistribution studies were performed. In the first experiment, the biodistribution of intravenous (i.v.) co-injected ^{89}Zr-DN30 (0.28 ± 0.01 MBq) and ^{131}I-DN30 (0.37 ± 0.01 MBq) was assessed in GTL-16-bearing nude mice. Unlabeled DN30 was added to the injection mixture so that each of the animals received 100 μg of mAb in total. This initial antibody dose was chosen sufficiently high to prevent rapid IgG2a isotype-related elimination of the mAb from the blood as has been described for the nude mouse model [26, 27] and sufficiently low to prevent antigen saturation in the tumor. The mean tumor size at the start of the experiment was 64 ± 33 mm^3. At 1, 2, 3 and 5 days post-injection (p.i.), four mice per time point were anaesthetized, bled, killed and dissected. After blood, tumor and normal tissues had been weighed, the amount of radioactivity in each sample was measured in a gamma counter. Radioactivity uptake was calculated as the percentage of the injected dose per gram of tissue (%ID/g).

In the second experiment, the relation between protein dose of ^{89}Zr-DN30 and biodistribution was investigated in GTL-16-bearing nude mice. Four groups of four mice received 0.39 ± 0.02 MBq ^{89}Zr-DN30 by i.v. injection. Unlabeled DN30 was added to the injection mixture so that per group the animals received 25, 50, 100, or 200 μg DN30 in total, respectively. The mean tumor size at the start of the experiment was 50 ± 34 mm^3 and was similar for the different groups. At day 3 p.i., all animals were anaesthetized, bled, killed and dissected, with further processing according to the above procedure.

In the third experiment, biodistribution of ^{89}Zr-DN30 (0.28 ± 0.01 MBq; 100 μg) was assessed in FaDu-bearing nude mice (n = 16). The mean tumor size at the start of the experiment was 149 ± 47 mm^3. At 1, 2, 3, and 4 days p.i., the mice were anaesthetized, bled, killed and dissected, with further processing according to the above procedure.

PET Imaging Procedures

Animal PET studies for imaging and quantification of tumor targeting of ^{89}Zr-DN30 were performed essentially as described by Verel et al. [28]. Briefly, PET studies were performed using a double-crystal-layer HRRT PET scanner (Siemens/CTI Knoxville), a dedicated small animal and human brain scanner [29]. Four GTL-16-xenograft-bearing nude mice were injected i.v. with 2.56 ± 0.04 MBq ^{89}Zr-DN30 (100 μg). The mean tumor size at the start of the experiment was 46 ± 19 mm^3. The animals were sedated using isoflurane and imaged at 10 min and at 1, 2, 3, and 4 days p.i. Three-dimensional (3D) emission scans were acquired in 64-bit list mode during 60 min using a 400–650-keV window. The 64-bit list mode file was first converted into a single-frame histogramme using a span of nine and subsequently reconstructed using a 3D OP-OSEM reconstruction with two iterations and 16 subsets. After reconstruction, regions of interest were drawn semiautomatic around the tumors using a 3D isocontour at 50% of maximum pixel value with background correction. Immediately after the last PET scan, the animals were killed, dissected and processed as described above.

In a second imaging study, a group of four FaDu-xenograft-bearing nude mice were injected i.v. with 1.78 ± 0.01 MBq ^{89}Zr-DN30 (100 μg). The mean tumor size at the start of the experiment was 231 ± 64 mm^3. Imaging was performed as described above.

Statistical Analyses

Differences in tissue uptake between co-injected conjugates were statistically analyzed for each time point with Statistical Package for Social Sciences (SPSS) 11.0 software using Student t-test for paired data. Two-sided significance levels were calculated and $P < 0.01$ was considered statistically significant. Statistical analysis of differences in tissue uptake between different groups was performed using Student t-test for unpaired data. Regression analysis of PET-defined ^{89}Zr tumor uptake versus ex-vivo-assessed ^{89}Zr tumor uptake was also performed with SPSS 11.0 software.

Results

Immunohistochemistry

The cell lines GTL-16 and FaDu both expressed Met (Figure 1A, B), but Met expression was highest in GTL-16 (~100,000 copies at outer cell surface). Met copy number could not accurately be determined for FaDu. Higher Met expression was also found for GLT-16 xenografts in comparison with FaDu xenografts (Figure 1C, D).

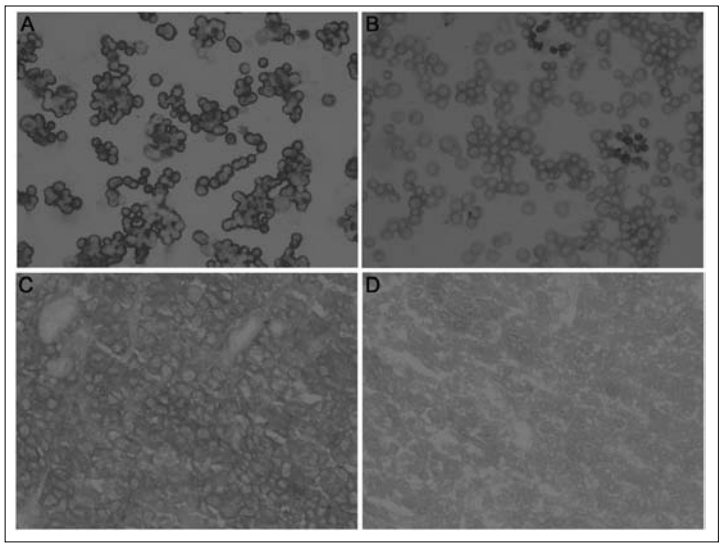

Figure 1. Immunohistochemical staining of Met expression with biotinylated DN30 on cytospins of GTL-16 (A) and FaDu (B) cells and on frozen sections of GTL-16 (C) and FaDu (D) xenografts

Radiolabeling

Radiolabeling of DN30 with ^{131}I or N-sucDf-DN30 with ^{89}Zr resulted in overall labeling yields of >85% and >70%, respectively. The radiochemical purity, as determined by ITLC, was always higher than 95% for both products. The specific radioactivities of the final products ranged from 30 to 80 MBq/mg for ^{131}I-DN30 and from 54 to 70 MBq/mg for ^{89}Zr-DN30. HPLC and SDS-PAGE analysis revealed optimal integrity of DN30, irrespective of whether the mAb was labelled with ^{131}I or ^{89}Zr. The immunoreactivity of both radioimmunoconjugates was always >70% at the highest cell concentration and >95% at infinite antigen excess.

Biodistribution

In the first study, we compared the biodistribution of ^{89}Zr-DN30 and ^{131}I-DN30 (100 µg DN30 total) in GTL-16-bearing nude mice. ^{89}Zr-DN30 showed a significantly higher tumor accumulation, as well as a significantly higher liver and spleen uptake compared to the ^{131}I-labeled counterpart (Table 1).

Table 1. Biodistribution of co-injected ^{89}Zr-DN30 and ^{131}I-DN30 in GTL-16 tumour-bearing nude mice up to 5 days after injection. Significant differences ($P < 0.01$) between ^{89}Zr-DN30 and ^{131}I-DN30 uptake are marked with an asterisk.

Biodistribution time	**1 d**	**2 d**	**3 d**	**5 d**
Uptake of ^{89}Zr-DN30 [%ID/g][a]				
Blood	17.1 (2.1)	13.3 (1.0)*	10.6 (3.2)*	8.8 (2.3)*
Tumour (GTL-16)	12.2 (4.3)*	17.3 (4.5)*	18.1 (4.5)*	19.6 (3.3)*
Tongue	4.2 (0.5)*	3.1 (0.5)*	2.8 (0.6)*	2.1 (0.4)
Sternum	2.9 (0.3)	3.1 (0.5)*	3.1 (0.3)*	2.2 (0.2)*
Heart	4.2 (0.6)	3.5 (0.6)	2.8 (0.6)	3.7 (1.0)
Lung	6.2 (0.4)	5.7 (0.2)	4.5 (0.7)	3.7 (0.6)
Liver	6.1 (0.3)*	6.3 (0.2)*	8.4 (2.4)*	7.2 (0.7)*
Spleen	6.6 (1.1)*	8.6 (0.9)*	7.9 (1.6)*	7.4 (1.8)*
Kidney	4.0 (0.6)	3.9 (0.2)*	3.5 (0.2)	3.1 (0.2)*
Bladder	3.3 (0.6)	3.3 (0.4)	3.2 (0.3)	2.9 (0.3)
Muscle	1.2 (0.2)	1.2 (0.1)	1.2 (0.2)	0.6 (0.2)
Colon	1.5 (0.2)*	1.9 (0.2)	1.8 (0.7)	1.3 (0.4)
Ileum	1.8 (0.3)	2.5 (0.7)	2.4 (1.2)	2.2 (0.8)
Stomach	1.5 (0.1)	1.7 (0.2)	1.5 (0.3)	1.6 (0.5)
Uptake of ^{131}I-DN30 [%ID/g][a]				
Blood	17.6 (2.1)	15.0 (0.9)	12.4 (3.2)	9.9 (2.0)
Tumour (GTL-16)	7.8 (3.1)	7.8 (1.1)	6.7 (1.5)	5.3 (1.0)
Tongue	4.6 (0.5)	3.7 (0.5)	2.5 (0.6)	2.1 (0.3)
Sternum	2.8 (0.3)	2.3 (0.5)	2.1 (0.4)	1.2 (0.3)
Heart	4.5 (0.7)	3.9 (0.7)	3.0 (0.8)	3.9 (0.9)
Lung	6.7 (0.3)	6.3 (0.3)	4.8 (0.7)	3.5 (0.6)
Liver	2.9 (0.5)	2.8 (0.3)	3.1 (0.8)	1.8 (0.1)
Spleen	3.8 (0.3)	4.2 (0.6)	4.0 (0.9)	2.2 (0.2)
Kidney	4.0 (0.8)	3.8 (0.2)	3.0 (0.4)	2.1 (0.3)
Bladder	4.2 (0.7)	4.7 (1.1)	3.5 (0.5)	2.7 (0.3)
Muscle	1.3 (0.2)	1.4 (0.3)	1.2 (0.2)	0.6 (0.1)
Colon	1.6 (0.2)	1.8 (0.1)	1.6 (0.4)	0.9 (0.2)
Ileum	1.8 (0.3)	2.1 (0.4)	1.7 (0.5)	1.2 (0.2)
Stomach	2.6 (0.7)	2.1 (0.2)	1.9 (0.3)	1.2 (0.2)

[a]All data are presented as mean ± S.D. (n=4).

The ^{89}Zr-DN30 tumor accumulation ranged from 12.2 ± 4.3%ID/g to 19.6 ± 3.3%ID/g and the ^{131}I-DN30 accumulation from 7.8 ± 3.1%ID/g to 5.3 ± 1.0%ID/g, in the time period between 1 and 5 days p.i. Small differences in uptake of both conjugates were found for blood and most other normal tissues. Nevertheless, tumor-to-normal tissue ratios were always higher for ^{89}Zr-DN30, except for liver and spleen at the earliest time points. In contrast to ^{89}Zr, levels of ^{131}I in tumors never exceeded levels of ^{131}I in blood. On the basis of these results, we selected ^{89}Zr-DN30 for the remaining biodistribution and PET imaging studies.

Table 2. Biodistribution of ^{89}Zr-labeled DN30 for four protein doses in GTL-16 tumour bearing mice at day 3 post injection. Significant differences ($P < 0.01$) in ^{89}Zr-DN30 uptake between the given protein doses are marked with an asterisk.

Protein dose	25 µg	50 µg	100 µg	200 µg
Uptake of ^{89}Zr-DN30 [%ID/g]				
Blood*	2.8 (4.4)	5.6 (1.8)	8.9 (2.7)	10.2 (1.0)
Tumor	14.3 (3.9)	16.6 (2.7)	18.4 (5.0)	15.1 (3.7)
Sternum	2.9 (0.2)	2.4 (0.3)	2.7 (0.4)	2.5 (0.3)
Heart	1.6 (1.1)	1.8 (0.3)	2.4 (0.4)	2.7 (0.5)
Lung	2.0 (1.4)	3.1 (0.7)	4.4 (1.0)	4.4 (0.3)
Liver	9.9 (2.4)	7.4 (1.1)	8.0 (2.0)	9.0 (5.1)
Spleen	11.0 (5.3)	8.4 (2.6)	8.0 (3.4)	6.6 (0.3)
Kidney	2.2 (0.2)	2.6 (0.2)	3.2 (0.1)	3.3 (0.3)
Muscle	0.7 (0.2)	0.8 (0.1)	1.1 (0.1)	1.0 (0.1)
Tumor/Tissue ratios				
T/Blood	5.0	2.9	2.1	1.5
T/Sternum	5.0	6.8	6.9	6.0
T/Heart	9.1	9.4	7.5	5.5
T/Lung	7.3	5.4	4.2	3.4
T/Liver	1.4	2.2	2.3	1.7
T/Spleen	1.3	2.0	2.3	2.3
T/Kidney	6.5	6.5	5.7	4.5
T/Muscle	21.5	20.1	17.5	15.4

[a]All data are presented as mean ± S.D. (n=4)

To investigate if 100 µg is an appropriate protein dose of mAb DN30 for efficient tumor targeting in mice, the biodistribution of ^{89}Zr-DN30 was assessed for four protein doses ranging from 25 to 200 µg in GTL-16-xenograft-bearing nude mice at day 3 p.i. The average uptake levels in blood, tumor, normal tissues and tumor-to-normal tissue ratios are shown in Table 2.

Tumor uptake levels combined with tumor-to-normal tissue ratios were considered most favorable for the 50 and 100 μg group. At the lowest protein dose, blood levels of DN30 were relatively low and strongly variable between mice, while, e.g. spleen uptake was high, which is indicative for rapid IgG2a-isotype-related elimination of mAbs in the nude mouse model [26, 27]. Therefore, we used the 100 μg mAb dose in the subsequent biodistribution and imaging studies.

In the third experiment, biodistribution of ^{89}Zr-DN30 was assessed in FaDu-bearing (low Met expression) mice up to 4 days p.i. (Table 3). Uptake of ^{89}Zr-DN30 in FaDu tumors was significantly lower than that in GTL-16 tumors, e.g. at 3 days p.i. the FaDu tumor uptake was 7.8 ± 1.2%ID/g compared to 18.1 ± 4.5%ID/g in the GTL-16 tumors ($P < 0.01$). This lower uptake correlates with the different expression levels of Met in these tumors as determined by immunohistochemistry (Figure 1).

Table 3. Biodistribution of ^{89}Zr-DN30 in FaDu tumor-bearing nude mice up to 4 days after injection.

Biodistribution time	**1 d**	**2 d**	**3 d**	**4 d**
Uptake of ^{89}Zr-DN30 [%ID/g][a]				
Blood	14.4 (1.0)	11.9 (1.5)	10.3 (1.5)	9.3 (2.3)
Tumor (FaDu)	6.3 (0.9)	9.3 (1.0)	7.8 (1.2)	6.7 (0.3)
Tongue	3.3 (0.5)	3.0 (0.3)	2.6 (0.4)	2.3 (0.9)
Sternum	2.5 (0.3)	2.7 (0.1)	2.5 (0.2)	3.0 (0.4)
Heart	3.3 (0.5)	3.3 (0.4)	2.9 (0.4)	2.7 (1.0)
Lung	5.7 (0.8)	5.3 (0.4)	4.5 (0.2)	4.8 (2.0)
Liver	4.1 (0.9)	4.8 (0.8)	4.7 (0.7)	4.9 (0.1)
Spleen	4.5 (0.7)	5.4 (1.4)	4.3 (0.8)	5.9 (0.9)
Kidney	3.3 (0.6)	3.6 (0.3)	3.1 (0.4)	3.0 (0.3)
Bladder	3.3 (0.8)	3.4 (0.3)	3.1 (0.3)	2.6 (0.6)
Muscle	1.3 (0.2)	1.3 (0.01)	1.1 (0.2)	0.9 (0.1)
Colon	1.6 (0.2)	2.0 (0.2)	1.3 (0.4)	1.0 (0.01)
Ileum	1.9 (0.5)	2.6 (0.7)	1.5 (0.5)	1.2 (0.1)
Stomach	1.6 (0.4)	1.6 (0.1)	1.3 (0.2)	1.0 (0.2)

[a]All data are presented as mean ± S.D. (n=4).

PET Imaging

Representative PET images of mice bearing Met-expressing human cancer xenografts, between 1 and 4 days after i.v. injection of ^{89}Zr-DN30, are shown in Figure 2 (GTL-16) and Figure 3 (FaDu). At the earliest imaging time point, 10 min p.i., only activity in the blood pool was observed (scans not shown). All tumors (arrows) could be clearly visualized in both xenograft hosts as early as 1 day p.i., and good delineation of the tumors persisted through the final imaging session. As expected from the

biodistribution data, tumor uptake was more pronounced in the GTL-16 xenografts. Tumor localization was obvious along with some blood pool, which diminished over time, and liver and spleen uptake. It is noteworthy that GTL-16 tumors as small as 11 mg were clearly visualized. A good correlation was found between PET-defined tumor uptake data and ex vivo tumor uptake measurements ($R^2 = 0.98$).

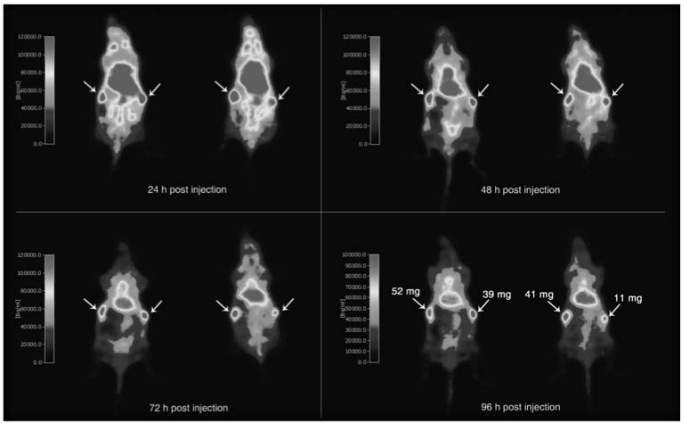

Figure 2. Sequential HRRT PET images (coronal slices) of two different GTL-16-xenograft-bearing nude mice at 1, 2, 3 and 4 days after i.v. injection with ^{89}Zr-DN30 (2.6 MBq, 100 µg mAb). Image planes have been chosen where both the left and right tumor are visible. Arrows indicate xenografts.

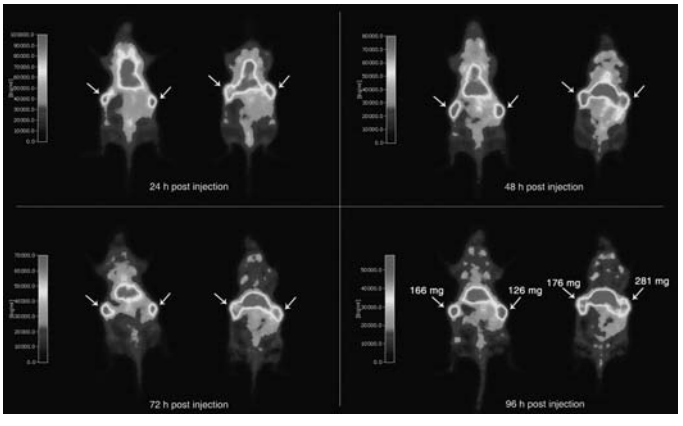

Figure 3. Sequential HRRT PET images (coronal slices) of two different FaDu-xenograft-bearing nude mice at 1, 2, 3 and 4 days after injection with ^{89}Zr-DN30 (1.8 MBq, 100 µg mAb). Image planes have been chosen where both the left and right tumor are visible. Arrows indicate xenografts.

Discussion

In the present study, we evaluated the potential of mAb DN30 for quantitative PET imaging of Met-expressing human tumor xenografts. In an earlier study, it was shown that murine mAb DN30, directed against the extracellular domain of Met, is able to promote receptor down-regulation and causes growth inhibition in vitro and in vivo [11]. A humanized mAb DN30, which is currently under construction, is an attractive candidate for clinical immunotherapy. For optimal application of anti-Met mAbs in in vivo therapeutic approaches, it is important to learn about the ideal mAb dosing for optimal tumor targeting (e.g. saturation of receptors), the uptake in critical normal organs to anticipate toxicity and the inter-patient variations in pharmacokinetics and tumor targeting [14]. As demonstrated herein, this can be performed by molecular imaging using PET. To the best of our knowledge, this is the first time ever an anti-Met mAb has been evaluated for its value in immuno-PET.

Visualization and quantification of mAb biodistribution using PET requires a suitable positron-emitting radionuclide. Only two positron emitters seem well suited for imaging of intact mAbs, ^{89}Zr ($t_{1/2}$ = 78.4 h) and ^{124}I ($t_{1/2}$ = 100.3 h) because the physical half-life of these radionuclides matches the time needed for mAbs to achieve optimal tumor-to-non-tumor ratios (2–4 days for intact mAbs). ^{64}Cu ($t_{1/2}$ = 12.7 h), ^{86}Y ($t_{1/2}$ = 14.7 h) and ^{76}Br ($t_{1/2}$ = 16.2 h) are also used for this purpose but are less optimal for imaging at later time points.

In this report, biodistribution and PET imaging studies were described in nude mice using two different xenograft lines with divergent levels of Met expression, the human gastric carcinoma cell line GTL-16 with high expression and the HNSCC cell line FaDu with low expression. The FaDu cell line was also chosen as a challenging model to examine imaging quality of radiolabeled DN30.

Both long-lived positron emitters, the residualizing radionuclide ^{89}Zr and the non-residualizing radionuclide ^{124}I, were considered as candidates for PET imaging with DN30. If a mAb is internalized after binding to the tumor cell, the use of residualizing radionuclide for imaging might be advantageous because of higher tumor-to-non-tumor ratios [18]. The biodistribution of co-injected ^{89}Zr-DN30 and ^{131}I-DN30 (^{131}I as a substitute for ^{124}I to facilitate simultaneous counting) in GTL-16-xenograft-bearing mice indeed revealed major differences in tumor uptake. Tumor uptake was substantially higher for ^{89}Zr compared to ^{131}I at all time points and almost four times higher at the latest time point (5 days p.i.). As a result, tumor-to-non-tumor ratios were significantly better for ^{89}Zr-DN30. In contrast to ^{89}Zr, levels of ^{131}I in tumors never exceeded levels of ^{131}I in blood. On the basis of these results, we concluded that the residualizing radionuclide ^{89}Zr is better suited for PET imaging with DN30 than non-residualizing iodine (^{124}I). Although, indirect radio-iodination

methodologies can be applied that will result in higher retention of radioactivity in tumor cells after the internalization of labeled mAbs [30].

By using PET with ^{89}Zr-DN30, GTL-16 tumors as small as 11 mg could be clearly visualized from day 1 p.i. onwards. Also, tumors with low Met expression, like the FaDu xenografts, could be clearly delineated with ^{89}Zr-DN30 immuno-PET. Moreover, the potential of ^{89}Zr-immuno-PET for non-invasive quantification of DN30 biodistribution was illustrated by the excellent correlation between PET-assessed tumor uptake data and ex vivo tumor uptake data (R^2 = 0.98). In clinical trials, quantitative PET imaging would be preferable over repeated tumor biopsies, especially because tumors are often heterogeneous (resulting in non-representative biopsies) and difficult to access.

Recently, the group of Vande Woude pioneered gamma-camera imaging for visualization of Met-expressing tumors [31]. For this purpose, they used the anti-Met mAbs (MetSeek™) designated Met3 and Met5. Antibodies were labeled with ^{125}I to enable gamma-camera imaging. Using relatively large tumors localized in the right thigh of the mice, i.e. far outside the abdominal region where ^{125}I uptake was high, Met5 gave better tumor visualization and retention than Met3. Because no ex vivo ^{125}I tissue uptake measurements have been performed in their study, it is difficult to compare Met3–Met5 with DN30 for tumor-targeting capacity. On the basis of our results, we hypothesize that imaging results would have been better when a residualizing gamma-emitting radionuclide had been used. But even then, the use of PET or PET–CT offers advantages for quantitative imaging.

Despite clear visualization of small tumors, ^{89}Zr-DN30 showed relatively high uptake in liver and spleen, especially when administered at relatively low protein dose (Table 2). Part of the liver and spleen uptake is due to residualization of ^{89}Zr after catabolism of the conjugate in these organs, as was also observed in our previous studies with ^{89}Zr-cetuximab (Erbitux) and ^{89}Zr-ibritumomab tiuxetan (Zevalin) in the same animal model [18, 23]. Nevertheless, we hypothesize that the enhanced uptake of radioactivity in liver and spleen might be partly an artifact related to the nude mouse model, which will not occur in humans. At this point, even better images can be expected in clinical studies.

DN30 is a murine mAb of the IgG2a isotype. Sharkey et al. [26] and Van Gog et al. [27] described the phenomenon of fast blood clearance of murine mAbs with concomitant high accumulation in liver and spleen, in various strains of outbred nu/nu mice. Fast blood clearance and enhanced liver and spleen uptake did especially occur when murine IgG2a or IgG2b isotype mAbs, young animals or a low mAb dose were used. The phenomenon was most prominent in animals with low endogenous IgG titers. The authors postulated that rapid removal of mAb from the blood might be mediated by Fc-binding receptors in, e.g. liver and spleen as long as endogenous mAb

titers are low. A very similar phenomenon was observed in this study when the mAb dose of DN30 was varied: lower mAb dose was associated with enhanced and variable blood clearance and a concomitant increased uptake in liver and particularly spleen (Table 2).

As far as the radiochemistry concerns, taking the step to clinical evaluation of immuno-PET with ^{89}Zr-labeled humanized or fully human anti-Met mAbs is relatively straightforward. Using the same radiochemical approach, we recently reported on an immuno-PET study with ^{89}Zr-labeled anti-CD44v6 cmAb U36 (75 MBq) for detection of lymph node metastases in 20 head-and-neck cancer patients [19, 32]. In addition, a clinical study has been started on the value of ^{89}Zr-ibritumomab tiuxetan for prediction of ^{90}Y-ibritumomab tiuxetan biodistribution with PET in non-Hodgkin's lymphoma patients [23]. With both ^{89}Zr conjugates, excellent PET images were obtained.

In the mean time, clinical immuno-PET trials with ^{89}Zr-trastuzumab (Herceptin) [33], ^{89}Zr-cetuximab, ^{89}Zr-rituximab (Rituxan) and ^{89}Zr-bevacizumab (Avastin) [34] are ongoing or in preparation. These trials revealed excellent tumor visualization [19, 23, 33], while low uptake levels in liver, kidney and spleen allow detection of abdominal metastases [33]. As a latest achievement, a new bi-functional chelate, a p-isothiocyanatobenzyl derivative of Df, was introduced for facile coupling of ^{89}Zr to mAbs [35]. In our view, immuno-PET might play an important future role in cancer staging and in the improvement and individualization of therapy with existing mAbs, as well as in the efficient development of novel mAbs, DN30 included [14].

Conclusion

The present study demonstrates that the anti-Met mAb DN30 labeled with the positron-emitting isotope ^{89}Zr can be used for semi-quantitative imaging of Met-expressing human tumor xenografts. Immuno-PET will learn whether effective tumor targeting with therapeutic anti-Met mAbs in patients is feasible.

Acknowledgments

This project was financially supported by the Dutch Technology Foundation (grant VBC.6120) and by the Associazione Italiana per la Ricerca sul Cancro. We thank the technical staff of BV Cyclotron and the Radionuclide Center for supplying and processing of ^{89}Zr, Floris van Velden for PET analyses and Otto Hoekstra for providing PET imaging facilities and for reviewing the manuscript.

References

1. Boccaccio C, Comoglio PM. Invasive growth: a MET-driven genetic programme for cancer and stem cells. Nat Rev Cancer 2006;6:637–45.
2. Schmidt L, Duh FM, Chen F, Kishida T, Glenn G, Choyke P, et al. Germline and somatic mutations in the tyrosine kinase domain of the MET proto-oncogene in papillary renal carcinomas. Nat Genet 1997;16:68–73.
3. Birchmeier C, Birchmeier W, Gherardi E, Vande Woude GF. Met, metastasis, motility and more. Nat Rev Mol Cell Biol 2003;4:915–25.
4. Trusolino L, Comoglio PM. Scatter-factor and semaphorin receptors: cell signalling for invasive growth. Nat Rev Cancer 2002;2:289–300.
5. Peruzzi B, Bottaro DP. Targeting the c-Met signaling pathway in cancer. Clin Cancer Res 2006;12:3657–60.
6. Lengyel E, Prechtel D, Resau JH, Gauger K, Welk A, Lindemann K, et al. C-Met overexpression in node-positive breast cancer identifies patients with poor clinical outcome independent of Her2/neu. Int J Cancer 2005;113:678–82.
7. Di Renzo MF, Olivero M, Giacomini A, Porte H, Chastre E, Mirossay L, et al. Overexpression and amplification of the Met/HGF receptor gene during the progression of colorectal cancer. Clin Cancer Res 1995;1:147–54.
8. Engelman JA, Zejnullahu K, Mitsudomi T, Song Y, Hyland C, Park JO, et al. MET amplification leads to gefitinib resistance in lung cancer by activating ERBB3 signaling. Science 2007;316:1039–43.
9. Corso S, Comoglio PM, Giordano S. Cancer therapy: can the challenge be MET? Trends Mol Med 2005;11:284–92.
10. Cao B, Su Y, Oskarsson M, Zhao P, Kort EJ, Fisher RJ, et al. Neutralizing monoclonal antibodies to hepatocyte growth factor/scatter factor (HGF/SF) display antitumor activity in animal models. Proc Natl Acad Sci U S A 2001;98:7443–8.
11. Petrelli A, Circosta P, Granziero L, Mazzone M, Pisacane A, Fenoglio S, et al. Ab-induced ectodomain shedding mediates hepatocyte growth factor receptor down-regulation and hampers biological activity. Proc Natl Acad Sci U S A 2006;103:5090–5.
12. Fan S, Wang JA, Yuan RQ, Rockwell S, Andres J, Zlatapolskiy A, et al. Scatter factor protects epithelial and carcinoma cells against apoptosis induced by DNA-damaging agents. Oncogene 1998;17:131–41.
13. Divgi CR, Pandit-Taskar N, Jungbluth AA, Reuter VE, Gonen M, Ruan S, et al. Preoperative characterisation of clear-cell renal carcinoma using iodine-124-labelled antibody chimeric G250 (^{124}I-cG250) and PET in patients with renal masses: a phase I trial. Lancet Oncol 2007;8:304–10.
14. Van Dongen GAMS, Visser GWM, Lub-de Hooge MN, De Vries EG, Perk LR. Immuno-PET: a navigator in monoclonal antibody development and applications. Oncologist 2007;12:1379–89.
15. Verel I, Visser GWM, Vosjan MJWD, Finn R, Boellaard R, Van Dongen GAMS. High-quality ^{124}I-labelled monoclonal antibodies for use as PET scouting agents prior to ^{131}I-radioimmunotherapy. Eur J Nucl Med Mol Imaging 2004;31:1645–52.
16. Verel I, Visser GWM, Boellaard R, Stigter-Van Walsum M, Snow GB, Van Dongen GAMS. ^{89}Zr

immuno-PET: comprehensive procedures for the production of ^{89}Zr-labeled monoclonal antibodies. J Nucl Med 2003;44:1271–81.

17. Verel I, Visser GWM, Boerman OC, Van Eerd JEM, Finn R, Boellaard R, et al. Long-lived positron emitters zirconium-89 and iodine-124 for scouting of therapeutic radioimmunoconjugates with PET. Cancer Biother Radiopharm 2003;18:655–61.
18. Perk LR, Visser GWM, Vosjan MJWD, Stigter-van Walsum M, Tijink BM, Leemans CR, et al. ^{89}Zr as a PET surrogate radioisotope for scouting biodistribution of the therapeutic radiometals ^{90}Y and ^{177}Lu in tumor-bearing nude mice after coupling to the internalizing antibody cetuximab. J Nucl Med 2005;46:1898–906.
19. Borjesson PKE, Jauw YWS, Boellaard R, De Bree R, Comans EFI, Roos JC, et al. Performance of immuno-positron emission tomography with zirconium-89-labeled chimeric monoclonal antibody U36 in the detection of lymph node metastases in head and neck cancer patients. Clin Cancer Res 2006;12:2133–40.
20. Prat M, Crepaldi T, Pennacchietti S, Bussolino F, Comoglio PM. Agonistic monoclonal antibodies against the Met receptor dissect the biological responses to HGF. J Cell Sci 1998;111:237–47.
21. Ponzetto C, Giordano S, Peverali F, Della Valle G, Abate ML, Vaula G, et al. C-met is amplified but not mutated in a cell line with an activated met tyrosine kinase. Oncogene 1991;6:553–9.
22. Rangan SRS. A new human cell line (FaDu) from a hypopharyngeal carcinoma. Cancer 1972;29:117–21.
23. Perk LR, Visser OJ, Stigter-van Walsum M, Vosjan MJWD, Visser GWM, Zijlstra JM, et al. Preparation and evaluation of ^{89}Zr-Zevalin for monitoring of ^{90}Y-Zevalin biodistribution with positron emission tomography. Eur J Nucl Med Mol Imaging 2006;33:1337–45.
24. Visser GW, Klok RP, Gebbinck JWK, Ter Linden T, Van Dongen GA, Molthoff CF. Optimal quality ^{131}I-monoclonal antibodies on high-dose labeling in a large reaction volume and temporarily coating the antibody with IODO-GEN. J Nucl Med 2001;42:509–19.
25. Lindmo T, Boven E, Cuttitta F, Fedorko J, Bunn PA. Determination of the immunoreactive fraction of radiolabeled monoclonal-antibodies by linear extrapolation to binding at infinite antigen excess. J Immunol Methods 1984;72:77-89.
26. Sharkey RM, Natale A, Goldenberg DM, Mattes MJ. Rapid blood clearance of immunoglobulin G2a and immunoglobulin G2b in nude mice. Cancer Res 1991;51:3102–7.
27. Van Gog FB, Brakenhoff RH, Snow GB, Van Dongen GAMS. Rapid elimination of mouse/human chimeric monoclonal antibodies in nude mice. Cancer Immunol Immunother 1997;44:103–11.
28. Verel I, Visser GWM, Boellaard R, Boerman OC, Van Eerd J, Snow GB, et al. Quantitative ^{89}Zr immuno-PET for in vivo scouting of 90Y-labeled monoclonal antibodies in xenograft-bearing nude mice. J Nucl Med 2003;44:1663–70.
29. De Jong HWAM, Van Velden FHP, Kloet RW, Buijs FL, Boellaard R, Lammertsma AA. Performance evaluation of the ECAT HRRT: an LSO-LYSO double layer high resolution, high sensitivity scanner. Phys Med Biol 2007;52:1505–26.
30. Vaidyanathan G, Zalutsky MR. Synthesis of N-succinimidyl 4-guanidinomethyl-3-[*I]iodobenzoate: a radio-iodination agent for labeling internalizing proteins and peptides. Nat Protoc 2007;2:282–6.
31. Hay RV, Cao B, Skinner RS, Su Y, Zhao P, Gustafson MF, et al. Nuclear imaging of Met-

expressing human and canine cancer xenografts with radiolabeled monoclonal antibodies (MetSeek). Clin Cancer Res 2005;11:7064s–9s.

32. Zalutsky MR. Potential of immuno-positron emission tomography for tumor imaging and immunotherapy planning. Clin Cancer Res 2006;12:1958–60.
33. Dijkers E, Lub-de Hooge MN, Kosterink JG, Jager PL, Brouwers AH, Perk LR, et al. Characterization of ^{89}Zr-trastuzumab for clinical HER2 immunoPET imaging. J Clin Oncol 2007;25(Suppl 1):3508.
34. Nagengast WB, De Vries EG, Hospers GA, Mulder NH, De Jong JR, Hollema H, et al. In vivo VEGF imaging with radiolabeled bevacizumab in a human ovarian tumor xenograft. J Nucl Med 2007;48:1313–9.
35. Perk LR, Visser GWM, Budde M, Vosjan MJWD, Jurek P, Kiefer GE, et al. Facile radiolabeling of monoclonal antibodies and other proteins with zirconium-89 or gallium-68 for PET imaging using p-isothiocyanatobenzyl-desferrioxamine. Nat Protoc 2008. DOI 10.1038/nprot.2008.22.

CHAPTER 6

p-Isothiocyanatobenzyl-desferrioxamine: a new bifunctional chelate for facile radiolabeling of monoclonal antibodies with zirconium-89 for immuno-PET imaging

Lars R. Perk
Maria J. W. D. Vosjan
Gerard W. M. Visser
Marianne Budde
Paul Jurek
Garry E. Kiefer
Guus A. M. S. van Dongen

Accepted for publication in European Journal of Nuclear Medicine and Molecular Imaging

Abstract

Immuno-Positron Emission Tomography (PET) is an exciting imaging tool for the selection of high potential antibodies (mAbs) for imaging and therapy. The positron emitter zirconium-89 (^{89}Zr) has ideal characteristics for immuno-PET with intact mAbs. In the past, we described a multi-step procedure for stable coupling of ^{89}Zr to mAbs via the bifunctional chelate (BFC) tetrafluorophenol-*N*-succinyldesferal (TFP-*N*-sucDf). To enable wide spread use of ^{89}Zr-immuno-PET, we recently introduced a chemically more facile route using the novel BFC *p*-isothiocyanatobenzyl-desferrioxamine B (Df-Bz-NCS). In the present study, we compared the novel BFC Df-Bz-NCS and the reference BFC TFP-*N*-sucDf for their performance in ^{89}Zr-immuno-PET. Three MAbs were premodified with Df-Bz-NCS and labeled with ^{89}Zr at different pH's to assess the reaction kinetics and robustness of the radiolabeling. Stability of both ^{89}Zr-Df-Bz-NCS- and ^{89}Zr-*N*-sucDf-conjugates was evaluated in different buffers and in human serum. Comparative biodistribution and animal-PET studies in mice bearing tumor xenografts were undertaken.

The selected conjugation conditions resulted in a chelate:mAb substitution ratio of about 1.5:1. Under optimal radiolabeling conditions (pH between 6.8 – 7.2), the radiochemical yield was always >85% after 60 min incubation at room temperature, resulting in radioimmunoconjugates with preserved integrity and immunoreactivity. The new radioimmunoconjugate was very stable in serum for up to 7 days at 37°C, with <5% ^{89}Zr release, but was slightly less stable compared to the reference conjugate when stored in buffer at 4°C. The biodistribution and imaging experiments showed high, selective, and similar accumulation of both radioimmunoconjugates in tumors in nude mice. In conclusion, the novel Df-Bz-NCS BFC allows efficient and easy preparation of optimally performing ^{89}Zr-labeled mAbs, facilitating further exploration of ^{89}Zr-immuno-PET as an imaging tool.

Introduction

Presently, hundreds of monoclonal antibodies (mAbs) and mAb fragments are under clinical development because of their excellent potential for diagnosis and systemic treatment of cancer and other pathological conditions [1]. Positron emission tomography (PET) offers an exciting imaging option to confirm and quantify selective tumor uptake of such targeting molecules [2-4].

To enable PET imaging of intact mAbs and mAb-fragments (immuno-PET), an appropriate positron emitter, with a half-life ($t_{1/2}$) that is compatible with the time needed to achieve optimal tumor-to-nontumor ratios (typically 2-4 days for intact mAbs, and 2-4 hours for mAb-fragments), has to be securely coupled to the targeting molecule. Among others, the following positron emitters for immuno-PET are under investigation at the moment: gallium-68 (^{68}Ga; $t_{1/2}$: 1.13 h), fluorine-18 (^{18}F; $t_{1/2}$: 1.83 h), copper-64 (^{64}Cu; $t_{1/2}$: 12.7 h), yttrium-86 (^{86}Y; $t_{1/2}$: 14.7 h), bromine-76 (^{76}Br; $t_{1/2}$: 16.2 h), zirconium-89 (^{89}Zr; $t_{1/2}$: 78.4 h), and iodine-124 (^{124}I; $t_{1/2}$: 100.3 h). Another important consideration in the choice of a positron emitter is whether the mAb or mAb fragment becomes internalized after binding to the target antigen. In that case, a positron emitter is needed that residualizes in the target cell after internalization, like ^{68}Ga, ^{64}Cu, ^{86}Y, and ^{89}Zr, to enable imaging at optimal contrast. These radionuclides have to be attached via chelating agents to mAbs and mAb-fragments.

For imaging of intact mAbs with PET, we recently described the large scale production of ^{89}Zr and a strategy for labeling mAbs with ^{89}Zr via a multi-step synthesis using a succinylated-derivative of desferrioxamine B (*N*-sucDf) as bifunctional chelate [5]. The utility of this approach was clearly demonstrated through high quality ^{89}Zr-mAb-PET images reported in preclinical and clinical studies [6-13]. The choice of desferrioxamine B is attractive because it is used clinically in a safe way for many years. The upcoming commercialization of ^{89}Zr will make this radionuclide broadly available for research and clinical applications.

A shortcoming of the aforementioned labeling approach is that the multi-step procedure is relatively complicated and time consuming, and therefore challenging with respect to Good Manufacturing Practice (GMP) compliancy. Recently, the newly developed *p*-isothiocyanatobenzyl-derivative of desferrioxamine B (Df-Bz-NCS; Macrocyclics, TX) was introduced that provides an efficient and rapid preparation of ^{89}Zr-labeled mAbs [14]. In addition, Df-Bz-NCS can also be utilized to label proteins at room temperature with gallium-68. ^{68}Ga is especially attractive for PET-imaging of fast kinetic targeting proteins like peptides, mAb fragments, and nontraditional scaffolds [15].

In this work, the synthesis of Df-Bz-NCS, it's subsequent coupling to mAbs, and the radiolabeling of Df-Bz-NCS conjugated mAbs with ^{89}Zr, are described. The *in vitro* stability of ^{89}Zr-Df-Bz-NCS-mAb conjugates is compared with the corresponding ^{89}Zr-*N*-sucDf-mAb conjugates. In addition, comparative biodistribution and animal-PET studies are presented.

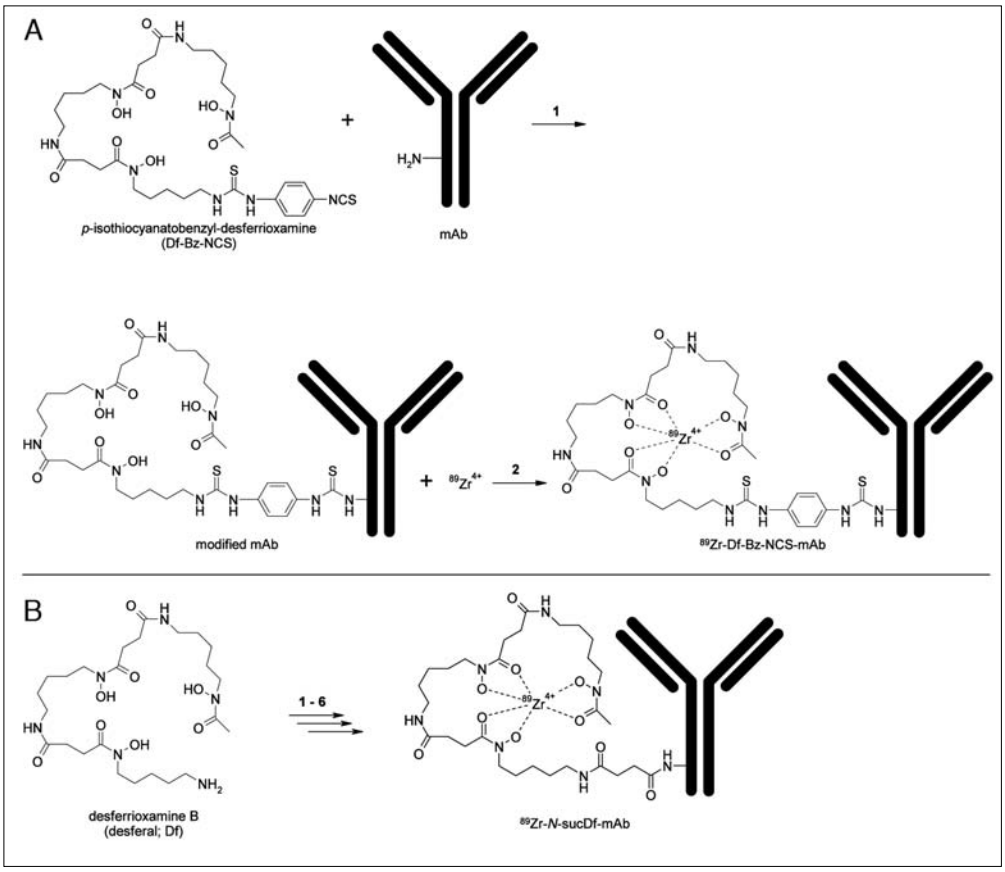

Figure 1. (**A**) Schematic representation of mAb modification with the new bifunctional chelate Df-Bz-NCS (**1**) and subsequent labeling with ^{89}Zr (**2**). (**B**) The multi-step reference procedure using desferrioxamine B as starting ligand.

Experimental Procedures

Materials, Monoclonal Antibodies, Cell Lines, and Radioactivity

All reagents were obtained from Sigma-Aldrich (St. Louis, MO) unless otherwise stated. Deionized water (18 MΩ) was used in all reactions. Df-Bz-NCS was obtained from Macrocyclics (cat. no. B-705). MAb cetuximab (Erbitux; 2.0 mg/mL) directed against the epidermal growth factor receptor (EGFR) was purchased from Merck (Darmstadt, Germany)[16]. Selection, production, and characterization of chimeric mAb U36 (cU36; 11.53 mg/mL) directed against CD44v6 has been described elsewhere [17]. MAb rituximab (MabThera; 10 mg/mL) directed against CD20 was purchased from Roche Nederland BV (Woerden, The Netherlands).

The human epidermoid cervical carcinoma cell line A431 and the CD20+ B-cell lymphoma cell line Ramos were both obtained from the American Type Culture Collection (www.atcc.com, ATCC number: CRL-1555 and CRL-1596, respectively). The head and neck squamous cell carcinoma (HNSCC) cell line FaDu was obtained from Karl-Heinz Heider (Boehringer Ingelheim, Vienna, Austria) [18], and the HNSCC cell line UM-SCC-11B was obtained from Dr. T.E. Carey (Ann Arbor, MI) [19].

^{89}Zr ($T_{1/2}$ = 78.4 h, β^+ = 22.6%; ~2.7 GBq/mL in 1 M oxalic acid) was produced by BV Cyclotron VU (Amsterdam, The Netherlands) by a (p,n) reaction on natural yttrium-89 (^{89}Y) and isolated with a hydroxamate column [5].

Synthesis of 1-(4-isothiocyanatophenyl)-3-[6,17-dihydroxy-7,10,18,21-tetroxo-27-[N-acetylhydroxyamino)-6,11,17,22-tetraazaheptaeicosane)thiourea (p-isothiocyanatobenzyl-desferrioxamine; Df-Bz-NCS)

Synthesis of the new Df-Bz-NCS ligand was performed by Macrocyclics (Dallas, TX). In short, Desferrioxamine B mesylate (Df; Desferal, Novartis, Basel) was dissolved in isopropanol/water while gently stirring. A chloroform solution of 1,4-phenylendiisothiocyanate and triethyl amine was then added and the reaction progress was monitored by reverse phase HPLC. Upon completion the reaction mixture was extracted with 0.1M HCl. The lower organic layer was concentrated in vacuo to remove the chloroform but not the isopropanol. The remaining organic solution was purified by reverse phase preparative HPLC using a water/acetonitrile gradient [Detector: UV/VIS at 275 nm. Column: Phenomenex Luna C18(2) (250x50 mm, 10 μm,). Sample prep: Direct injection of the isopropanol solution. Mobile phase: 0-10 min 40/60 A/B; 10–15 min ramp 40/60 to 90/10 A/B; 15-25 min 90/10 A/B; A = CH_3CN, B = H_2O. Flow rate = 100 mL/min. Retention time of product was ~10 min. Desired fractions were placed at -20°C to precipitate the product. The final product was isolated by filtration as a white solid (41% yield).

Analytical data final product:
^{1}H NMR (D_6-DMSO): δ 1.21 (m, -CH_2, 6H), 1.38 (m, -CH_2, 4H), 1.95 (s, -CH_3, 3H), 2.27 (m, -CH_2, 4H), 2.99 (m, CH_2, 4H), 3.45 (m, CH_2, 8H), 7.35 (d, 2,6-ArH, J = 8.9 Hz, 2H), 7.75 (d, 3,5=ArH, J=8.9 Hz, 2H), 7.75 (m, N-H, 2H), 7.88 (bs, N-H, 1H), 9.59 (m, N-OH, 4H). ^{13}C NMR: δ 19.18 (CH_3), 22.34, 22.35, 22.44, 24.88, 24.90, 24.94, 24.96, 24.98, 26.42, 26.88, 27.66, 28.78, 28.79, 28.83, 37.28, 37.92, 42.57, 42.60, 42.63, 45.67, 45.97, 121.92, 123.50, 124.98, 131.58, 138.17 (N=C=S), 169.00 (C=O), 170.20 (C=O), 170.84 (C=O), 179.02 (C=S). Elemental analysis calculated (%) for $C_{33}H_{52}N_8O_8S_2$: C 52.64, H 6.96, N 14.88, S 8.52, found C 52.43, H 7.08, N 14.81, S 8.59. m/z: (ESI+); 775 (100% $[M + Na]^+$), (ESI-); 751 (100% $[M-H]^-$). Chromatographic purity: > 98% Detector: UV/VIS at 225 nm. Column: Restek Ultra IBD (100x4.6 mm, 3 µm, 100 A). Sample prep: a 1.0 mg/mL solution prepared in DMSO. Mobile phase: 0-10 min ramp 5/95 to 95/5 A/B; 10-15 min 95/5 A/B; A = 0.1% TFA in CH_3CN, B = 0.1% TFA in H_2O.

Preparation of ^{89}Zr-Labeled Df-Bz-NCS-mAb

cU36, cetuximab, or rituximab were premodified with Df-Bz-NCS essentially as described recently by Perk et al. [14](Figure 1A). In short, while gently shaking, a 3-fold molar excess of Df-Bz-NCS (in 20 µL DMSO) was added to the mAb (2 – 10 mg in 1 mL 0.1 M $NaHCO_3$ buffer, pH 9.0), and incubated for 30 min. at 37°C. Nonconjugated chelate was removed by size exclusion chromatography using a PD10 column (GE Healthcare Life Sciences) and 0.9% sodium chloride/gentisic acid 5 mg/mL (pH 5.0) as eluent. Subsequently, Df-Bz-NCS-mAb (1 - 2 mg) was labeled with ^{89}Zr (37 - 250 MBq) in 0.25 M HEPES buffer (pH 7.0) at room temperature in a volume of 2 mL. Other pH values were obtained by adjusting the HEPES buffer to chosen pH values. Finally, ^{89}Zr-Df-Bz-NCS-mAb was purified by size exclusion chromatography (PD10 column) using 0.25 M sodium acetate/gentisic acid 5 mg/mL buffer (pH 5.5) or 0.9% sodium chloride/gentisic acid 5 mg/mL (pH 5.0) as the mobile phase.

Preparation of ^{89}Zr-Labeled N-sucDf-mAb

As reference to the new method for ^{89}Zr labeling, Df was also coupled to mAbs via the multi-step procedure as previously described by Verel et al. [5](Figure 1B). In short, the chelate Df was succinylated (N-sucDf), temporarily filled with stable iron [Fe(III)], and coupled to the lysine residues of the mAb (cU36 or cetuximab) by means of a tetrafluorophenol-N-sucDf ester. After removal of Fe(III) by transchelation to EDTA at 35°C, the premodified MAb was purified on a PD10 column. Approximately 1 N-sucDf moiety was coupled per mAb molecule. Subsequently, N-sucDf-mAb (1 - 2 mg) was labeled with ^{89}Zr (37 - 185 MBq) in 0.25 M HEPES buffer at pH 7.0. Finally, ^{89}Zr-N-

sucDf-mAb was purified on a PD10 column using 0.9% sodium chloride/gentisic acid 5 mg/mL (pH 5.0) or 0.25 M sodium acetate/gentisic acid 5 mg/mL buffer (pH 5.5) as the mobile phase.

Analyses

After each preparation of ^{89}Zr-labeled Df-Bz-NCS-mAb or N-sucDf-mAb, the conjugates were analyzed by instant thin-layer chromatography (ITLC) for radiolabeling efficiency and radiochemical purity, and by high performance liquid chromatography (HPLC) and sodium dodecyl sulfate-polyacrylamide gel electrophoresis (SDS-PAGE) followed by phosphor imager analyses for integrity, and by a cell-binding assay for immunoreactivity. ITLC analyses of ^{89}Zr-labeled N-sucDf-mAb or Df-Bz-NCS-mAb was performed on silica gel impregnated glass fibre sheets (Pall Corp., East Hills, NY). As the mobile phase, 0.02 M citrate buffer (pH 5.0) was used.

HPLC monitoring of the final products was performed on a Jasco HPLC system using a Superdex™ 200 10/300 GL size exclusion column (GE Healthcare Life Sciences). As eluent a mixture of 0.05 M sodium phosphate and 0.15 M sodium chloride (pH 6.8) was used at a flow rate of 0.5 mL/min. Electrophoresis was performed on a Phastgel System (GE Healthcare Life Sciences) using preformed 7.5% SDS-PAGE gels under non-reducing conditions.

The immunoreactivity was determined by measuring binding of ^{89}Zr-cU36, ^{89}Zr-cetuximab, or ^{89}Zr-rituximab (10000 cpm/mL) to a serial dilution of 0.2% glutaraldehyde-fixed 11B cells, or 2% paraformaldehyde-fixed A431, or Ramos cells, respectively, essentially as described by Lindmo et al. [20].

Determination of Chelate-to-mAb Ratio

The Df-Bz-NCS to mAb molar ratio was determined following a general method as described by Meares et al. [21]. In short, conjugates were labeled according to the aforementioned procedure with a known nanomolar excess of zirconium oxalate solution spiked with ^{89}Zr.

The degree of modification with Df-Bz-NCS was also characterized by electrospray ionization fourier transform mass spectrometry (FT-MS) analysis. For this purpose lysozym (14.3 kDa) was used as a model protein, because antibodies are more difficult to analyze by FT-MS due to their large size and variable glycosylation. Lysozym was purchased from Sigma-Aldrich. Lysozym (280 nmol; 5 mg/mL) was premodified with a three-fold molar excess of Df-Bz-NCS. The pre-modified lysozym was purified and desalted by extensive dialysis (Slide-A-Lyzer dialysis cassettes; Pierce biotechnology) against deionized water.

FT-MS was performed using a hybrid LTQ-FT mass spectrometer (ThermoFisher, Bremen, Germany). Dialyzed samples were diluted 10X and 100X giving an end concentration of 14 or 1.4 μM in 30% acetonitrile/0.1% formic acid for direct infusion. Diluted, modified protein (10 μL) was infused in the mass spectrometer using a Triversa nanomate chip-based nanospray interface (Advion, Ithaca, NY) operated at 1.4 keV. Spectra were acquired from 200-2000 Da at 100.000 resolution allowing observation of the 9^+, 10^+ and 11^+ charge states with isotopic resolution.

In Vitro Stability

For assessment of the in vitro stability of ^{89}Zr-Df-Bz-NCS-mAb in comparison with the reference conjugate ^{89}Zr-N-sucDf-mAb, two sets of experiments were performed. In a first set, labeled mAbs were stored at 4°C (storage and transportation conditions) and room temperature in 0.9% NaCl/gentisic acid 5 mg/mL or 0.25 M sodium acetate/gentisic acid 5 mg/mL. Final activity concentration was between 30 – 40 MBq/mL, specific activity was between 67 - 86 MBq/mg mAb. At various time points, aliquots were taken and analyzed by TLC, SDS-PAGE and HPLC.

In a second set, purified radiolabeled mAbs were added to freshly prepared human serum (1:4 v/v dilution; sodium azide added to 0.02%) at a final concentration of the radiolabeled conjugates of ~1.3 nmol/mL and ~45 MBq/mL. The samples were incubated at 37°C in a CO_2-enriched atmosphere (5% CO_2). At various time points, aliquots were taken and analyzed by TLC, SDS-PAGE, and HPLC.

Evaluation of In Vivo Biodistribution

For assessment of biodistribution and the in vivo stability of the new ^{89}Zr-Df-Bz-NCS-mAb conjugate in comparison with the established ^{89}Zr-N-sucDf–mAb conjugate, two sets of experiments were performed with nude mice bearing subcutaneously implanted human xenografts of the HNSCC line FaDu or the vulvar tumor line A431 at two lateral sides. In one experiment, the moderately internalizing cU36 mAb was tested, in the other the extensively internalizing mAb cetuximab [22]. Female mice (HSD:Athymic Nude-Foxn1^{nu}, 21-31 g; Harlan) were 8 to 10 weeks old at the time of the experiments. All animal experiments were done according to NIH Principles of Laboratory Animal Care and Dutch national law (“Wet op de dierproeven”, Stb 1985, 336).

In a first experiment, mice bearing FaDu xenografts (two groups of n=8) were injected intravenously (i.v.) with either ^{89}Zr-Df-Bz-NCS-cU36 (0.28 ± 0.01 MBq) or the reference compound ^{89}Zr-N-sucDf-cU36 (0.37 ± 0.01 MBq). Unlabeled mAb cU36 was

added to the injection mixture to bring the total mAb dose to 100 µg per mouse. At 72 and 144 h post injection, four mice of each group were anesthetized, bled, killed, and dissected. After blood, tumor, and normal tissues had been weighed, the amount of radioactivity in each sample was measured in a gamma counter. Radioactivity uptake was calculated as the percentage of the injected dose per gram of tissue (%ID/g).

In a second experiment, mice bearing A431 xenografts (two groups of n=16) were injected i.v. with either ^{89}Zr-Df-Bz-NCS-cetuximab (0.28 ± 0.01 MBq) or the reference compound ^{89}Zr-N-sucDf-cetuximab (0.37 ± 0.01 MBq). Unlabeled cetuximab was added to the injection mixture to bring the total mAb dose to 100 µg per mouse. At 24, 48, 72, and 120 h post injection, four mice of each group were anesthetized, bled, killed, and dissected, with further processing according to the above procedure.

PET Study

PET imaging was performed on a double-crystal-layer HRRT PET scanner (Siemens/CTI), a dedicated small animal and human brain scanner, as described earlier [13, 23]. FaDu xenograft-bearing nude mice (two groups of n=3) were anesthetized by inhalation of 2% isoflurane, injected with either 4.12 ± 0.04 MBq ^{89}Zr-Df-Bz-NCS-cU36 (~200 µg mAb) or 4.03 ± 0.09 MBq ^{89}Zr-N-sucDf-cU36 (~200 µg mAb) via the retroorbital plexus, and scanned at 72 h post injection.

Transmission scans for attenuation and scatter correction were routinely obtained with each scan in two-dimensional mode using a single point ^{137}Cs source. Three-dimensional emission scans were acquired in 64-bit list mode during 60 min using a 400-650 keV window. The 64-bit list mode file was first converted into a single-frame histogram using a span of 9, and subsequently reconstructed using a 3D ANW-OSEM reconstruction algorithm with 2 iterations and 16 subsets and a matrix size of 256x256, including corrections for normalization, decay and dead time. For visualization of the images, Amide's A Medical Imaging Data Examiner (AMIDE) was used, freely available for download online [24]. Immediately after the PET scan the animals were killed, blood, tumors, major organs and tissues were collected, weighed, and counted in a gamma-counter.

Statistical Analyses

Differences in tissue uptake between injected conjugates were statistically analyzed for each time point with SPSS 15.0 software using Student t-test for unpaired data. Two-sided significance levels were calculated and $P < 0.01$ was considered statistically significant.

Results

Preparation of ^{89}Zr-Df-Bz-NCS-mAb

^{89}Zr-Df-Bz-NCS-mAb was prepared according to the chemical route as shown in Figure 1A. First, Df-Bz-NCS is coupled to the lysine groups of a mAb. Conjugation conditions selected for this step comprised the addition of a 3-fold molar excess of Df-Bz-NCS to the mAb solution (13 - 66 nmol mAb), a reaction pH of 9.0, and incubation for 30 min. at 37°C. These conditions resulted in a reproducible chelate:mAb substitution ratio of about 1.5:1, irrespective cU36, cetuximab or rituximab was used, as assessed by trace labeling with ^{89}Zr in a standard solution of Zr-oxalate. To verify the results above, protein mass-spectrometry analysis was performed on Df-Bz-NCS conjugated to lysozym. This protein can easily be analyzed by FT-MS. The FT-MS method revealed a very similar substitution ratio as the radioactive method (Figure 2).

In the next step, Df-Bz-NCS-mAbs were labeled with ^{89}Zr in HEPES buffer (final concentration 0.25 M). After 60 min incubation at room temperature at pH 6.8 – 7.2, the amount of ^{89}Zr trans-chelated from oxalate to Df-Bz-NCS-mAb was always more than 85% (mean, 91.9 ± 4.6%). The time courses of ^{89}Zr-complexation of mAb cU36 conjugated with Df-Bz-NCS at different pH's are shown in Figure 3. Labeling efficiency was distinctly higher at pH 6.8 and 7.2 than at pH 6.0, 6.2 and 7.4.

Labeling of mAb cU36, cetuximab or rituximab modified with Df-Bz-NCS resulted in overall yields after purification of always >80% (mean, 87.0 ± 4.6%). The radiochemical purity was always >95% (mean, 97.5 ± 0.7%; determined with ITLC and confirmed by HPLC). The immunoreactive fraction of the different ^{89}Zr-Df-Bz-NCS-mAb preparations ranged from 84.1% to 96.8% at the highest cell concentration, and was similar to those of their ^{131}I-labeled counterparts (data not shown). HPLC and SDS-

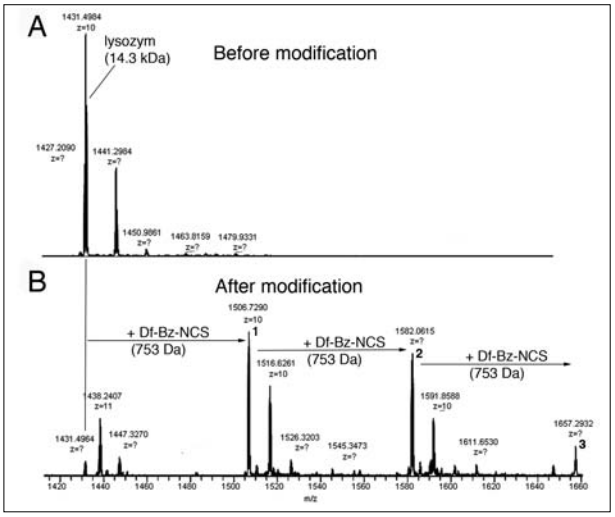

Figure 2. FT-MS analysis of lysozym before (A) and after modification with the bifunctional chelate Df-Bz-NCS (B). The peak at *m/z* 1431 is the unmodified lysozym. After modification, the mass of lysozym has increased by 753, 1506, 2258 Da corresponding to addition of 1, 2, or 3 Df-Bz-NCS chelates. On average 1.5 chelates were coupled per lysozym.

PAGE analyses revealed optimal integrity of the different mAbs after modification and labeling with ^{89}Zr (illustrated in reference 14).

Evaluation of the In Vitro Stability

^{89}Zr-labeled Df-Bz-NCS-mAb and *N*-sucDf-mAb conjugates were both stored in 0.9% NaCl/gentisic acid 5 mg/mL and in 0.25 M sodium acetate/gentisic acid 5 mg/mL at 4°C over several days to evaluate the *in vitro* stability. To anticipate effects of insufficient cooling, the conjugates were also analyzed after storage at room temperature (21°C). Storing the ^{89}Zr-Df-Bz-NCS-mAb conjugates in 0.25 M sodium acetate/gentisic acid 5 mg/mL buffer (pH 5.5) at 4°C gave the best results; only 0.9 ± 0.4% of the initially bound ^{89}Zr was dissociated from the mAb after 48 h, and 4.1 ± 1.3% after 144 h. Upon storage in the same buffer at room temperature (21°C), 6.1 ± 1.4% and 10.5 ± 2.1% was dissociated after 48 h and 144 h, respectively. Also upon storage in 0.9% NaCl/gentisic acid 5 mg/mL (pH 5.0) at 4°C the radioimmunoconjugates remained reasonably stable, showing 13.2 ± 2.8% dissociation after 144 h. However, storage in the same buffer at room temperature resulted in rapid release of radioactivity from the conjugate, 48.4 ± 5.7%. The corresponding ^{89}Zr-*N*-SucDf-mAb conjugates remained very stable, showing less than 5% release after 144 h under all conditions investigated.

The in vitro stability data for the ^{89}Zr-Df-Bz-NCS-cU36 and ^{89}Zr-*N*-sucDf-cU36 conjugates, when incubated in freshly prepared human serum at 37°C, showed that loss of ^{89}Zr from both conjugates over a 7 day period was very small. The percentages dissociated at day 3 were 2.3 ± 0.1% for the Df-Bz-NCS conjugate and 3.4 ± 0.6% for the *N*-sucDf conjugate, and at day 7 were 4.0 ± 0.6% for the Df-Bz-NCS conjugate and 4.7 ± 0.5% for the *N*-sucDf conjugate, respectively.

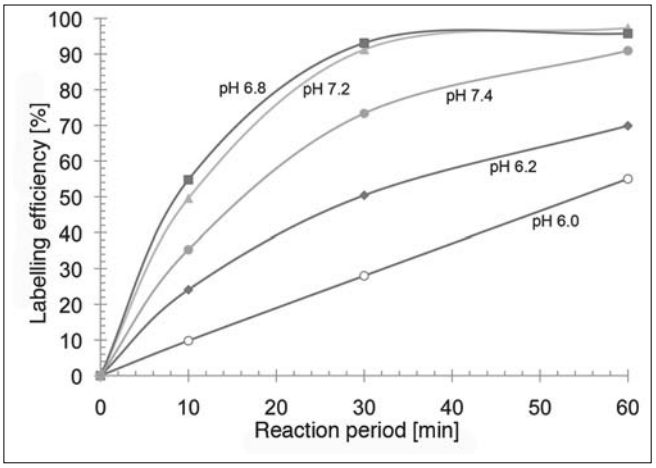

Figure 3. Time course of ^{89}Zr complexation of mAb cU36 conjugated with Df-Bz-NCS at different pH and at room temperature.

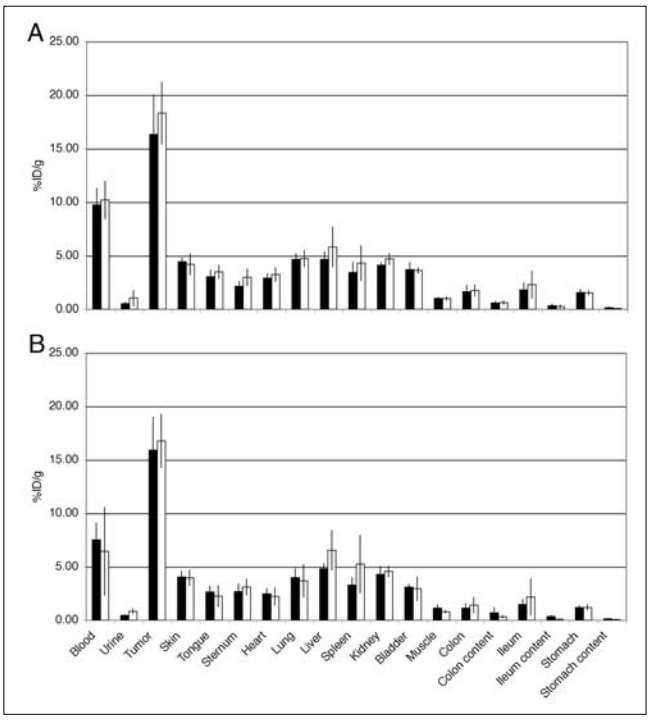

Figure 4. Biodistribution of ^{89}Zr-Df-Bz-NCS-cU36 (*black bars*) and ^{89}Zr-*N*-sucDf-cU36 (*white bars*) in FaDu tumor-bearing nude mice at 72 h (A) and 144 h (B) after injection. Total administered mAb dose: 100 µg. Mean (%ID/g) ± SD at each time point after injection (*n* = 4 animals per time point for each conjugate).

Evaluation of the In Vivo Biodistribution

Two sets of biodistribution studies were performed. In the first experiment, ^{89}Zr-Df-Bz-NCS-cU36 and the reference compound ^{89}Zr-*N*-sucDf-cU36 were injected into FaDu-bearing nude mice. At 72 and 144 h after injection, the average %ID/g of tumor, blood, normal tissue, and gastrointestinal contents was determined (Figure 4). No significant differences in the biodistribution of both conjugates were found.

Only a minor proportion of mAb cU36 internalizes after binding to its target antigen, therefore in the second biodistribution study the anti-EGFR mAb cetuximab was chosen because of the high rate of internalization. ^{89}Zr-Df-Bz-NCS-cetuximab and the reference compound ^{89}Zr-*N*-sucDf-cetuximab were injected into A431-bearing nude mice. At 24, 48, 72, and 120 h after injection, the average %ID/g of tumor, blood, normal tissue, and gastrointestinal contents was determined (Figure 5). The overall biodistribution of the two radioimmunoconjugates was very similar, showing no significant differences except for blood levels at 24 and 120 h after injection (Figure 5; significant differences (P<0.01) are indicated with an asterisk). The ^{89}Zr-Df-Bz-NCS-cetuximab tumor accumulation ranged from 15.6 ± 4.4 %ID/g to 23.1 ± 7.1 %ID/g and the ^{89}Zr-*N*-sucDf-cetuximab accumulation from 12.3 ± 3.2 %ID/g to 25.3 ± 6.1 %ID/g, in the time period between 24 and 120 h post injection.

PET Study

To exclude ^{89}Zr uptake in tissues not evaluated in the biodistribution experiments, a PET imaging study was performed. Representative PET images of FaDu xenograft-bearing nude mice at 72 hours after injection with ^{89}Zr-Df-Bz-NCS-cU36 or ^{89}Zr-*N*-sucDf-cU36 are shown in Figure 6A or 6B, respectively. Immuno-PET with both radioimmunoconjugates revealed clear delineation of the tumors (arrows), whereas no prominent uptake of radioactivity was observed in other tissues, except for the liver in which ^{89}Zr residualizes after catabolism of the conjugates.

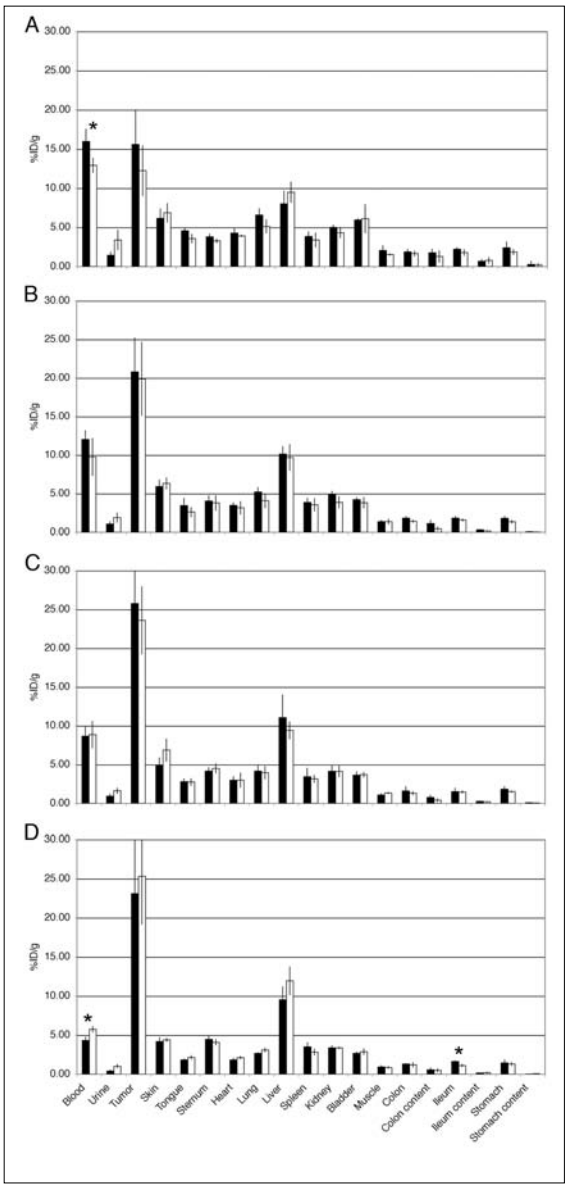

Figure 5. Biodistribution of ^{89}Zr-Df-Bz-NCS-cetuximab (*black bars*) and ^{89}Zr-*N*-sucDf-cetuximab (*white bars*) in A431 tumor-bearing nude mice at 24 h (A), 48 h (B), 72 h (C), and 120 h (D) after injection. Total administered mAb dose: 100 µg. Mean (%ID/g) ± SD at each time point after injection (n = 4 animals per time point for each conjugate). Significant differences (P < 0.01) in biodistribution between both radioimmunoconjugates are marked with an asterisk

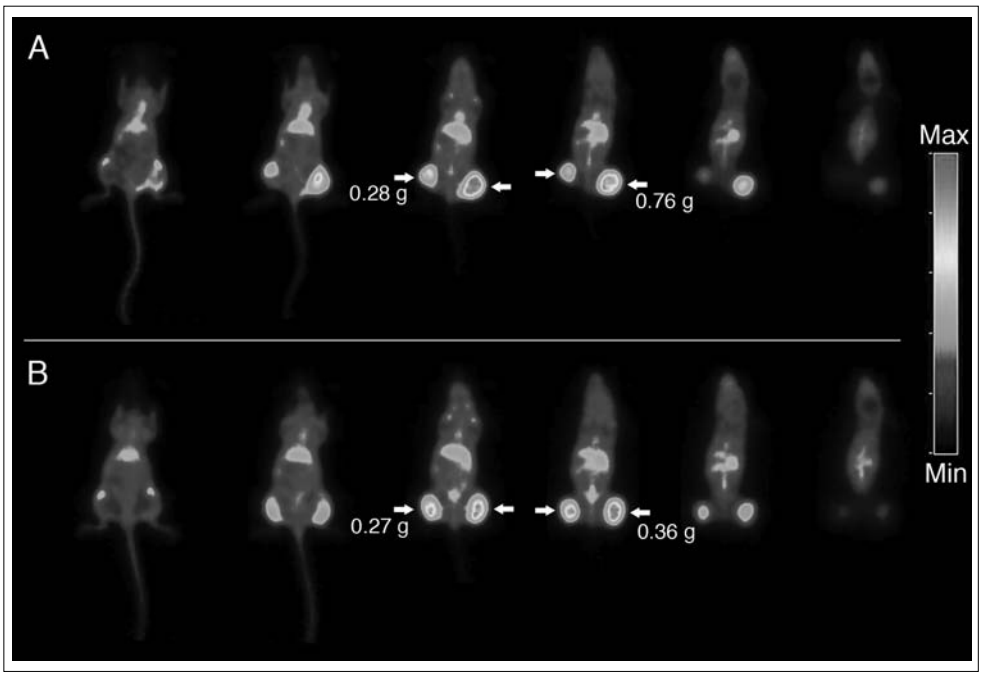

Figure 6. HRRT PET images (coronal slices) of two different FaDu xenograft bearing nude mice at 72 hours after injection with ^{89}Zr-Df-Bz-NCS-cU36 (A) or with ^{89}Zr-*N*-sucDf-cU36 (B). Slices from ventral (*left*) to dorsal (*right*). Images demonstrate high level of radiolabeled antibody accumulating in the tumor (Arrows point to flank tumors) and low levels of tracer uptake in nontarget tissues.

Discussion

Immuno-PET, the tracking and quantification of mAbs and mAb-fragments with PET *in vivo*, is an exciting novel option to improve diagnostics and to guide mAb-based therapy [2]. Availability of positron emitters with a proper half-life, sophisticated radiochemistry, and advanced animal as well as clinical PET and PET-CT scanners, is crucial in these developments.

In the present report, we have described a method for labeling mAbs with the long-lived positron emitter ^{89}Zr using the novel bifunctional chelate Df-Bz-NCS. ^{89}Zr has ideal characteristics for immuno-PET with intact mAbs, especially when these mAbs becomes internalized upon binding to their cellular target. Radioimmunoconjugates produced by this method were stable in storage buffer as well as in human serum *in vitro*. Biodistribution and imaging experiments showed high and selective accumulation in tumors in nude mice.

The chelate Df has frequently been used for radiolabeling of mAbs in the past, but these conjugates have never been evaluated clinically [25-28]. More recently, Verel *et al.* [5] developed a sophisticated method for stable coupling of ^{89}Zr to mAbs using a succinylated-derivative of Df, which was used as the reference method in the present study (Fig. 1B). ^{89}Zr-labeled mAbs prepared according to this method have been successfully tested preclinically and clinically [6-13]. In the past and ongoing clinical studies, neither adverse reactions nor significant changes in blood and urine values were observed after injection of these conjugates. Moreover, no antibody responses directed against the Df chelate were observed indicating that its immunogenicity is low [11]. These data illustrate that ^{89}Zr-labeled Df-mAbs can be used safely in patients. However, a shortcoming of the aforementioned method is that the multi-step procedure is relatively complicated and time consuming, and therefore challenging with respect GMP compliancy.

Recently, the commercial available *p*-isothiocyanatobenzyl-derivative of Df (Df-Bz-NCS) was introduced that might provide an efficient and rapid preparation of ^{89}Zr-labeled mAbs. Bifunctional chelates bearing isothiocyanate as the reactive group for conjugation to mAbs or other biologicals are frequently used [29]. The isothiocyanate group of the bifunctional chelate forms a thiourea bond with a primary amine of the protein or mAb.

Coupling of Df-Bz-NCS to mAbs was very efficient. A reproducible chelate:mAb substitution ratio of 1.5:1 was obtained in a typical conjugation reaction with several different mAbs using only a 3-fold molar excess of Df-Bz-NCS. The chelate:mAb substitution ratio was chosen to be kept below 2, since one cannot unlimitedly modify lysine groups without alteration of the pharmacokinetics and immunoreactivity of the mAb [30, 31].

The rate of complexation of ^{89}Zr into the Df-Bz-NCS conjugate was very similar as compared to the reference *N*-sucDf conjugate reported by Verel et al. [5], indicating that the different chemical linkages (e.g. =S instead of =O group in de side chain which might be involved in $^{89}Zr^{4+}$ coordination) have no influence on the complexation rate. At the pH-optimum, almost quantitative complexation was reached after 30 minutes at room temperature. The resulting radioimmunoconjugates showed no impairment of immunoreactivity and integrity of the mAb. Besides, Df-Bz-NCS can also be utilized to label proteins at room temperature with ^{68}Ga (not part of the current study) [14].

Radioimmunoconjugates were stored in various media to find the optimal conditions for storage and transportation over several days. The ^{89}Zr-Df-Bz-NCS-mAb can best be stored at 4°C in sodium acetate buffer in presence of the antioxidant gentisic acid. Under these conditions, only a minor portion of the initially bound ^{89}Zr was dissociated from the mAb after 144 h. The need for protection of the radioimmunoconjugate against radiation damage during storage has been shown in

previous studies [5, 32]. The presence of the antioxidant ascorbic acid during storage of high-dose ^{90}Y- or ^{131}I-labeled mAbs proved to be beneficial, however ascorbic acid cannot be used during storage of ^{89}Zr-labeled Df-mAbs, because this reagent causes detachment of ^{89}Zr from Df by reducing Zr^{4+} to Zr^{2+} [5].

In general, the new ^{89}Zr-Df-Bz-NCS conjugate, depending on the storage conditions applied, is slightly less stable than the reference radioimmunoconjugate. Especially, the presence of Cl^--ions in the storage buffer impaired the integrity of the radioimmunoconjugates, most likely due to the radiation-induced formation of OCl^--ions reacting with the SH-group of the enolized thiourea-unit. The thus formed intermediary sulphenyl chloride bonds, and sulphonyl chloride bonds arising upon further oxidation, are known to undergo a series of reactions, among which are coupling reactions and cleavage of methionyl peptide bonds. TLC data also indicated that most of the deterioration is not detachment of ^{89}Zr from the Df-chelate itself, but disruption of the Zr-Df unit.

The *in vitro* stability of the ^{89}Zr-Df-Bz-NCS conjugate and the ^{89}Zr-*N*-sucDf conjugate was also compared in freshly prepared human serum at 37°C. The stability of both conjugates under these conditions was very comparable and high, showing less than 4.7% release after a 7 days incubation period. Serum acts as a oxidisable scavenger and protects against directs hits of the mAb molecule, minimizing the radiation-induced deterioration of the mAb. Comparable *in vitro* stability data of ^{89}Zr-*N*-sucDf conjugates were previously reported by our group [22].

To investigate whether the new linker used for coupling of Df to the mAbs affects the biodistribution properties in mice, two sets of biodistribution experiments were performed. In the first experiment, the biodistribution of ^{89}Zr-Df-Bz-NCS-cU36 and the reference compound ^{89}Zr-*N*-sucDf-cU36 was compared in FaDu-bearing nude mice. In this model, no significant differences in the biodistribution between both conjugates were found. However, only a minor proportion of mAb cU36 internalizes after binding to its target antigen, therefore in the second biodistribution study the anti-EGFR mAb cetuximab was chosen because of the high rate of internalization [22]. Also in this model, a very similar biodistribution was found. Although, some significant differences were found, e.g. blood levels at 24 and 120 h after injection. Overall, both studies indicate that the different linkers used do not affect the biodistribution properties in nude mice. Moreover, none of the normal organs showed an adverse high uptake. Aforementioned results were confirmed in comparative immuno-PET studies with both chelates. PET images did not show accumulation of radioactivity in bone, which would have been indicative for free ^{89}Zr.

Conclusions

In the present study we evaluated the newly developed bifunctional chelate Df-Bz-NCS for radiolabeling of mAbs with ^{89}Zr for PET-imaging. The two-step procedure allows efficient and rapid preparation of ^{89}Zr-labeled mAbs. Resulting ^{89}Zr-Df-Bz-NCS-mAb conjugates appeared optimal with respect to radiochemical purity, integrity, and immunoreactivity. Furthermore, the radioimmunoconjugates were stable in serum *in vitro* and comparative biodistribution and imaging experiments showed high and selective accumulation in tumors in nude mice. Special emphasis should be given to the storage conditions. The recent commercialization of ^{89}Zr and the availability of an easy to use radiolabeling strategy using Df-Bz-NCS allow further exploration of ^{89}Zr-immuno-PET as an imaging tool for the selection of high potential candidate mAbs for therapy as well as for the selection of patients with the highest chance of benefit from mAb-based therapy [2].

Acknowledgements

This project was financially supported by the Dutch Technology Foundation (STW, grant VBC.6120). The authors thank the technical staff of BV Cyclotron VU and the Radionuclide Centre for supply and processing of ^{89}Zr, Sander Piersma and Connie Jimenez for FT-MS analyses, Marc Huisman for PET analyses, and Marijke Stigter-van Walsum for technical assistance with animal studies.

Addendum

See page 137 for a detailed protocol for labeling mAbs with ^{89}Zr or ^{68}Ga using the bifunctional chelate described in this chapter.

References

1. Carter PJ. Potent antibody therapeutics by design. Nat Rev Immunol 2006;6:343-57.
2. Van Dongen GAMS, Visser GWM, Lub-de Hooge MN, de Vries EG, Perk LR. Immuno-PET: a navigator in monoclonal antibody development and applications. Oncologist 2007;12:1379-89.
3. Nayak TK, Brechbiel MW. Radioimmunoimaging with longer-lived positron-emitting radionuclides: potentials and challenges. Bioconjug Chem 2009 Jan 6. [Epub ahead of print]
4. Wu AM. Antibodies and antimatter: the resurgence of immuno-PET. J Nucl Med 2009;50:2-5.
5. Verel I, Visser GWM, Boellaard R, Stigter-Van Walsum M, Snow GB, Van Dongen GAMS. Zr-89 immuno-PET: comprehensive procedures for the production of Zr-89-labeled monoclonal antibodies. J Nucl Med 2003;44:1271-81.
6. Verel I, Visser GWM, Boellaard R, Boerman OC, Van Eerd J, Snow GB, et al. Quantitative Zr-89 immuno-PET for in vivo scouting of Y-90-labeled monoclonal antibodies in xenograft-bearing nude mice. J Nucl Med 2003;44:1663-70.
7. Verel I, Visser GWM, Boerman OC, Van Eerd JEM, Finn R, Boellaard R, et al. Long-lived positron emitters zirconium-89 and iodine-124 for scouting of therapeutic radioimmunoconjugates with PET. Cancer Biother Radiopharm 2003;18:655-61.
8. Brouwers A, Verel I, Van Eerd J, Visser G, Steffens M, Oosterwijk E, et al. PET radioimmunoscintigraphy of renal cell cancer using ^{89}Zr-labeled cG250 monoclonal antibody in nude rats. Cancer Biother Radiopharm 2004;19:155-63.
9. Nagengast WB, de Vries EG, Hospers GA, Mulder NH, de Jong JR, Hollema H, et al. In vivo VEGF imaging with radiolabeled bevacizumab in a human ovarian tumor xenograft. J Nucl Med 2007;48:1313-9.
10. Dijkers E, Lub-de Hooge MN, Kosterink JG, Jager PL, Brouwers AH, Perk LR, et al. Characterization of ^{89}Zr-trastuzumab for clinical HER2 immunoPET imaging. J Clin Oncol 2007;25:3508S.
11. Borjesson PKE, Jauw YWS, Boellaard R, de Bree R, Comans EFI, Roos JC, et al. Performance of immuno-positron emission tomography with zirconium-89-labeled chimeric monoclonal antibody U36 in the detection of lymph node metastases in head and neck cancer patients. Clin Cancer Res 2006;12:2133-40.
12. Perk LR, Visser OJ, Stigter-Van Walsum M, Vosjan MJWD, Visser GWM, Zijlstra JM, et al. Preparation and evaluation of ^{89}Zr-Zevalin for monitoring of ^{90}Y-Zevalin biodistribution with positron emission tomography. Eur J Nucl Med Mol Imaging 2006;33:1337-45.
13. Perk LR, Stigter-van Walsum M, Visser GWM, Kloet RW, Vosjan MJWD, Leemans CR, et al. Quantitative PET imaging of Met-expressing human cancer xenografts with ^{89}Zr-labelled monoclonal antibody DN30. Eur J Nucl Med Mol Imaging 2008;35:1857-67.
14. Perk LR, Visser GWM, Budde M, Vosjan MJWD, Jurek P, Kiefer GE, et al. Facile radiolabeling of monoclonal antibodies and other proteins with zirconium-89 or gallium-68 for PET imaging using p-isothiocyanatobenzyl-desferrioxamine. Nat Prot 2008; DOI: 10.1038/nprot.2008.22.
15. Maecke HR, Hofmann M, Haberkorn U. ^{68}Ga-Labeled peptides in tumor imaging. J Nucl Med 2005;46:172S-8S.
16. Mendelsohn J, Baselga J. Status of epidermal growth factor receptor antagonists in the biology and treatment of cancer. J Clin Oncol 2003;21:2787-99.

17. Schrijvers AHGJ, Quak JJ, Uyterlinde AM, van Walsum M, Meijer CJLM, Snow GB, et al. MAb U36, a novel monoclonal antibody successful in immunotargeting of squamous cell carcinoma of the head and neck. Cancer Res 1993;53:4383-90.
18. Rangan SR. A new human cell line (FaDu) from a hypopharyngeal carcinoma. Cancer 1972;29:117-21.
19. Welters MJP, Fichtinger-Schepman AMJ, Baan RA, Hermsen MA, van d, V, Cloos J, et al. Relationship between the parameters cellular differentiation, doubling time and platinum accumulation and cisplatin sensitivity in a panel of head and neck cancer cell lines. Int J Cancer 1997;71:410-5.
20. Lindmo T, Boven E, Cuttitta F, Fedorko J, Bunn PA. Determination of the immunoreactive fraction of radiolabeled monoclonal-antibodies by linear extrapolation to binding at infinite antigen excess. J Immunol Methods 1984;72:77-89.
21. Meares CF, McCall MJ, Reardan DT, Goodwin DA, Diamanti CI, McTigue M. Conjugation of antibodies with bifunctional chelating agents: isothiocyanate and bromoacetamide reagents, methods of analysis, and subsequent addition of metal ions. Anal Biochem 1984;142:68-78.
22. Perk LR, Visser GWM, Vosjan MJWD, Stigter-Van Walsum M, Tijink BM, Leemans CR, et al. ^{89}Zr as a PET surrogate radioisotope for scouting biodistribution of the therapeutic radiometals ^{90}Y and ^{177}Lu in tumor-bearing nude mice after coupling to the internalizing antibody cetuximab. J Nucl Med 2005;46:1898-906.
23. De Jong HWAM, van Velden FHP, Kloet RW, Buijs FL, Boellaard R, Lammertsma AA. Performance evaluation of the ECAT HRRT: an LSO-LYSO double layer high resolution, high sensitivity scanner. Phys Med Biol 2007;52:1505-26.
24. Loening AM, Gambhir SS. AMIDE: a free software tool for multimodality image analysis. Mol Imaging 2003;2:131-7.
25. Yokoyama A, Ohmomo Y, Horiuchi K, Saji H, Tanaka H, Yamamoto K, et al. Deferoxamine, a promising bifunctional chelating agent for labeling proteins with gallium: Ga-67 DF-HSA: concise communication. J Nucl Med 1982;23:909-14.
26. Koizumi M, Endo K, Kunimatsu M, Sakahara H, Nakashima T, Kawamura Y, et al. ^{67}Ga-labeled antibodies for immunoscintigraphy and evaluation of tumor targeting of drug-antibody conjugates in mice. Cancer Res 1988;48:1189-94.
27. Pochon S, Buchegger F, Pelegrin A, Mach JP, Offord RE, Ryser JE, et al. A novel derivative of the chelon desferrioxamine for site-specific conjugation to antibodies. Int J Cancer 1989;43:1188-94.
28. Meijs WE, Haisma HJ, Klok RP, van Gog FB, Kievit E, Pinedo HM, et al. Zirconium-labeled monoclonal antibodies and their distribution in tumor- bearing nude mice. J Nucl Med 1997;38:112-8.
29. Liu S. Bifunctional coupling agents for radiolabeling of biomolecules and target-specific delivery of metallic radionuclides. Adv Drug Deliv Rev 2008;60:1347-70.
30. Van Gog FB, Visser GWM, Klok R, Van der Schors R, Snow GB, Van Dongen GAMS. Monoclonal antibodies labeled with rhenium-186 using the MAG3 chelate: relationship between the number of chelated groups and biodistribution characteristics. J Nucl Med 1996;37:352-62.
31. Kukis DL, DeNardo GL, DeNardo SJ, Mirick GR, Miers LA, Greiner DP, et al. Effect of the extent of chelate substitution on the immunoreactivity and biodistribution of 2IT-BAT-Lym-1 immunoconjugates. Cancer Res 1995;55:878-84.

32. Chakrabarti MC, Le N, Paik CH, De Graff WG, Carrasquillo JA. Prevention of radiolysis of monoclonal antibody during labeling. J Nucl Med 1996;37:1384-8.

ADDENDUM

Protocol: Facile radiolabeling of mAbs and other proteins with ^{89}Zr or ^{68}Ga for PET imaging using the bifunctional chelate *p*-isothiocyanatobenzyl-desferrioxamine

Lars R. Perk
Maria J. W. D. Vosjan
Gerard W. M. Visser
Marianne Budde
Paul Jurek
Garry E. Kiefer
Guus A. M. S. van Dongen

Nature Protocols 2008; DOI: 10.1038/nprot.2008.22 published online

Materials

Reagents

- Antibody or protein to be conjugated (typically 2-10 mg)
- p-isothiocyanatobenzyl-desferrioxamine (Df-Bz-NCS; Macrocyclics, cat. no. B-705; molecular weight=752.9 g/mol)
- Distilled, deionized water (Milli-Q; greater than 18 MΩ resistance)
- DMSO (Aldrich, cat. no. 494429)
- Sodium carbonate; 0.1 M and 2.0 M solutions in water (Aldrich, cat. no. 204420)
- Normal (0.9%) saline (B.Braun, cat. no. 5/12251178/1197)
- Gentisic acid (Fluka, cat. no. 37550)
- 0.9% NaCl/gentisic acid 5 mg/ml (pH = 4.9-5.3; see REAGENT SETUP)
- Oxalic acid; 1.0 M solution in water (Fluka, cat. no. 75688)
- HEPES buffer solution (Invitrogen, cat. no. 15630-049; see REAGENT SETUP)
- Sodium hydroxide (NaOH); 1.0 M solution in water (Riedel-de Haën, cat. no. 30620)
- Citric acid monohydrate (Fluka, cat. no. 27491)
- Hydrochloric acid (HCl), Trace SELECT Ultra; 30% (9.5 M), 0.1 M, 1.0 M and 4.0 M solutions in water (Fluka, cat. no. 96208)
- Ammonium acetate (Fluka, cat. no. 73594)
- Sodium acetate trihydrate (J.T. Baker, cat. no. 0256)
- 3.0 M and 0.25 M ammonium acetate buffer (see REAGENT SETUP)
- Sodium dihydrogen phosphate monohydrate (Merck, cat. no. 1.06346.0500)
- Disodium hydrogen phosphate anhydrous (Merck, cat. no. 1.06566.0100)
- Sodium chloride (Merck, cat. no. 1.06404.0500)
- Sodium azide (Merck, cat. no. 1.06688.0100) !CAUTION Highly toxic
- EDTA disodium salt (Sigma-Aldrich, cat. no. E1644)
- ITLC eluent (see REAGENT SETUP)
- HPLC eluent (see REAGENT SETUP)
- Zirconium-89 in 1.0 M oxalic acid (IBA molecular; www.iba.be/molecular)
- Gallium-68 (see EQUIPMENT)

!CAUTION: ^{89}Zr and ^{68}Ga are radionuclides emitting positrons and γ-radiations. ^{89}Zr and ^{68}Ga should be handled by following local radiation safety guidelines.

Equipment

- Calibrated pH meter
- Eppendorf tubes, Protein LoBind Tubes, 1.5 ml (Eppendorf, order no. 0030 108.116)
- Disposable PD-10 desalting columns (GE Healthcare Life Sciences, cat. no. 17-0851-01)
- Thermomixer comfort (Eppendorf, order no. 5355 000.011)
- Sterile/clean glass reaction vials, 20 ml
- Polystyrene round-bottom test tubes, 5 ml, snap cap (BD Falcon, cat. no. 352058)
- Silica gel impregnated glass fiber sheets (ITLC; Pall Corp., cat. no. 61886), approximately 1 × 12 cm in size with a faint pencil mark 1.5 cm from one end.

- SPE cartridge Chromafix 30-PS-HCO3 (Macherey-Nagel, cat. no. 731 876)
- High performance liquid chromatograph with a UV and a γ-detector connected in series
- HPLC column: SuperdexTM 200 10/300 GL (GE Healthcare Life Sciences, cat. no. 17-5175-01)
- 68Ge/68Ga-generator (Eckert & Ziegler Isotope Products)

Reagent Setup

- 0.9% NaCl/gentisic acid 5 mg/ml (pH = 4.9-5.3). Dissolve 0.5 g gentisic acid in 100 ml normal (0.9%) saline, add 0.88 ml 2.0 M sodium carbonate. Homogenise until no more CO_2 is formed (release pressure in bottle) and check pH. Acceptance range: pH 4.9-5.3.
- 0.25 M sodium acetate/gentisic acid 5 mg/ml (pH = 5.4-5.6). Dissolve 3.4 g sodium acetate (Mw 136.08 g/mol) in 100 ml Water for injection. Set the pH to 5.5 by adding concentrated H_2SO_4. Prepare a 100 mg/ml gentisic acid solution in water. Set the pH to 5.5 by adding 2.0 M Na_2CO_3. Add 1.75 ml 100 mg/ml gentisic acid solution to 50 ml 0.25 M sodium acetate solution and check the pH. Acceptance range: pH 5.4-5.6.
- 0.5 M HEPES buffer (pH = 7.1-7.3). Add 18 ml of water to 20 ml 1 M HEPES solution. Check pH. pH < 7.1 adjust pH with 1 M NaOH. pH > 7.3 adjust pH with 1 M HCl. Adjust volume to 40 ml with water.
- 0.25 M ammonium acetate buffer (pH = 5.4 – 5.6). Dissolve 9.64 g of ammonium acetate in 0.5 liter of water, add 1.4 ml 30% HCl. Mix well and check the pH. Acceptance range: pH 5.4-5.6.
- 3.0 M ammonium acetate buffer (pH = 7.1-7.3). Dissolve 11.6 g of ammonium acetate in 50 ml of water. Mix well and check the pH. Acceptance range: pH 7.1-7.3.
- ITLC eluent (pH = 4.8-5.0). Dissolve 420 mg citric acid monohydrate in 100 ml Milli-Q water, add 0.98 ml 2.0 M sodium carbonate. Mix well and check the pH. Acceptance range: pH 4.8-5.0.
- HPLC eluent (pH = 6.2-7.0). Dissolve 13.8 g of sodium dihydrogen phosphate monohydrate, 14.2 g of disodium hydrogen phosphate, 17.4 g of sodium chloride, and 1.3 g of sodium azide in 2 l of water. Mix well and check the pH. Acceptance range: pH 6.2-7.0. Pass the eluent through a Millipore filter and rigorously degas before use.

Procedure

This procedure may be scaled up or down, maintaining the same molar ratios of reagents.

Conjugation reaction

1. Pipette the required amount of protein solution (max. 1 ml; by preference between 2 and 10 mg/ml protein) into an eppendorf tube. Adjust the reaction mixture to a total volume of 1 ml by adding a sufficient amount of normal saline into the tube.
CRITICAL STEP Concentrations lower than 2 mg/ml will strongly decrease the efficiency of the conjugation reaction.

2. Adjust pH of the protein solution to pH = 8.9 – 9.1 with 0.1 M Na_2CO_3 (max. 0.1 ml).
CRITICAL STEP Alternatively, the desired pH for the reaction can be obtained by adding a stronger sodium carbonate buffer or by dialyzing the protein stock solution against 0.1 M sodium bicarbonate buffer (pH 9.0).

3. Dissolve Df-Bz-NCS in DMSO at a concentration of between 2 and 5 mM (1.5-3.8 mg/ml) depending on the amount of protein or antibody used. Add this to the protein solution to give a 3-fold molar excess of the chelator over the molar amount of protein and mix immediately. Keep the DMSO concentration below 5% in the reaction mixture.
CRITICAL STEP Typically, 20 µl 5 mM Df-Bz-NCS (100 nmol) in DMSO is added to 5 mg intact antibody (33 nmol). In that case, between 0.9-1.5 Df moieties will be coupled per antibody molecule.

4. Incubate the reaction for 30 min at 37°C using a Thermomixer.

5. This step can be performed using option A or option B depending on whether Df-conjugated proteins are radiolabeled with ^{89}Zr or ^{68}Ga, respectively.

A. Purification of Df-protein and subsequent labeling with ^{89}Zr.

i. Rinse a PD10 column with 20 ml 0.9% NaCl/gentisic acid 5 mg/ml (pH = 4.9-5.3).

ii. Pipette the conjugation reaction mixture onto the column and discard the flow-through.

iii. Pipette 1.5 ml 0.9% NaCl/gentisic acid 5 mg/ml (pH = 4.9-5.3) onto the column and discard the flow-through.

iv. Pipette 2 ml 0.9% NaCl/gentisic acid 5 mg/ml (pH = 4.9-5.3) onto the PD-10 column

and collect the Df-protein.

PAUSE POINT The Df-protein can be stored at -20°C until the day of planned use. The Df-protein should be stable in storage for at least several weeks.

v. Pipette the required volume (= a) of ^{89}Zr oxalic acid solution (max. 200 µl, between 37 and 185 MBq) into a glass "reaction vial".
!CAUTION Follow appropriate radiation safety measures for steps v. – xiii.

vi. While gently shaking, add 200 µl – _____(= a, see v.) = _____ µl 1M oxalic acid into the reaction vial. Subsequently, pipette 90 µl 2 M Na_2CO_3 into the reaction vial and incubate for 3 minutes at room temperature.

vii. While gently shaking, pipette successively 0.30 ml 0.5 M HEPES (pH = 7.2), 0.71 ml of modified protein (typically 1-3 mg), and 0.70 ml 0.5 M HEPES (pH = 7.2) into the reaction vial.
CRITICAL STEP The pH of the labeling reaction should be in the range of 6.8-7.2.

viii. Incubate for 1 h at room temperature while gently shaking the reaction mixture. Radiolabeling efficiency (typically >85%) can be determined by instant thin-layer chromatography (ITLC) using silica-gel strips and 20 mM citric acid (pH 4.8-5.0)(ITLC eluent) as solvent. A 0.5-2.0 µl aliquot of the reaction solution can be directly applied to the ITLC sheet. Radiolabeled protein (Rf = 0.0 - 0.1) and unbound ^{89}Zr (Rf = 0.4 – 1.0).

ix. Meanwhile, rinse a PD10 column with 20 ml 0.25 M sodium acetate/gentisic acid 5 mg/ml (pH = 5.4-5.6).

x. After 1 h incubation, pipette the reaction mixture onto the column and discard the flow-through.

xi. Pipette 1.5 ml 0.25 M sodium acetate/gentisic acid 5 mg/ml (pH = 5.4-5.6) onto the column and discard the flow-through.

xii. Pipette 2 ml 0.25 M sodium acetate/gentisic acid 5 mg/ml (pH = 5.4-5.6) to the PD-10 column and collect the purified radiolabeled protein.

xiii. Analyze the purified radiolabeled protein by ITLC and HPLC. When the radiochemical purity is greater than 95% it is ready for storage at 4 °C or dilution in

0.25 M sodium acetate/gentisic acid 5 mg/ml (pH = 5.4-5.6) for in vitro or in vivo studies. The radiolabeled protein should be stable in storage for at least several days.
CRITICAL STEP Gentisic acid is introduced during labeling and storage to prevent deterioration of the protein integrity by radiation. Consideration should also be given to assessment of the biological function of the protein after the conjugation and labeling reaction.

B. Purification of Df-protein and subsequent labeling with ^{68}Ga.
i. Rinse a PD10 column with 20 ml 0.25 M ammonium acetate (pH = 5.5).

ii. Pipette the conjugation reaction mixture onto the column and discard the flow-through.

iii. Pipette 1.5 ml 0.25 M ammonium acetate (pH = 5.5) onto the column and discard the flow-through.

iv. Pipette 2 ml 0.25 M ammonium acetate (pH = 5.5) onto the PD-10 column and collect the Df-protein.

PAUSE POINT The Df-protein can be stored at -20°C until the day of planned use. The Df-protein should be stable in storage for at least several weeks.

v. Pipette the required volume (= a) of preconcentrated and purified ^{68}Ga (max. 200 µl) into a 5 ml test tube. For preconcentration and purification of ^{68}Ga see Box 1.
!CAUTION Follow appropriate radiation safety measures for steps v. – xiii.

vi. While gently shaking, add 2 x _____(= a, see v.) = _____ µl 3 M ammonium acetate into the reaction vial and incubate for 3 minutes at room temperature.

vii. While gently shaking, slowly add 0.2-1.0 ml of the modified protein (typically 0.5-2 mg) into the reaction vial. Adjust the reaction mixture to a total volume of 1.5 ml by adding a sufficient amount of 0.25 M ammonium acetate (pH = 5.5) into the tube.
CRITICAL STEP The pH of the labeling reaction should be in the range of 5-6.

viii. Incubate for 5 min at room temperature while gently shaking the reaction mixture. Radiolabeling efficiency (typically >90%) can be determined by instant thin-layer chromatography (ITLC) using silica-gel strips and 20 mM citric acid (pH 4.8-5.0) containing 50 mM EDTA as solvent. A 0.5-2.0 µl aliquot of the reaction solution can be directly applied to the ITLC sheet. Radiolabeled protein (Rf = 0.0 - 0.1) and unreacted ^{68}Ga (Rf = 0.4 – 1.0).

ix. Meanwhile, rinse a PD10 column with 20 ml 0.25 M sodium acetate/gentisic acid 5 mg/ml (pH = 5.4-5.6).

x. After 5 min incubation, pipette the reaction mixture onto the column and discard the flow-through.

xi. Pipette 2.0 ml 0.25 M sodium acetate/gentisic acid 5 mg/ml (pH = 5.4-5.6) onto the column and discard the flow-through.

xii. Pipette 1.5 ml 0.25 M sodium acetate/gentisic acid 5 mg/ml (pH = 5.4-5.6) onto the PD-10 column and collect the purified radiolabeled protein.

xiii. Analyze the purified ^{68}Ga-labeled protein by ITLC and HPLC.

Time Taken

Steps 1-4: 45 min
Steps 5A i-iv: 15 min
Steps 5A v-xiii: 1.5 h
Steps 5B i-iv: 15 min
Steps 5B v-xiii: 20 min

BOX 1 Purification and concentration of the ^{68}Ga eluate using anion-exchange chromatography as described by Velikyan et al. [1].

1. Activate a Chromafix 30-PS-HCO_3 cartridge by washing with 1 ml 100% ethanol, 1 ml Milli-Q water, and 1 ml 4 M HCl, successively.
2. Elute the ^{68}Ge/^{68}Ga-generator with 0.1 M HCl according to the manufacturer protocol.
3. Collect the generator eluate and add enough 30% HCl giving a final HCl concentration of 4.0 M HCl.
4. Slowly load the generator eluate onto the activated Chromafix cartridge (flow rate of 0.5-1 ml/min). Discard the flow through.
5. Wash the cartridge with 2 ml 4 M HCl and subsequently dry by sucking air through the cartridge.
6. Elute with small fractions of Milli-Q water (50-100 µl). Collect the purified and concentrated ^{68}Ga and measure the activity.

Troubleshooting

Table 1. Troubleshooting table

PROBLEM	POSSIBLE REASONS	SOLUTION
Low labeling yield	Low conjugation efficiency; incorrect pH during labeling; contamination with metal ions; old/degraded Ge/Ga-generator	A higher molar excess of SCN-Bz-Df can be chosen in the conjugation reaction; removal of trace metal contamination (*2*)
mAb aggregation	Heterogenic mAb/Df ratio due to imperfect mixing; radiolysis	Ensure that the conjugation reaction mixture is stirred while adding the chelate; ensure that gentisic acid is added to the reaction buffers when indicated
Low radiochemical purity	Insufficient purification	Alternatively, ultrafiltration or dialysis can be applied in the purification step

References

1. Velikyan I, Beyer GJ, Langstrom B. Microwave-supported preparation of Ga-68 bioconjugates with high specific radioactivity. Bioconjug Chem 2004;15:554-60.
2. Wadas TJ, Anderson CJ. Radiolabeling of TETA- and CB-TE2A-conjugated peptides with copper-64. Nat Protoc 2006;1:3062-8.

CHAPTER 7

Summary, discussion, and future perspectives

Summary, Discussion, and Future Perspectives

Presently, hundreds of monoclonal antibodies (mAbs) and mAb fragments are under clinical development, because of their excellent potential for diagnosis and systemic treatment of cancer and other pathological conditions [1, 2]. To date, the US Food and Drugs Administration has approved 22 mAbs, 19 of which are intact immunoglobulins. The market for mAbs is the fastest-growing segment of the pharmaceutical industry. In 2007, therapeutic monoclonal antibodies brought in more than US$26 billion [3].

Despite clinical optimism, the efficacy of current mAbs is still quite limited, with benefit for just a portion of patients. Therefore, and since the costs of mAb therapy is excessive, the important question to be solved is: how to improve the efficacy of mAb-based therapy and how to identify patients with the highest chance of benefit. As discussed in **chapter 1**, quantitative imaging of mAbs can be a valuable tool to speed up and guide mAb drug development and to tailor therapy with existing mAbs by providing information regarding the expression status of cell surface targets. Apart from intact mAb molecules, interest in mAb-fragments and other small-protein scaffolds as a source of binding molecules for molecular targeting and imaging is growing [4].

Intact mAbs have a long residence time in humans ranging from a few days to weeks, which results in optimal tumor-to-nontumor ratios at 2-4 days post injection. Constructs lacking the immunoglobulin fragment crystalizable (Fc) region and having a lower molecular weight are cleared much more rapidly from the blood. This means that high-contrast images can be obtained within a few hours after tracer injection. The absolute tumor uptake, however, is often lower. These characteristics in general make intact mAbs the format of choice for therapy, while the optimal format for diagnosis is still under discussion. Whether fragments can be used for the selection of patients for therapy with intact mAbs remains to be seen, since the biodistribution and pharmacokinetic characteristics of both constructs might be totally different. In our view, the best way to predict the behavior of a therapeutic mAb is by using the same format and protein dose in the scouting imaging procedure as in therapy. Moreover, such approach requires just one pharmaceutical, thus reducing the costs of combined diagnosis and therapy.

Initial planar imaging and single photon emission tomography (SPECT) camera imaging studies with mAbs were very informative, however, there was still room for improvement. Compared to SPECT, positron emission tomography (PET) has a higher spatial resolution and sensitivity and the ability to quantitate the radioactivity uptake in tumor and normal organs. We foresee that PET imaging of antibodies (immuno-PET) can be a valuable tool at several stages of mAb development and clinical application: (1) To guide optimal use of approved mAbs, e.g. to select patients,

to assess the target expression status and to determine optimum dosages, and thereby minimize side effects. (2) As a scouting procedure prior to radioimmunotherapy (RIT) to perform dosimetry. In this setting, immuno-PET is particularly attractive, because of the small therapeutic window of RIT with bone marrow being dose limiting. (3) To guide first in man clinical trials with new mAbs, to learn about the ideal mAb dosing for optimal tumor targeting, to evaluate the uptake in critical normal organs to anticipate toxicity, and to assess the interpatient variations in pharmacokinetics and tumor targeting. mAb imaging might provide this information in an efficient and safe way. Stakeholders in this arena are physicians (who want to have patients treated in an optimal way), pharmaceutical companies (who want to have rapid and cheap drug development, and application of mAbs in the appropriate patient group), insurance companies and health care authorities (who want to have optimal efficacy of medicines, at minimum price) and first of all patient groups (who want to have highest probability for cure, at minimum morbidity).

Successful implementation of immuno-PET in mAb development and daily practice requires the steady supply of clinical grade positron-emitting radionuclides such as ^{68}Ga, ^{18}F, ^{64}Cu, ^{86}Y, ^{76}Br, ^{89}Zr and ^{124}I, efficient procedures for securely and stable coupling of these positron-emitting radionuclides to the targeting molecule in a Good Manufacturing Practice (GMP) compliant way, and advanced animal as well as clinical PET, PET-CT, or PET-MRI scanners. Therefore, we aimed to further implement immuno-PET in preclinical and clinical applications by describing procedures for the efficient production and processing of ^{68}Ga, ^{89}Zr, and ^{124}I, by stable coupling of these radionuclides to mAbs and mAb-fragments, and by performing proof of principle studies.

Tumor targeting using radiolabeled mAbs in RIT can be an attractive approach in cancer treatment. Currently, the U.S. Food and Drug Administration (FDA) has approved two RIT pharmaceuticals for the treatment of non-Hodgkin's lymphoma: the anti-CD20 mAbs ibritumomab tiuxetan (Zevalin™) and tositumomab (Bexxar™) labeled with the β^--emitters yttrium-90 (^{90}Y; $t_{1/2}$:64 hours) and iodine-131 (^{131}I; $t_{1/2}$: 192 hours), respectively. Besides ^{90}Y and ^{131}I, also lutetium-177 (^{177}Lu; $t_{1/2}$: 161 hours) is a commonly used β-emitter in RIT studies. The biodistribution of these radiolabeled therapeutic mAbs and others may be accurately predicted, and delivery of radiation dose to tumors and critical organs estimated, by performing an immuno-PET scouting procedure prior to RIT. A prerequisite for this approach is that the PET and RIT conjugates of the mAb of interest must provide similar radioactivity biodistributions, and therefore radionuclides (and if required chelates) with comparable chemical properties have to be chosen. Differences in radioactivity distribution might occur in several instances: when the mAb conjugates show altered and deviating pharmacokinetics (e.g. as a result of radiolabeling), when the radionuclide-chelate

complexes exhibit different in vivo stabilities, when the radionuclides show deviating redistributions after release from the conjugate or catabolism (e.g., after internalization of the radioimmunoconjugate by the tumor cell), or when combinations of these and possibly other factors occur.

In a preliminary study, it was shown that ^{89}Zr might be an excellent candidate to predict the distribution of ^{90}Y-labeled mAbs (Verel *et al*.). The combined used of ^{89}Zr-labeled mAbs with ^{90}Y-labeled mAbs is especially attractive, because ^{90}Y is a pure β-emitter lacking γ-emission for SPECT imaging. In **chapter 2**, we more thoroughly evaluated the potential of ^{89}Zr to predict the biodistribution of the residualizing radiometals ^{90}Y (^{88}Y was used as a γ-emitting substitute for ^{90}Y) as well as ^{177}Lu, when labeled to a mAb via the chelate *p*-SCN-Bz-DOTA or *p*-SCN-Bz-DTPA. Cetuximab was chosen as a model mAb because it abundantly internalizes after binding to the epidermal growth factor receptor (EGFR).

The different radiolabeling procedures did not result in impairment of the integrity or immunoreactivity of the mAb. Preceding the biodistribution studies, the in vitro stability of the different radioimmunoconjugates was analyzed in freshly prepared human serum. The stability of all conjugates was high and did not differ significantly up to 7 days of incubation in serum at 37°C. For easy comparison of the biodistributions, ^{89}Zr-*N*-sucDf-cetuximab was administered to tumor-bearing nude mice simultaneously with ^{88}Y-DOTA-cetuximab, ^{177}Lu-DOTA-cetuximab, ^{88}Y-DTPA-cetuximab, or ^{177}Lu-DTPA-cetuximab, respectively. ^{89}Zr-mAb tracer uptake in tumor, blood, and nontarget tissues was very similar to that of ^{88}Y/^{177}Lu-mAb, except for the thighbone and sternum showing a slightly higher accumulation of ^{89}Zr.

In **chapter 3**, the use of ^{89}Zr-immuno-PET as a scouting procedure prior to RIT was clinically implemented. In standard RIT with ^{90}Y-Zevalin™ a pretherapy SPECT imaging study with indium-111 (^{111}In; $t_{1/2}$: 67.3 h) is not strictly required, despite the fact that it had been part of the clinical trials leading to FDA approval of Zevalin™. However, in myeloablative RIT high doses of ^{90}Y are administered, and therefore guidance of these RIT studies with accurate dosimetry is higly desirable for prevention of unacceptable dose exposition to normal organs and for evaluation of dose-response relationships. As indicated earlier, immuno-PET is better suited than SPECT for tracer quantification.

As a potential PET-surrogate for ^{90}Y, the positron emitter ^{86}Y is receiving attention [5]. The use of the same element is advantageous, however, the half-life of ^{86}Y is rather short ($t_{1/2}$: 14.7 h) for predicting ^{90}Y dosimetry of slowly clearing mAbs. Therefore, the introduction of ^{89}Zr-Zevalin™-PET in high-dose myeloablative ^{90}Y-Zevalin™ RIT might be an attractive alternative for prediction of ^{90}Y-Zevalin™ biodistribution and dosimetry.

Since only MX-DTPA (tiuxetan) premodified ibritumomab was available for

clinical use, and DTPA does not complex the four-valent ^{89}Zr, *N*-sucDf was coupled as a second chelate to Zevalin™. Subsequent labeling of this modified conjugate with ^{89}Zr resulted in reproducible and good labeling yields while preserving the immunoreactivity and integrity of the mAb. ^{89}Zr-Zevalin™ could be stored at 4°C alone or formulated together with a clinical dose of ^{90}Y-Zevalin™ for at least 24 h without unacceptable loss of radiochemical purity and immunoreactivity.

To demonstrate that the newly developed double-chelator modified Zevalin™ labeled with ^{89}Zr can be used for localisation of ^{90}Y-Zevalin™, a biodistribution study was conducted in nude mice bearing Ramos B-cell lymphoma tumors. This study revealed that both radioimmunoconjugates have a very comparable distribution, showing high levels of radioactivity accumulating in tumors and low levels of tracer uptake in nontarget tissues. Although, there were some significant differences between ^{89}Zr-Zevalin™ and ^{90}Y-Zevalin™ uptake in liver and bone at later time points. A pilot PET imaging study with ^{89}Zr-Zevalin™ in a patient with CD20+ B-cell non-Hodgkin's lymphoma showed clear uptake of ^{89}Zr-Zevalin™ in all tumor lesions previously identified by [^{18}F]FDG-PET. ^{89}Zr-Zevalin™ seems well suited to predict ^{90}Y-Zevalin™ dosimetry. For prediction of dose delivery to bone marrow, ^{89}Zr-immuno-PET seems less suitable owing to differing bone uptake of ^{89}Zr and ^{90}Y.

On the basis of these encouraging findings, two clinical trials with ^{89}Zr-Zevalin™ and ^{89}Zr-rituximab as scouting procedure prior to RIT with ^{90}Y-Zevalin™ and ^{90}Y-rituximab, respectively, were recently started. Preliminary data indicated that the pharmacokinetic characteristics of corresponding ^{89}Zr-mAb and ^{90}Y-mAbs conjugates are identical.

Immuno-PET might have value for guidance of the optimal use of FDA approved mAbs, like cetuximab and ibritumomab tiuxetan in chapter 2 and 3, but also for in vivo characterization of new targeting ligands directed against novel critical tumor targets. Angiogenesis is one of the hallmarks of cancer [6], and therefore considerable efforts have been made recently to image as well as to eradicate tumor vasculature, preferably in a combined fashion. One approach aims the neutralization of growth factors and other angiogenic mediators involved in endothelial cell migration and proliferation. The potential of this approach is best exemplified by studies aiming the neutralization of vascular endothelial growth factor (VEGF) activity, either by capturing the growth factor itself or by blockage of its receptor [7, 8]. The neutralizing humanized anti-VEGF monoclonal antibody (mAb) bevacizumab (Avastin, Genentech) has recently been approved for use in combination with 5-fluorouracil-based chemotherapy as a first-line treatment for metastatic colorectal cancer [9]. A potential hurdle in neutralizing one critical pro-angiogenic factor is that the other redundant pro-angiogenic factors may compensate for the one that is inhibited.

Another approach is the targeted destruction of established tumor vasculature,

e.g. by mAbs directed against markers of angiogenesis [7, 8]. An interesting candidate target for this approach is the splice variant of fibronectin (FN) containing extra domain B (ED-B). FN is an extracellular matrix component that is widely expressed in a variety of normal tissues and body fluids [10]. Different FN isoforms can be generated by the alternative splicing of the FN-pre-mRNA, a process modulated by cytokines and extracellular pH [11]. The ED-B containing isoform of FN is immunohistochemically undetectable in normal adult tissue, with the exception of tissues undergoing physiological remodeling (e.g. endometrium and ovary) and during wound healing [12]. Furthermore, it has been demonstrated that ED-B is a marker of tumor angiogenesis [12]. ED-B is highly conserved in different species, having 100% homology in all mammalians thus far studied (human, rat, mouse). Recently, a human bivalent "small immunoprotein" directed against ED-B, designated L19-SIP, has been developed. L19-SIP is explored in several therapeutic approaches, including RIT with ^{131}I-L19-SIP [13].

^{76}Br and ^{124}I are promising candidate positron emitters for L19-SIP immuno-PET in combination with ^{131}I-L19-SIP RIT, however, availability of clinical grade material is a problem for both. In **chapter 4**, infrastructure and procedures were developed for efficient GMP-compliant production of large batches of ^{124}I (>2 GBq), and efficient ^{124}I-labeling of L19-SIP and other proteins. ^{124}I was produced using a biomedical cyclotron (IBA cyclone 18/9) by an (p,n)-reaction on highly enriched tellurium-124 (^{124}Te) dioxide. ^{124}I was isolated using a dry distillation process. The final product showed a high radionuclidic (>99.0%) and radiochemical (>95% as iodide) purity and a low tellurium (<1 μg/mL) and endotoxin (<1.5 EU/mL) content. As a result, clinical grade ^{124}I is now available for worldwide distribution, not only for immuno-PET applications but also for selection of patients with thyroid cancer for ^{131}I therapy (Figure 1).

Although labeling with radioiodine isotopes has been a widespread practice for decades, in several studies labeling yields were often suboptimal and the quality of the resulting ^{124}I-labeled mAbs did not always meet the quality standards required nowadays. L19-SIP was efficiently labeled with ^{124}I using a low amount of the mild oxidant IODO-GEN, and taking the I/mAb molar ratio and interference of radiolytic processes into account to arrive at optimal quality ^{124}I-L19-SIP conjugates, with preserved integrity and immunoreactivity. This was demonstrated with the aid of biodistribution studies and PET imaging studies in tumor-bearing nude mice. The biodistribution of ^{124}I-L19-SIP was fully concordant with ^{131}I-L19-SIP. Normal tissue accumulation of ^{124}I/^{131}I-L19-SIP was significantly lower than previously reported for ^{76}Br-L19-SIP [14]. As a result high tumor-to-normal tissue ratios were obtained with ^{124}I-L19-SIP, resulting in clear visualization of tumors by PET imaging, even when tumors were small (~50 mm^3).

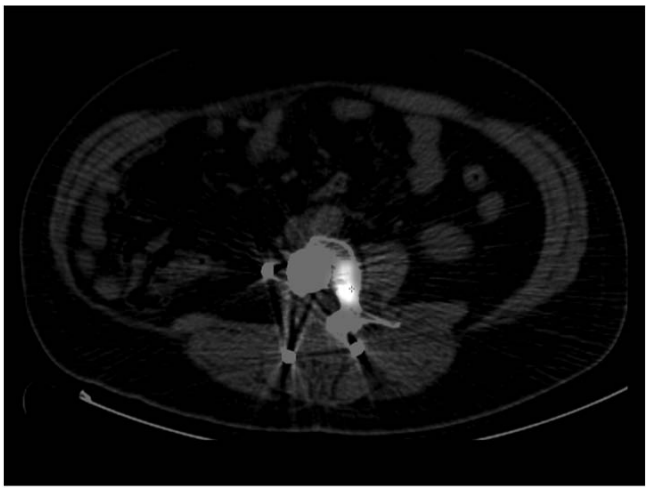

Figure 1. Patient with metastasized thyroid cancer. After extensive vertebral surgery and several treatments with ^{131}I, it remained unclear whether vital tumor tissue was still present. ^{124}I-PET-CT clearly shows iodine uptake (i.e. vital tumor) at the left side of the vertebra. Therefore, adjuvant high dose ^{131}I therapy is recommended for this patient.

To further illustrate the potential of immuno-PET for imaging the targeting of angiogenesis, outside the framework of this thesis also studies were performed with ^{89}Zr-bevacizumab [15]. These studies revealed that ^{89}Zr-bevacizumab could be used for in vivo VEGF visualization and quantification. Selective uptake of ^{89}Zr-bevacizumab in tumor blood vessels and its extracellular matrix was observed, presumably due to localization of large VEGF isoform. This data indicate that not only growth factor receptors can be imaged and quantitated by immuno-PET, but also the corresponding growth factors. This might shed new light on the physiological role of growth factors in tumor growth, and on strategies aiming the neutralization or the decreased synthesis of these growth factors.

Another appealing target in oncology is the *MET* oncogene, encoding the tyrosine kinase receptor (c-Met) for Hepatocyte Growth Factor (HGF), which controls genetic programs leading to cell growth, invasion, metastasis, and protection from apoptosis. The c-Met receptor is frequently overexpressed in tumors of many histotypes. Moreover, Engelman et al. recently showed that lung tumors can develop resistance to EGFR inhibitors as a result of amplification of the *MET* oncogene, while inhibition of Met signaling restored their sensitivity to EGFR inhibitors.

Recently, it was shown that the murine mAb DN30 directed against the extracellular domain of Met is able to promote receptor down-regulation and causes tumor growth inhibition *in vitro* and *in vivo* [16]. For optimal application of DN30 and other anti-Met mAbs in in vivo therapeutic approaches, it is important to learn about the ideal mAb dosing for optimal tumor targeting (e.g. saturation of receptors), the uptake in critical normal organs to anticipate toxicity, and the interpatient variations in pharmacokinetics and tumor targeting. The answer to these questions might be obtained by molecular imaging using PET.

In **Chapter 5**, we considered the potential of immuno-PET with either ^{89}Zr- (residualizing radionuclide) or ^{124}I- (non-residualizing radionuclide) labeled DN30 for imaging of Met expressing tumors. The biodistribution of coinjected ^{89}Zr-DN30 and ^{131}I-DN30 (^{131}I was used as a substitute for ^{124}I) was compared in GTL-16 xenograft bearing nude mice. GTL-16 cells have a high Met expression. In this model, tumor uptake was substantially higher for ^{89}Zr compared to ^{131}I at all time points, and almost four times higher at the latest time point (5 days p.i.). As a result, tumor-to-nontumor ratios were significantly better for ^{89}Zr-DN30. We concluded that ^{89}Zr is better suited for PET imaging with DN30 than ^{124}I. Using animal-PET with ^{89}Zr-DN30, GTL-16 tumors as small as 11 mg could be clearly visualized. Also tumors with low Met expression, like the head and neck squamous cell carcinoma xenograft line FaDu, could be clearly delineated with ^{89}Zr-DN30 immuno-PET. Moreover, an excellent correlation was found between PET-assessed tumor uptake and ex vivo assessed tumor uptake (R^2=0.98). Despite clear visualization of small tumors, ^{89}Zr-DN30 showed relatively high uptake in liver and spleen, especially when administered in low protein dose. A similar phenomenon was reported earlier with murine mAbs of the IgG_{2a} isotype. This phenomenon is related to the nude mouse model used, and is not expected to occur in patients.

For ^{89}Zr-immuno-PET imaging of mAbs, Verel *et al.* developed an elegant strategy for large scale production of highly pure ^{89}Zr as well as for the labeling of mAbs with ^{89}Zr via a multistep synthesis using a succinylated-derivative of desferrioxamine B (*N*-sucDf) [17]. The utility of this approach was clearly demonstrated in this thesis (chapter 2, 3, and 5) and by several other research groups in preclinical as well as clinical studies through high quality PET images showing selective tumor accumulation of ^{89}Zr-labeled mAbs [15, 18-21]. In these clinical studies, no abnormal accumulation of radioactivity at nontarget sites like liver, kidney or bone was observed. Also, no adverse reactions or significant changes in blood and urine values of the patients were observed after injections of these ^{89}Zr-*N*-sucDf-mAb conjugates. No antibody responses directed against the Df chelate were observed indicating that its immunogenicity is low [21]. However, the aforementioned multistep procedure is relatively complicated and time consuming, and therefore challenging with respect to Good Manufacturing Practice (GMP) compliancy. These are shortcomings for broad scale routine clinical application.

In **Chapter 6**, a novel *p*-isothiocyanatobenzyl-derivative of desferrioxamine B (Df-Bz-NCS) was introduced and fully chemically characterized. This bifuntional chelate (BFC) allows efficient and rapid preparation of ^{89}Zr-labeled mAbs. The two steps procedure comprises: (1) conjugation of the bifunctional Df-Bz-NCS chelate to a primary amine-group of a mAb or protein by forming a thiourea bond, (2) radiolabeling of the premodified mAb with ^{89}Zr at room temperature followed by

purification using gel filtration. A 3-fold molar excess of Df-Bz-NCS was chosen in the conjugation reaction to arrive at a chelate:mAb substitution ratio of 1.5:1. Almost quantitative complexation of ^{89}Zr was reached after 30 minutes of radiolabeling at pH 6.8 - 7.2 at room temperature. Resulting ^{89}Zr-Df-Bz-NCS-mAb conjugates appeared optimal with respect to radiochemical purity, integrity, and immunoreactivity.

Stability of both the ^{89}Zr-Df-Bz-NCS-mAb conjugate and the reference ^{89}Zr-*N*-sucDf-mAb conjugate was evaluated in different buffers and in serum. Both radioimmunoconjugates were stable in buffer when stored at 4°C and in human serum at 37°C for several days. Only when stored at room temperature, which is uncommon practice for biotech products, and especially in the presence of Cl^--ions in the storage buffer, the new ^{89}Zr-Df-Bz-NCS conjugate was less stable than the reference ^{89}Zr-*N*-sucDf-mAb conjugate. Comparative biodistribution and imaging experiments in two different nude mouse models showed high and selective accumulation in tumors in nude mice. Moreover, the biodistribution of the ^{89}Zr-Df-Bz-NCS-mAb conjugate and the reference ^{89}Zr-*N*-sucDf-mAb conjugate was very similar, indicating that the different linkers used do not affect the biodistribution properties in nude mice.

This new bifunctional chelate is now commercial available and can be produced on request in accordance with GMP regulation. Besides this new BFC, also highly pure ^{89}Zr has become commercially available. Alternate, the increased availability of ^{89}Zr and the less complex conjugation and radiolabeling scheme allow further implementation of ^{89}Zr-immuno-PET in preclinical and clinical research. In addition, Df-Bz-NCS can also be utilized to label proteins at room temperature with ^{68}Ga [22]. A practical protocol for labeling of mAbs with ^{89}Zr or ^{68}Ga via this new bifunctional chelate has been provided as an addendum to chapter 6.

In conclusion, clinical-grade ^{89}Zr and ^{124}I, and efficient radiolabeling methods to produce optimal quality radioimmunoconjugates have now become available. Other longer-lived positron emitters, like ^{64}Cu, will become commercially available for clinical studies in the near future. Alternative approaches involving pretargeted delivery of radionuclides have been shown to improve target-to-nontarget ratios [23]. Depending on the desired application, antibody, and mAb format, an appropriate selection between positron emitters and labeling strategies can be made for optimal use in immuno-PET. Major challenges remain the high radiation dose accompanied with an immuno-PET imaging procedure, which is especially a concern in non-oncology patients, and the loss of spatial resolution as a result of high-energy positrons. Technical developments in scanner technology and software will further improve PET sensitivity and resolution, allowing lower doses of injected radioactivity for comparable image quality and improved possibilities for facile quantification.

On the basis of the encouraging findings reported in this thesis and by others, several clinical trials have recently been started at different centers with ^{89}Zr-labeled mAbs, e.g. ^{89}Zr-trastuzumab, ^{89}Zr-cetuximab, ^{89}Zr-rituximab, ^{89}Zr-Zevalin™, and ^{89}Zr-bevacizumab [15, 20, 24, 25]. Preliminary data of these trials revealed excellent tumor visualization and high-resolution images. While the first ^{89}Zr-immuno-PET studies ever aimed the detection of lymph node metastases in head and neck cancer patients [21], next trials in head and neck cancer will be started shortly to evaluate some of the aforementioned therapeutic approaches. Among others, this will comprise the evaluation of mAbs capable of blocking EGF-EGFR or HGF-cMet signal transduction, or targeting tumor angiogenesis.

References

1. Carter PJ. Potent antibody therapeutics by design. Nat Rev Immunol 2006;6:343-57.
2. Reichert JM, Valge-Archer VE. Development trends for monoclonal antibody cancer therapeutics. Nat Rev Drug Discov 2007;6:349-56.
3. Ledford H. Monoclonal antibodies come of age. Nature 2008;455:437.
4. Wu AM. Antibodies and antimatter: the resurgence of immuno-PET. J Nucl Med 2009;50:2-5.
5. Schneider DW, Heitner T, Alicke B, Light DR, McLean K, Satozawa N, et al. In vivo biodistribution, PET imaging, and tumor accumulation of ^{86}Y- and ^{111}In-Antimindin/RG-1, engineered antibody fragments in LNCaP tumor-bearing nude mice. J Nucl Med 2009;50:435-43.
6. Hanahan D, Weinberg RA. The hallmarks of cancer. Cell 2000;100:57-70.
7. Brack SS, Dinkelborg LM, Neri D. Molecular targeting of angiogenesis for imaging and therapy. Eur J Nucl Med Mol Imaging 2004;31:1327-41.
8. Neri D, Bicknell R. Tumour vascular targeting. Nat Rev Cancer 2005;5:436-46.
9. Salesi N, Bossone G, Veltri E, Di CB, Marolla P, Pacetti U, et al. Clinical experience with bevacizumab in colorectal cancer. Anticancer Res 2005;25:3619-23.
10. Borsi L, Balza E, Bestagno M, Castellani P, Carnemolla B, Biro A, et al. Selective targeting of tumoral vasculature: comparison of different formats of an antibody (L19) to the ED-B domain of fibronectin. Int J Cancer 2002 ;102:75-85.
11. Ebbinghaus C, Scheuermann J, Neri D, Elia G. Diagnostic and therapeutic applications of recombinant antibodies: targeting the extra-domain B of fibronectin, a marker of tumor angiogenesis. Curr Pharm Des 2004;10:1537-49.
12. Castellani P, Viale G, Dorcaratto A, Nicolo G, Kaczmarek J, Querze G, et al. The fibronectin isoform containing the ED-B oncofetal domain: a marker of angiogenesis. Int J Cancer 1994;59:612-8.
13. Sauer S, Erba PA, Petrini M, et al. Expression of the oncofetal ED-B-containing fibronectin isoform in hematologic tumors enables ED-B-targeted ^{131}I-L19SIP radioimmunotherapy in Hodgkin lymphoma patients. Blood 2009;113:2265-74.

14. Rossin R, Berndorff D, Friebe M, Dinkelborg LM, Welch MJ. Small-animal PET of tumor angiogenesis using a ^{76}Br-labeled human recombinant antibody fragment to the ED-B Domain of fibronectin. J Nucl Med 2007;48:1172-9.
15. Nagengast WB, de Vries EG, Hospers GA, Mulder NH, de Jong JR, Hollema H, et al. In vivo VEGF imaging with radiolabeled bevacizumab in a human ovarian tumor xenograft. J Nucl Med 2007;48:1313-9.
16. Petrelli A, Circosta P, Granziero L, Mazzone M, Pisacane A, Fenoglio S, et al. Ab-induced ectodomain shedding mediates hepatocyte growth factor receptor down-regulation and hampers biological activity. Proc Natl Acad Sci USA 2006;103:5090-5.
17. Verel I, Visser GWM, Boellaard R, Stigter-Van Walsum M, Snow GB, Van Dongen GAMS. Zr-89 Immuno-PET: comprehensive procedures for the production of Zr-89-labeled monoclonal antibodies. J Nucl Med 2003;44:1271-81.
18. Verel I, Visser GWM, Boellaard R, Boerman OC, Van Eerd J, Snow GB, et al. Quantitative Zr-89 immuno-PET for in vivo scouting of Y-90-labeled monoclonal antibodies in xenograft-bearing nude mice. J Nucl Med 2003;44:1663-70.
19. Brouwers A, Verel I, Van Eerd J, Visser G, Steffens M, Oosterwijk E, et al. PET radioimmunoscintigraphy of renal cell cancer using 89Zr-labeled cG250 monoclonal antibody in nude rats. Cancer Biother Radiopharm 2004;19:155-63.
20. Aerts HJ, Dubois L, Perk L, Vermaelen P, Van Dongen GA, Wouters BG, et al. Disparity between in vivo EGFR expression and 89Zr-labeled cetuximab uptake assessed with PET. J Nucl Med 2009;50:123-31.
21. Borjesson PK, Jauw YW, Boellaard R, de Bree R, Comans EF, Roos JC, et al. Performance of immuno-positron emission tomography with zirconium-89-labeled chimeric monoclonal antibody U36 in the detection of lymph node metastases in head and neck cancer patients. Clin Cancer Res 2006;12:2133-40.
22. Perk LR, Visser GWM, Budde M, Vosjan MJWD, Jurek P, Kiefer GE, et al. Facile radiolabeling of monoclonal antibodies and other proteins with zirconium-89 or gallium-68 for PET imaging using p-isothiocyanatobenzyl-desferrioxamine. Nat Protoc 2008; DOI: 10.1038/nprot.2008.22.
23. Goldenberg DM, Sharkey RM, Paganelli G, Barbet J, Chatal JF. Antibody pretargeting advances cancer radioimmunodetection and radioimmunotherapy. J Clin Oncol 2006;24:823-34.
24. Dijkers ECF, Kosterink JGW, Rademaker AP, Perk LR, van Dongen GAMS, Bart J, et al. Development and Characterization of Clinical-Grade ^{89}Zr-Trastuzumab for HER2/*neu* ImmunoPET Imaging. J Nucl Med 2009;50:974-81.
25. Perk LR, Visser OJ, Stigter-Van Walsum M, Vosjan MJ, Visser GW, Zijlstra JM, et al. Preparation and evaluation of ^{89}Zr-Zevalin for monitoring of ^{90}Y-Zevalin biodistribution with positron emission tomography. Eur J Nucl Med Mol Imaging 2006;33:1337-45.

CHAPTER 8

Nederlandse samenvatting

Samenvatting

Tumor-selectieve monoklonale antilichamen (mAbs) zijn succesvol gebleken in de behandeling van kanker. Er wordt dan ook veel onderzoek gedaan naar nieuwe mAbs en mAb-fragmenten voor de diagnostiek en behandeling van kanker en andere ziekten [1, 2]. Op dit moment zijn er 22 mAbs goedgekeurd door de "US Food and Drugs Administration" (FDA), waarvan 19 intacte antilichamen. MAbs vormen aldus de snelst groeiende markt voor de farmaceutische industrie. In 2007 werd er wereldwijd voor 26 miljard dollar aan therapeutische mAbs verkocht [3].

Desalniettemin is de effectiviteit van de meeste mAbs beperkt; slechts een kleine groep patiënten heeft baat bij een behandeling met mAbs. Daarnaast is de behandeling met mAbs vaak erg duur. Het is dus belangrijk om de effectiviteit te verhogen en de juiste patiënten te selecteren voor behandeling met deze mAbs. Door aan mAbs radioactieve isotopen te koppelen kunnen deze met een camera zichtbaar gemaakt worden (scintigrafie), en hiermee ontstaat een nauwkeuriger inzicht in het gedrag van een mAb (**hoofdstuk 1**). Scintigrafie geeft inzicht in de distributie van het betreffende mAb in het lichaam en de expressie status van de receptor waartegen het mAb is gericht (Figuur 1).

Er wordt een drietal scintigrafie technieken onderscheiden, te weten planair met behulp van een gammacamera, 'single photon' emissie computer tomografie (SPECT) veelal met een meerkops gammacamera en positron emissie tomografie (PET) eveneens met een speciale camera, de PET-camera [4]. Eerdere studies met mAbs die radioactief gelabeld waren met technetium-99m (^{99m}Tc), wezen uit dat SPECT imaging net zo geschikt is voor tumordetectie als conventionele beeldvormende methoden als CT en MRI. Echter de detectie van kleine tumoren, het scherp afbeelden van grotere tumoren, en het kwantificeren van de hoeveelheid radioactief gelabeld mAb in tumoren en gezond weefsel bleek problematisch.

Bij PET past men radionucliden toe die positief geladen deeltjes (positronen) uitzenden, bijvoorbeeld fluor-18 (^{18}F), gallium-68 (^{68}Ga), zirkonium-89 (^{89}Zr) en jodium-124 (^{124}I). In het lichaam versmelt een positron met een elektron (annihilatie). De deeltjes worden daarbij omgezet in twee fotonen met een energie van 511 keV die onder een hoek van 180° het lichaam verlaten. Een PET-scanner bestaat uit een ring van detectoren, waarin fotonen alleen als informatief beschouwd worden in geval van gelijktijdige inslag in twee tegenover elkaar liggende detectoren (Figuur 1D). Doordat bij PET relatief veel meer fotonen daadwerkelijk de detectoren bereiken, levert dat een enorme winst op in detectiegevoeligheid in vergelijking met de gammacamera. Daardoor is de gevoeligheid van PET vele malen groter dan van SPECT en is de resolutie van ongeveer 5 mm hoger dan de resolutie van 1 tot 1,5 cm bij een gammacamera [4]. Bovendien kunnen met een PET scan kwantitatieve distributie gegevens verkregen worden.

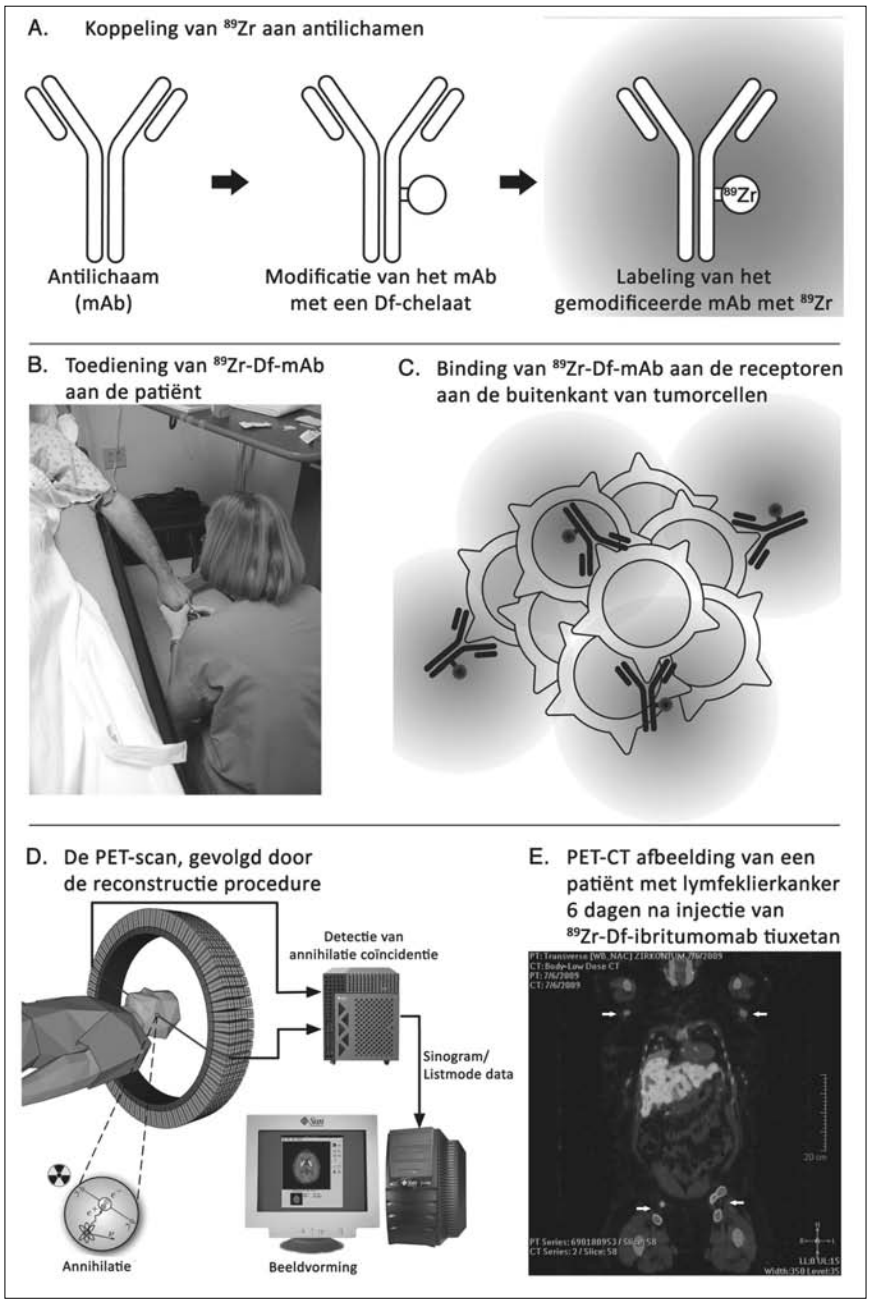

Figuur 1. Principe van een immuno-PET procedure. Dit schema toont de verschillende stappen in een immuno-PET procedure. (A) Koppeling van de positron emitter aan het mAb. (B) Toediening van het radioimmunoconjugaat aan de patiënt. (C) Binding van het radioimmunoconjugaat aan de tumor. (D) De patiënt wordt op verschillende tijdstippen na injectie gescand met behulp van een PET camera en de beelden worden softwarematig verwerkt. (E) De uiteindelijke PET-CT afbeelding van de patiënt. Zichtbaar zijn de tumoren in de lies en in de oksels (aangegeven met pijlen). Tevens zichtbaar, niet specifieke ophoping in de lever.

Wij voorzien dan ook dat PET imaging van mAbs en mAb-fragmenten gelabeld met een positron emitter (immuno-PET genoemd) kan bijdragen aan een versnelde ontwikkeling van (nieuwe) mAb therapieën door:

1. De effectiviteit van de huidige mAbs te vergroten, door de juiste patiënten te selecteren, de receptor expressie te bepalen, en de optimale therapeutische dosering vast te stellen. Hierdoor wordt de weg naar individualisering van behandeling geopend ("personalized medicine");
2. Het toepassen van immuno-PET als 'scouting' procedure voorafgaande aan therapie met radioactief gelabelde mAbs (radioimmunotherapie = RIT);
3. Het begeleiden van preklinische en fase I/II klinische studies met nieuwe mAbs. Hiermee kan op efficiënte wijze essentiële informatie worden verkregen over de farmacokinetiek en distributie van nieuwe mAbs.

Bovenstaande is niet alleen in het belang van artsen (voor de optimale behandeling van hun patiënten), farmaceutische bedrijven (voor efficiënte ontwikkeling van nieuwe medicatie), en verzekeraars en overheid (om de kosten van de gezondheidszorg laag te houden), maar vooral ook in het belang van patiënten die een optimale en effectieve therapie verwachten met weinig bijwerkingen.

Voor de succesvolle implementatie van immuno-PET in het dagelijks klinische gebruik en tijdens de ontwikkeling van nieuwe therapeutische antilichamen is de beschikbaarheid van hoge kwaliteit positron emitters, simpele en robuuste labelingmethoden om positron emitters aan mAbs te koppelen die voldoen aan de laatste GMP (goede manier van produceren) richtlijnen, en geavanceerde scanners essentieel. Behalve de beschikbaarheid van de positron emitter, is ook van belang dat de fysische halveringstijd ($T_{½}$) van de positron emitter overeenkomt met de verblijftijd van het geneesmiddel in het lichaam. Voor bovengenoemde mAbs is de verblijftijd enkele dagen tot weken. Er zijn in feite maar twee positron emitters die voor PET imaging van intacte mAbs in aanmerking komen, namelijk ^{89}Zr en ^{124}I met een halveringstijd van respectievelijk 78,4 en 100,3 uur. Het doel van dit proefschrift was dan ook het toepassen van immuno-PET in (pre)klinische studies te bevorderen door: (1) procedures te ontwikkelen voor een efficiënte productie van de positron emitters ^{89}Zr en ^{124}I; (2) het opzetten van robuuste methoden voor de koppeling van deze positron emitters aan mAbs en mAb fragmenten; (3) het uitvoeren van preklinische en klinische studies om de meerwaarde van immuno-PET aan te tonen ("proof of principle").

In diverse preklinische studies met tumordragende muizen werd de waarde van immuno-PET met ^{89}Zr- en ^{124}I-gelabelde mAbs geëvalueerd. Er werd onder andere gekeken of immuno-PET kan worden toegepast als scouting procedure voorafgaande aan radioimmunotherapie (RIT). Bij RIT worden therapeutische radionucliden aan het

mAb gekoppeld, en na injectie in de patiënt, door het mAb naar de tumor gebracht, waardoor deze selectief bestraald wordt. Meestal worden hiervoor de beta-emitters yttrium-90 (^{90}Y), jodium-131 (^{131}I) of lutetium-177 (^{177}Lu) gebruikt. Tot nu toe zijn twee RIT radiofarmaca goedgekeurd door de FDA, namelijk de anti-CD20 mAbs ^{90}Y-ibritumomab tiuxetan (Zevalin®) en ^{131}I-tositumomab (Bexxar®). Beiden worden toegepast bij de behandeling van lymfeklierkanker (met name het non-Hodgkin lymfoom). De verdeling van deze radioactief gelabelde mAbs in tumor, bloed en verschillende organen, en de stralingsafgifte die daaruit berekend kan worden (dosimetrie), kan wellicht goed bepaald worden met behulp van een immuno-PET scouting procedure vóór de eigenlijke RIT behandeling.

In een eerdere studie toonde Verel *et al*. [5] al aan dat de positron emitter ^{89}Zr een goede kandidaat kan zijn om de biodistributie van ^{90}Y-gelabelde mAbs te voorspellen. Dit is vooral interessant omdat ^{90}Y een pure beta emitter is die zelf geen gamma straling uitzendt, waardoor beeldvorming met behulp van een gammacamera of SPECT-camera niet mogelijk is. In **hoofdstuk 2** werd deze optie nader onderzocht door de *in vitro* en *in vivo* eigenschappen van ^{89}Zr-gelabelde mAbs te vergelijken met die van ^{88}Y- (^{88}Y als surrogaat voor ^{90}Y) en ^{177}Lu-gelabelde mAbs. Cetuximab werd als model mAb gebruikt, omdat het volledig wordt opgenomen (internalisatie) door de (tumor)cel na binding aan zijn aangrijpingspunt (target), in dit geval de epidermale groeifactor receptor (EGFR). Omdat ^{89}Zr, $^{88/90}$Y en ^{177}Lu niet rechtstreeks aan het mAb gekoppeld kunnen worden, werd gebruik gemaakt van verschillende typen chelaten. Voor ^{89}Zr was dat een variant van het chelaat desferrioxamine B (Df) en voor ^{88}Y en ^{177}Lu waren dat de chelaten DTPA of DOTA. De uiteindelijke radioimmunoconjugaten die werden vergeleken in deze studie waren ^{89}Zr-*N*-sucDf-cetuximab, ^{88}Y-DTPA-cetuximab, ^{177}Lu-DTPA-cetuximab, ^{88}Y-DOTA-cetuximab en ^{177}Lu-DOTA-cetuximab.

De immunoreactiviteit en integriteit van cetuximab bleef in alle gevallen behouden na koppeling van de chelaten en de daaropvolgende labeling met de desbetreffende radionucliden. Hierna werd de *in vitro* stabiliteit van de gelabelde mAbs vergeleken door deze te bewaren in humaan serum bij 37°C. Tot 7 dagen na de start van het experiment was de stabiliteit van alle conjugaten goed. De biodistributie van deze vijf radioimmunoconjugaten werd bepaald in tumordragende muizen door op diverse tijdstippen de verdeling van de radioactiviteit in tumor, bloed, urine en verschillende organen te meten. De biodistributie van de vijf conjugaten was in alle gevallen zeer vergelijkbaar, behalve de opname in bot (beenmerg), die voor ^{89}Zr licht verhoogd was t.o.v. de andere radionucliden. Dit bevestigt dat ^{89}Zr-gelabelde mAbs gebruikt kunnen worden voor bepaling/voorspelling van de biodistributie van ^{90}Y- en ^{177}Lu-gelabelde mAbs.

In **hoofdstuk 3** werd de (pre)klinische toepasbaarheid van ^{89}Zr-immuno-PET als scouting procedure voor ^{90}Y-mAb RIT nader onderzocht. Voorafgaand aan

radioimmunotherapie met ^{90}Y-ibritumomab tiuxetan wordt in de klinische praktijk soms een SPECT scan met behulp van indium-111 (^{111}In) uitgevoerd om patiënten met een ongewenste verdeling van ^{90}Y-ibritumomab tiuxetan uit te kunnen sluiten voor therapie. Met name bij hoge dosis radioimmunotherapie is het belangrijk om een goed beeld te krijgen van de biodistributie van het conjugaat om zodoende de stralingsdosis te kunnen vaststellen. Echter zoals al eerder aangegeven is PET hiervoor meer geschikt dan SPECT. Het doel van de studie beschreven in hoofdstuk 3 was dan ook het ontwikkelen van een klinisch toepasbaar ^{89}Zr-*N*-sucDf-ibritumomab tiuxetan conjugaat. Dit omvat het modificeren van het antilichaam, het optimaliseren van de labeling, het evalueren van de stabiliteit en immunoreactiviteit en het uitvoeren van een biodistributie studie in een muismodel.

Om ^{89}Zr stabiel te kunnen koppelen aan ibritumomab tiuxetan was het nodig om eerst het chelaat Df te koppelen aan het mAb. Het gemodificeerde mAb kon vervolgens efficiënt worden gelabeld met ^{89}Zr, wat resulteerde in radioimmunoconjugaten die hun immunoreactiviteit en integriteit hadden behouden. Het ^{89}Zr-*N*-sucDf-ibritumomab tiuxetan conjugaat, dat werd bewaard bij 4°C in de aanwezigheid van ^{90}Y-ibritumomab tiuxetan, bleef minstens 24 uur stabiel. De biodistributie van ^{89}Zr-*N*-sucDf-ibritumomab tiuxetan werd vergeleken met die van ^{90}Y-ibritumomab tiuxetan in naakte muizen met een geïmplanteerd humaan lymfoom op verschillende tijdstippen na injectie. De twee radioimmunoconjugaten vertoonden vergelijkbare opname in de tumor, bloed en andere organen, behalve in beenmerg en lever op latere tijdstippen. Vervolgens werd een pilot immuno-PET studie uitgevoerd in een patiënt met een CD20+ B-cel lymfoom. Deze pilot studie toonde aan dat ^{89}Zr-*N*-sucDf-ibritumomab tiuxetan selectief ophoopt in tumor laesies die eerder waren aangetoond met behulp van een [^{18}F]FDG PET scan (Figuur 1E). Op basis van deze resultaten werd geconcludeerd dat ^{89}Zr-*N*-sucDf-ibritumomab tiuxetan geschikt is voor het bepalen van ^{90}Y-ibritumomab tiuxetan biodistributie en dus voor verdere evaluatie in klinische studies. Inmiddels lopen er twee klinische studies (in het VUmc en in Brussel) waarbij ^{89}Zr-immuno-PET wordt toegepast als scouting procedure voorafgaande aan RIT met respectievelijk ^{90}Y-ibritumomab tiuxetan en ^{90}Y-rituximab.

Immuno-PET kan ook toegepast worden om een versnelde ontwikkeling van nieuwe mAbs en mAb fragmenten, al dan niet gericht tegen een nieuw niet-gevalideerd target, mogelijk te maken. Immuno-PET kan bijvoorbeeld informatie geven over de ideale dosering (bijv. receptor verzadiging), over de opname in kritische organen zodat geanticipeerd kan worden op toxiciteit, en over verschillen in farmacokinetiek en biodistributie tussen patiënten onderling. Immuno-PET kan hierbij een onderscheid maken tussen kansrijke en kansloze mAbs en zodoende bijdragen aan efficiëntere en daardoor goedkopere geneesmiddelenontwikkeling met minder patiënten in trials en toch meer informatie.

Targets voor mAb therapie die momenteel zeer in de belangstelling staan zijn moleculen die betrokken zijn bij de vorming van nieuwe bloedvaten (angiogenese) [6, 7]. Dit proces speelt een belangrijke rol bij de voedselvoorziening en aldus in het groeiproces van een tumor, en in het ontstaan van uitzaaiingen [8]. Één van deze nieuwe targets is "extra domain B" (ED-B) van fibronectine. Aangetoond is dat ED-B niet voorkomt op gezonde cellen in volwassenen, behalve bij vrouwen in het baarmoederhalsslijmvlies en in het ovarium tijdens de menstruatiecyclus, en dat het een specifieke marker is voor tumor angiogenese [9]. Recentelijk werd een mAb fragment ontwikkeld dat specifiek bindt aan ED-B [10]. Dit fragment, L19 "small immunoprotein" (L19-SIP), wordt op dit moment in verschillende klinische studies geëvalueerd, onder andere in een RIT studie met ^{131}I-gelabeld L19-SIP [11].

Voor het bepalen van de biodistributie van ^{131}I-L19-SIP met behulp van immuno-PET lijken twee positron emitters met name geschikt, broom-76 (^{76}Br) en ^{124}I. De beschikbaarheid van beide isotopen voor klinische studies is echter beperkt. In **hoofdstuk 4** worden daarom procedures beschreven voor een efficiënte productie van ^{124}I (>2 GBq) volgens de laatste GMP richtlijnen en voor een efficiënte labeling van L19-SIP en andere eiwitten met ^{124}I. ^{124}I werd geproduceerd met een 18 MeV cyclotron door middel van een (p,n)-reactie. Hierbij werd tellurium-124 (^{124}Te; 99,5 % verrijkt) dioxide beschoten met 12,5 MeV protonen. Met behulp van droge destillatie werd ^{124}I verkregen met een hoge radionuclidische (>99,0 %) en radiochemische (>95,0 % jodide) zuiverheid en met een lage verontreiniging van tellurium (<1 μg/ml) en endotoxinen (<1,5 EU/ml). ^{124}I voor humaan gebruik is nu wereldwijd beschikbaar, niet alleen voor immuno-PET studies, maar ook voor de diagnostiek en selectie van patiënten met of verdacht van recidief schildkliercarcinoom (in plaats van de huidige praktijk van 'blinde ^{131}I therapie' met haar bijwerkingen) (Figuur 2).

Hoewel labeling met jodium radioisotopen een algemeen toegepaste methode is, zijn de labelingopbrengsten in veel studies nog steeds suboptimaal en voldoet de kwaliteit van de resulterende ^{124}I-mAb conjugaten vaak niet aan de eisen die vandaag de dag gesteld worden. Door gebruik te maken van het milde oxidant IODO-GEN en door het toevoegen van carrier (^{127}I) aan het reactiemengsel, kon L19-SIP efficiënt worden gelabeld met ^{124}I met behoud van de integriteit en immunoreactiviteit van het mAb. Dit laatste werd aangetoond in biodistributie en PET-imaging studies in tumordragende muizen. De biodistributie van ^{124}I-L19-SIP kwam overeen met die van ^{131}I-L19-SIP, terwijl tumoren met een doorsnede van slechts enkele millimeters (>50 mm^3) konden worden afgebeeld.

Een ander target dat momenteel zeer in de belangstelling staat is de c-MET receptor. Deze receptor komt regelmatig tot overexpressie in verschillende typen tumoren, zoals darm-, long- en hoofd-halstumoren (http://www.vai.org/met). Recentelijk werd door de groep van Paolo Comoglio in Turijn een mAb ontwikkeld dat

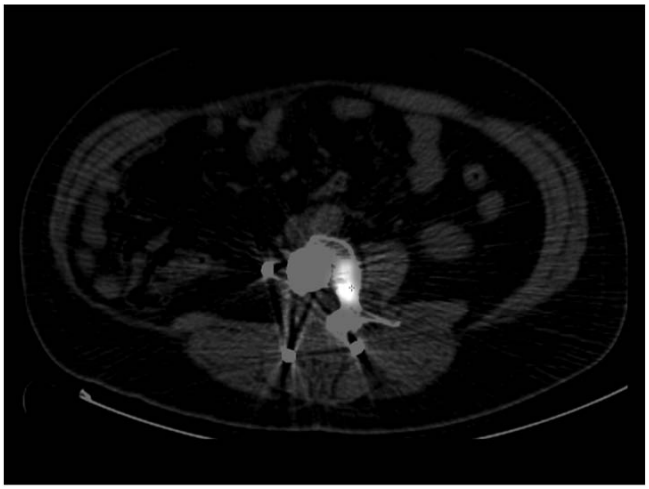

Figuur 2. Patiënt met een gemetastaseerd schildklier-carcinoom. Na uitgebreide wervelchirurgie en diverse behandelingen met radioactief jodium (^{131}I) was onduidelijk of er nog vitaal tumorweefsel aanwezig was. ^{124}I-PET-CT toont evidente jodium-opname (= tumor activiteit) links in een wervel. Er is dus een indicatie voor aanvullende hoge dosis therapie met ^{131}I.

specifiek bindt aan deze receptor. Behandeling met dit mAb (DN30 genaamd) resulteerde in substantiële groeiremming van tumoren, zowel *in vitro* als *in vivo* [12]. Om de stap naar de kliniek te versnellen hebben we in **hoofdstuk 5** een immuno-PET studie uitgevoerd om meer inzicht te krijgen in de biodistributie en farmacokinetiek van anti-c-MET mAbs, in het bijzonder mAb DN30. Om te kijken welk conjugaat het meest in aanmerking zou komen voor immuno-PET, werd eerst de biodistributie van ^{89}Zr-DN30 vergeleken met die van ^{131}I-DN30 (^{131}I als surrogaat voor ^{124}I) in GTL-16 xenograft dragende muizen. GTL-16 cellen hebben een hoge c-MET expressie. Tumor ophoping van ^{89}Zr-DN30 was vele malen hoger dan die van ^{131}I-DN30, resulterend in zeer gunstige tumor/non-tumor ratio's voor ^{89}Zr-DN30. Wij concludeerden dat ^{89}Zr geschikter is voor PET imaging met DN30 dan ^{124}I. De opname van ^{89}Zr-DN30 in tumoren kon uitstekend in beeld worden gebracht met behulp van de PET camera, zelfs kleine tumoren (11 mg) en tumoren met een lage c-MET expressie konden worden afgebeeld. Daarnaast werd een uitstekende correlatie (R^2=0,98) gevonden tussen de opname van ^{89}Zr in tumoren bepaald met behulp van PET imaging (niet-invasieve methode) en bepaald door het meten van radioactiviteit in uitgenomen tumoren met behulp van een gamma-teller (invasieve methode). Ondanks deze mooie resultaten was de ophoping van ^{89}Zr-DN30 in de lever en milt relatief hoog. Dit laatste is waarschijnlijk een gevolg van het gekozen muismodel in combinatie met het IgG_{2a} isotype van DN30. Naar verwachting zal een dergelijke ophoping bij patiënten niet plaatsvinden.

Om ^{89}Zr stabiel aan mAbs te kunnen koppelen heeft onze groep in 2003 een chemische route ontwikkeld gebruikmakend van een variant van het bifunctionele chelaat desferrioxamine B (Df). Het uiteindelijk conjugaat, dat na 6 chemische

stappen wordt verkregen, wordt aangeduid als ^{89}Zr-*N*-sucDf-mAb [13]. Deze procedure werd succesvol geëvalueerd en toegepast in diverse preklinische en klinische studies binnen en buiten het VU medisch centrum [5, 14-17]. Ondanks dit succes bleek deze methode tamelijk omslachtig voor grootschalige klinische implementatie. In **hoofdstuk 6** wordt een nieuw Df chelaat geïntroduceerd, gebruikmakend van een *p*-isothiocyanaatbenzyl groep als "linker". Met behulp van dit nieuwe Df-Bz-NCS chelaat kan ^{89}Zr in een tweestaps procedure gekoppeld worden aan mAbs en andere eiwitten. In stap 1 wordt een 3-voudige overmaat van het chelaat toegevoegd aan de reactie dit resulteert in een chelaat/mAb substitutie ratio van 1.5/1. Vervolgens wordt het gemodificeerde mAb gezuiverd met behulp van gelfiltratie. Het gemodificeerde mAb wordt in stap 2 gelabeld met ^{89}Zr en vervolgens gezuiverd. Onder optimale labelingcondities (pH tussen 6,8 – 7,2) kon bijna volledige inbouw van ^{89}Zr worden bereikt na 30 minuten incubatie bij kamertemperatuur. Dit resulteerde in ^{89}Zr-Df-Bz-NCS-mAb conjugaten die hun integriteit en immunoreactiviteit volledig behouden hadden. De *in vitro* stabiliteit van ^{89}Zr-Df-Bz-NCS-mAb conjugaten werd bepaald in verschillende buffers en in humaan serum. Deze nieuwe radioimmunoconjugaten bleken stabiel in verschillende buffers en in humaan serum gedurende 7 dagen, indien zij bewaard werden bij respectievelijk 4°C (in buffer) en 37°C (in serum). Vergeleken met ^{89}Zr-*N*-sucDf-mAb conjugaten, bleken ^{89}Zr-Df-Bz-NCS-mAb conjugaten minder stabiel indien bewaard bij 21°C in buffer. Het *in vivo* gedrag van ^{89}Zr-Df-Bz-NCS-mAb conjugaten werd geëvalueerd door middel van vergelijkende biodistributie en PET imaging studies in twee verschillende muismodellen. Uit beide studies bleek dat ^{89}Zr-Df-Bz-NCS-mAb conjugaten selectief ophopen in tumoren en dat de opname in bloed, urine en organen zeer vergelijkbaar is met die van de overeenkomstige ^{89}Zr-*N*-sucDf-mAb conjugaten.

Intussen is het nieuwe bifunctionele chelaat commercieel verkrijgbaar en op verzoek wordt het geproduceerd volgens GMP richtlijnen. Samenvattend: de verbeterde beschikbaarheid van ^{89}Zr en de simpelere chemie voor koppeling van ^{89}Zr aan mAbs maakt verdere implementatie van ^{89}Zr-immuno-PET in preklinisch en klinisch onderzoek mogelijk. Als een addendum aan hoofdstuk 6 is een praktisch protocol toegevoegd voor de koppeling van ^{89}Zr alsmede ^{68}Ga aan mAbs en mAb fragmenten met behulp van het nieuwe chelaat.

Concluderend: kwalitatief hoogwaardig ^{89}Zr en ^{124}I en efficiënte koppelingmethoden, resulterend in radioimmunoconjugaten met een optimale kwaliteit, zijn beschikbaar gekomen. In de nabije toekomst zullen andere langlevende positron emitters commercieel beschikbaar zijn voor klinisch gebruik, zoals koper-64 (^{64}Cu). Ook zijn er alternatieve methoden voor de koppeling van radionucliden aan eiwitten in ontwikkeling (i.e. "pretargeting"), resulterend in gunstige target/non-target ratio's

[18]. Afhankelijk van de toepassing, het mAb en het mAb formaat, kan een afgewogen keuze worden gemaakt tussen de beschikbare positron emitters en koppelingmethoden zodat een optimaal resultaat kan worden behaald met immuno-PET. Daarnaast zullen technische ontwikkelingen in scanner techniek en software de detectiegevoeligheid en resolutie van de PET-scanner verder verhogen.

Op basis van de resultaten beschreven in dit proefschrift en door anderen zijn er inmiddels verschillende klinische studies gestart met ^{89}Zr-gelabelde mAbs in verschillende centra, onder andere met ^{89}Zr-trastuzumab, ^{89}Zr-cetuximab, ^{89}Zr-rituximab, ^{89}Zr-ibritumomab tiuxetan en ^{89}Zr-bevacizumab [14, 16, 19, 20]. Daarnaast hebben een aantal toonaangevende farmaceutische bedrijven kenbaar gemaakt immuno-PET te willen implementeren in hun strategie voor efficiënte geneesmiddelenontwikkeling.

Referenties

1. Carter PJ. Potent antibody therapeutics by design. Nat Rev Immunol 2006;6:343-57.
2. Reichert JM, Valge-Archer VE. Development trends for monoclonal antibody cancer therapeutics. Nat Rev Drug Discov 2007;6:349-56.
3. Ledford H. Monoclonal antibodies come of age. Nature 2008;455:437.
4. Beeldvormende technieken binnen de kankerbestrijding. Vizier op de toekomst. Signaleringscommissie Kanker van KWF Kankerbestrijding: KWF kankerbestrijding; April 2005
5. Verel I, Visser GWM, Boellaard R, Boerman OC, Van Eerd J, Snow GB, et al. Quantitative Zr-89 immuno-PET for in vivo scouting of Y-90-labeled monoclonal antibodies in xenograft-bearing nude mice. J Nucl Med 2003;44:1663-70.
6. Brack SS, Dinkelborg LM, Neri D. Molecular targeting of angiogenesis for imaging and therapy. Eur J Nucl Med Mol Imaging 2004;31:1327-41.
7. Neri D, Bicknell R. Tumour vascular targeting. Nat Rev Cancer 2005;5:436-46.
8. Hanahan D, Weinberg RA. The hallmarks of cancer. Cell 2000;100:57-70.
9. Castellani P, Viale G, Dorcaratto A, Nicolo G, Kaczmarek J, Querze G, et al. The fibronectin isoform containing the ED-B oncofetal domain: a marker of angiogenesis. Int J Cancer 1994;59:612-8.
10. Borsi L, Balza E, Bestagno M, Castellani P, Carnemolla B, Biro A, et al. Selective targeting of tumoral vasculature: comparison of different formats of an antibody (L19) to the ED-B domain of fibronectin. Int J Cancer 2002 ;102:75-85.
11. Sauer S, Erba PA, Petrini M, et al. Expression of the oncofetal ED-B-containing fibronectin isoform in hematologic tumors enables ED-B-targeted ^{131}I-L19SIP radioimmunotherapy in Hodgkin lymphoma patients. Blood 2009;113:2265-74.
12. Petrelli A, Circosta P, Granziero L, Mazzone M, Pisacane A, Fenoglio S, et al. Ab-induced ectodomain shedding mediates hepatocyte growth factor receptor down-regulation and hampers biological activity. Proc Natl Acad Sci USA 2006;103:5090-5.

13. Verel I, Visser GWM, Boellaard R, Stigter-Van Walsum M, Snow GB, Van Dongen GAMS. Zr-89 Immuno-PET: comprehensive procedures for the production of Zr-89-labeled monoclonal antibodies. J Nucl Med 2003;44:1271-81.
14. Nagengast WB, de Vries EG, Hospers GA, Mulder NH, de Jong JR, Hollema H, et al. In vivo VEGF imaging with radiolabeled bevacizumab in a human ovarian tumor xenograft. J Nucl Med 2007;48:1313-9
15. Brouwers A, Verel I, Van Eerd J, Visser G, Steffens M, Oosterwijk E, et al. PET radioimmunoscintigraphy of renal cell cancer using 89Zr-labeled cG250 monoclonal antibody in nude rats. Cancer Biother Radiopharm 2004;19:155-63.
16. Aerts HJ, Dubois L, Perk L, Vermaelen P, Van Dongen GAMS, Wouters BG, et al. Disparity between in vivo EGFR expression and 89Zr-labeled cetuximab uptake assessed with PET. J Nucl Med 2009;50:123-31.
17. Borjesson PK, Jauw YW, Boellaard R, de Bree R, Comans EF, Roos JC, et al. Performance of immuno-positron emission tomography with zirconium-89-labeled chimeric monoclonal antibody U36 in the detection of lymph node metastases in head and neck cancer patients. Clin Cancer Res 2006;12:2133-40.
18. Goldenberg DM, Sharkey RM, Paganelli G, Barbet J, Chatal JF. Antibody pretargeting advances cancer radioimmunodetection and radioimmunotherapy. J Clin Oncol 2006;24:823-34.
19. Dijkers ECF**,** Kosterink JGW, Rademaker AP, Perk LR, van Dongen GAMS, Bart J, et al**.** Development and Characterization of Clinical-Grade ^{89}Zr-Trastuzumab for HER2/*neu* ImmunoPET Imaging**.** J Nucl Med 2009;50:974-81.
20. Perk LR, Visser OJ, Stigter-Van Walsum M, Vosjan MJ, Visser GW, Zijlstra JM, et al. Preparation and evaluation of ^{89}Zr-Zevalin for monitoring of ^{90}Y-Zevalin biodistribution with positron emission tomography. Eur J Nucl Med Mol Imaging 2006;33:1337-45.

APPENDICES

Curriculum vitae

Publications

Dankwoord

Color figures

Curriculum Vitae

De auteur van dit proefschrift werd in 1977 geboren in Sneek. Hij doorliep het Hoger Algemeen Voortgezet Onderwijs (HAVO) en het Voortgezet Wetenschappelijk Onderwijs (VWO) aan de RSG Magister Alvinus te Sneek, waar hij in 1997 VWO eindexamen deed. Datzelfde jaar startte hij met de studie Moleculaire Wetenschappen aan de Universiteit Wageningen. Tijdens zijn studie deed hij onderzoek naar de biosynthese route van het sesquiterpeen artemisinine onder begeleiding van dr. ir. H.J. Bouwmeester. Hierna liep hij stage aan de NTNU (Norges Teknisk-Naturvitenskapelige Universitet) te Trondheim in Noorwegen, met als stageonderwerp chemo-enzymatische synthese van (+)-goniothalamin. Het doctoraalexamen werd behaald in november 2002. In maart 2003 werd begonnen met het promotieonderzoek waarvan de resultaten zijn beschreven in dit proefschrift. Dit vond plaats op de afdeling Keel-, Neus-, en Oorheelkunde van de Vrije Universiteit Medisch Centrum te Amsterdam (hoofd prof. dr. C.R. Leemans) onder begeleiding van prof. dr. G.A.M.S. van Dongen, in samenwerking met de afdeling Nucleaire Geneeskunde & PET research onder begeleiding van dr. G.W.M. Visser. Sinds maart 2008 is hij werkzaam als R&D manager bij de BV Cyclotron VU.

Publications

Perk LR, Vosjan MJWD, Visser GWM, Budde M, Jurek P, Kiefer GE, van Dongen GAMS. *p*-Isothiocyanatobenzyl-desferrioxamine: a new bifunctional chelate for facile radiolabeling of monoclonal antibodies with zirconium-89 for immuno-PET imaging. Eur J Nucl Med Mol Imaging 2009; accepted.

Tijink BM, Perk LR, Budde M, Stigter-van Walsum M, Visser GWM, Kloet RW, Dinkelborg LM, Leemans CR, Neri D, van Dongen GAMS. ^{124}I-L19-SIP for immuno-PET imaging of tumour vasculature and guidance of ^{131}I-L19-SIP radioimmunotherapy. Eur J Nucl Med Mol Imaging 2009;36:1235-44.

Dijkers EC, Kosterink JG, Rademaker AP, Perk LR, van Dongen GAMS, Bart J, de Jong JR, de Vries EGE, Lub-de Hooge MN. Development and characterization of clinical-grade ^{89}Zr-trastuzumab for HER2/neu immunoPET imaging. J Nucl Med 2009;50:974-81.

Aerts HJ, Dubois L, Perk L, Vermaelen P, van Dongen GAMS, Wouters BG, Lambin P. Disparity between in vivo EGFR expression and ^{89}Zr-labeled cetuximab uptake assessed with PET. J Nucl Med 2009;50:123-31.

Perk LR, Stigter-van Walsum M, Visser GWM, Kloet RW, Vosjan MJWD, Leemans CR, Giaccone G, Albano R, Comoglio PM, van Dongen GAMS. Quantitative PET imaging of Met-expressing human cancer xenografts with ^{89}Zr-labelled monoclonal antibody DN30. Eur J Nucl Med Mol Imaging 2008;35:1857-67.

Van Dongen GAMS, Visser GWM, Lub-de Hooge MN, de Vries EGE, Perk LR. Immuno-PET: a navigator in antibody development and applications. Oncologist 2007;12:1379-89.

Nagengast WB, de Vries EGE, Hospers GA, Mulder NH, de Jong JR, Hollema H, Brouwers AH, van Dongen GAMS, Perk LR, Lub-de Hooge MN. In vivo VEGF imaging with radiolabeled bevacizumab in a human ovarian tumor xenograft. J Nucl Med 2007;48:1313-1319.

Perk LR, Visser OJ, Stigter-van Walsum M, Vosjan MJWD, Visser GWM, Zijlstra JM, Huijgens PC, van Dongen GAMS. Preparation and evaluation of ^{89}Zr-Zevalin for monitoring of ^{90}Y-Zevalin biodistribution with positron emission tomography. Eur J Nucl Med Mol Imaging 2006;33:1337-1345.

Visser OJ, Perk LR, Zijlstra JM, van Dongen GAMS, Huijgens PC, van de Loosdrecht AA. Radioimmunotherapy for indolent B-cell non-Hodgkin lymphoma in relapsed, refractory and transformed disease. BioDrugs 2006;20:201-207.

Perk LR, Visser GWM, Vosjan MJWD, Stigter-van Walsum M, Tijink BM, Leemans CR, van Dongen GAMS. ^{89}Zr as a PET surrogate radioisotope for scouting biodistribution of the therapeutic radiometals 90Y and 177Lu in tumorbearing nude mice after coupling to the internalizing antibody cetuximab. J Nucl Med 2005;46:1898-1906.

Bertea CM, Freije JR, van der Woude H, Verstappen FWA, Perk L, Marquez V, De Kraker JW, Posthumus MA, Jansen BJM, de Groot Æ, Franssen MCR, Bouwmeester HJ. Identification of intermediates and enzymes involved in the early steps of artemisinin biosynthesis in Artemisia annua. Planta Med 2005;71:40-47.

Sundby E, Perk L, Anthonsen T, Aasen AJ, Hansen TV. Synthesis of (+)-goniothalamin and its enantiomer by combination of lipase catalyzed resolution and alkene metathesis. Tetrahedron 2004;60:521-524.

Dankwoord

Eindelijk, het is af! Uiteraard was dit niet gelukt zonder de hulp van velen. Daarvoor wil ik graag een aantal mensen bedanken die mij gedurende de afgelopen jaren hebben ondersteund en geholpen.

Allereerst zou ik mijn beide promotoren willen bedanken. Prof. dr. G.A.M.S van Dongen, beste Guus, je enthousiasme is overweldigend, ook als de resultaten tegen zaten bleef je altijd positief. Ik heb veel van je geleerd en erg genoten van je brede kijk op de (wetenschappelijke) wereld. Ik hoop dat we in de toekomst nog veel mogen samenwerken. Prof. dr. C.R. Leemans, beste René, ook jou wil ik bedanken voor de samenwerking.

Ook wil ik mijn copromotor bedanken. Dr. G.W.M. Visser, beste Gerard, ik zal je scherpe blik op mijn onderzoeksresultaten en op mijn manuscripten missen. Zonder jou was dit promotieonderzoek de bietenbrug op gegaan!

De leden van de promotiecommissie, prof. dr. E.G.E. De Vries, prof. dr. P. Lambin, prof. dr. O.C. Boerman, prof. dr. O.S. Hoestra, prof. dr. H.M.W. Verheul en dr. N.H. Hendriksen, wil ik hartelijk bedanken voor de tijd en aandacht die zij aan mijn werk hebben besteed.

Maria, dank je wel voor je fantastische inzet. Een betere analist kun je je niet wensen. Ik ben blij dat jij mij als paranimf terzijde wilt staan. Heel veel succes gewenst met je eigen promotieonderzoek. Ook Marijke, Marianne en Liesbet bedankt! Jullie hulp bij alle opwerkingen, labelingen, analyses en biodistributie studies was onmisbaar.

Mijn kamergenoten van de AIO-kamer, door de jaren heen in wisselende samenstelling, dank voor alle gezelligheid. Serge, Hester en Bernard, met jullie heb ik het grootste deel van mijn promotieperiode gedeeld. Het was een super tijd! Hopelijk blijven we in de toekomst ook samen schaatsen, wielrennen of borrelen. Ook alle andere collega AIO's, Peggy, Géke, Lisa, Jantien, Tieneke, Pontus, Asaf, Sanne, Derrek en Marlon, ik wens jullie allen heel veel succes met de afronding van jullie eigen promotie.

Beste Boudewijn en Ruud, ik heb erg genoten van de gezamenlijke discussies. Jullie vormen samen met Guus een prachtig team. Ook dank aan alle andere toenmalige KNO tumorbiologie collega's, Arjen, Frederike, Michiel, Thijs, Marijke, Aafke. Ik mis de koffie met koekjes op het CCA nu al.

Alle medewerkers van de afdeling Nucleaire Geneeskunde & PET research wil ik bedanken voor hun inzet. In het bijzonder Leo en Arjan, zonder jullie was menig ^{89}Zr productie in het honderd gelopen. Het Radionucliden Centrum was als een tweede thuis. Ook de andere KNO-medewerkers op het RNC, Danielle en Annelies, bedankt voor de goede sfeer op Y2 en de nuttige tips tijdens de woensdagmiddagwerkbespreking. Ook Reina Kloet wil ik bedanken voor de vele PET reconstructies.

De medewerkers van de BV Cyclotron, mijn huidige collega's, bedankt voor het produceren van ^{89}Zr en ^{124}I. Door jullie inzet zijn beide isotopen nu commercieel verkrijgbaar.

Otto Visser en Josée Zijlstra, bedankt voor de leuke samenwerking. De mogelijkheid om met de patiënten in contact te komen heb ik erg gewaardeerd.

Mijn collega-onderzoekers uit het UMCG en het UMC St Radboud wil ik bedanken voor de plezierige en goede samenwerking. Het is leuk om te zien dat de positron emitters ^{89}Zr en ^{124}I ook een belangrijke plaats in jullie onderzoek hebben ingenomen.

Prof. dr. Paolo Comoglio, dr. Raffaella Albano, prof. dr. Giuseppe Giaccone, prof. dr. Garry Kiefer, dr. Paul Jurek, prof. dr. Dario Neri, and dr. Ludger Dinkelborg, thank you very much for the fruitful collaborations.

Tot slot wil ik mijn ouders, mijn broer, familie en vrienden bedanken voor hun steun en interesse. Lieve pap en mam, heel erg bedankt voor alle mogelijkheden en vertrouwen die jullie mij hebben gegeven. Ik hoop dat mijn lekenpraatje ook voor jullie verheldert waar ik de afgelopen jaren mee bezig ben geweest.

Lieve Esther, bedankt voor je liefdevolle steun en de nodige afleiding! Een dikke kus! Ook bedankt voor alle hulp bij het nakijken en corrigeren van dit proefschrift.

Color Figures

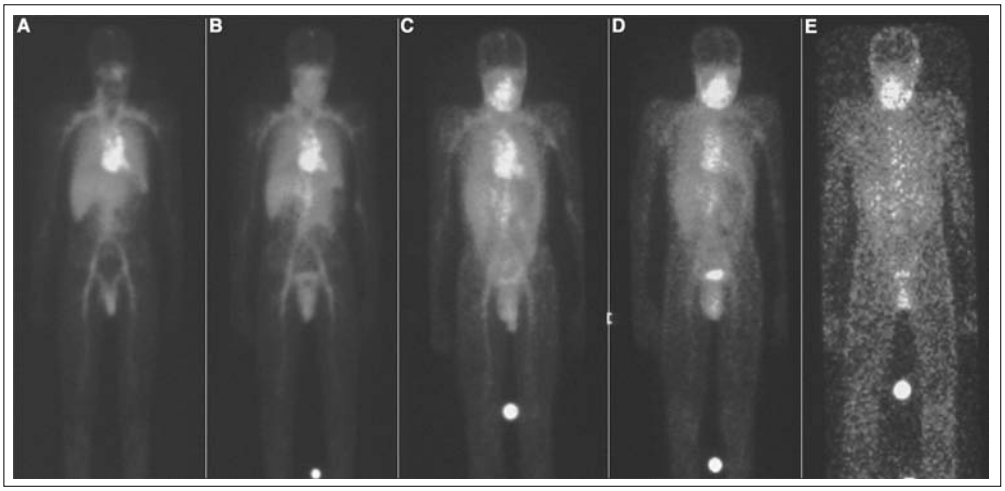

Figure 2. Planar whole body scans acquired 1 (A), 24 (B), 72 (C), 144 (D), and 312 hours (E) after administration of ^{186}Re-cmAb U36 to a patient with a tumor in the right oropharynx. Immediately after injection the mAb resides in the blood pool. Relative uptake of the radioimmunoconjugate in the tumor increases over time, while the tumor becomes better delineated as background activity decreases.

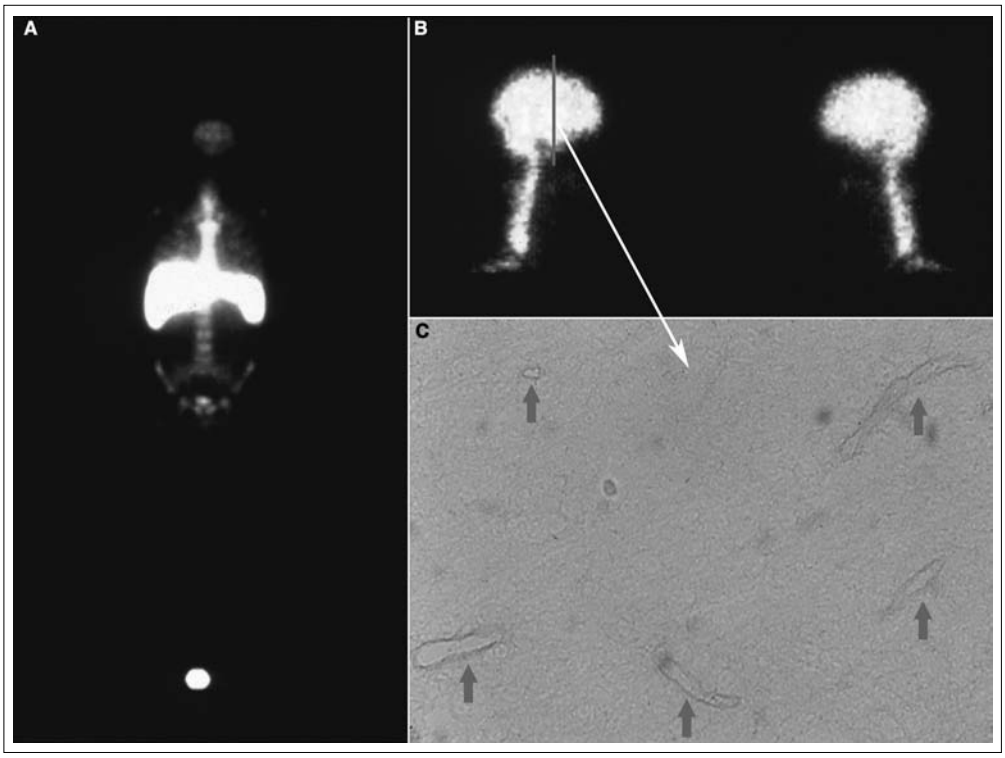

Figure 3. (A) Planar whole body scan acquired immediately after administration of ^{99m}Tc-cmAb SF25 to a patient with a primary tumor in the right tonsil. Note the extensive uptake in liver, spleen and bone marrow. No radioimmunoconjugate is left in the blood pool. (B) Planar right lateral image of the head and neck of the same patient 21 hours p.i., showing activity in the whole brain area. The primary tumor is not visualized. (C) Immunoperoxidase staining of brain tissue with cmAb SF25. There is distinct staining of endothelium of blood vessels.

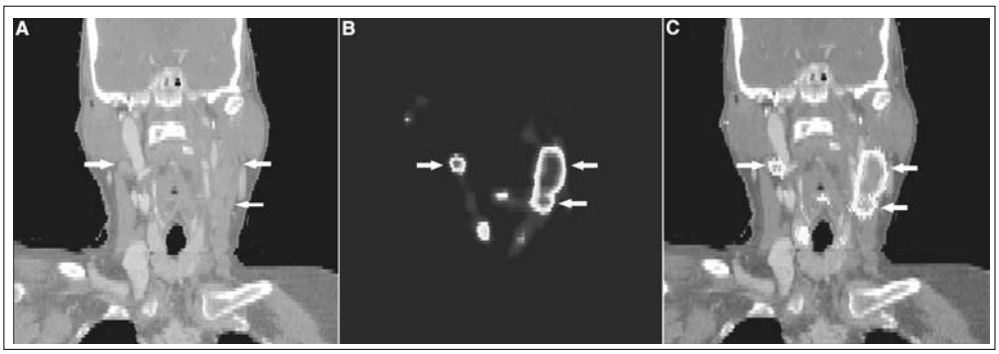

Figure 11. Fusion (C) of CT (A) and coronal immuno-PET (B) images with ^{89}Zr-cmAb U36 of a head and neck cancer patient with a tumor in the left tonsil and lymph node metastases (small arrows) at the left (level II and III) and right (level II) side of the neck. Images were obtained 72 hours p.i.. In these slices, only the lymph node metastases are visible.

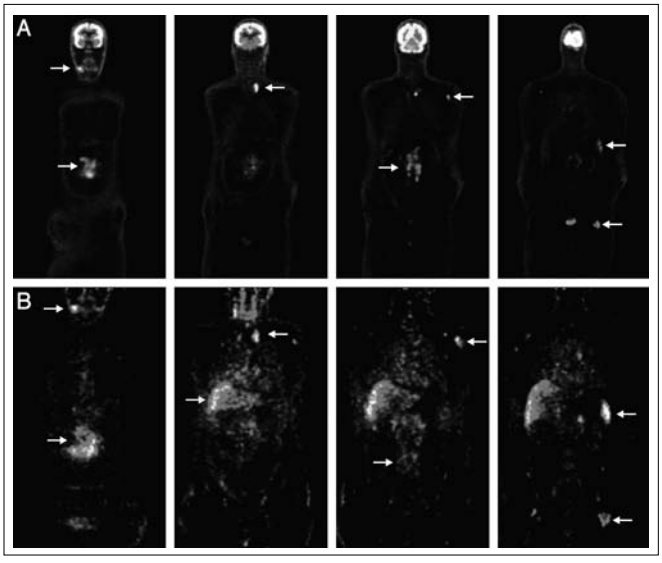

Figure 3. (A) [^{18}F]FDG-PET scan of the NHL patient. Coronal images from anterior (left) to posterior (right), with visualization of cervical, mediastinal, left caput humeri, splenic, para-aortic and inguinal lymphomas. Localizations are indicated by white arrows. (B) ^{89}Zr-Zevalin immuno-PET scan 96 h p.i. of the same NHL patient. Coronal images from anterior (left) to posterior (right); slices correspond to those of the [^{18}F]FDG-PET scan. Tumor localizations are indicated by white arrows. Note targeting of tumor localizations also visualized by [^{18}F]FDG-PET. Liver uptake (yellow arrow) is probably due to retention of ^{89}Zr after catabolism of the conjugate.

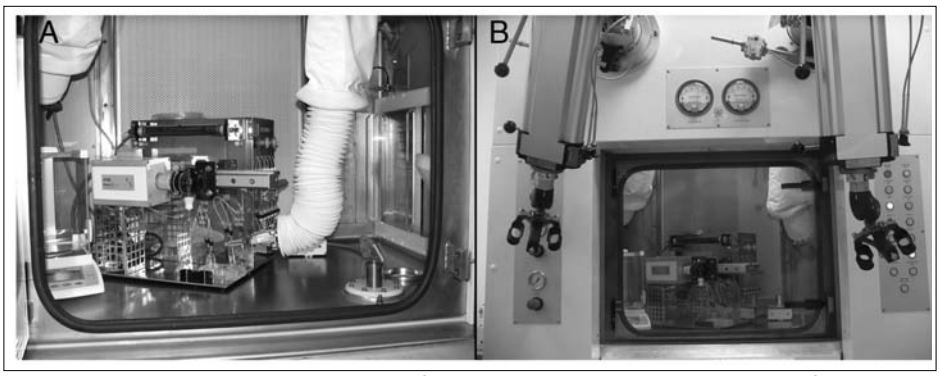

Figure 1. GMP compliant harvesting of ^{124}I. A TERIMO module for harvesting ^{124}I from the target disc by dry distillation (A) is localized in a hot-cell (B) integrated in a clean room meeting GMP conditions (GMP grade C).

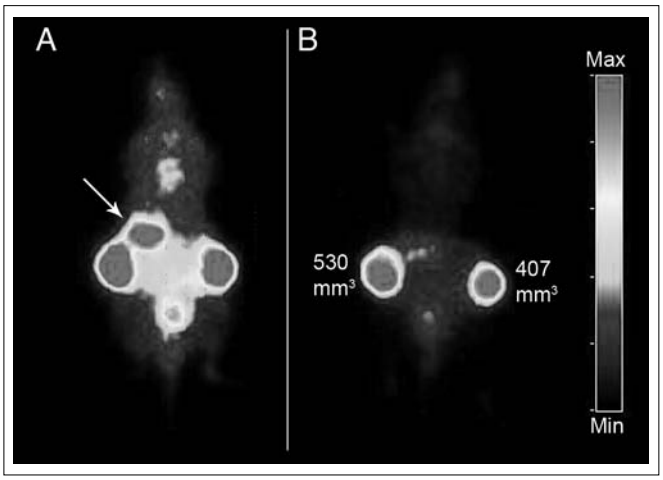

Figure 5. PET images of FaDu xenograft bearing nude mouse injected with ^{124}I-L19-SIP (3.7 MBq, 25 µg). Coronal images were acquired at 24 (A) and 48 h (B) after injection. Image planes have been chosen where both tumors were visible. Uptake of ^{124}I in the stomach (arrow) and to some extend in bladder (urine) is visible at 24 h p.i., but has disappeared at 48 h p.i.

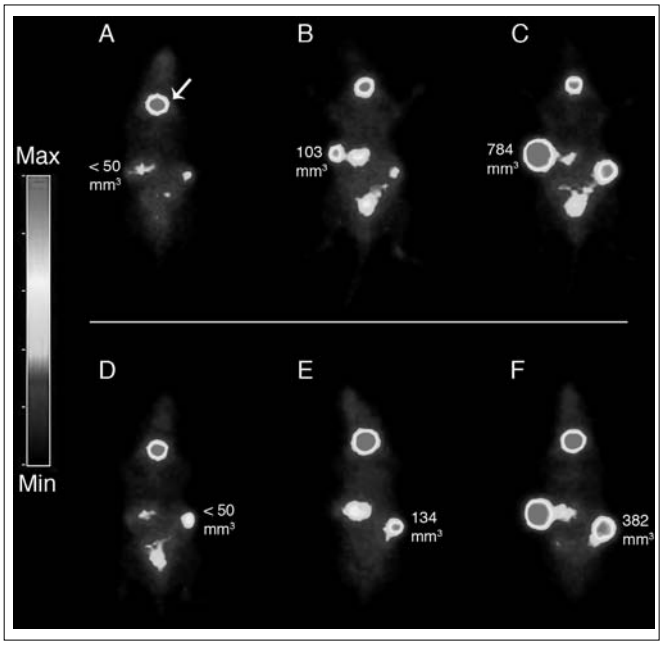

Figure 6. Serial PET images of FaDu xenograft bearing nude mouse injected with ^{124}I-L19-SIP (3.7 MBq, 25 µg). At 1 (A, D), 2 (B, E) and 3 (C, F) weeks after tumor implantation ^{124}I-L19-SIP was administered, and 48 h later coronal images were acquired. Image planes have been chosen where the left tumor (upper panel, A, B, C) or right tumor (lower panel, D, E, F is optimally visible. In contrast to Fig. 5, the thyroid (arrow) is visible because this organ was not blocked by potassium iodide in this experiment.

Chapter 5

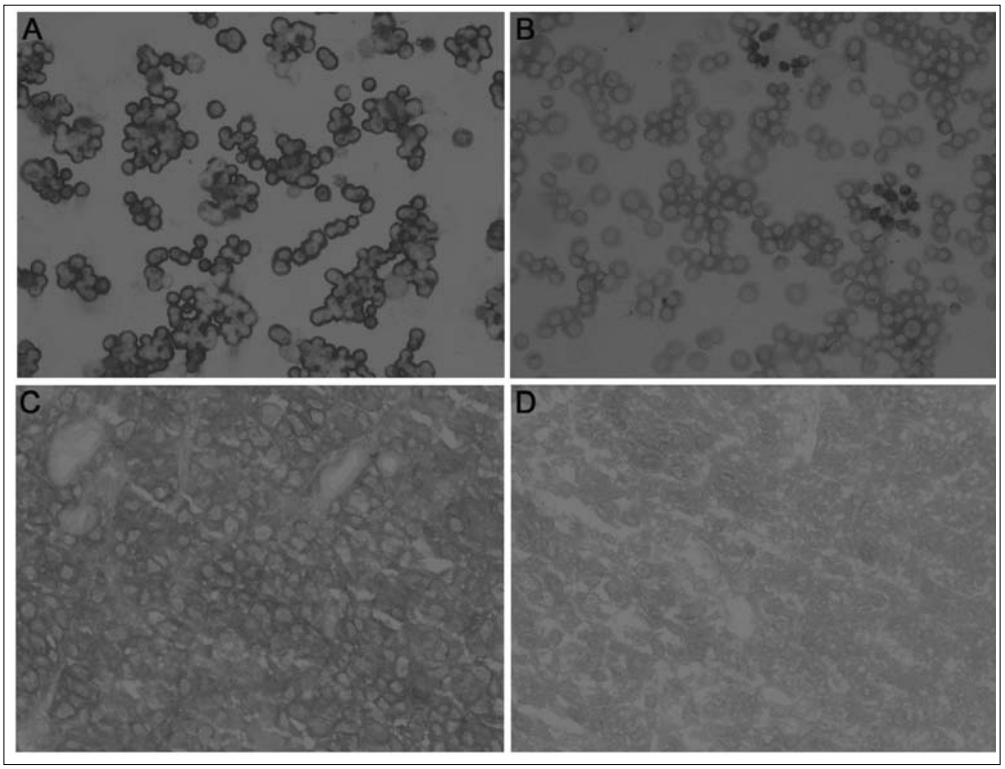

Figure 1. Immunohisto-chemical staining of Met expression with biotiny-lated DN30 on cytospins of GTL-16 (A) and FaDu (B) cells and on frozen sections of GTL-16 (C) and FaDu (D) xenografts

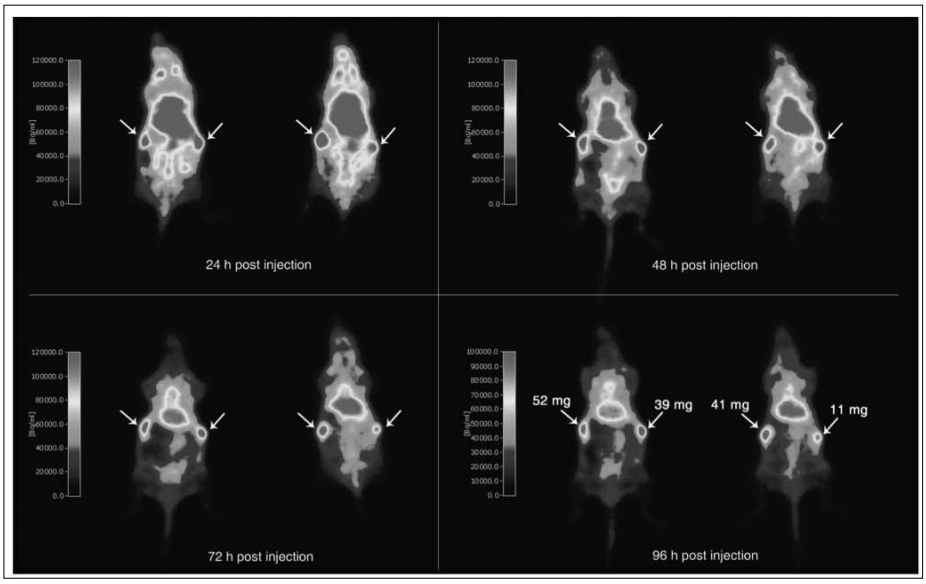

Figure 2. Sequential HRRT PET images (coronal slices) of two different GTL-16-xenograft-bearing nude mice at 1, 2, 3 and 4 days after i.v. injection with ^{89}Zr-DN30 (2.6 MBq, 100 µg mAb). Image planes have been chosen where both the left and right tumor are visible. Arrows indicate xenografts.

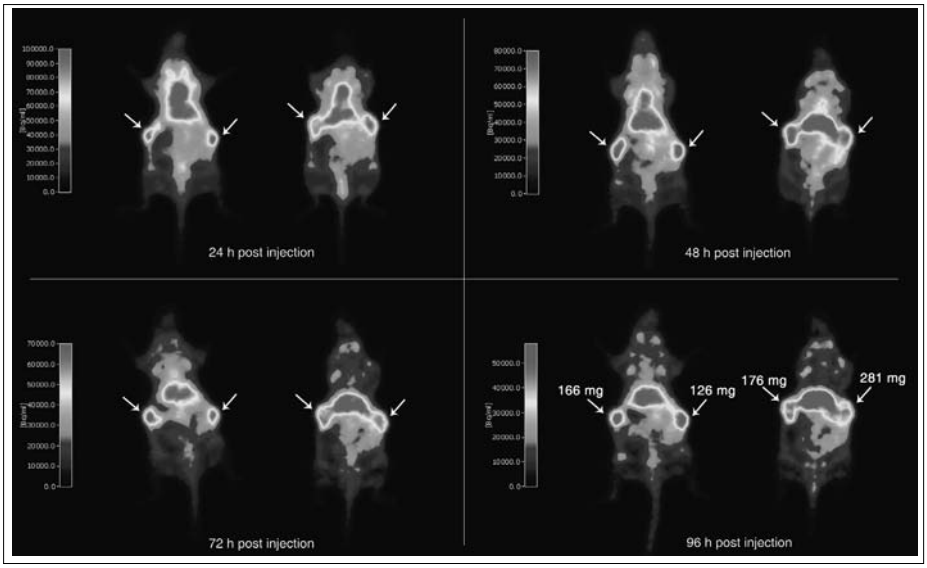

Figure 3. Sequential HRRT PET images (coronal slices) of two different FaDu-xenograft-bearing nude mice at 1, 2, 3 and 4 days after injection with ^{89}Zr-DN30 (1.8 MBq, 100 µg mAb). Image planes have been chosen where both the left and right tumor are visible. Arrows indicate xenografts.

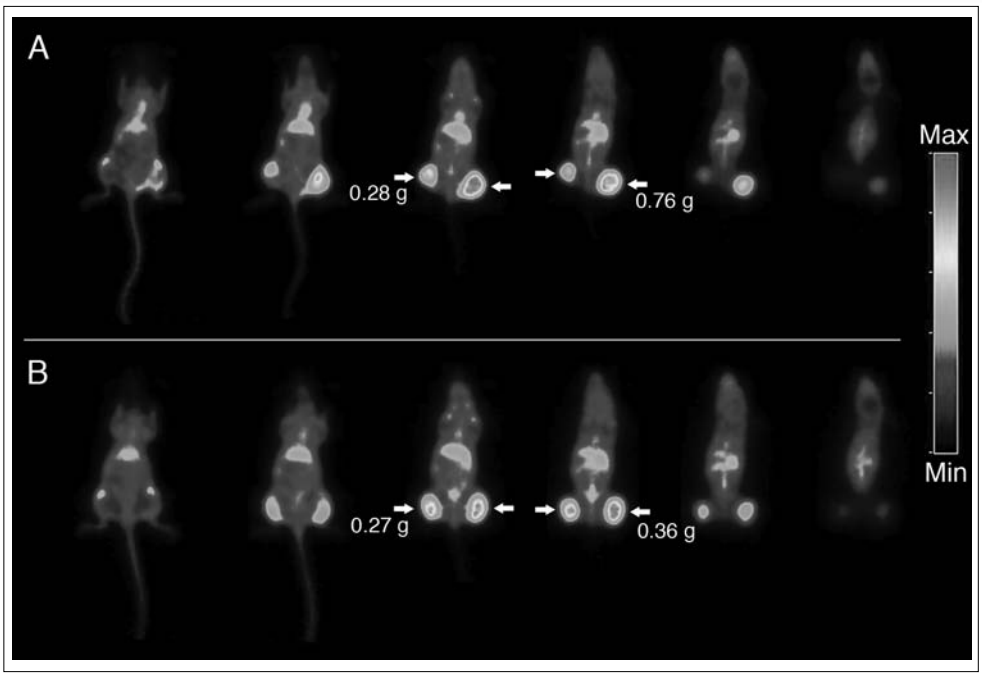

Figure 6. HRRT PET images (coronal slices) of two different FaDu xenograft bearing nude mice at 72 hours after injection with ^{89}Zr-Df-Bz-NCS-cU36 (A) or with ^{89}Zr-*N*-sucDf-cU36 (B). Slices from ventral (*left*) to dorsal (*right*). Images demonstrate high level of radiolabeled antibody accumulating in the tumor (Arrows point to flank tumors) and low levels of tracer uptake in nontarget tissues.

Chapter 7

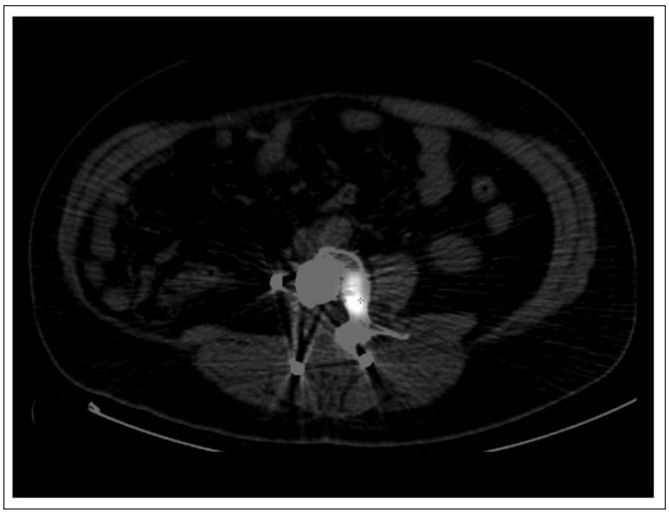

Figure 1. Patient with metastasized thyroid cancer. After extensive vertebral surgery and several treatments with ^{131}I, it remained unclear whether vital tumor tissue was still present. ^{124}I-PET-CT clearly shows iodine uptake (i.e. vital tumor) at the left side of the vertebra. Therefore, adjuvant high dose ^{131}I therapy is recommended for this patient.

Chapter 8

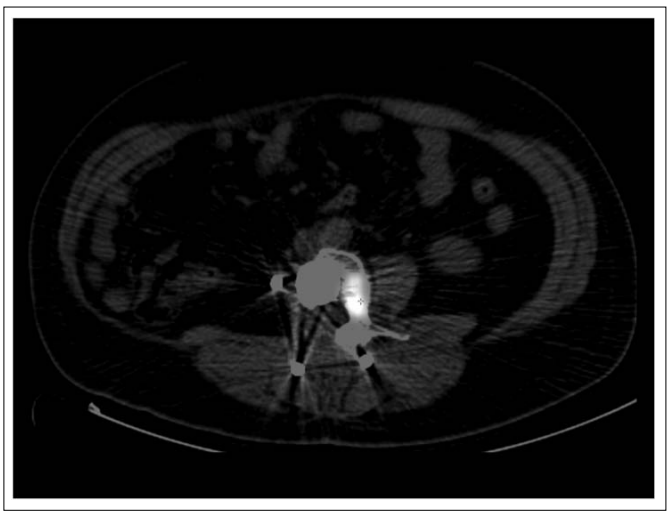

Figuur 2. Patiënt met een gemetastaseerd schildklier-carcinoom. Na uitgebreide wervelchirurgie en diverse behandelingen met radioactief jodium (^{131}I) was onduidelijk of er nog vitaal tumorweefsel aanwezig was. ^{124}I-PET-CT toont evidente jodium-opname (= tumor activiteit) links in een wervel. Er is dus een indicatie voor aanvullende hoge dosis therapie met ^{131}I.

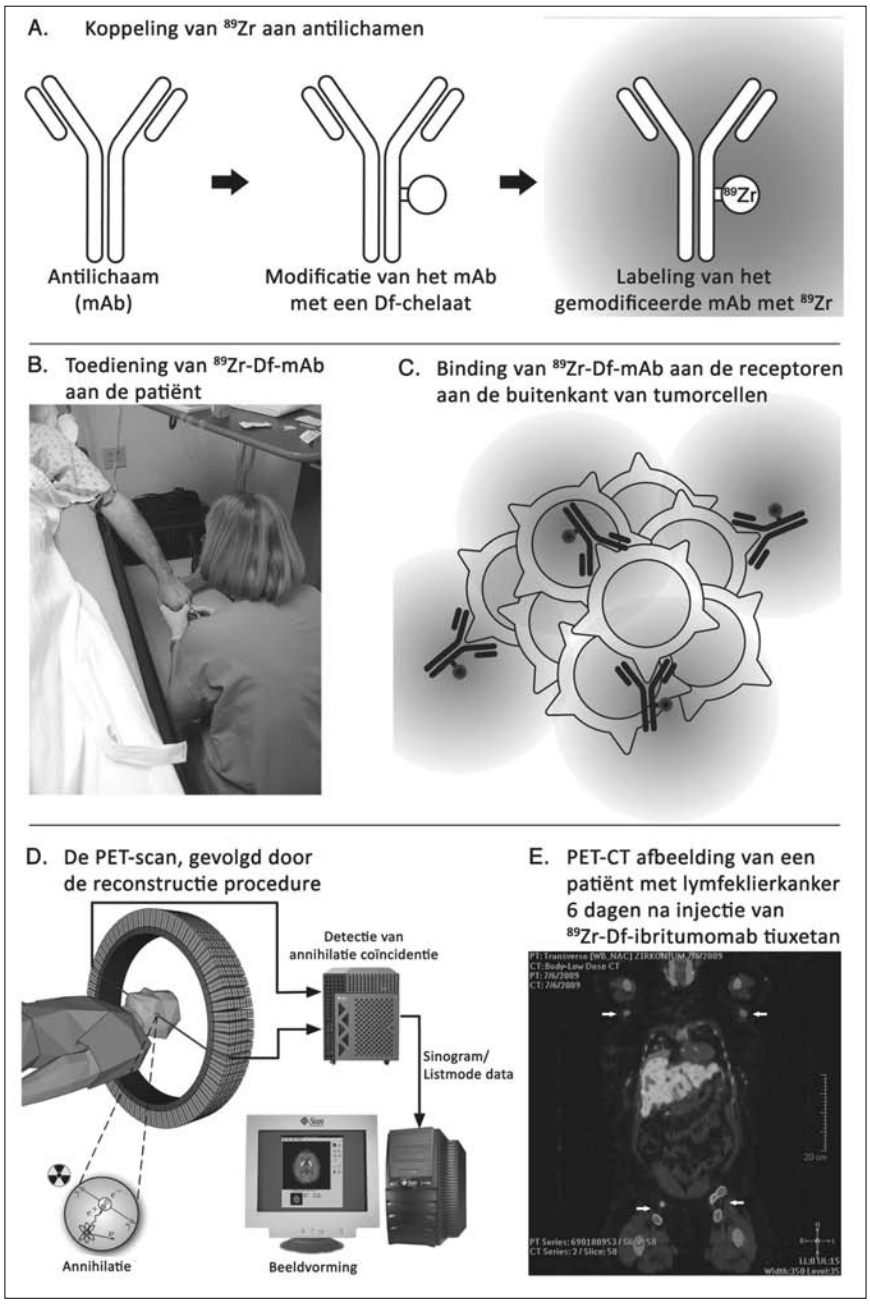

Figuur 1. Principe van een immuno-PET procedure. Dit schema toont de verschillende stappen in een immuno-PET procedure. (A) Koppeling van de positron emitter aan het mAb. (B) Toediening van het radioimmunoconjugaat aan de patiënt. (C) Binding van het radioimmunoconjugaat aan de tumor. (D) De patiënt wordt op verschillende tijdstippen na injectie gescand met behulp van een PET camera en de beelden worden softwarematig verwerkt. (E) De uiteindelijke PET-CT afbeelding van de patiënt. Zichtbaar zijn de tumoren in de lies en in de oksels (aangegeven met pijlen). Tevens zichtbaar, niet specifieke ophoping in de lever.